University of Plymouth

PEARL **https://pearl.plymouth.ac.uk**

04 University of Plymouth Research Theses 01 Research Theses Main Collection

2016

Effects of marine environment exposure on the static and fatigue mechanical properties of carbon fibre-epoxy composite

Meng, Maozhou

http://hdl.handle.net/10026.1/5341

http://dx.doi.org/10.24382/4728
Plymouth University

All content in PEARL is protected by copyright law. Author manuscripts are made available in accordance with publisher policies. Please cite only the published version using the details provided on the item record or document. In the absence of an open licence (e.g. Creative Commons), permissions for further reuse of content should be sought from the publisher or author.

This copy of the thesis has been supplied on condition that anyone who consults it is understood to recognise that its copyright rests with its author and that no quotation from the thesis and no information derived from it may be published without the author's prior consent.

Effects of marine environment exposure on the static and fatigue mechanical properties of carbon fibre-epoxy composite

by

Maozhou Meng

A thesis submitted to the University of Plymouth in partial fulfillment for the degree of

Doctor of Philosophy

School of Marine Science and Engineering

University of Plymouth

January 2016

ABSTRACT

This thesis studies the static and fatigue failure of carbon fibre-epoxy composite for marine use. The primary objective is to investigate the effects of sea water ingress on the static and cyclic performance of laminated composites, by using the combination of experimental, numerical and analytical approaches.

Experiments were carried out to collect evidence, including data and images, for further analysis. Samples were made from autoclave-cured carbon fibre-epoxy pre-preg for the static, moisture diffusion and fatigue tests. Three chambers were used in the diffusion test, containing fresh water (tap water), sea water and sea water at 70 bar hydrostatic pressure respectively. And the chambers were placed in an oven at a constant temperature 50 °C in order to accelerate the water absorption. Optical and scanning electron microscopies (SEM) were employed to inspect for manufacturing defects and to identify the failure modes. Some formulae were derived to predict the material properties of laminated composites, to validate the mechanical tests, and to explain the failure criteria of composites.

Finite element analysis (FEA) was employed to study the phenomena that were observed in the experiments. FEA has the aim to simulate the static, diffusion and fatigue behaviour involving multiphysics and multiscale effects. The FEA modelling has revealed details of the stress and moisture distributions, which have helped to understand the failure mechanisms of laminated composites.

Classical laminate theory (CLT) was employed to develop an analytical model. The basic principles of CLT were extended to three-dimensions, and the analytical solution was critically compared with the FEA results. Some MATLAB tools based on CLT were developed to predict the properties of laminated composites and to analyse the experimental data. These MATLAB codes are shown in the appendix.

This thesis has contributed to an improved knowledge of the failure mechanisms of composite materials in both normal and marine environments, and to optimize structural design of FRP composites.

KEY WORDS: CFRP; fatigue; failure mechanism; bending; marine environment; moisture; FEA; CLT.

ACKNOWLEDGEMENT

First of all, I would like to express my sincere gratitude to Prof Huirong Le who has directed me into this fascinating academic field with his continuous encouragement and support. His valuable advice and sharp insights, as well as his patience and understanding during difficult times built the solid foundation of this thesis. I would like to gratefully thank Dr Stephen Grove and Dr MD Jahir Rizvi for their constructive comments and substantive guidance for my study. Many thanks go to Prof Long-yuan Li for his advice on FEA modelling, Dr Richard Cullen for his kind help with composites manufacturing, Terry Richards and Dr Zoltan Gombos for their support of the mechanical tests, Dr John Summerscales for his comments on my published papers, Miss Urvashi Danookdharree for her help on SEM study, and Prof Stephen Tsai for his advice on omni strain envelope transformation.

I would like to sincerely acknowledge the financial support provided by School of Marine Science and Engineering, University of Plymouth, for my PhD study through a UK Scholarship for Excellence. I would also like to thank the Santander University Networks for providing the Santander Seed-Corn Research Scholarship, Henry Lester Trust Ltd for the providing Henry Lester Scholarship.

Immense appreciation attributes to my intimate friends and colleagues for their precious help and companionship during the past two years. It is them who helped me to adapt to a new environment and showed me the joy of a new life style.

I am deeply grateful to my family in China, my ever beloved parents who brought me to this wonderful world, loved me from the very beginning and guided me right from wrong. Without their love and support, I would not be able to go this far. Last but not least, many thanks to my girlfriend, Shanshan Cheng, for patiently enduring and supporting me in the preparation of this thesis.

AUTHOR'S DECLARATION

At no time during the registration for the degree of Doctor of Philosophy has the author been registered for any other University award without prior agreement of the Graduate Committee.

Work submitted for this research degree at the University of Plymouth has not formed part of any other degree either at University of Plymouth or at another establishment.

This PhD study was financed with the aid of School of Marine Science and Engineering, University of Plymouth for the UK PhD scholarship.

External Contacts: mengmaozhou@gmail.com

Word count of main body of thesis: 45,774 words

Signed: _____

Date: _____

CONTENTS

ABSTRACT i

ACKNOWLEDGEMENT ii

AUTHOR'S DECLARATION iii

CONTENTS iv

LIST OF FIGURES viii

LIST OF TABLES xix

NOMENCLATURE xxi

Chapter 1 – INTRODUCTION 1

1.1 Marine composites 1

1.2 Composite fatigue 3

1.3 Research scope and objectives 4

1.4 Methodology 5

1.5 Structure of this thesis 6

Chapter 2 – LITERATURE REVIEW 9

2.1 CFRP composites 9

2.1.1 Carbon fibre 9

2.1.2 Epoxy 11

2.2 Composite failure 13

2.2.1 Tensile 14

2.2.2 Compressive 14

2.2.3 Bending 17

2.2.4 First ply failure 18

2.3 Fatigue analysis 18

2.3.1 Low cycle and high cycle fatigue 18

2.3.2 Fatigue failure criteria 19
2.3.3 Cycle count 21
2.4 Marine environment 22
2.4.1 Moisture 22
2.4.2 Temperature 25
2.4.3 Pressure 26
2.4.4 Saline 27
2.4.5 Other aspects 28
2.5 Research methods 28
2.5.1 Experimental model 28
2.5.2 Numerical model 30
2.5.3 Analytical model 32
2.6 Summary 32
Chapter 3 – MANUFACTURE AND INSPECTION 34
3.1 Specimen manufacturing 34
3.2 Specimen inspection 39
3.2.1 Void inspection 39
3.2.2 Fibre misalignment 40
3.2.3 Fibre packing 42
3.3 Extensional classical laminate theory (CLT) 45
3.3.1 Elastic properties 45
3.3.2 Extensional CLT formulae 49
3.3.3 Hygrothermal and thermal properties 52
3.4 Summary 53
Chapter 4 – Bending tests and modelling 54
4.1 Experiment setup 54

4.2 3D FEA modelling 57
4.2.1 Model definition 57
4.2.2 Flexural strength and modulus 62
4.2.3 Interlaminar shear strength 68
4.3 Unequal compressive/tensile moduli 78
4.3.1 Failure criteria 79
4.3.2 Unidirectional laminate 82
4.3.3 Multi-directional laminate 85
4.3.4 Fibre microbuckling 89
4.4 Summary 91
Chapter 5 – MOISTURE DIFFUSION MEASUREMENT AND MODELLING 93
5.1 Experimental setup 93
5.1.1 Diffusion test 94
5.1.2 Bending test 98
5.2 Multi-scale FEA modelling 100
5.2.1 Definition of micro-model 100
5.2.2 Definition of macro-model 104
5.3 Failure mechanisms 106
5.3.1 Moisture diffusion 106
5.3.2 Hygrothermal expansion 110
5.3.3 Interaction between bending and diffusion 113
5.4 SEM analysis 122
5.5 Summary 126
Chapter 6 – INTERATION BETWEEN WATER INGRESS AND FATIGUE 128
6.1 Fatigue tests 128
6.1.1 Machine setup 128

6.1.2 Fatigue life 134
6.1.3 Fatigue stiffness 137
6.2 Creep tests 148
6.2.1 Machine setup 148
6.2.2 Creep stiffness 153
6.3 Buckling-driven delamination 157
6.3.1 Virtual crack closure technique 157
6.3.2 FEA implementation 159
6.4 Summary 167
Chapter 7 – CONCLUSIONS 169
7.1 Summary of findings 169
7.2 Contributions to knowledge 173
7.3 Future research 174
REFERENCES 175
PUBLICATIONS 194
CONFERENCE PRESENTATIONS 195
APPENDIX A: MATLAB Code for 3D CLT 196
APPENDIX B: MATLAB Code for failure envelopes 216
APPENDIX C: MATLAB Code for 3-point bending 234
APPENDIX D: MATLAB Code for 4-poing bending 252

LIST OF FIGURES

Figure 1.1 The 600-kW marine current turbine installed in Strangford Lough in County Down, Northern Ireland (SIEMENS, 2008)..... 2

Figure 1.2 Comparison of fatigue strengths of CFRP/GFRP composites, steel, aluminium and titanium. Source: The Japan Carbon Fibre Manufacturers Association (JCMA, 2014)...... 4

Figure 1.3 The flow chart of the project 8

Figure 2.1 The curing reaction of hardener and epoxy ring..... 12

Figure 2.2 Composite failure mechanisms in micro scale: (a) fibre fracture; (b) fibre pull-out; (c) matrix fracture; (d) fibre/matrix debonding; (e) fibre kinking; (f) fibre radial split...... 13

Figure 2.3 Ratio of longitudinal compressive modulus to tensile modulus of various CFRP and GFRP composites. The average and their respective coefficient of variation are also shown in the figure. Data source: Polymer matrix composites material handbook (Dept. of defense, 1997). 16

Figure 2.4 Fatigue characteristic of FRP composites 19

Figure 2.5 Rain-flow counting example: (a) spectrum loading; (b) clockwise rotated time history; (c) stress-strain hysteresis loop...... 22

Figure 3.1 Schematics of crosslink network of 977-2 epoxy resin. The value n is in the range of 0-25...... 34

Figure 3.2 (a) Schematic representation of carbon fibre (Kardos, 1985), and (b) region of fibre-epoxy interface (Meng, Rizvi et al., 2016) 35

Figure 3.3 The temperature history of the autoclave 36

Figure 3.4 The preparation of pre-preg CFRP composite: (a); tailored specimens; (b) pre-preg plates sealed in vacuum bag before being cured; (c) pre-preg plates after being cured. 37

Figure 3.5 The cutting pattern of the composite laminates. UD and UT laminates were cut from one panel with perpendicular orientation, while CP and AP were from the other. 37

Figure 3.6 (a) Preparation of the polished laminate specimens for the microscopic study; (b) the specimens were placed on the optical microscope; (c) images extract and data processing 39

Figure 3.7 Optical microscopic image of the unidirectional laminate. A huge void was found, which was probably because of the manufacturing process. 40

Figure 3.8 Schematics of the measurement of fibre misalignment in a long fibre UD laminate (a), and a typical microscope image of the cross-section of UD laminate (b) 41

Figure 3.9 Normalized fibre misalignment angle in long fibre CFRP composite. Approximately ten thousand fibres are included in the statistics. 42

Figure 3.10 Fibre lattice of a unidirectional laminate 43

Figure 3.11 Statistics of fibre distance of a unidirectional laminate. Approximate two thousand specimens are included in the statistics. 44

Figure 3.12 Illustration of composite lamina, off-axial lamina and laminate 45

Figure 3.13 (a) Comparison between experimental data for axial and transverse Young's moduli, E1 and E2 for polyester/glass fibre composites (Hull and Clyne, 1996); (b) comparison of classic formulae and FEA result for transverse modulus (Cytec 977-2-HTS) 46

Figure 3.14 A bulk object under hydrostatic stress 47

Figure 4.1 Illustration of the 3-point bending test 54

Figure 4.2 The offset of the 3-point bending 55

Figure 4.3 Modelling conditions were equal to testing conditions. The two 'simply supported' boundary conditions at two ends were replaced by positive distributed loads ($P/2$). 58

Figure 4.4 Boundary conditions applied in a) symmetric laminates and b) angle-ply laminate 59

Figure 4.5 Mesh plot of $20mm \times 10mm$ laminate with local refinement. The edge area was refined to investigate the free edge effect. 61

Figure 4.6 The effect of mesh size near the edge region on the distribution of global interlaminar shear stress in short-beam angle-ply laminate. The results show that 0.5 was sufficient to get mesh independency. 61

Figure 4.7 Distribution of tensile stress σ_1 on bottom surface of long-beam unidirectional laminate. The stress (FEA) shows a minor fluctuation about 2% between the free edge and central areas. 63

Figure 4.8 Microscope image of failure mode in a long-beam unidirectional laminate under three-point bending (side-view). Approximate 70% of the plies failed by compression, and fibre microbuckling could be observed on the compressive side. $\lambda_0 \approx 12 \times 2r$: half wavelength of fibre microbuckling; β=30°: orientation of microbuckling band. 63

Figure 4.9 Deflection-load curves of long-beam unidirectional laminate under three-point bending. Laminate failed rapidly after the first 'stiffness losses' appeared. 64

Figure 4.10 Schematic diagram of fibre microbuckling of long-beam unidirectional laminate. With the same fibre orientation, the second ply is likely to 'buckle' following the first ply by the compressive stress, and then followed by the third ply, and so on. 65

Figure 4.11 Distributions of stress components σ_1 (left) and σ_2 (right) in long-beam cross-ply laminate and their side-views 65

Figure 4.12 Through-thickness distributions of flexural stress σ_1 (s11) and σ_2 (s22) at central point of long-beam cross-ply laminate. The stresses jump rapidly at the interface between longitudinal and transverse plies. 66

Figure 4.13 Schematics of fibre microbuckling of long-beam cross-ply laminate. With the support of the second ply, the first ply is more difficult to fail by microbuckling. 66

Figure 4.14 Typical microscope failure image of long-beam cross-ply laminate (left) and its tensile failure in 3-point bending (right). 67

Figure 4.15 Deflection-load curves of long-beam cross-ply laminate. The small and large 'stiffness losses' represent the failure of transverse and longitudinal plies. ..67

Figure 4.16 Distribution of Tsai-Hill 'failure factor' in long-beam cross-ply laminate. The transverse plies exceeded the failure criterion rather than the surface plies. 68

Figure 4.17 Distribution of interlaminar shear stress τ_{13} on middle plane of short-beam unidirectional laminate. The higher value at free edge region implies the crack could be initialized from this area. 69

Figure 4.18 Typical failure images of short-beam unidirectional laminate and the distribution of out-of-plane normal stress σ_3. The combination of interlaminar shear stress τ_{13} and out-of-plane normal stress σ_3 leads to delamination at compressive (top) part of the laminate 70

Figure 4.19 Distribution of interlaminar shear stress τ_{13} of short-beam cross-ply laminate. The free edge effect is slight, compared with short-beam unidirectional laminate. 70

Figure 4.20 Distributions of normal stress σ_2 (left) and σ_3 (right) in short-beam cross-ply laminate and their side-views. The maximum stresses appeared at the second ply (90°), and strong free edge effect on σ_3 is observed. 71

Figure 4.21 Typical microscope failure image of short-beam cross-ply laminate. The initial delamination began from the 2nd ply, corresponding to the maximum σ_2 and σ_3 in Figure 4.20. 71

Figure 4.22 Interlaminar shear stress τ_{xz} and τ_{13} distribution through-thicknesses in short-beam angle-ply laminate (CLT). The discrete τ_{13} represents the complicated lamina orientation. 72

Figure 4.23 Distributions of interlaminar shear stress through-thicknesses in short-beam angle-ply (3D FEA model). The 'stress peaks' at edge area converge to CLT at centre, and the maximum value appears at z=1.44mm (interface of 4-5 plies)...73

Figure 4.24 3D distribution of τ_{13} in short-beam angle-ply laminate. The slice plot reveals the distribution of τ_{13} in 3D scale, and the surface plot shows the variation of τ_{13} in different plies with particular fibre orientation. 74

Figure 4.25 Contour curves of interlaminar shear stress τ_{13} in short-beam angle-ply laminate (z=1.44mm). The extremely high stress only appears near the edge area. 74

Figure 4.26 Interaction between axial stress and shear stress in off-axis laminate (according to CLT). The value of η represents the couple of normal stress to shear stress. 75

Figure 4.27 Slice plot (upper) and surface plot (lower) of in-plane shear stress in short-beam angle-ply laminate. The values of τ_{12} near the middle area of top and bottom surfaces are so high that strong distortion was observed in the bending test. 77

Figure 4.28 Typical failure image of angle-ply laminate under bending test condition. Cracks appeared at free edge area, but without penetrating inside the volume. The positions of cracks correspond to a peak of interlaminar shear stress, as shown in Fig.4-23. Specimen twisting induced by in-plane shear stress was observed. 77

Figure 4.29 Deflection-load curves in angle-ply laminate from three-point bending test. Each crack represented a 'stiffness losses' in bending test. 78

Figure 4.30 Failure envelopes of T800-Cytec CFRP composite in strain space 81

Figure 4.31 Omni envelopes of T800/Cytec (left) and T700/C-Ply 55 (right) with different λ values 82

Figure 4.32 Unidirectional laminate under bending. The compressive stress and tensile stress re-distribute through-thickness due to the unequal compressive and tensile moduli. 83

Figure 4.33 Sandwich structure representation of a multi-directional laminate: compressive sheet, core, and tensile sheet. Neutral plane shifts to the bottom side but is still located in the core area. 86

Figure 4.34 A schematic of a single fibre microbuckling in unidirectional lamina. On the fibre concave side, the fibre compressive strain is expected to be higher, and the fibre is more likely to break. 89

Figure 5.1 The hydrostatic chamber used in the diffusion test 94

Figure 5.2 Moisture diffusion in UD/UT/CP/AP laminates immersed at 50°C sea water ('Sea'), tap water ('Tap') and sea water with 70bar hydrostatic pressure ('SP') 96

Figure 5.3 Orthotropic moisture diffusivity assumption and the two geometries for the calculation of longitudinal and transverse diffusivities 96

Figure 5.4 Hygrothermal expansion of UT $[90]_{16}$ laminate varying with moisture content 98

Figure 5.5 Typical flexural force-extension curves of UD/UT/CP laminates 99

Figure 5.6 Measured ILSS (MPa) of UD/CP/AP laminates before (0M) and after moisture diffusion. 0-M: dry condition; 1-M: 1-month immersion; 3-M: 3-month immersion. 99

Figure 5.7 Optical microscopic image of a UT specimen and schematics of FEA model 101

Figure 5.8 The boundary conditions for the multiphysics micro model: species transport and structural mechanics 102

Figure 5.9 A local view of the mesh, showing the three phases in the micro model 103

Figure 5.10 Moisture distribution according to FEA in AP short beam laminate after 30 days' water immersion. The slice plot shows a smooth distribution of moisture concentration regardless of the ply orientations. 108

Figure 5.11 FEA moisture distribution of AP short beam laminate along the mid-line after 6/30/60/90 days' water immersion respectively. The moisture diffused smoothly inside the laminate, and converged to saturation. 108

Figure 5.12 Comparison of mass gain: Fick's fit and FEA computation with various values of D_{in} 109

Figure 5.13 Moisture distribution in the micro model after one hour immersion (dimension unit: μm) 110

Figure 5.14 FEA out-of-plane hygrothermal expansion of UD/UT/CP/AP short beam laminates 111

Figure 5.15 FEA result for interlaminar shear stress τ_{13} induced by hygrothermal effect in AP short beam laminate after one month's diffusion 112

Figure 5.16 FEA result for interlaminar shear stress τ_{13} induced by hygrothermal expansion in CP short beam laminate from macro-model after one month's water absorption 113

Figure 5.17 The through-thickness distribution of σ_2 at central point (x=10mm, y=5mm) of CP short beam laminate in the time domain from macro-model. The transverse stress shifts into compression. 114

Figure 5.18 FEA through-thickness distribution of τ_{13} after one month's diffusion in AP short beam laminate from macro-model 115

Figure 5.19 Typical failure image of AP short beam laminate in ILSS test (side view). (a) in dry condition; (b) after one month's tap water immersion. 115

Figure 5.20 Typical failure image of UD short beam laminate in ILSS bending test (side view): (a) in dry condition, (b) after 1-month's water immersion. The delamination was uncompleted in wet condition (b). 116

Figure 5.21 Flexural strength of CP/UD/UT laminates after 3-month's water absorption. The values were normalized by the measurement in dry condition. . 117

Figure 5.22 Flexural modulus of CP/UD/UT laminates after 3-month's water absorption. The values were normalized by the measurement in dry condition. . 118

Figure 5.23 (a) Schematics of stress distribution and the chosen line for the stress plot; (b) First principal stress distribution along the chosen line. The mean value is also shown in the figure. 120

Figure 5.24 a) Schematics of the chosen line for the strain plot; (b) First principal strain distribution along the chosen line. 120

Figure 5.25 Distribution of the first principal strain. Peak values were found at interphases. 121

Figure 5.26 The distributions of the first principal stress along five chosen paths in the central 121

Figure 5.27 Through-thickness distribution of interlaminar shear stress of macro model for angle-ply laminate: (a) dry condition and (b) after one-month immersion. 122

Figure 5.28 SEM image of dry sample with a local magnification 123

Figure 5.29 SEM image of tap water condition 123

Figure 5.30 SEM image of sea water condition 124

Figure 5.31 EDS analysis of the sea water condition: (a) analysis point; (b) elemental content 125

Figure 5.32 EDS analysis of the dry condition: (a) analysis point; (b) elemental content 126

Figure 6.1 Sinusoidal cyclic loading condition of the fatigue test 128

Figure 6.2 Fatigue test condition: (a) 3-point bending for specimen without immersion (Dry-3P); (b) 4-point bending for specimen without immersion (Dry-4P) and for immersed specimen without the cover of wet sponge (Wet2-4P); and (c) 4-point bending for immersed specimen covered by wet sponge (Wet1-4P). 131

Figure 6.3 Loading history at the beginning of the fatigue test for the cross-ply laminate 132

Figure 6.4 The reaction force (a) and deflection (b) responses of a UD specimen at the moment when the specimen broke 133

Figure 6.5 The reaction force (a) and deflection (b) responses of a CP specimen at the stage when the specimen broke 133

Figure 6.6 The reaction force (a) and deflection (b) responses when the machine was manually stopped 134

Figure 6.7 Fatigue life of CP laminate. The fatigue cycle is plotted as logarithm scale. Wet1-4P: immersed specimen, covered by wet sponge while 4-point bending

fatigue testing; Wet2-4P: immersed specimen, without wet sponge cover while testing. 135

Figure 6.8 Fatigue life of UD laminate. Tap: tap water immersion; Sea: sea water immersion; SP: sea water immersion with 70 bars hydrostatic pressure. 136

Figure 6.9 Schematics of 4-point bending and the distribution of moment 138

Figure 6.10 The typical hysteresis loops of the deflection-reaction force of CP-dry laminate in 3-point bending fatigue test at the 80% UFS loading level 139

Figure 6.11 The typical hysteresis loops of the CP-dry laminate in 3-point bending fatigue test at the 80% UFS loading level in view of deflection-normalized stiffness. The stiffness was normalized to the value of dry condition. The directions of the hysteresis loops are also shown as two coloured arrows in the figure. 140

Figure 6.12 Typical fracture image of the CP laminate in 4-point bending fatigue test at the 80% UFS loading level. The specimen survived after withstanding more than five million cycles. 141

Figure 6.13 Typical fatigue stiffness of the CP-dry laminates with 'infinite fatigue life' in both 3-point and 4-point bending fatigue tests at the 80% UFS loading level. The fatigue stiffness was normalized to the flexural modulus which was tested in quasi-static bending. 142

Figure 6.14 Typical fatigue stiffness of the CP-dry laminates in both 3-point and 4-point bending fatigue tests at 90% UFS loading level. Both the two specimens failed. 143

Figure 6.15 Typical fatigue stiffness of the UD-dry laminate in 4-point bending fatigue test at 80% UFS loading level. No UD-dry specimen was tested in 3-point bending at this loading level. 144

Figure 6.16 Typical fatigue stiffness of the UD-dry laminates in both 3-point and 4-point bending fatigue test at 90% UFS loading level 144

Figure 6.17 Typical fatigue stiffness of the CP laminates in 4-point bending fatigue test in dry and wet environments 145

Figure 6.18 Typical fatigue stiffness of the UD laminates in 4-point bending fatigue test in dry and wet environments 146

Figure 6.19 Comparison of the CP specimen failure mode in 3-point bending test: (a) quasi-static bending and (b) bending fatigue 147

Figure 6.20 Comparison of the CP specimen failure mode in 4-point bending test: (a) quasi-static bending and (b) bending fatigue 147

Figure 6.21 Typical failure modes of CP and UD laminates tested in 4-point quasi-static bending 148

Figure 6.22 3-point bending creep test for the angle-ply laminate 149

Figure 6.23 The loading curves of the angle-ply laminates in quasi-static 3-point bending test. DA: angle-ply laminate without immersion; SA: sea water immersion; SPA: sea water immersion with 70bar hydrostatic pressure; TA: tap water immersion. The 'DA1' specimen was tested at 1mm/min strain rate, while all the others were at 2mm/min. 150

Figure 6.24 The failure mode of AP-dry specimen in 3-point bending quasi-static test 151

Figure 6.25 The typical loading curve of an AP-dry specimen in 3-point bending creep test, showing linear relationship between load and deflection 152

Figure 6.26 The typical deflection curve of an AP-dry specimen in 3-point bending creep test at the creep deformation stage, showing a perfect power law by the loading time. The power law fitting results are also shown in the figure. 153

Figure 6.27 Creep stiffness of AP specimen at 200N 156

Figure 6.28 Creep stiffness of AP specimen at 300N 156

Figure 6.29 Creep stiffness of AP specimen at 400N 157

Figure 6.30 Configuration of the virtual crack closure technique 158

Figure 6.31 Schematics of fatigue crack growth relative to the Paris law. There is no fatigue crack initiation or growth when the strain energy release rate is lower than G_{thress}. 159

Figure 6.32 Schematics of the three layers FEA model 159

Figure 6.33 Mesh plot of the three layer FEA model and the loading history. An initial crack (0.2 mm) was embedded at the interface between ply15 and ply16

under the load cell. The crack path (shown as red dots) is also shown in the figure. 161

Figure 6.34 Stress distribution in the bending fatigue. A magnified view of the delamination is also shown in the figure. 161

Figure 6.35 Relation between reaction force and deflection for three cases: (a) FEA simulation without initial crack; (b) FEA simulation with 0.2mm initial crack; and (c) a typical experimental curve of CP-dry specimen. 162

Figure 6.36 Distributions of mode I and mode II strain energy release rates along the crack path when the buckling initialized. The crack path was normalized. ... 163

Figure 6.37 Distributions of mode I and mode II strain energy release rates along the crack path after the catastrophic delamination. The contact region enlarged due to the tangential slide of the specimen/load cell and the buckling deformation of ply16. 163

Figure 6.38 Distribution of longitudinal stress component (s11) of the 3D solid FEA model: (a) isotropic view; (b) side view; and (c) a magnified side view. 165

Figure 6.39 Bonding state of the interfacial elements as the fatigue crack propagating (top view). The blue elements denote debonding state while the red elements denote bonding state. 166

Figure 6.40 Development of the buckling-driven delamination in bending fatigue: (a) edge cracks initialized; (b) edge cracks penetrated through width; (c) foregoing edge cracks; (d) buckling and buckling-driven delamination 166

LIST OF TABLES

Table 2-1 Comparison of properties for several typical fibres (data source: Wikipedia and respective product technical data sheet) 10

Table 2-2 Comparison of properties for several typical matrices (data source: Wikipedia and respective product technical data sheet) 12

Table 2-3 Longitudinal tensile/compressive moduli of CFRP composites and their strengths. Data source: Polymer matrix composites material handbook (Dept. of defense, 1997). 15

Table 2-4 Comparison of longitudinal and transverse CTE (α) and thermal conductivity (ρ) of some common glass fibres, carbon fibres and epoxy resins (data source: Wikipedia and respective product technical data sheet) 26

Table 2-5 Chemical analyses of mean river water and seawater, and a comparison of relative concentrations in river water and ocean (Livingstone, 1963) 27

Table 3-1 Laminate configuration 36

Table 3-2 Mechanical properties of the fibre and matrix of Cytec 977-2-12kHTS. The fibre transverse modulus is estimated as 10% of its longitudinal modulus, according to references (Bowles and Tompkins, 1989; Voyiadjis and Kattan, 2005; Hyer, 2009) 38

Table 3-3 Material properties of lamina 49

Table 3-4 Material properties of the laminates. The flexural modulus is also listed in the Table 52

Table 4-1 Experimental results from three-point bending tests and the Standard Deviations 57

Table 4-2 Loading forces in different groups of coupons 58

Table 4-3 Maximum ply normal stress and interlaminar shear stress by 3D CLT 62

Table 4-4 Engineering constants (Tsai and Melo, 2014) and the interaction ratio (CLT) 76

Table 4-5 Engineering constant of two CFRP composites and their strength (Tsai and Melo, 2014) 81

Table 4-6 Normalized flexural properties of two layups of HTS-12K/977-2 when λ=0.9 and λ=1 88

Table 4-7 Value of maximum fibre compressive strain on fibre concave side ε_f^c various to the λ_0 value and the maximum compressive strain on the top surface $\left(\varepsilon_1^c\right)_{\max}$ 90

Table 5-1 Accelerated diffusion test results (50°C) 97

Table 5-2 Bending test results and their Standard Deviations (SDs) 100

Table 5-3 Mechanical and chemical properties of carbon fibre and epoxy 103

Table 5-4 Material properties for moisture diffusion modelling 105

Table 5-5 Geometries and boundary conditions in different groups of coupons .. 106

Table 6-1 Loading levels of the UD and CP laminates for the fatigue test. The level '100%' represents the ultimate flexural strength which was tested in quasi-static bending. 130

Table 6-2 Flexural modulus of AP laminate at different loading level and immersions 152

Table 6-3 The fitting results of the four parameters for equation (6-15). The R^2 value is also given in the table (the unit of stress: MPa; time: minute). 155

Table 6-4 Material properties for FEA simulation. The out-of-plane direction in 3D corresponds to the transverse direction in 2D model, i.e. E_y=E_3. For the comparison, the properties of CP $[0/90]_{4s}$ laminate are also shown in the table. .. 160

NOMENCLATURE

$[a],[b],[d]$	Block matrices of $\begin{bmatrix} a & b \\ b & d \end{bmatrix}$ matrix (inversed $\begin{bmatrix} A & B \\ B & D \end{bmatrix}$ matrix)
c_1, c_2, c_3, c_4	Parameters of Paris law
C_1, C_2, C_3, C_4	Parameters of Creep stiffness
r_1, r_2	Radius of load cell and support rollers
q	Mesh quality factor
t	Time
w, h, l	Width, height and length of laminate
$[A],[B],[D]$	Block matrices of $\begin{bmatrix} A & B \\ B & D \end{bmatrix}$ matrix
$\overline{C}$	Off-axis stiffness matrix of lamina
$\left(\overline{C_{ij}}\right)_k$	Off-axis stiffness matrix of the kth ply
D, D_T, D_L	Apparent, transverse and longitudinal moisture diffusivities
$D_{\max}$	Maximum deflection
E_{app}^f	Apparent flexural modulus
E_{CLT}^f, E_x^f	Flexural modulus evaluated by CLT
E_1^f, E_2^f, E_3^f	Principal elastic moduli of fibre
E_1, E_2, E_3	Principal elastic moduli of lamina
E_a	Activation energy for diffusion
E_m	Elastic modulus of matrix
$F_{\max}$	Maximum flexure force
$G_{12}^f, G_{23}^f, G_{13}^f$	Principal shear moduli of fibre

G_{12}, G_{23}, G_{13}	Principal shear moduli of lamina
G_i	Coefficient of Tsai-Wu failure criterion
G_m	Shear moduli of matrix
I	Moment of inertia
K, K_f, K_m	Bulk moduli of lamina, fibre and matrix
L	Span
M, M_x	Moment
M, M_∞	Moisture mass gain and the maximum mass gain at saturation
$N_{x,y,xy}, M_{x,y,xy}$	Force and moment per unit length
P	Sinusoidal pressure
$Q_{ij}, \overline{Q}_{ij}$	Extensional compliance matrix of unidirectional and off-axis lamina
Q_x	Force per unit length along the width
R	Gas constant
S	Compliance matrix of lamina
$\overline{S}$	Off-axis compliance matrix of lamina
T_ε, T_σ	Transformation matrices of strain and stress
V_f	Fibre volume fraction
V	Volume of a mesh element
W_m	Matrix fraction in weight
α	Coefficient of thermal expansion
β	Coefficient of hygrothermal expansion
γ_{xy}	In-plane shear strain
ε	Normal strain

ζ	Halpin-Tsai adjusted parameter, for rectangle section $\zeta = 1$
η	Parameter of BK law
η_{xyx}, η_{xyy}	Interaction ratio
κ	Curvature
$\nu_{12}, \nu_{23}, \nu_{13}$	Principal Poisson's ratios of lamina
$\nu_{12}^{f}, \nu_{23}^{f}, \nu_{13}^{f}$	Principal Poisson's ratios of fibre
ν_m	Poisson's ratio of matrix
π	Circumference ratio
λ_0	Half-wavelength of fibres microbuckling
θ	Angle
ρ_c, ρ_f, ρ_m	Densities of composite, fibre and matrix
$\sigma_1, \sigma_2, \sigma_3$	Normal stress in local coordinate system
$\sigma_x, \sigma_y, \sigma_z$	Normal stress in global coordinate system
$\left(\sigma_1^{ult}\right)^t, \left(\sigma_2^{ult}\right)^t$	Principal tensile strength of lamina
$\left(\sigma_1^{ult}\right)^c$	Longitudinal compressive strength of lamina
$\left(\sigma_2^{ult}\right)^f$	Transverse flexural strength of lamina
$\left(\sigma_f^{ult}\right)^t$	Ultimate tensile strength of fibre
$\left(\sigma_m^{ult}\right)^t, \left(\sigma_m^{ult}\right)^f$	Ultimate tensile and flexural strength of matrix
$\tau_{12}, \tau_{13}, \tau_{23}$	Shear stress in local coordinate system
$\tau_{12}^{ult}, \tau_{23}^{ult}, \tau_{13}^{ult}$	Shear strength of lamina
$\tau_{xy}, \tau_{xz}, \tau_{yz}$	Shear stress in global coordinate system

CHAPTER 1 – INTRODUCTION

1.1 Marine composites

The origins of fibre reinforced plastics (FRP) composites can be dated back to the 1900s when chemists were trying to produce high strength mouldable materials, however the extensive use of FRP composites in industry only began in the 1930s when the mass production of glass strands was invented (Milewski and Rosato, 1981). The early introduction of the FRP composites to marine structures started at the Second World War when the UK Royal navy was seeking to build ship hulls for a warship (HMS Wilton) based on the potential for minesweeper (Colledge and Warlow, 2003). Compared with the aerospace industry, where high strength and stiffness to weight is essential, the use of marine composites was driven by their superior performance of environmental resistance and fatigue life. FRP composites have been used for critical marine structures, such as propellers (Marsh, 2004), ship hulls (Hull and Clyne, 1996), shafts (Greene, 1999), pipes & tanks (Smith, 1991; Selvaraju and Ilaiyavel, 2011).

FRP composites are normally divided into engineering composites and advanced composites based on their performance. Traditional marine composites were made of glass fibre and polyester, however with the increasing demand of the performance characteristics the use of carbon/epoxy composites are growing rapidly. According to the American Composites Manufacturing Association (ACMA), the shipment of marine composites in 2014 was approximate 0.3 billion dollars in the US and this value is expected to have a growth of 65% by 2020 (ACMA, 2015). Although these data are for the United States, it is similar to data worldwide. The growth of the shipment of marine composites has benefited from the development of marine renewable energy and the offshore platforms. Since FRP composites can be moulded to very complex shapes, these materials have been used to construct blades in tidal or underwater turbines (Mohan, 2008). Siemens has installed the world's first commercial marine current power plant supplying eco-friendly power to over 1500 households in Northern Ireland in 2008 (**Figure 1.1**), which incorporates two CFRP turbine blades (SIEMENS, 2008). ANDRITZ HYDRO Hammerfest has developed a 1-MW tidal turbine and installed at

the European Marine Energy Centre (EMEC), Scotland in December 2011, which features composite blades designed by Gurit to withstand an aggressive subsea environment (Hammerfest, 2011).

Figure 1.1 The 600-kW marine current turbine installed in Strangford Lough in County Down, Northern Ireland (SIEMENS, 2008)

The challenges for composite materials used in marine environment include the long exposure time to moisture, temperature, numerous ionic species as well as microorganisms. Recently, Summerscales gave a general review on the marine environmental effects on the durability of FRP composites (Summerscales, 2014). The loss in the mechanical properties of composite materials is mainly attributed to the plasticisation of polymeric matrix. However, previous investigations of the long-term performance of current commercial FRP composites in the marine environment mainly considered moisture diffusion and are often based on accelerated laboratory studies due to the slow processes involved.

1.2 Composite fatigue

The determination of the resistance to combined states of cyclic stress is a fundamental problem concerning the engineering uses of FRP composites. The fatigue failure of FRP composites is much more complicated than isotropic materials such as metals because the predominant state of stress within composites with orthotropic/anisotropic properties is multi-dimensional. The failures in FRP composites include fibre breakage, matrix cracking, interfacial debonding and delamination (Hashin, 1981). In view of the complexity of microstructural damage accumulation during fatigue cycling, there is little hope for resolving such problems particularly fatigue crack development by micromechanics methods even when the applied stresses are smaller than the material strength. One has to extract the complex stress fields, the inherent anisotropic and nonlinear behaviour to understand the nature of fatigue, as fatigue can cause extensive damage throughout the specimen volume combined with a variety of failure modes instead of a single crack.

The fatigue performance is generally plotted as the applied stress level against the fatigue cycle count under cyclic load, either: (1) constant stress cycling until loss of strength and (2) constant amplitude cycling until loss of stiffness. Most of the current composite failure criteria are stress dominated, therefore these stress dominated failure criteria are occasionally extended to fatigue (Tsai and Melo, 2014). In low cycle fatigue, stiffness reduction is an acceptable failure criterion for many components which incorporate composite materials, because the change of stiffness is a precise, easily measured and interpreted indicator of damage which can be directly related to the degradation of composites (Reifsnider, Stinchcomb et al., 1977).

There are plenty of theories to describe the strength and fatigue life of FRP composites, however no agreed analytical model can account for all the possible failure processes within a composite. Given the broad range of usage and diverse variety of composites in use in the marine environment, theoretical calculations as to the fatigue life of a given composite should only be used as a first-order indicator (Greene, 1999). Empirical data suggest that FRP composites perform much better in fatigue than common metals (Weeton, Thomas et al., 1987). **Figure 1.2** illustrates the fatigue strength characteristics for some metals and FRP composites.

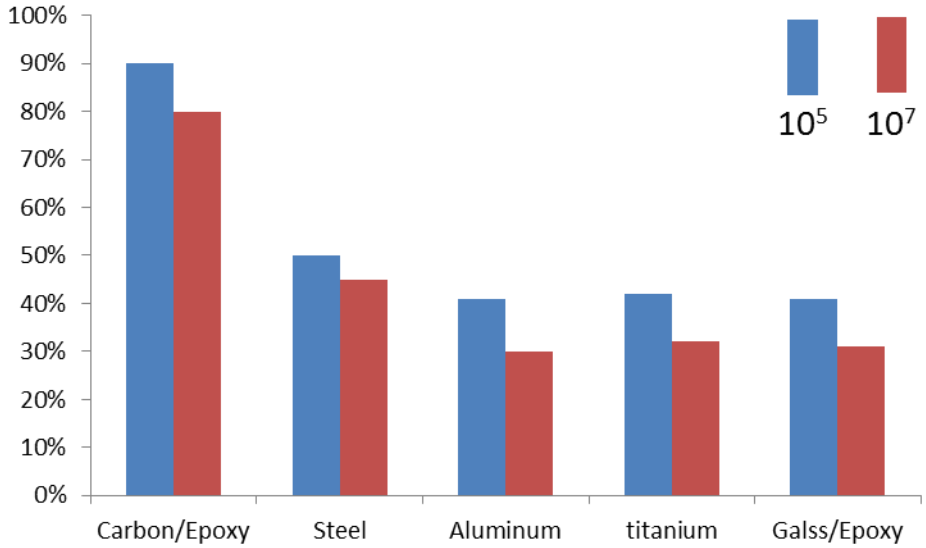

Figure 1.2 Comparison of fatigue strengths of CFRP/GFRP composites, steel, aluminium and titanium. Source: The Japan Carbon Fibre Manufacturers Association (JCMA, 2014).

1.3 Research scope and objectives

Composite structures used in the marine environment are subjected to both mechanical loads and environmental effects. For many marine structures, it is expected to serve several decades in order to reduce the maintenance cost, therefore environmental fatigue is the main concern for the engineering designer due to the degradation effects of the environment. As fatigue failure is a process of accumulation of structural fracture, the research scope of this thesis will cover the failure mechanisms of CFRP composites, from static failure to fatigue crack propagation. Typically, laminated composites made up of pre-preg carbon fibre-epoxy were used for the study.

Considerable research had been carried out to investigate the marine environmental effects on either mechanical property, i.e. uniaxial tensile strength/modulus or chemical properties, i.e. moisture diffusion of FRP composites. However there is still a lack of knowledge on the fracture mechanics of FRP composites when water ingress is considered which is essential to fatigue failure since the water ingress is also a very slow process. The work undertaken in this thesis will therefore have the aim of providing better understanding of the effects of water ingress on the failure mechanisms of laminated composites. The primary objective is to investigate the failure initiation

and the crack propagation of laminated composites in a simulated marine environment. The specific objectives are listed as follows:

- To manufacture laminated composites in common stacking sequences and to evaluate the relation between manufacturing defects and failure initiation.

- To develop an analytical model to analyse the experimental data, and to predict the mechanical and chemical properties of laminated composites at both lamina and laminate levels.

- To develop a FEA model to investigate the failure initiation, a FEA model to investigate the moisture diffusion coupled with stress distribution, and a FEA model to investigate the fatigue crack propagation.

- To conduct diffusion tests for the investigation of the effects of sea water ingress on the degradation of static and fatigue performance.

- To conduct static and fatigue tests to collect experimental evidence and to compare with the analytical and FEA models.

1.4 Methodology

This research is conducted by the methodology shown below,

- Pre-preg carbon-epoxy is used to manufacture composite specimens with some common stacking sequences, i.e. unidirectional ($[0]_{16}$), unidirectional transverse ($[90]_{16}$), cross-ply ($[0/90]_{4s}$ and $[90/0]_{4s}$), angle-ply ($[+45/-45]_{4s}$.
- Accelerated diffusion tests are carried out in a simulated marine environment to investigate the moisture diffusivity and hygrothermal expansion.
- Bending tests are carried out to investigate the flexural modulus, flexural strength, interlaminar shear strength and bending fatigue of both dry and immersed specimens.
- Finite Element Analysis (FEA) is used to simulate the static, diffusion and fatigue behaviour of the dry and immersed specimens. Three commercial FEA

packages were used in this study: (a) COMSOL Multiphysics for the modelling of quasi-static bending, time-dependent moisture diffusion, and the coupling of hygrothermal expansion with bending; (b) ANSYS ACP for the modelling of the effects of unequal tensile/compressive moduli; and (c) ABAQUS/Standard for the modelling of bending fatigue.

- Classical Laminate Theory (CLT) is used to develop a series of tools to predict the properties of FRP composites with different stacking sequences, as well as the stress/strain distributions and failure mechanisms. The CLT tools were programmed in MATLAB platform.

The FEA and CLT are conducted by a 'forensic' approach: a) the mechanical and diffusion tests were carried out first; b) and then the experimental data were input into the FEA and CLT models, c) finally the results of the later models were used to analyse the failure mechanisms observed in the experiments.

1.5 Structure of this thesis

The objectives of the project are pursued through a combination of experimental, numerical and analytical approaches. This thesis is organised in seven chapters. **Figure 1.3** shows a flow chart of the research of the three approaches (experimental, numerical and analytical), including four sections: manufacturing, static test, diffusion test, and fatigue and creep tests. The four sections of the flow chart comprise the main body of this thesis, while each section corresponds to one chapter in the thesis.

Chapter 2 provides a detailed literature review of the project: CFRP composites, composite fatigue and marine environment, which are divided into the construction of CFRP composites, composite failure modes, categories of fatigue, marine environmental effects and research methods. The knowledge gap and context for the contributions of this research are also presented at the end of this chapter.

Chapter 3 presents the preparation of the specimens as well as the evaluation of manufacturing defects. The statistical study of carbon fibre packing by optical microscope is also presented in this chapter. CLT and some derived formulae for the prediction of mechanical/chemical properties are also presented in this chapter.

Chapter 4 reports the static tests for dry specimens to examine the flexural properties of CFRP composite with variety of stacking sequences. FEA and CLT provide the detailed distribution of stress/strain to investigate the failure mechanisms.

Chapter 5 reports the accelerated diffusion test and the static tests for immersed specimens. FEA and CLT provide supplemental details of the coupling effects of water absorption. Some experimental apparatus, such as DSC, SEM and optical microscope, are employed to extract the evidence in critical region.

Chapter 6 reports the bending fatigue and creep for both dry and immersed specimens. In this thesis, the creep is considered as a special type of fatigue (R=1), therefore it is also included.

Chapter 7 summarizes the main findings of this project and the conclusions of the work in this thesis. Recommendations for possible future research are also outlined there.

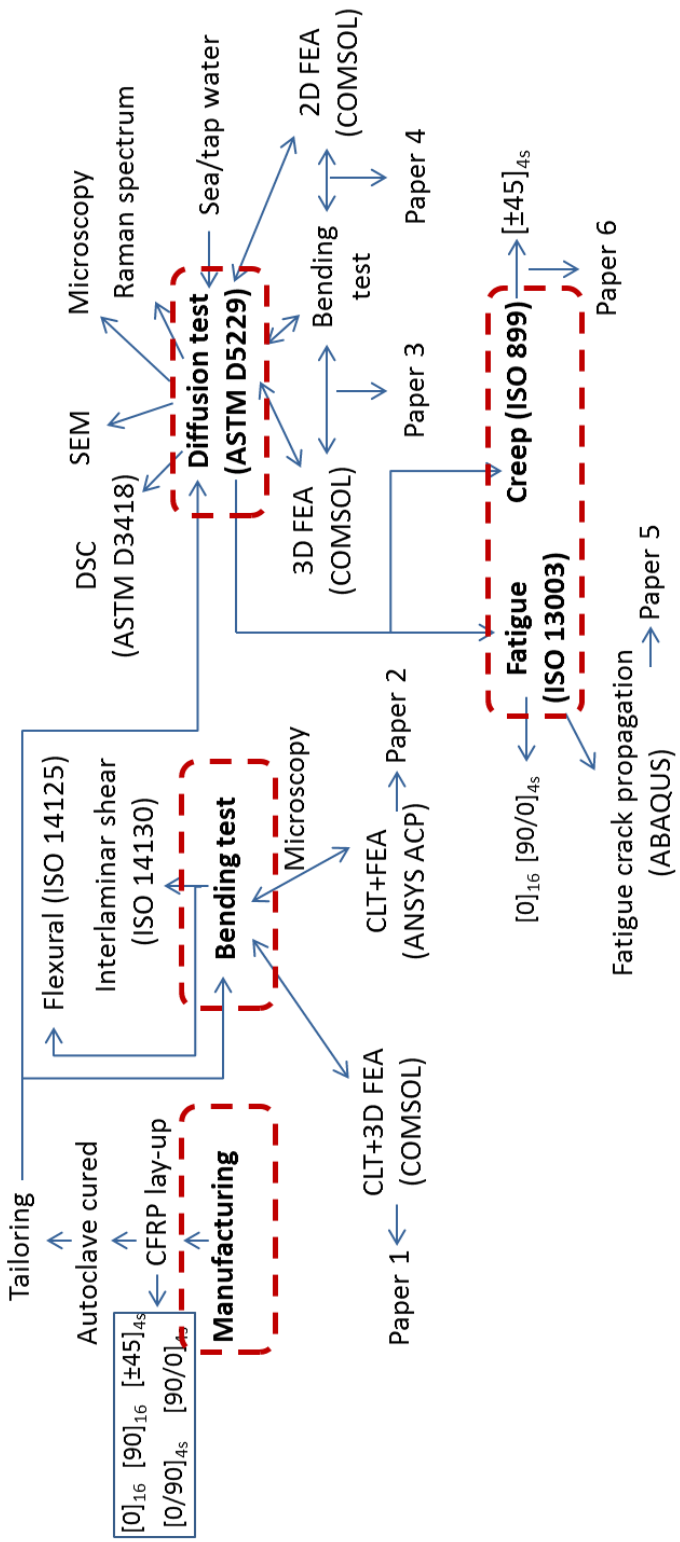

Figure 1.3 **The flow chart of the project**

CHAPTER 2 – LITERATURE REVIEW

2.1 CFRP composites

Structural materials can be generally divided into four basic categories as metals, polymers, ceramics and composites (Gibson, 1994). FRP composites consist of polymeric matrices which are reinforced by fibres. According to its definition, the FRP composites are orthotropic/anisotropic materials whose properties are determined by the matrix, fibre, their volume fractions and the manufacturing method. The fibres are usually glass, carbon, aramid or natural fibre such as bamboo, while the polymers are usually thermoset (epoxy, vinyl ester, polyester) or thermoplastic (PEEK, Polyproplyene). Since the first FRP composite was invented by Baekeland in 1909 (Furge, 2010), a variety of fibres and polymers were invented and their strengths have been improved significantly during the last century, as well as the performance of their composites. In this section, carbon fibre, epoxy, and the marine environmental resistance of their composites are reviewed.

2.1.1 *Carbon fibre*

Fibres are such materials that have a much longer length than the other dimensions. This relationship between length and the other dimensions is defined as aspect ratio which is simply the ratio of length to the diameter of fibre (Strong, 2008). The most common fibres used in FRP composites are glass, carbon and aramid. It is widely considered that as the fibres get thinner, they get stronger (Gordon, 1976). **Table 2-1** shows the comparison of tensile properties for several key fibre types.

The demand for reinforcement fibres with strength and stiffness has led to the development of carbon or graphite fibres which are usually produced by subjecting organic precursor fibres such as polyacrylonitrile (PAN), rayon or pitch to a sequence of heat treatments so that the precursor is converted to carbon by pyrolysis. Higher temperature pyrolysis leads to higher carbon content which results in the difference between carbon fibre (less than 95% carbon) and graphite fibre (at least 99% carbon) (Schwartz, 1984). PAN-based fibres have good properties with relatively low costs for standard modulus products (E=200~300GPa), while pitch-based fibres present higher modulus and thermal conductivity (Strong, 2008). Carbon fibres have good thermal

conductivity and moderately good electrical conductivity, and the coefficient of thermal expansion (CTE) in longitudinal direction is negative (e.g. the typical value of T300 carbon fibre $\alpha = -0.6 \times 10^{-6} m \cdot m^{-1} \cdot K^{-1}$), which is quite different from the most other materials. Carbon fibres do not absorb water and are resistant to many chemical solutions which make them particularly resistant to marine environmental exposure. However, when used to reinforce polymeric matrices, evidence shows that CFRP composites are also affected by the environment (Sumsion, 1976; Morton, Kellas et al., 1988; Tucker, 1991).

Table 2-1 Comparison of properties for several typical fibres (data source: Wikipedia and respective product technical data sheet)

Fibre type	Modulus (GPa)	Strength (MPa)	Density (g/cc)	Diameter (μm)
E-glass	69	3447	2.5	25
S-glass	83	4585	2.5	9
Carbon Toray T300 (Standard modulus)	230	3530	1.82	6.91
Carbon Toray M40 (Intermediate modulus)	392	2740	1.81	6.53
Carbon Toray M55J (Ultra-high modulus)	540	4020	1.91	4.92
Aramid (High toughness)	83	3606	1.4	17
Aramid (High modulus)	131	3999	1.4	
Aramid (Ultra-high modulus)	186	3406	1.5	
UHMWPE (Standard modulus)	117	2585	0.97	
UHMWPE (High modulus)	172	2999	0.97	
Boron	386	3447	2.5	102
SiC	414	3447	3	10
Spider silk	97	1000	1.3	3.57

Glass fibre and aramid are the other two common reinforcement fibres. Fatigue studies of glass fibres and their FRP composites in water, air and sulphuric acid showed that fatigue crack propagation resistance of the fibre and the composites decreased due to the

environmental exposure (Bledzki, Spaude et al., 1985; French and Pritchard, 1993; Ellyin and Maser, 2004). According to Chiou's study, sea water ingress showed insensitivity in the growth of edge delamination in cross-ply GFRP composite laminates (Chiou and Bradley, 1993). Aramid fibres are known to absorb water and are affected by temperature as they are polymeric fibres, and it has been reported that the strength of Kevlar/epoxy composites at elevated temperature decreased in the range of 40%-60% when in the saturated state (Allred, 1981). There are some others less common fibres, such as boron fibres, silicon carbide fibres and carbon nanotubes. They are only used in specific applications, thus are not included in this review.

2.1.2 *Epoxy*

The matrix holds the fibres together in a structural unit and protects them from external damage, transfers and distributes the applied loads to the fibres. From this point of view, a strong interface bond between matrix and fibre is usually desired. Polymeric matrices are divided into two types: (a) thermosets are resins that are usually liquids at room temperature and moulded by a heating process; (b) thermoplastics are resins that are solids at room temperature and melted or softened to the desired shape by heating. One important property of polymeric matrices is the so-called glass transition temperature (Tg). This thermal transition occurs below the melting point, however marks a change from a rigid solid to one that is more pliable and then the bonding within the composites reduces significantly. It has been reported that water absorption decreased the glass transition temperature of polymers (Chamis, 1984; Chateauminois, Chabert et al., 1993; Zafar, Bertocco et al., 2012). The most common use of polymeric matrices in FRP composites are epoxy, polyester and poyetheretherketone (PEEK). **Table 2-2** shows the comparison of properties for several types of polymeric matrices.

Epoxy resins, characterized by an epoxy ring, are produced from reacting epichlorohydrin with bisphenol A to form diglycidyl ethers of bisphenol A. The crosslinking reaction in epoxy resins is based on the opening of the epoxy ring by a hardener (or called curing agent) which has amine groups (NH_2) on both of its ends (Brandrup, Immergut et al., 1999), shown in **Figure 2.1**.

The curing reaction creates a hydroxyl (OH-) group on one of the carbons that previously was part of the epoxy ring. The hydroxyl groups created from the curing

reaction present high surface energy which is a characteristic of materials that are good in adhesion. One of the advantages of epoxy resins in the composites moulding process is its small shrinkage during the curing reaction. Epoxy-based FRP composites present excellent physical, chemical and mechanical properties; however its cost is also higher than the other polymeric matrices.

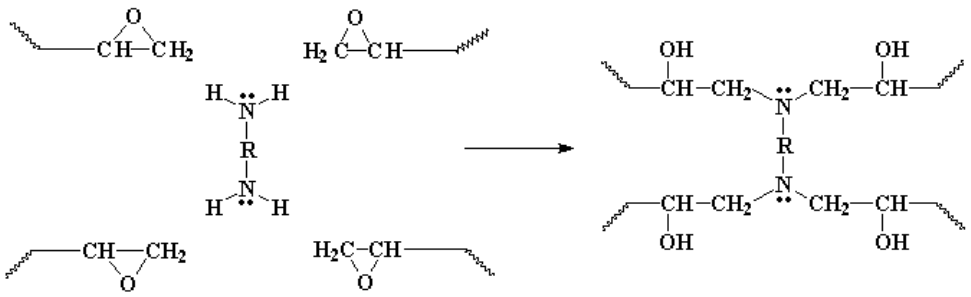

Figure 2.1 The curing reaction of hardener and epoxy ring

Table 2-2 Comparison of properties for several typical matrices (data source: Wikipedia and respective product technical data sheet)

Property	Epoxy [a]	Vinyl ester [b]	Polyester [c]	Polyimide [d]	PEEK [e]
Flexural modulus (GPa)	3.5	3.1	3.6	0.4	4.3
Flexural strength (MPa)	197	124	41	120	130
Tensile modulus (GPa)	3.5	3.3	3.7	0.4	3.7
Tensile strength (MPa)	81	81	79	40	110
Density (g/cc)	1.31	1.12	1.2	1.31	1.3
Tg (°C)	212	102	140	338	143
Saturated moisture (Wt. %)	1.5	1.5	1.5	4.4	0.5

a: CyCom 977-2; b: Derakane 411; c: Hetron 197; d: CyCom 2237; e: Victrex 150G

Polyester is another common thermoset widely used to construct marine structures due to the relatively lower cost, however seawater durability studies showed that the polyester based FRP composites experienced significant water absorption and suffered chemical degradation of the matrix and fibre/matrix interphase region (Kootsookos and

Mouritz, 2004), therefore the protection of surface coating is essential for this type of composites. PEEK, a thermoplastics, presents high strength, high modulus, high environmental resistance (Olabisi and Adewale, 1997), however the use of thermoplastics is limited to those structures of small scale due to its limitation of manufacturing method (Greene, 1999).

2.2 Composite failure

Fatigue is a process of damage accumulation so that the analysis of composite fatigue requires an insight into the failure modes that are unique to this type of material. Composite failures can be classified into either strength dominated, which is identified by a stress limit, or stiffness dominated which is identified by a strain limit (Lubin, 2013). Most of the current failure criteria for composites are stress dominated, such as Tsai-Wu and Tsai-Hill criteria. Tsai and Melo proposed an invariant-based theory for composites which is a strain dominated failure criterion (Tsai and Melo, 2014). **Figure 2.2** illustrates the six common composite failure modes at micro scale. The catastrophic failure of composite structures at macro scale, i.e. tension, compression and interlaminar shear, is associated with the combination of some of these failure modes at the micro scale.

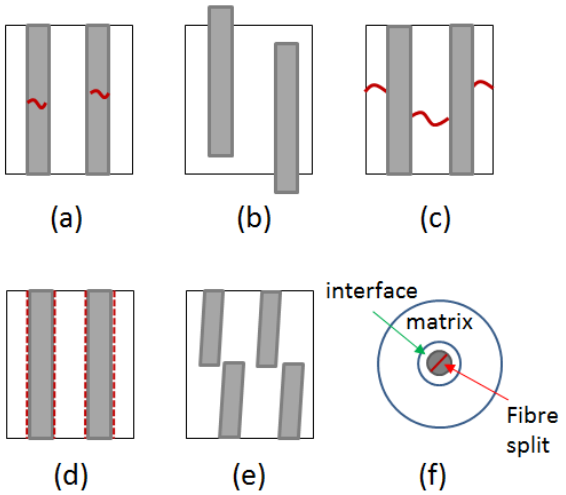

Figure 2.2 Composite failure mechanisms in micro scale: (a) fibre fracture; (b) fibre pull-out; (c) matrix fracture; (d) fibre/matrix debonding; (e) fibre kinking; (f) fibre radial split.

2.2.1 *Tensile*

The tensile failure of composites includes uniaxial tension and off-axial tension. The failure by uniaxial tension is fairly rare since it is strongest in tension along the fibre primary axis. The uniaxial tensile failure of FRP composite lamina is mainly controlled by the fibre ultimate stress since the fibre ultimate strain is typically lower than that of matrix and the matrix may not attain its ultimate stress when fibres fail (Kelly and Davies, 1965),

$$\sigma_t^{ult} = \sigma_f^{ult} V_f + E_m \varepsilon_f^{ult} (1 - V_f) \qquad (2\text{-}1)$$

where $\sigma_t^{ult}, \sigma_f^{ult}$ are the ultimate tensile strengths of composite and fibre respectively, V_f is the fibre volume fraction, E_m is the elastic modulus of matrix, ε_f^{ult} is the ultimate strain of fibre.

There are two standard test methods commonly used for the determination of tensile properties of FRP composites: ISO527 and ASTM D3039.

For an off-axis lamina, the stress tensor can be expressed in terms of stresses in global coordinates using plane stress transformation equations (Hull and Clyne, 1996),

$$\begin{aligned} \sigma_1 &= \sigma_x \cos^2 \theta \\ \sigma_2 &= \sigma_x \sin^2 \theta \\ \tau_{12} &= -\sigma_x \sin\theta \cos\theta \end{aligned} \qquad (2\text{-}2)$$

Off-axis tensile failure can be predicted by applying the in-plane strength parameters to equations (2-1) and (2-2). The transformation creates a stress vector in the transverse direction and a coupling term of in-plane shear stress. The transverse stress increases to the maximum value when the off-axis angle increases to 90° while the longitudinal stress retrieves to zero. A statistical study of many commercial CFRP composites showed that the coupling term presents the maximum value at an off-axial angle about 11° with very small standard deviation (Meng, Le et al., 2015a).

2.2.2 *Compressive*

The compressive failure of FRP composites includes uniaxial compression and off-axis compression. Compared with the tensile mode, composite compressive failure is usually considered to be a microbuckling problem which is influenced by many factors

including fibre size and shape (Hajianmaleki and Qatu, 2011; Sutcliffe, 2013), fibre waviness (Piggott, 1995; Basu, Waas et al., 2006; Lemanski and Sutcliffe, 2012), fibre/matrix bond strength (Zhang, Li et al., 2013), fibre/matrix stiffness and strength (Kyriakides, Arseculeratne et al., 1995; Schultheisz and Waas, 1996). Fibres having smaller diameter usually present higher tensile strength, however, according to the beam theory, such fibres are easier to buckle than those made with larger diameter. This is the dilemma in composite manufacturing.

Considering the loading condition and possible micro-scale structural defects in long fibre reinforced plastics composites, the compressive modulus is likely to be different from the tensile modulus (Meng, Le et al., 2015b). This will be more obvious in CFRP than GFRP composites since the diameter of carbon fibre is normally smaller than that of glass fibre.

Table 2-3 Longitudinal tensile/compressive moduli of CFRP composites and their strengths. Data source: Polymer matrix composites material handbook (Dept. of defense, 1997).

	E_1^t (GPa)	E_1^c (GPa)	$\frac{E_1^c}{E_1^t}$	$(\sigma_1^t)_{ult}$ (GPa)	$(\sigma_1^c)_{ult}$ (GPa)	$\frac{(\sigma_1^c)_{ult}}{(\sigma_1^t)_{ult}}$
Celion 12k/938	136	119	0.87	1.88	1.39	0.74
AS4 12k/3502	133	124	0.93	1.78	1.41	0.79
HITEX 33 6k/E7K8	125	118	0.94	2.16	1.44	0.67
AS4 12k/938	154	125	0.81	2.17	1.57	0.73
AS4/3501-6	135	123	0.91	2.01	1.45	0.72
T300 15k/976	135	129	0.95	1.45	1.30	0.89
AS4 12k/997	137	123	0.89	2.25	1.58	0.70
IM6 12k/APC-2	149	134	0.90	2.41	1.15	0.48
HTS40/977-2 (Jumahat, Soutis et al., 2010)	140	112	0.80	2.52	1.40	0.56
Cytec/977-2 (Cytec, 2012)	165	152	0.92	2.69	1.59	0.59
Avg.	141	126	0.89	2.13	1.43	0.69
SDs	12	11	0.05	0.37	0.14	0.12
Coeff var	8.4%	8.7%	5.8%	17.3%	9.5%	17.5%

In **Table 2-3**, there are ten commercial CFRP composites and their ratios of compressive/tensile moduli are very close. For these CFRP composites, the average ratio of compressive modulus to tensile modulus is around 0.9. In fact, with the increase

of statistical specimens, the standard deviation decreases and the coefficient of variation has a tiny drop from 5.8% to 4.6%, as shown in **Figure 2.3**. The actual value depends on the volume fraction of fibres and the manufacturing process. The ratios of compressive/tensile strengths are also included in the statistics, and the average value presents around 60%-70%.

A parameter is introduced to indicate the ratio of longitudinal compressive modulus to tensile modulus, $\lambda = E_1^c / E_1^t$. **Figure 2.3** shows data for the ratio of compressive strength to tensile strength of CFRP composites, and the ratio of compressive modulus to tensile modulus of CFRP/GFRP composites.

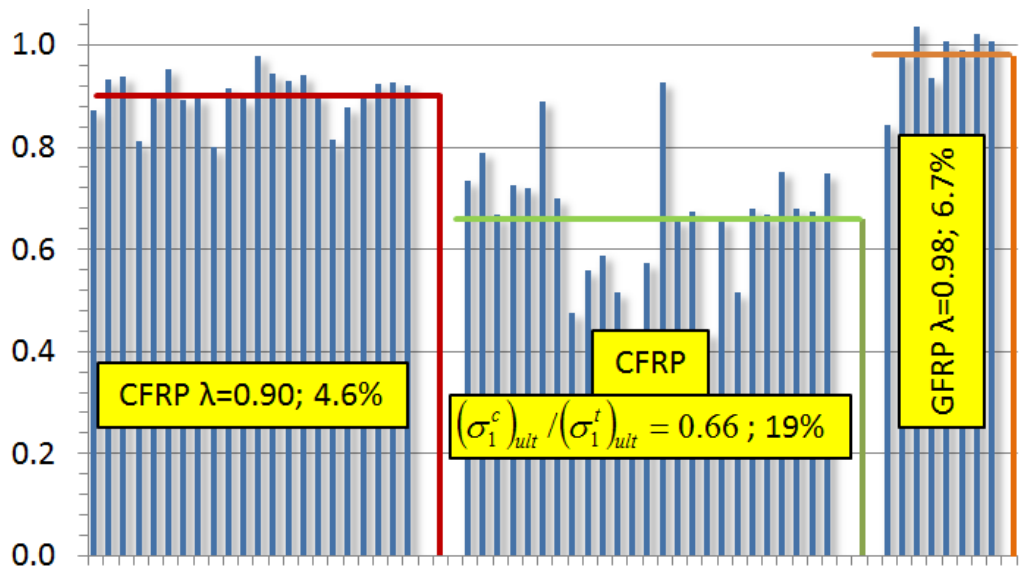

Figure 2.3 Ratio of longitudinal compressive modulus to tensile modulus of various CFRP and GFRP composites. The average and their respective coefficient of variation are also shown in the figure. Data source: Polymer matrix composites material handbook (Dept. of defense, 1997).

The compressive failure has been reported to be associated with the fibre waviness and microbuckling (Jones, 1976; Jones, 1978; Budiansky and Fleck, 1993; De Morais, 1996; Naik and Kumar, 1999). Considering the fibre microbuckling problem, the prediction of composite compressive strength involves shear strength of matrix, fibre distribution (or fibre volume fraction) and fibre geometric parameter. A shear crippling model was proposed for the compressive strength by (Hahn and Williams, 1986),

$$\sigma_c^{ult} = V_f \left(\frac{G_{12}\tau_y}{\tau_y + \frac{\pi f_0 G_{12}}{L}} \right) \tag{2-3}$$

where τ_y is the composite shear yield stress; f_0/L is a fibre curvature parameter which is determined by a set of typical known experimental results. For T300/934 carbon/epoxy composite, the prediction of the compressive strength at different temperatures matched experiment when fibre curvature parameter had a value of 0.0041 (Fox, Sykes Jr et al., 1987).

There are two standard test methods commonly used for the determination of compressive properties of FRP composites: ISO14126 and ASTM D3410.

2.2.3 *Bending*

The bending behaviour of FRP composites is essential to the compressive properties because the composites are under both compression and tension. A laminate with unequal moduli may not behave symmetrically in bending, such as the stress and strain distributions through-thickness, even though the layup is symmetric. Therefore, for many classical theories, such as classical beam theory (CBT) and classical laminate theory (CLT), the compressive modulus should be introduced in order to eliminate the unequal terms.

Several papers have described work to modify CBT for the determination of flexural properties of laminated composites. (Chamis, 1969; Chamis, 1972; Chamis, 1974) used continuum mechanics to derive the formula of maximum deflection in three-point bending using unequal compressive and tensile moduli. (Zhou and Davies, 1995; Zhou and Davies, 1995) used statistical methods and assumed a higher compressive modulus to characterize the failure mechanics of thick glass woven roving/polyester laminates. (Mujika, Carbajal et al., 2006; Carbajal and Mujika, 2009) used strain gauges to determine the compressive and tensile moduli of unidirectional laminates by measuring the compressive strain and tensile strain at the top and bottom surfaces of specimens in three-point and four-point bending. However, the effects of unequal moduli on the flexural properties and the failure strength of multi-directional filament laminate composites have not been well understood.

In bending, composites are subjected to both tension and compression, which is fundamentally different from uniaxial loading. Composite flexural properties are usually determined by ISO14125 or ASTM D7264.

According to continuum mechanics, bending produces a through-thickness shear and later on induces interlaminar shear stress which causes composite delamination (Kaw, 2006). Interlaminar shear strength is one of the most important strength parameters for composite failure modes. The composite apparent interlaminar shear strength is usually determined by bending test by a short-beam method following the ISO12130 or ASTM C1425.

2.2.4 *First ply failure*

Considering 'damage accumulation' in fatigue, composite structures fail when first ply failure occurs, and the load corresponding to this failure is the design limit load. The first ply failure criterion was originally introduced by the aerospace industry which requires the maximum strain in all plies to be no more than 0.4% (Tsai and Melo, 2014). Following the aerospace industry, this criterion has been widely used in the marine industry for composite design. The American Bureau of Shipping (ABS) provides a guidance for classing high-speed craft using the first ply failure criterion (ABS, 2001),

$$\varepsilon_{crit} = \frac{\sigma_i^{ult}}{E_i\left[\left|\bar{y} - y_i\right| + \frac{1}{2}t_i\right]} \qquad (2\text{-}4)$$

Where σ_i^{ult} and E_i are the strength/modulus of ply under consideration, $\sigma_i^{ult} = \sigma_t^{ult}, E_i = E_t$ for a ply in the outer skin and $\sigma_i^{ult} = \sigma_c^{ult}, E_i = E_c$ for the inner ply; $\bar{y}, y_i$ are the distances from the bottom to the neutral plane and the ply under consideration; t_i is the thickness of the ply under consideration.

2.3 Fatigue analysis

2.3.1 *Low cycle and high cycle fatigue*

Composite fatigue initiates and accumulates from the failure modes shown in **Figure 2.2**, and these failure conditions are associated with the number of cycles. In FEA

modelling, the number of cycles for fatigue failure of less than 10^5 is classified as low-cycle fatigue while greater than 10^5 is high-cycle fatigue (ANSYS, 2013). The fatigue properties of FRP composites are typically determined by ISO13003 or ASTM D3479. The American Society for Testing Materials (ASTM) also provides a standard for the mode I fatigue growth (low-cycle fatigue) (D6115, 2011). **Figure 2.4** gives an illustration of characteristic of FRP composite fatigue (Strong, 2008).

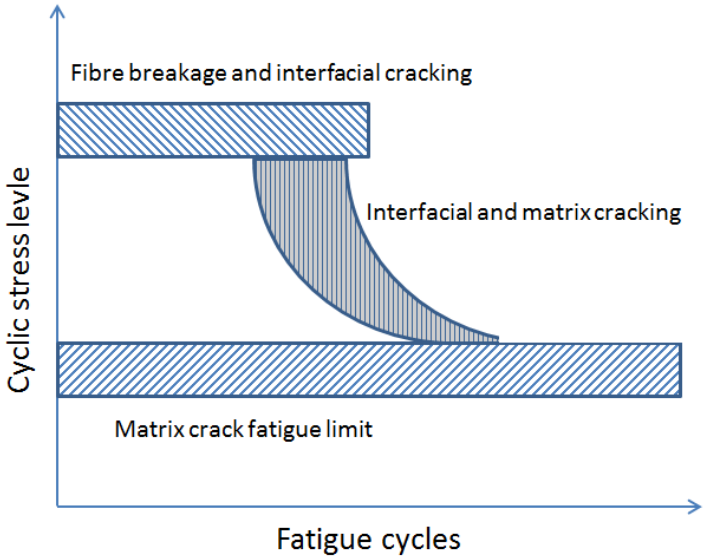

Figure 2.4 Fatigue characteristic of FRP composites

Low-cycle fatigue for FRP composites typically results in fibre fracture and interfacial cracking under high stress levels which is classified as fibre mode, while the high-cycle fatigue more commonly results in matrix cracking under low stress level which is classified as matrix mode.

2.3.2 *Fatigue failure criteria*

Fatigue failure has been investigated in the context of metal fatigue which is empirically predicted based on such simple assumptions that principal normal stress, shear stress, and strain-energy density of distortional strain-energy density associated with the cyclic stresses determine the fatigue failure (Gough and Pollard, 1935). In this sense, the fatigue failure criteria are constructed by combining a single stress component with the fatigue life, which is plotted as fatigue life against stress (also known as S-N curve, or

Wöhler curve). Assuming isotropic material properties, a more general fatigue failure criterion was developed in terms of invariants of the stress tensor (Hashin, 1981).

Based on the transverse isotropy of FRP composite materials and recognising their different failure modes, a failure criterion for static condition was established (stress ratio R=1) (Hashin, 1980), and later it was extended to cyclic stress with variety of stress ratios (Hashin, 1981),

$$\left(\frac{\sigma}{\sigma_A}\right)^2 \cos^4\theta + \left(\frac{\sigma}{\tau_A}\right)^2 \cos^2\theta \sin^2\theta = 1 \qquad (2\text{-}5)$$

$$\left(\frac{\sigma}{\sigma_T}\right)^2 \sin^4\theta + \left(\frac{\sigma}{\tau_A}\right)^2 \cos^2\theta \sin^2\theta = 1 \qquad (2\text{-}6)$$

where θ is the fibre off-axis angle; σ_A, σ_T, and τ_A are functions of R and N, $\sigma_A = \sigma_A(R,N), \sigma_T = \sigma_T(R,N), \tau_A = \tau_A(R,N)$. Equation (2-5) is fibre mode, while equation (2-6) is matrix mode. Fatigue failure occurs in the mode which corresponds to the lowest fatigue lifetime. The coefficients presented in equations (2-5, 2-6) can be determined by the fatigue failure tests of two off-axis angles either in fibre mode or matrix mode.

The fatigue failure criteria are developed to predict the S-N curves. With the principles of fracture mechanics, a more ambitious task was undertaken to predict fatigue crack propagation. The pioneering work was carried out by (Paris, Gomez et al., 1961) who introduced the stress intensity factor to characterize the rate of crack propagation,

$$\frac{da}{dN} = m(\Delta K)^n \qquad (2\text{-}7)$$

where da/dN is the crack growth rate advance per cycle; ΔK is the range of stress intensity factor; m and n are the material properties. The stress intensity factor is usually replaced by strain energy release rate,

$$G = \frac{K^2}{E} \qquad \text{Plane stress, (2-8)}$$

$$G = \frac{\left(1-\nu^2\right)K^2}{E} \qquad \text{Plane strain, (2-9)}$$

Because the strain energy release rate is easy to extract through J-integration around the crack tip, it is commonly used in numerical simulation. Although Paris' law was originally derived for isotropic materials like metals, it is also commonly used to predict fatigue behaviour of transverse isotropy. The range of energy release rate in equation (2-8) ΔG is then replaced by the equivalent energy release rate ΔG_{equiv}.

In principle, crack propagation starts from the 'initiation' phase and continues with the 'propagation' phase where the Paris law is supposed to hold, up to a stage with fast crack propagation leading to final failure.

2.3.3 *Cycle count*

According to the fatigue failure criteria, the safety of composite structures is designated by the fatigue cycle. In the most common case of fatigue tests, constant amplitude stress or strain is applied. In the real applications of composite structures, the loading ratio varies over time and the cumulative damage calculation needs to be done in order to determine the total amount of fatigue damage and which cycle combination causes such damage. There are several cycle counting methods used in fatigue analysis, in which many of them are included by the ASTM standard (E1049-85, 1994).

Among the current counting methods for fatigue analysis, the rain-flow counting algorithm is the one that allows the application of Miner's rule in order to assess the damage accumulation of a structure subject to complex loading, and has been successfully used for design of wind turbine components (Schluter, 1991). The rain-flow algorithm was proposed by Tatsuo et al in 1968 (Matsuishi and Endo, 1968), and developed to a more widely referenced and utilized algorithms by (Downing and Socie, 1982). The range size of cycle counting history specifies the number of divisions of the rain-flow matrix. A large range size provides greater precision, however it will take longer to solve. **Figure 2.5** gives an example of rain-flow cycle counting. According to the rain-flow counting algorithm, there are three full cycles counted in the figure (a-b-a', d-e-d', g-h-g') and three half-cycles (0-a-a'-c, c-d-d'-f, f-g-g'-i).

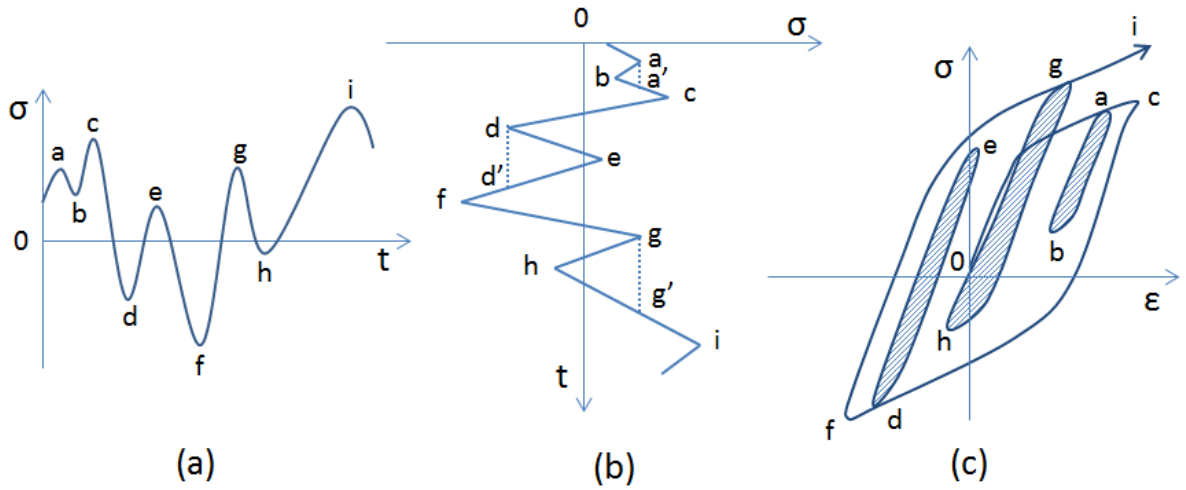

Figure 2.5 Rain-flow counting example: (a) spectrum loading; (b) clockwise rotated time history; (c) stress-strain hysteresis loop.

2.4 Marine environment

Composite structures exposed in the marine environment are subjected to many environmental aspects. This chapter reviews the effects of moisture, temperature, pressure, saline and ultraviolet exposure. These environmental conditions show particularly important effects on FRP composite properties that are matrix dominated. Effects of temperature are usually referred to as 'thermal' effects, whereas those of moisture are often referred to as 'hygrothermal' effects (Gibson, 1994).

2.4.1 *Moisture*

The hygrothermal degradation of FRP composites is mainly divided into two categories: the reduction of the glass transition temperature Tg (Khan, Nesbitt et al., 2010; Zafar, Bertocco et al., 2012), and the hygrothermal stress induced by the hygrothermal expansion (Gibson, 1994). Most significantly, moisture reduces the Tg of polymer matrix due to plasticisation of the matrix as a result of interruption of Van Der Waals bonds between the polymer chains (Wolff, 1993), which also leads to the decrease of matrix dominated stiffness and strength of FRP composites. Typically, the combination of moisture and temperature is considered simultaneously to determine synergistic effects of these two exposures. According to the previous studies, temperature does not

change the saturated moisture content but accelerates the process of diffusion. For many polymer composites, the temperature distribution approaches equilibrium about one million times faster than the moisture concentration (Shen and Springer, 1976). Therefore, the short time-scale fluctuations in temperature can be neglected compared to the evolution of moisture content.

Moisture diffusion in isotropic material, such as pure polymer, is governed by Fick's first and second laws (Smith and Hashemi, 2006). However, many previous publications, e.g. (Shen and Springer, 1976; Vinson, 1978; Cairns and Adams, 1981; Springer, 1981), have shown that moisture diffusion in polymer-based composites also follow Fick's laws. For a thin plate ($w/h >> 1, l/h >> 1$), the moisture content can be derived from Fick's first and second laws which is presented as (Kumar, Sridhar et al., 2008),

$$M = \begin{cases} \left(\dfrac{4M_\infty \sqrt{D}}{h\sqrt{\pi}} \right) \sqrt{t}, \left(t << 0.05h^2 / D \right) \\ M_\infty \left[1 - \dfrac{8}{\pi} \exp\left(\dfrac{-Dt\pi^2}{h^2} \right) \right], \left(t > 0.05h^2 / D \right) \end{cases} \tag{2-10}$$

or the ASTM calculation (D5229/D5229M, 2004),

$$M = M_\infty \left[1 - \exp\left(-7.3 \left(\frac{Dt}{h^2} \right)^{0.75} \right) \right] \tag{2-11}$$

where M_∞ is the maximum mass gain; D is the moisture diffusivity, l, w and h are the length, width and thickness of the plate; and t is time.

The apparent diffusivity can be calculated at the beginning of diffusion (linear stage of the plot of moisture content M to the square root of time $\sqrt{t}$) (D5229/D5229M, 2004),

$$D = \pi \left(\frac{h}{4M_\infty} \right)^2 \left(\frac{M_2 - M_1}{\sqrt{t_2} - \sqrt{t_1}} \right)^2 \tag{2-12}$$

The diffusivity that appears in Fick's laws is related to temperature by the Arrhenius relationship (Gibson, 1994),

$$D = D_0 \exp\left(\frac{-E_a}{RT}\right) \tag{2-13}$$

where R is the gas constant having a value of $R = 8.31 J \cdot mol^{-1} \cdot K^{-1}$; D_0 is material constant; and E_a is the activation energy for diffusion. The exponential function indicates that the moisture diffusivity is extremely sensitive to temperature and may increase by two orders of magnitude with a temperature rise of 100K (Loos and Springer, 1979; Harper and Weitsman, 1985).

If the dimension is finite, the longitudinal moisture diffusivity D_L and transverse diffusivity D_T should be used to compensate the edge correction (Pomies, Carlsson et al., 1995),

$$D_T = D / ECF \tag{2-14}$$

$$ECF = \left(1 + \frac{h}{l}\sqrt{\frac{D_L}{D_T}} + \frac{h}{w}\right) \tag{2-15}$$

$$\sqrt{D} = \frac{w+h}{w}\sqrt{D_T} + \frac{h}{l}\sqrt{D_L} \tag{2-16}$$

The apparent moisture diffusivity D is determined by equation (2-12), while D_L and D_T can be determined by two different samples,

$$\begin{cases} D_T = \left(l_1\sqrt{D_1} - l_2\sqrt{D_2}\right)^2 \cdot \left(\frac{w_1+h}{w_1}\cdot l_1 - \frac{w_2+h}{w_2}\cdot l_2\right)^{-2} \\ D_L = \left[\frac{l_1}{h}\left(\sqrt{D_1} - \frac{w_1+h}{w_1}\sqrt{D_T}\right)\right]^2 \end{cases} \tag{2-17}$$

where l_1, w_1, l_2, w_2 l1 are the length and width of the two samples; D_1 and D_2 are the apparent moisture diffusivities of the samples. With a very long length l and short width w, equation (2-17) is reduced to (Meng, Rizvi et al., 2015c),

$$\sqrt{D_1} = \frac{w_1+h}{w_1}\sqrt{D_T} \tag{2-18}$$

With a very long width w and short length l, equation (2-17) is reduced to,

$$\sqrt{D_2} = \sqrt{D_T} + \frac{h}{l_2}\sqrt{D_L} \qquad (2\text{-}19)$$

Previous experimental observations (Shen and Springer, 1976; Cairns and Adams, 1984) have demonstrated that, for polymer composites, the expansion induced by moisture absorption is generally a linear function of moisture content if the range of moisture content is less than 2%. This relation is normally used to determine the coefficient of hygrothermal expansion (CHE) in a unidirectional lamina, and classical laminate theory (CLT) can be employed to calculate the CHE at the laminate level (Gibson, 1994). Since the moisture distribution inside composites is non-uniform throughout any given ply, CLT is unlikely to predict the hygrothermal expansion and the associated stresses for a laminate with a complicated lay-up. The effects of hygrothermal stress built up, along with additional external mechanical loading, on the physical properties of CFRP appear not to have been investigated extensively.

Because the fibre does not absorb moisture, the 'rule of mixture' should be taken into account, and the principal CHE values at the lamina level can be calculated by (Gibson, 1994),

$$\begin{cases} \beta_1 = \dfrac{E_m}{E_1}\dfrac{\rho_c}{\rho_m}\beta_m \\ \beta_2 = (1+\nu_m)\dfrac{\rho_c}{\rho_m}\beta_m - \beta_1\nu_{12} \end{cases} \qquad (2\text{-}20)$$

$$\rho_c = \rho_f V_f + \rho_m(1-V_f) \qquad (2\text{-}21)$$

where β_1 and β_2 are the longitudinal and transverse coefficient of hygrothermal expansion; ρ_c, ρ_f and ρ_m are the density of composite, fibre and matrix. The coefficient of hygrothermal expansion in polymers, β_m, ranges between 0.2% and 0.5% per 1% moisture weight gain (Adamson, 1980; Cairns and Adams, 1984). Typically, for many epoxy matrices, the β_m value is in the order of 0.32 (Walrath and Adams, 1980).

2.4.2 *Temperature*

The increase of temperature may cause a gradual softening of the polymer matrix, while the value of Tg shows an reduction of the order of 20% when the polymer matrix saturates, compared with the dry condition (Gibson, 1994). For some extremely

temperature conditions such as fire exposure, the degradation effects also include the decomposition of the materials itself (Griffis, Nemes et al., 1986). When the composite structures are exposed to direct sunlight, the surface temperature of the component will depend on the colour of a surface, showing approximate 20°C to the ambient temperature for white and up to 60°C for the black (Summerscales, 2014).

The main consideration is the thermal expansion when the FRP composites are cured at high temperature and cooled down. The coefficient of thermal expansion (CTE) of both glass fibre and carbon fibre are quite different from that of resin, therefore the swelling or contraction of the polymer matrix is resisted by the fibres and residual stresses develop in composites. **Table 2-4** gives the thermal properties of some fibres and epoxy (Chamis, 1987; Daniel and Ishai, 1994).

Table 2-4 Comparison of longitudinal and transverse CTE (α) and thermal conductivity (ρ) of some common glass fibres, carbon fibres and epoxy resins (data source: Wikipedia and respective product technical data sheet)

Material	α_1 (10^{-6}m/m/K)	α_2 (10^{-6}m/m/K)	ρ_1 (W/m/K)	ρ_2 (W/m/K)
E-glass	5	5	36	36
S-glass	5	5	13	13
Carbon T300	-0.6	10.1	1003	100
Carbon HMS	-1	6.8	1003	100
Epoxy 934	43.9	43.9	0.2	0.2
Epoxy 5208	43.9	43.9	0.2	0.2

2.4.3 *Pressure*

The effect of pressure on FRP composites can be divided into the glass transition temperature and the moisture diffusion. (Mijovic, 1985) investigated the effect of pressure on the Tg of carbon/epoxy composite and found that it increased when tested under a vacuum environment. However, when a hydrostatic pressure was applied on carbon/polymer composite, it was found that the pressure had no effect on the moisture diffusivity however the saturated moisture content increased compared with the ambient environment (Tucker and Brown, 1989).

2.4.4 *Saline*

Saline is the main cause of chemical corrosion in the marine environment. Although the composition of sea water varies with ocean position and depth, sodium chloride makes up approximately 85% of the solutions in sea water. ASTM D1141 provides a guideline for the preparation of substitute sea water (D1141-98, 2008). **Table 2-5** shows a comparison between fresh water and seawater (Livingstone, 1963).

Investigation of degradation in seawater has been carried out. (Springer, 1983) had reported extensive test data on the effect of seawater immersion on the mechanical properties of glass/polyester under different temperature conditions. (Wood and Bradley, 1997) investigated the interfacial strength of carbon/glass/epoxy composite by immersing the hybrid composites in seawater and reported that the damage was initiated at the boundaries of resin rich regions regardless of the conditioning process. (Kootsookos and Mouritz, 2004) compared seawater degradation of different types of FRP composites and reported that polyester-based composites were less chemically stable than vinyl ester-based composites. Although the seawater immersion test has been reported by some literatures, the mechanisms of the degradation of FRP composites caused by chemical solutions in seawater are not well known.

Table 2-5 Chemical analyses of mean river water and seawater, and a comparison of relative concentrations in river water and ocean (Livingstone, 1963)

Species	River(mg/L)	Sea(mg/L)	Ratio(times)
Ca	15	410	27
Mg	4.1	1350	329
Na	6.3	10500	1667
K	2.3	390	170
HCO_3	60	142	2
Cl	7.8	19000	2436
SO_4	11	2700	245
SiO_2	13.1	6.4	0.489
Fe	0.67	0.003	0.004
Al	0.07	0.001	0.014

The effect of electrochemical processes on the properties of carbon-based composites in seawater has also been considered since carbon fibre is electro conductive. (Alias and

Brown, 1992) investigated the carbon/vinyl ester and hybrid carbon/glass/vinyl ester composites connected with metals in artificial seawater solution with 3.5% NaCl and found that the matrix was significantly damaged due to the galvanic action. The Kobold marine turbine, which was settled in the Messina channel in Italy, has suffered severe galvanic corrosion due to the electrical conductivity of carbon fibre (INSEAN, 2007).

2.4.5 *Other aspects*

Sunlight contains ultraviolet light which has been known to cause degradation of polymeric materials. Among the three common resins used in marine composites, epoxy resins are generally the most sensitive to the ultraviolet light and vinyl ester is the next because there are epoxy linkages in it, however polyester is the least sensitive of the three to ultraviolet light (Greene, 1999). According to (Ashbee, 1993), ultraviolet light degradation involves the fading of aesthetic appearance of the surface since the ultraviolet only affects a depth of about ten micrometres of the structure.

The biodegradation of FRP composites has also been investigated. (Wagner, Little et al., 1996) studied the microbiologically-influenced degradation of epoxy-based and vinyl ester-based carbon and glass fibres composites exposed to a variety of bacteria. They found that carbon/epoxy composites were not degraded in the microbial environment and for the vinyl ester-based composites; the hydrogen-producing bacteria provided biofilms that disrupted the moisture diffusion.

2.5 Research methods

Considerable work has been carried out on the physical and mechanical analyses of FRP composites in both ambient and marine environments, and particular properties were investigated by experimental, numerical and analytical approaches. This section discusses the current use of the three main research methods, with emphasis on mechanical performance and environmental exposure.

2.5.1 *Experimental model*

The choice of the particular experimental technique is tied to the aspects of degradation which need to be measured. The aspects which are of interest are generally divided into: (a) mechanical properties including tensile/compressive moduli, tensile/compressive

strengths, flexural/interlaminar shear strengths and failure modes; (b) physical properties including moisture diffusivity, hygrothermal expansion and Tg. In literature, most of the work follows the standard techniques and standard equipment specified by ISO, ASTM or other standardization organizations to perform the actual tests so as to present data in a standard form.

A variety of mechanical tests have been used to determine the properties of FRP composites following marine exposure, and then these data can be used to compare with those measured in ambient conditions. The standards for particular mechanical tests have been discussed in the section 2.2-2.4; additionally the optical microscope or scanning electronic microscope (SEM) is used to identify the failure modes following the mechanical tests.

Due to the very slow process of moisture diffusion in polymeric matrices, accelerated diffusion tests are usually carried out to find out the saturated moisture content and moisture diffusivity by using Fick's laws rather than testing at room temperature, and the Arrhenius relation is used to correlate the moisture diffusivity. Hygrothermal expansion is widely measured by vernier calliper which sometimes provides insufficient accuracy (only ±0.01mm). (Kumar, Sridhar et al., 2008) used a vernier calliper to measure the hygrothermal expansion of a unidirectional 913-HTA CFRP composite in the three directions: length, width and thickness. However, the result is doubtful since the expansion along longitudinal direction is expected to be very small which is out of the precision of a vernier calliper.

Dynamic mechanical analysis (DMA) and differential scanning calorimetry (DSC) are used to determine the Tg of FRP composites. DMA measures the change in mechanical behaviour of materials, i.e. damping properties to determine the Tg. (Birger, Moshonov et al., 1989) used DMA to investigate the Tg of carbon/epoxy composites in dry and wet condition and reported that the Tg increased with elevated temperature ageing and decreased with moisture absorption. DSC measures the change of thermal absorption in crystallization of materials to determine the Tg. (Mijovic, 1985) investigated the temperature and pressure exposure of carbon/epoxy composite by using DSC and found the physical aging phenomenon after the exposure.

Raman spectroscopy is employed to investigate the stress/strain stage of carbon fibre. (Zafar, Bertocco et al., 2012) extracted the Raman spectrum (G band) of carbon/epoxy composite to determine the stress in carbon fibre in order to correlate the hygrothermal expansion of composites. With the increase of strain of carbon fibre, the intensity of G band shifts to a higher wavenumber. Non-destructive detection, such as acoustic emission (Kotsikos, Evans et al., 2000) and CT scanning (Grogan, 2015), has been used to study the material damage evolution.

2.5.2 *Numerical model*

Numerical simulation has been widely used to predict the mechanical behaviour of FRP composites. Some commercial software packages, which are based on shell elements, are available, such as ANSYS Advanced Composites Pre-post (ACP), ABAQUS and SOLIDWORKS. However, classical numerical methods based on infinitely thickness plates have experienced difficulties on regions near boundaries. This is because these commercial software packages consider the composites as shell elements which ignore the effects of the thickness of the component. The shell method suffers from poor accuracy in case of thick laminate. Three-dimensional numerical analysis has been used to examine the stress distribution in laminated composites. The pioneer work was carried out by Pipes and Pagano using the Finite Difference Method (FDM) (Pipes and Pagano, 1970; Pagano, 1978). They demonstrated the singularity of interlaminar shear stress at the edge region in an angle-ply laminate under tensile stress. Similar work investigated the interlaminar shear stress at free edges using FEA (Wang and Crossman, 1977; Murthy and Chamis, 1987; Kassapoglou, 1990), Eigen-function expansions (Pipes, 1980; Wang and Choi, 1982), Boundary Layer theory (BLT) (Tang, 1975; Tang and Levy, 1975), and Layer-wise theory (LWT) (Lee and Chen, 1996). A good review by (Kant and Swaminathan, 2000) has covered the analytical and numerical methods on free-edge problems of interlaminar shear stress up to the year 2000.

Previous work on 3D analysis has illustrated the increase of interlaminar shear stress at the edge region. Although the global load may be lower than the composites strength, the interlaminar shear stress can induce initial delamination at edge region which reduces the fatigue life of composites. This phenomenon had been reported in composites design and manufacturing (Foye and Baker, 1970). In order to investigate

the free edge effect on interlaminar shear stress, most of the previous works focused on uniform axial loads. This type of loading condition ignores some stress components, such as out-of-plane stresses, which nevertheless have a significant effect on the bending failure behaviour. Moreover, with the decrease of the support span in bending, these stress components play an increasingly important role in composite failure modes. Due to the nature of bending, laminates are subjected to tension, compression and shear, so all of the six stress components should be considered when evaluating failure criteria. However, there have been few reports on the free edge effect in bending.

Due to the limitation of computing power, earlier works on 3D analysis could only consider a few plies for the demonstration. When composite laminates are made of many plies with complicated orientation, the prediction of these models may lead to inaccurate results. (Pipes and Pagano, 1970) illustrated the singularity of interlaminar shear stress at edge region of an angle-ply laminate which consisted of four plies. Additionally, the FEA model for angle-ply laminate is unlikely to be simplified as symmetric in bending, due to the complicated ply lay-up pattern. This means that a full model need to be considered and significant computing resources are required for modelling.

Since fracture mechanics was established as a discipline, many mathematical techniques have been developed to predict crack growth, in which some of the most popular methods used for the delamination of composites are extended finite element method (XFEM) (Melenk and Babuška, 1996; Abdelaziz and Hamouine, 2008; Belytschko, Gracie et al., 2009), cohesive element method (CZM) (Chowdhury and Narasimhan, 2000; Park and Paulino, 2011) and virtual crack closure technique (VCCT) (Rybicki and Kanninen, 1977; Raju, 1987; Irwin, 1997). The advantage of XFEM, predicting the onset of the crack by maximum principal stress/strain, is commonly combined with the other methods to model the crack initiation and propagation. The fracture criterion of XFEM is based on tensile strength which is unlikely to predict the onset of the crack in the present case which suffers compression delamination. On the other hand, VCCT is the only technique so far which models fatigue crack propagation, so that the development of the crack propagation is commonly implemented by VCCT.

2.5.3 *Analytical model*

Classical Laminate Theory (CLT) (Kaw, 2006), First-order Shear Deformation Theory (FSDT) (Yang, Norris et al., 1966; Whitney and Pagano, 1970) and Refined Shear Deformation Theory (RSDT) (Jing and Tzeng, 1993) are used to predict the mechanical behaviour of infinite composite plates. Because these classical theories are based on the assumption of infinitely wide plates, which is similar with the numerical model, the edge effect is not included. Moreover, these methods consider the composite as a shell; as a consequence, some of the stress components, such as out-of-plane stresses, are neglected.

2.6 Summary

This chapter has presented a literature review on the CFRP composites and corresponding marine environmental effects. Most attention has been paid to the failure analysis of FRP composites, including material constitution, failure modes, environmental degradation, as well as relevant standard test methods. Some conclusions as well as the research gaps drawn from the literature are summarised as follows:

- The material properties of FRP composites are orthotropic which is fundamentally different from those of isotropic materials such as metals. The performance of FRP composites is determined by the combination of the types of fibres, matrices and their volume fraction as well as the manufacturing process. Carbon-epoxy composites present better performance in the marine environment; however their costs are also higher. Both the fibres and matrices have been well studied; however there is still lack of literature on the interphase due to the limitation of research techniques. Therefore, study of stress transfer among the fibre, matrix and their interphase will be conducted by FEA simulation which is presented in Chapter 5.
- FRP composites show a variety of failure modes which is dependent on the constituent materials, stack-up sequence and the loading conditions. An insight into the stress/strain distribution is required to understand the composite failures. There is no single failure criterion which can cover all the failure modes of FRP composites. Most of the current investigations of FRP composites are based on

test coupons following standard test methods; however there is still a lack of literature on the linkage between small coupons and the practical structures. Therefore, study of stress/strain distribution will be investigated by a 3D FEA model to unveil the failure initiation, which is presented in Chapter 4.

- Degradation of FRP composites in marine environment exposure has been widely recognized. The main consideration is due to moisture degradation. Most of the previous studies only provided a shallow view of the degradation such as the modulus, strength and Tg. There is still lack of literature on the mechanisms of this degradation in view of multiscale and multiphysics. Therefore, a 3D FEA model will be developed to combine the diffusion test in order to investigate the moisture degradation on the mechanical and chemical properties, which is presented in Chapter 5.
- Fatigue analysis of FRP composites is widely based on empirical equations, and most of the work focused on glass fibre composites. In view of the complexity of microstructural damage accumulation during fatigue cycling there is little hope for determining the fatigue life of FRP composites using a universal criterion. It is envisaged that hygrothermal stresses caused by moisture diffusion may play an important role in the initiation of damage and fatigue. Therefore, the interaction between fatigue and water ingress will be investigated by FEA simulation, which is presented in Chapter 6.
- Experimental, numerical and analytical models have been built up for investigating the performance of FRP composites. The previous studies employed either an individual model or the combination of two; however literature on multiphysics and multiscale analysis is still rare. Therefore, this thesis will try to combine the three approaches to investigate the effects of marine environment exposure on the static and fatigue mechanical properties of FRP composites from micro scale to macro scale.

CHAPTER 3 – MANUFACTURE AND INSPECTION

This chapter presents the preparation of specimens, the evaluation of manufacturing defects, and the prediction of laminate properties. The traditional classical laminate theory (CLT) is extended to 3D version, and some MATLAB tools based on the 3D CLT is then developed not only to predict the mechanical and chemical properties of composite laminates but also analyse the experimental data. Some derived formulae for the prediction of mechanical/physical performance are also presented in this chapter.

3.1 Specimen manufacturing

High strength carbon fibre/epoxy pre-preg (product code: Cytec 977-2-12kHTS-34-300), provided by Cytec Industries Incorporated, was used in this project. This is a high temperature (180°C) curing toughened epoxy resin with 212°C glass transition temperature (T_g) which is formulated for autoclave moulding. The aromatic epoxide-amine network (Rasoldier, Colin et al., 2008) constitutes of bisphenol A diglycidyl ether (commonly abbreviated BADGE, or DGEBA) and diaminodiphenyl sulfone (DDS). It can be seen from **Figure 3.1** that the DGEBA contribute hydroxyl radicals which are hydrophilic.

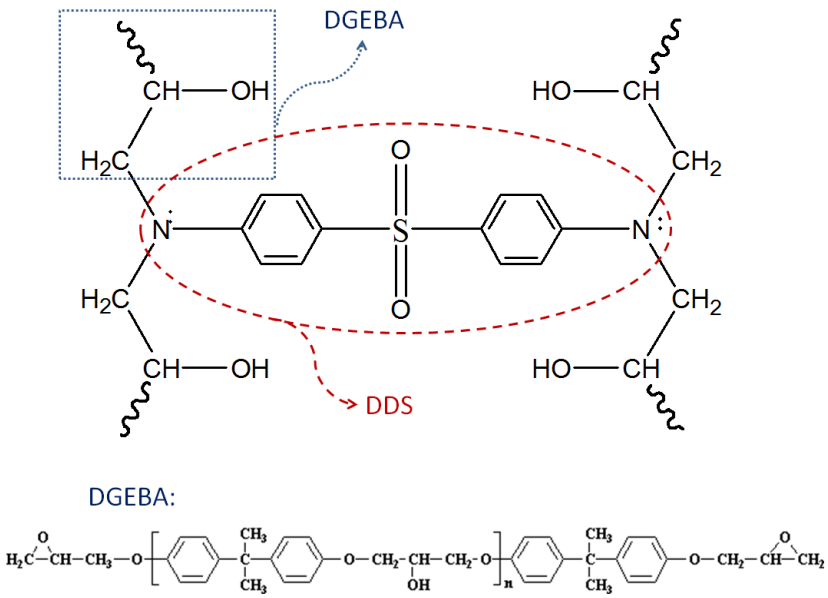

Figure 3.1 Schematics of crosslink network of 977-2 epoxy resin. The value n is in the range of 0-25.

The fibre is a PAN-based carbon fibre which presents parallel graphite layers to the surface near the skin region (Johnson, 1987). Therefore, the transverse elastic properties of carbon fibre are significantly lower than the longitudinal properties. Studies have suggested that the transverse modulus is about 10% of its longitudinal value (Bowles and Tompkins, 1989; Voyiadjis and Kattan, 2005; Hyer, 2009). In terms of the composite, the interface is usually considered as the chemically bonded junction between resin (including the size) and the fibre surface. The link between resin and fibre is very complicated. (Kardos, 1985) suggested that the link contains five zones which are shown in **Figure 3.2** (b), where A is the fibre, B is a layer of reactive site on the fibre surface, C is the third-phase interlayer referred to above, D is size, and E is the matrix. The typical thickness of the interphase is 0.1μm on 7μm diameter fibres, which is variable for different types of fibre surface treatment (Hughes, 1991). According to (Waltersson, 1985), approximately 33% of the region of the fibre/matrix interface was not well bonded within carbon-epoxy composite, therefore it was suggested that the mechanical properties of the interphase (e.g. elastic modulus and tensile strength) could be up to 1/3 lower than the matrix.

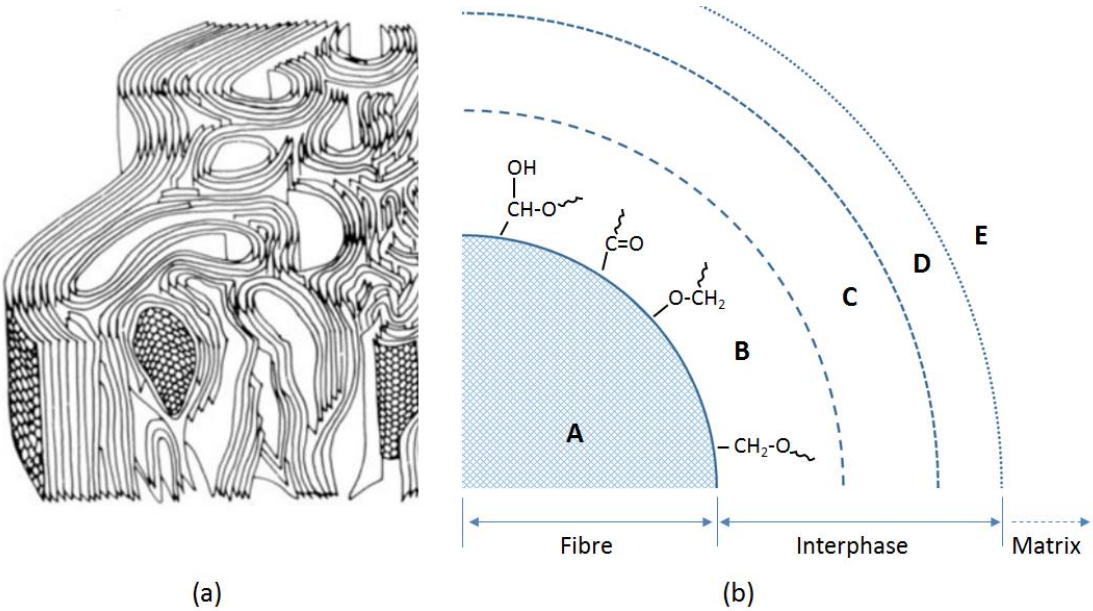

Figure 3.2 (a) Schematic representation of carbon fibre (Kardos, 1985), and (b) region of fibre-epoxy interface (Meng, Rizvi et al., 2016)

Five different laminate layers were investigated for the mechanical and physical tests. The composite laminates were to be tested in bending following (ISO12130, 1998;

ISO14125, 1998) which required a nominal thickness of 2 mm. Therefore all of the laminates were made up of 16 plies. Table 3-1 shows the laminate configuration.

Table 3-1 Laminate configuration

Laminate	Lay-up	Thickness (mm)	Ply-thickness (mm)
UD	$[0]_{16}$	2.08	0.13
UT	$[90]_{16}$	2.08	0.13
CP-1	$[90/0]_{4s}$	1.92	0.12
CP-2	$[0/90]_{4s}$	1.92	0.12
AP	$[+45/-45]_{4s}$	1.92	0.12

The pre-preg was placed on a mould and sealed in a vacuum bag, and then were autoclave-cured at 6 bar (0.6 MPa, 85 psi) pressure. A heating rate of 3˚C/min from room temperature to 180˚C was applied, and then the pre-preg plates were held at 180˚C for 120 minutes and cooled down at room temperature. In order to make the laminate 'self-balance' to reduce the distortion due to the thermal expansion, the laminates were designed in symmetry and the middle two plies were set at the same fibre orientation. **Figure 3.3** shows the temperature history of the autoclave, while **Figure 3.4** shows the preparation of specimens.

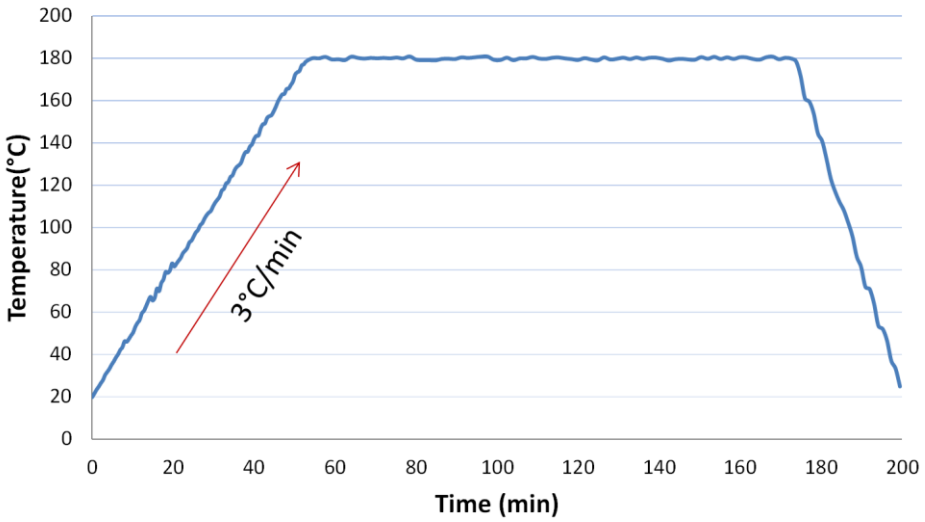

Figure 3.3 The temperature history of the autoclave

These five lay-ups (unidirectional $[0]_{16}$, unidirectional transverse $[90]_{16}$, cross-ply $[0/90]_{4s}$ cross-ply $[90/0]_{4s}$, and angle-ply $[+45/-45]_{4s}$) are the simplest examples of

laminates which show a range of behaviour: the unidirectional laminates (longitudinal $[0]_{16}$, transverse $[90]_{16}$) are respectively fibre and matrix dominated which show the strongest and weakest mechanical properties, while the cross-ply ($[0/90]_{4s}$, $[90/0]_{4s}$) and angle-ply ($[+45/-45]_{4s}$) laminates present intermediate properties. The stress distributions and failure modes for a given laminate lay-up could be extended from these five layups. The two unidirectional laminates were cut from the same composite plates with different cutting orientations, as well as the cross-ply and angle-ply laminates. The cutting pattern is shown in **Figure 3.5**.

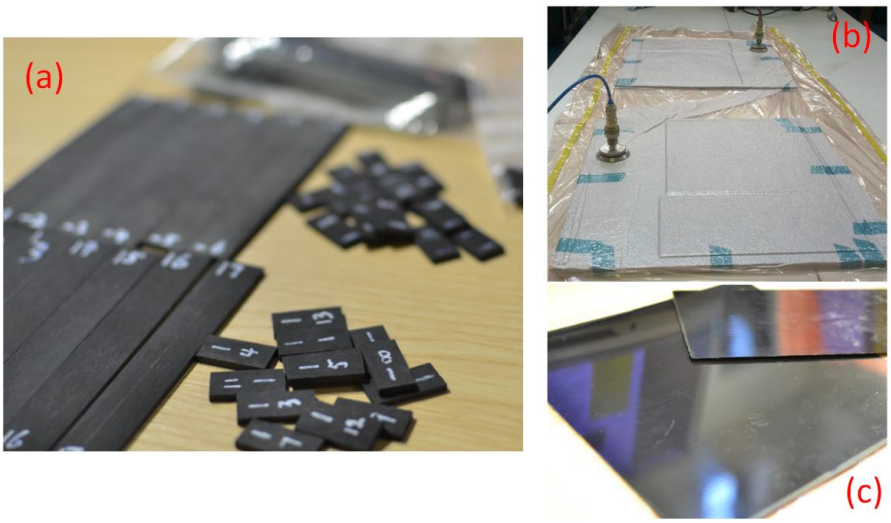

Figure 3.4 The preparation of pre-preg CFRP composite: (a); tailored specimens; (b) pre-preg plates sealed in vacuum bag before being cured; (c) pre-preg plates after being cured.

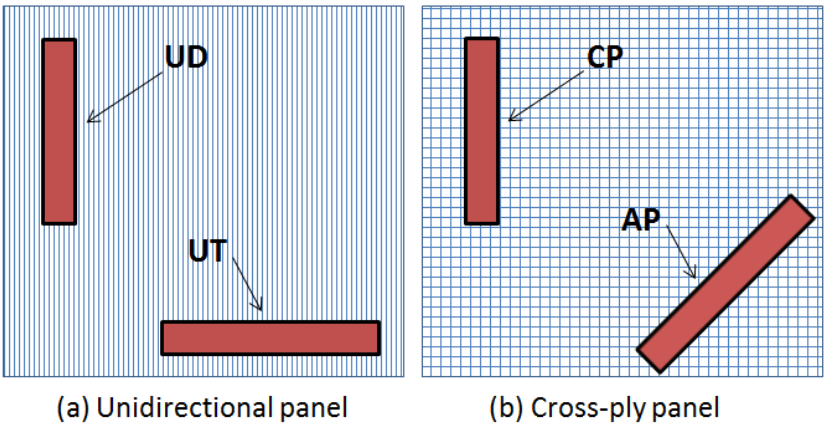

Figure 3.5 The cutting pattern of the composite laminates. UD and UT laminates were cut from one panel with perpendicular orientation, while CP and AP were from the other.

The final thicknesses of the laminated composites were not consistent. There are two possible reasons: a) the surface morphology of unidirectional laminate is tougher than cross-ply laminate; b) the void content in unidirectional laminate is higher than that in cross-ply laminate. These manufacturing defects may lead to an apparent thickness difference.

The material properties of carbon fibre (HTS) and epoxy (977-2) from the manufacturers' data sheets (Toho-Tenax; Cytec, 2012) are illustrated in **Table 3-2**. It can be seen from the table that the flexural strength of the matrix is much higher than the tensile strength. This may affect the flexural strength of transverse unidirectional laminate ($[90]_{16}$). The fibre volume fraction V_f can be calculated from weight percentage of matrix W_m,

$$V_f = \frac{(1-W_m)/\rho_f}{(1-W_m)/\rho_f + W_m/\rho_f} = \frac{\rho_m(1-W_m)}{\rho_m(1-W_m)+\rho_f W_m} \qquad (3\text{-}1)$$

where ρ_f, ρ_m are the densities of fibre and matrix respectively.

Substituting the values in **Table 3-2** into equation (3-1), the fibre volume fraction can be estimated as $V_f = 57.9\%$.

Table 3-2 Mechanical properties of the fibre and matrix of Cytec 977-2-12kHTS. The fibre transverse modulus is estimated as 10% of its longitudinal modulus, according to references (Bowles and Tompkins, 1989; Voyiadjis and Kattan, 2005; Hyer, 2009)

Symbol	E_1^f	$E_2^f = E_3^f$	$\nu_{12}^f = \nu_{13}^f$	ν_{23}^f	ρ_f	ρ_m
Value	238GPa	23.8GPa	0.2	0.4	1.77 gcm^{-3}	1.31 gcm^{-3}
Symbol	W_m*	E_m	ν_m	$(\sigma_f^{ult})^t$	$(\sigma_m^{ult})^t$	$(\sigma_m^{ult})^f$
Value	35%	3.52GPa	0.34	4.3GPa	81.4 MPa	197MPa

***W_m is the matrix fraction in weight; $(\sigma_f^{ult})^t$ and $(\sigma_m^{ult})^t$ are the tensile strength of fibre and matrix; $(\sigma_m^{ult})^f$ is flexural strength of matrix.**

3.2 Specimen inspection

Manufacturing defects are inevitable in FRP composites. The main considerations are the void content and the fibre misalignment. The effects of void content include: (a) the reduction of fibre volume fraction which affects the modulus and strength of the composite; (b) the introduction of stress concentration which initializes the crack tip and leads to fatigue failure. Fibre misalignment also reduces the mechanical performance, i.e. modulus and strength; moreover it may increase the risk of fibre micro-buckling under compression.

3.2.1 *Void inspection*

The void content in FRP composites may have a range of less than 1% to as high as 7% depending on the manufacturing processes. The evaluation of void content for FRP composite includes qualitative and quantitative inspections.

Only the qualitative inspection, which was carried out using an optical microscope, was conducted in this thesis. The specimens were set in a mould and encapsulated by transparent resin, and then ground and polished to be optically flat using a suspension containing 1.5μm diamond particles, as shown in **Figure 3.6**. The polished specimens were then inspected by an optical microscope using 100 magnifications (OLYMPUS BX60M), and the images were taken and processed by OLYMPUS STREAM software (version 1.9).

(a) (b) (c)

Figure 3.6 (a) Preparation of the polished laminate specimens for the microscopic study; (b) the specimens were placed on the optical microscope; (c) images extract and data processing

Figure 3.7 shows a void in a microscopic image of a cross-section of a unidirectional laminate. The edge and centre of the composite plates were inspected, however, no voids were found in cross-ply and angle-ply laminates. In accordance with the real thickness of composite laminates, the ply thicknesses of UD and CP/AP laminates were adjusted to fit the total thickness (shown in **Table 3-1**).

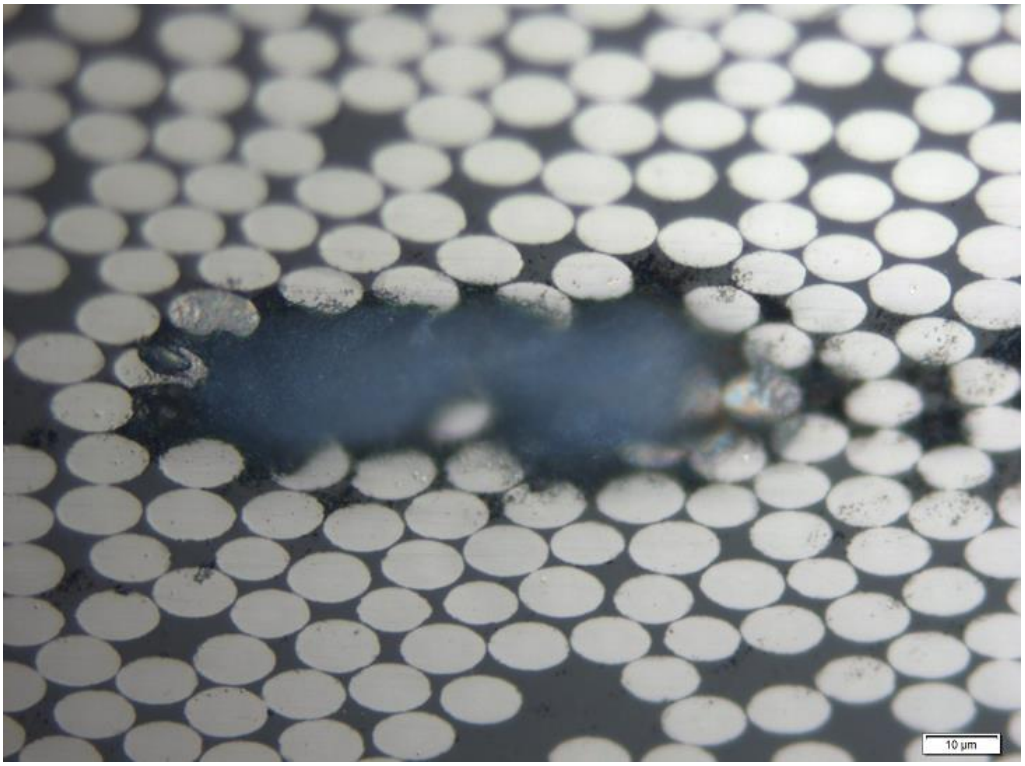

Figure 3.7 Optical microscopic image of the unidirectional laminate. A huge void was found, which was probably because of the manufacturing process.

ASTM provides a standard for the quantitative inspection of void content of FRP composites using resin burn-off method (ASTM-D2734, 2009), however this is out of the scope of this project.

3.2.2 *Fibre misalignment*

Fibre misalignment was evaluated by using the same technique as the inspection of void content. **Figure 3.8** gives an indirect approach to measure the misalignment angle in a long fibre laminate. If it is assumed that the fibre is perfectly circular, the projection of

the fibre cross-section on horizontal plane is an ellipse, and the misalignment angle can be calculated by the ratio of short/long radius,

$$\theta_1 = \sin^{-1}(r_2 / r_1) \tag{3-2}$$

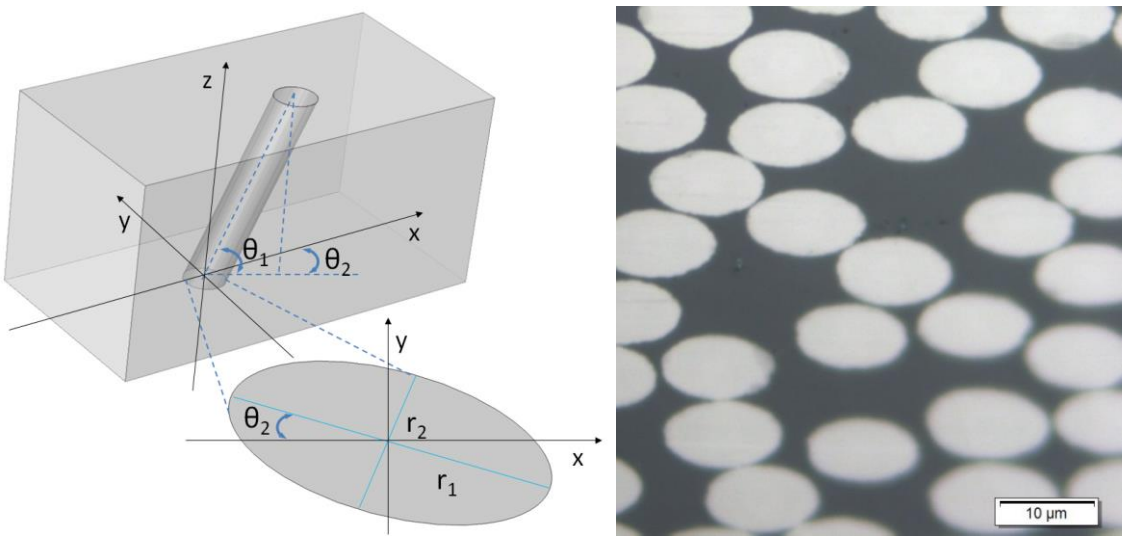

(a) (b)

Figure 3.8 Schematics of the measurement of fibre misalignment in a long fibre UD laminate (a), and a typical microscope image of the cross-section of UD laminate (b)

It should be noted that the gradient of sinusoidal function around 90° (equivalent to $r_2 / r_1 = 1$) is very small which increases the difficulty of the measurement. Therefore, the unidirectional laminate was consolidated in the mould at a proper oblique angle (35° in this thesis), in order to extract a measureable value of r_2 / r_1.

The measurements of the fibre misalignment angle were then imported into MATLAB for the fitting using DFITTOOL toolbox. **Figure 3.9** shows the normalized angle of fibre misalignment of HTS-12K/977-2 unidirectional laminate. The distribution of misalignment angles show a good fit to a normal distribution (Gaussian distribution),

$$f(\theta_1) = \frac{1}{\sqrt{2\pi}\sigma_0} \exp\left(-\frac{(\theta_1 - \mu_0)^2}{2\sigma_0^2} \right) \tag{3-3}$$

where μ_0 and σ_0 are the parameter of expectation and standard deviation respectively. For HTS-12K/977-2 unidirectional laminate $\mu_0 = 0, \sigma_0 = 2.03$.

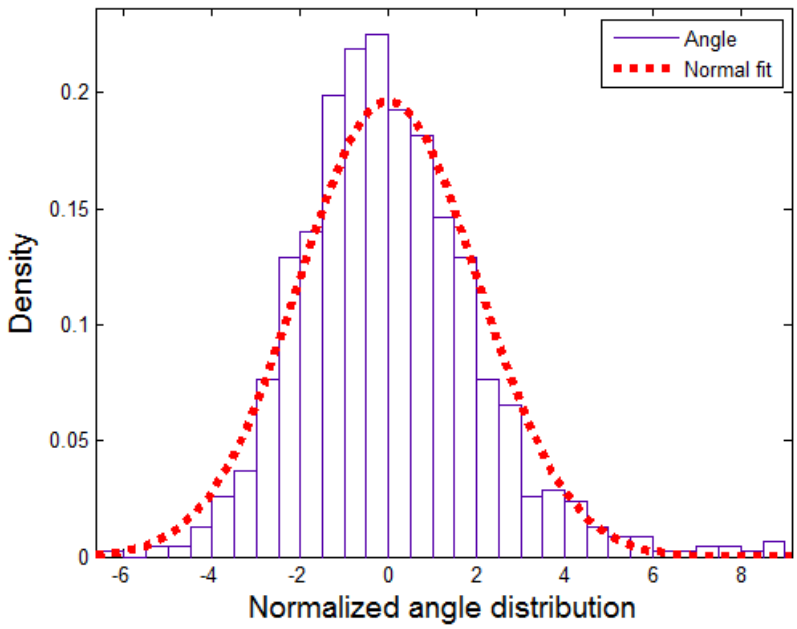

Figure 3.9 Normalized fibre misalignment angle in long fibre CFRP composite. Approximately ten thousand fibres are included in the statistics.

In Figure 3.8, it can be seen that the misalignment angle can extend up to ±6°. Although the spectral density of these angles is very small, the compressive failure may well initialize from these fibres and propagate through the whole laminate, and as a consequence the compressive strength is expected lower than tensile strength.

3.2.3 *Fibre packing*

Regardless of the stacking sequence of a composite laminate, all the fibres in each ply are assumed to be aligned parallel to each other. There are several fibre packing assumptions to predict the maximum theoretical fibre volume fraction, such as hexagonal and square lattices (Hull and Clyne, 1996),

$$V_f = \frac{\pi}{2\sqrt{3}}\left(\frac{r}{R}\right)^2 \qquad \text{(Hexagonal)} \qquad (3\text{-}4)$$

$$V_f = \frac{\pi}{4}\left(\frac{r}{R}\right)^2 \qquad \text{(Square)} \qquad (3\text{-}5)$$

where V_f is the fibre volume fraction, r is the radius of a single fibre and R is half of the central distance between two adjacent fibres.

Theoretically, it is predicted that the maximum fibre volume fraction is $V_f = 0.907$ for hexagonal lattice and 0.785 for square lattice by equation (3-4) and equation (3-5). For many carbon fibres, the average radius is approximately 3.5μm (such as HTS used in this thesis). Considering the inversion of equation (3-4) and equation (3-5), the central distance between two adjacent fibres within a composite ply with $V_f = 0.58$ can be calculated as 8.75μm (hexagonal) and 8.14μm (square).

Due to the inevitable limitations of the current manufacturing technique, the fibre lattice cannot be perfectly hexagonal or square. **Figure 3.10** shows the real fibre lattice of a unidirectional laminate (Cytec 977-2-12kHTS). A mixture of the hexagonal and square lattices can be seen from the figure, with quite a few resin rich volumes.

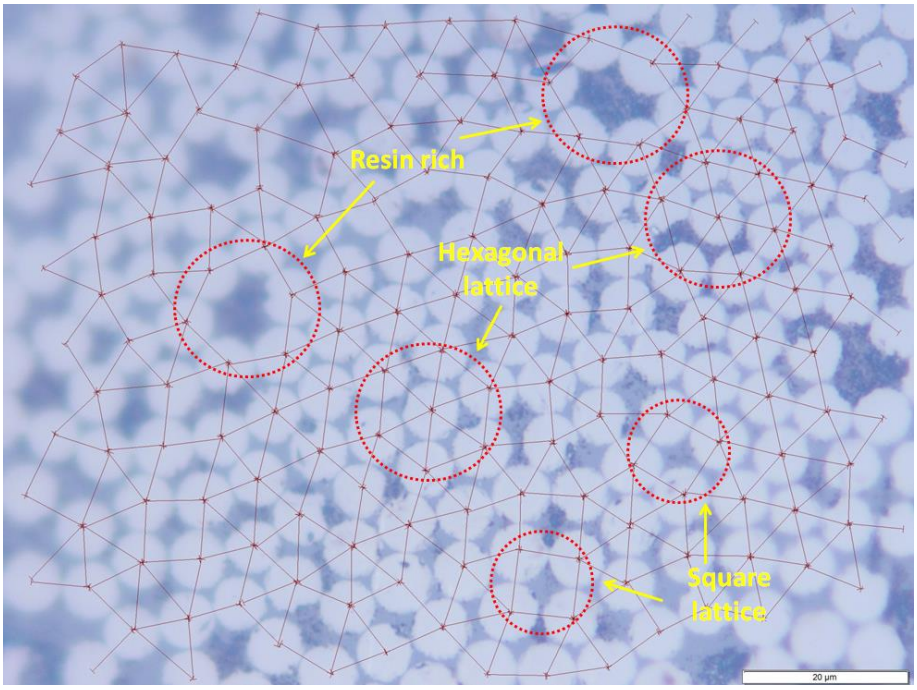

Figure 3.10 Fibre lattice of a unidirectional laminate

Figure 3.11 shows the statistics of the central distance between two adjacent fibres of Cytec 977-2-12kHTS unidirectional laminate ($V_f = 0.58$) based on the fibre lattice shown in **Figure 3.10**. The Weibull fitting (MATWORKS, 2013) is also shown in the figure with probability density given by:

$$f(d) = \frac{k}{\lambda}\left(\frac{d-d_0}{\lambda}\right)^{k-1} d^{-\left(\frac{d-d_0}{\lambda}\right)} \qquad (3\text{-}6)$$

where λ is the scale factor, k is the shape factor, d is the fibre spacing and d_0 is the threshold fibre spacing. For HTS-12K/977-2 unidirectional laminate $\lambda = 1.39 \pm 0.02, k = 1.50 \pm 0.023$ and $d_0 = 6.5\mu m$. A reasonably good fit was obtained.

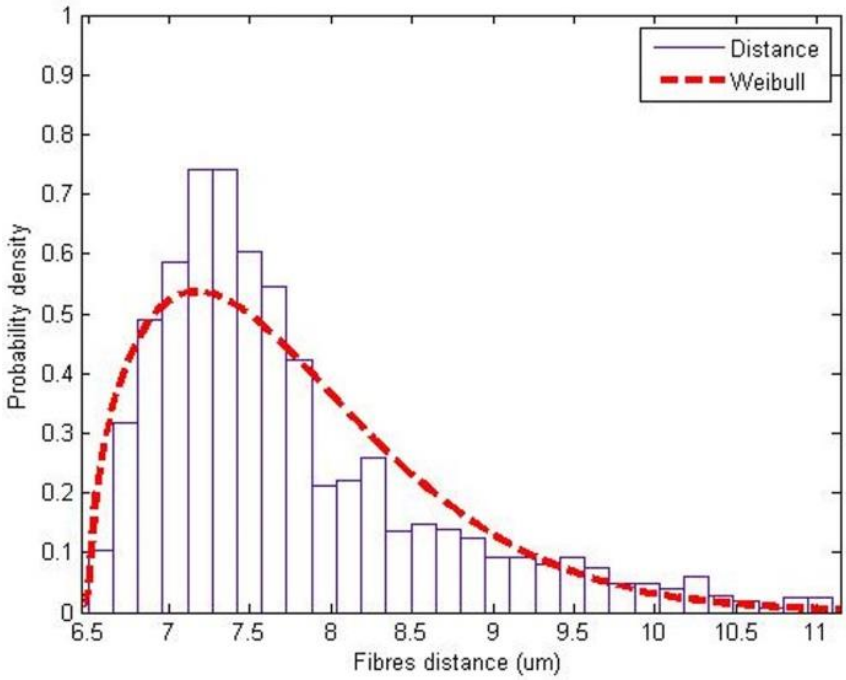

Figure 3.11 Statistics of fibre distance of a unidirectional laminate. Approximate two thousand specimens are included in the statistics.

It is interesting to note that the average central distance from the statistical analysis (7.705μm) is shorter than the predictions of either a square lattice (8.144μm) or a hexagonal lattice (8.751μm) based on equation (3-4) and equation (3-5). One possible reason is that the compaction of fibres tends to squeeze the resin out, resulting in resin rich volumes which reduce the overall fibre volume fraction.

The gaps between the adjacent fibres are very narrow, showing only 0.7μm on average. It can be seen from **Figure 3.11** that some fibre separations are less than 7μm (the average diameter of carbon fibres). One possible reason is that the radius of these fibres is slightly smaller than the average value. Nevertheless, **Figure 3.11** suggests that there

are many fibres presenting a very narrow gap which affects both the moisture distribution and stress distribution.

3.3 Extensional classical laminate theory (CLT)

Classical laminate theory (CLT) is widely used to predict the in-plane performance of FRP composites. This traditional approach is based on the plane stress assumption which neglects the out-of-plane components. In this thesis, the CLT formula was extended to 3D so that all the stress components in composite laminates can be extracted as well as the mechanical and physical properties.

3.3.1 *Elastic properties*

The elastic properties of FRP composites are considered at lamina level (a kind of orthotropic material) and laminate level (a stack of composite laminas which are bonded to provided required engineering properties). **Figure 3.12** illustrates the composite constituent and the coordinate systems.

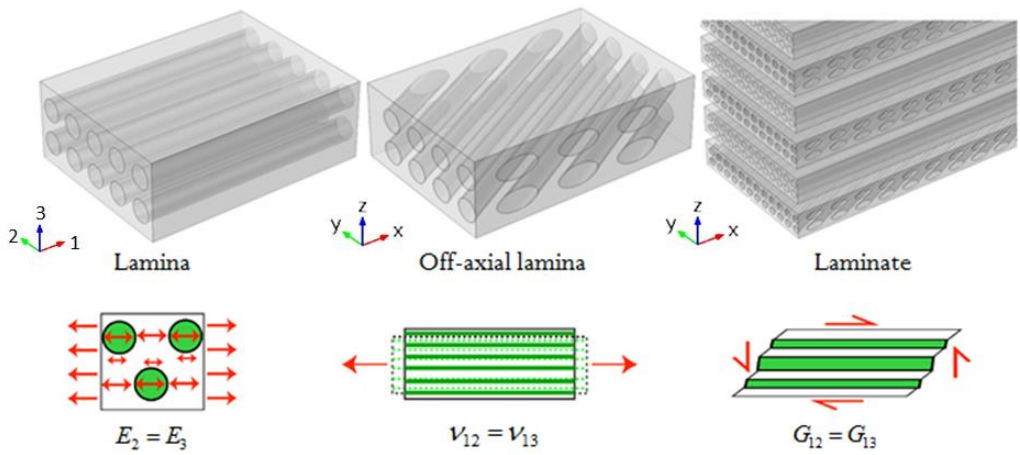

Figure 3.12 Illustration of composite lamina, off-axial lamina and laminate

It is important to note that two coordinate systems are involved: a) the local coordinate system represents stress or strain in the lamina level (subscripts 1, 2, and 3), and b) the global coordinate system represents stress and strain at the laminate level (subscripts x, y, and z). Due to the orthotropic structure, some elastic properties are not independent. As can be seen in **Figure 3.12**, the transverse modulus E_2 is assumed to be the same as the out-of-plane modulus E_3.

The longitudinal modulus and in-plane Poisson' ratio can be calculated by using the 'rule of mixture' (Hull and Clyne, 1996),

$$E_1 = V_f E_1^f + (1 - V_f) E_m \tag{3-7}$$

$$\nu_{12} = V_f \nu_{12}^f + (1 - V_f) \nu_m \tag{3-8}$$

Compared with glass or organic fibres which are isotropic, carbon fibre presents very high longitudinal modulus/strength and much lower transverse properties. Therefore, the fibre longitudinal properties only can be used for equation (3-7) and equation (3-8), while the other components of fibre should be applied to predict the transverse properties of the lamina.

There are quite a few theories for the prediction of transverse modulus (E_2) and in-plane shear modulus, such as 'equal stress' and Halpin-Tsai equations. According to (Brintrup, 1975), the transverse modulus of FRP composite distributes between the 'Equal stress' curve and 'Halpin-Tsai' curve, as shown in **Figure 3.13**(a). A parametric study of FEA simulation (solved by COMSOL Multiphysics) gives a similar result, shown in **Figure 3.13**(b).

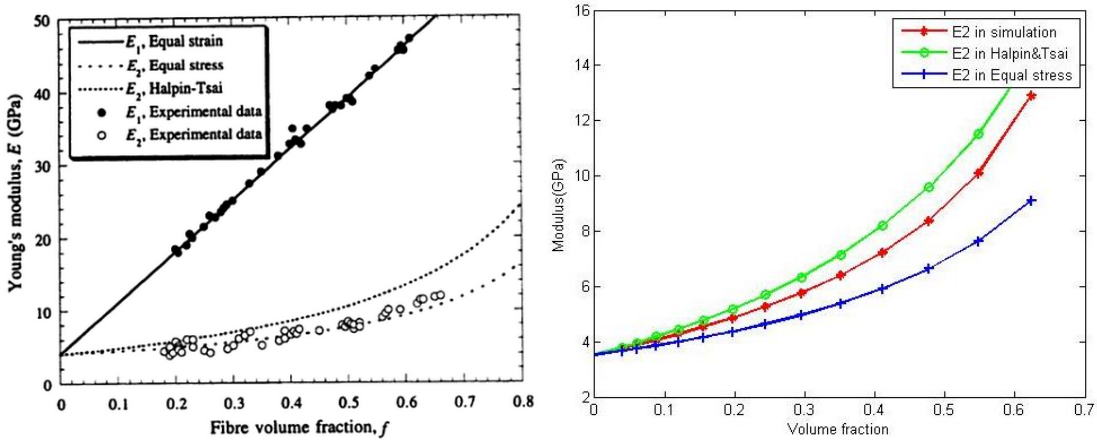

(a) (b)

Figure 3.13 (a) Comparison between experimental data for axial and transverse Young's moduli, E1 and E2 for polyester/glass fibre composites (Hull and Clyne, 1996); (b) comparison of classic formulae and FEA result for transverse modulus (Cytec 977-2-HTS)

However, it is unrealistic to run a FEA model for every type of composites. Generally, Halpin-Tsai theory can provide empirical result, therefore in this thesis, the transverse

modulus (E_2) and in-plane shear modulus (G_{12}) were calculated by the Halpin-Tsai equation, (Halpin and Kardos, 1976),

$$E_2 = \frac{E_m(1+\zeta\eta V_f)}{1-\eta V_f}$$
$$\eta = \frac{E_2^f / E_m - 1}{E_2^f / E_m + \zeta} \tag{3-9}$$

$$G_{12} = \frac{G_m(1+\zeta\eta V_f)}{1-\eta V_f}$$
$$\eta = \frac{G_{12}^f / G_m - 1}{G_{12}^f / G_m + \zeta} \tag{3-10}$$

where ζ is the geometric parameter. In this thesis, the calculation was based on ζ=1.

There is no agreed formula to calculate the transverse material properties (ν_{23}, G_{23}). In this thesis, a formula, based on hydrostatic assumption, was derived to evaluate the transverse Poisson's ratio.

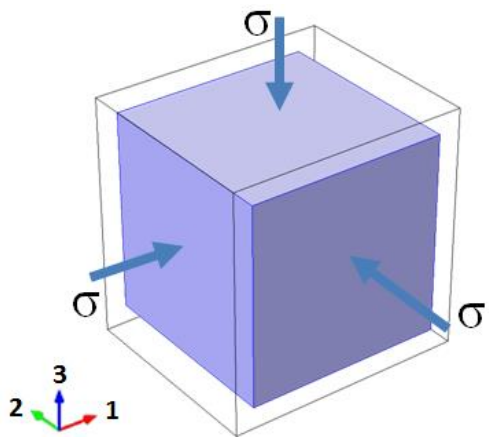

Figure 3.14 A bulk object under hydrostatic stress

Considering hydrostatic stress applied in a bulk object, as shown in **Figure 3.14**, the stresses of three principal directions are equal to each other,

$$\sigma_1 = \sigma_2 = \sigma_3 = \sigma \tag{3-11}$$

The bulk modulus is defined as,

$$K = \sigma / \Delta V \tag{3-12}$$

According to the principle of mechanics, the relationship between stress and strain for orthotropic materials is defined as,

$$\begin{bmatrix} \varepsilon_1 \\ \varepsilon_2 \\ \varepsilon_3 \end{bmatrix} = \begin{bmatrix} 1/E_1 & -\nu_{21}/E_2 & -\nu_{31}/E_3 \\ -\nu_{12}/E_1 & 1/E_2 & -\nu_{32}/E_3 \\ -\nu_{13}/E_1 & -\nu_{23}/E_2 & 1/E_3 \end{bmatrix} \begin{bmatrix} \sigma_1 \\ \sigma_2 \\ \sigma_3 \end{bmatrix} \tag{3-13}$$

For unidirectional lamina,

$$E_2 = E_3, \nu_{12} = \nu_{13}, \nu_{21} = \nu_{31}, \nu_{23} = \nu_{32} \tag{3-14}$$

So that the equation (3-13) can be rewritten as,

$$\varepsilon_1 + \varepsilon_2 + \varepsilon_3 = \sigma \left[\frac{1-2\nu_{12}}{E_1} + \frac{2(1-\nu_{21}-\nu_{23})}{E_2} \right] = \Delta V \tag{3-15}$$

Combining equations (3-12) and (3-15),

$$\nu_{23} = 1 - \nu_{21} - \frac{E_2}{2K} + \frac{E_2(1-2\nu_{12})}{2E_1} \tag{3-16}$$

$$K = \frac{E_1 E_2}{2E_1(1-\nu_{21}-\nu_{23}) + E_2(1-2\nu_{21})} \tag{3-17}$$

For isotropic material, $E = E_2 = E_1, \nu = \nu_{12} = \nu_{21} = \nu_{23}$, equation (3-17) becomes $K = E/3(1-2\nu)$. Once the transverse Poisson's ratio is calculated, the corresponding shear modulus can be evaluated by,

$$G_{23} = \frac{E_2}{2(1+\nu_{23})} \tag{3-18}$$

According to equation (3-16), the transverse Poisson's ratio can be calculated from bulk modulus, while the bulk modulus is calculated by Halpin-Tsai empirical equation (Halpin and Kardos, 1976),

$$\begin{aligned} K &= \frac{K_m(1+\zeta\eta V_f)}{1-\eta V_f} \\ \eta &= \frac{K_f/K_m - 1}{K_f/K_m + \zeta} \end{aligned} \tag{3-19}$$

As the formulae for the composite lamina have been well defined, substituting the material properties of fibre and matrix shown in **Table 3-2**, the mechanical properties were then calculated, as shown in **Table 3-3**.

Table 3-3 Material properties of lamina

Symbol	E_1	$E_2 = E_3$	$G_{12} = G_{13}$	G_{23}	$\nu_{12} = \nu_{13}$	ν_{23}
Value	139GPa	8.8GPa	4.7GPa	3.0GPa	0.26	0.48

3.3.2 *Extensional CLT formulae*

Because of the material symmetry, the composite compliance matrix S is reduced to an orthotropic matrix. Applying the well-known stiffness transformation law (Lekhnitskiĭ, 1963), the off-axis compliance matrix $\overline{S}$ and stiffness matrix $\overline{C}$ in 3D scale can be extended as,

$$\begin{aligned} \overline{S} &= T_{\varepsilon}^{-1} S T_{\sigma} \\ \overline{C} &= \left[\overline{S}\right]^{-1} \end{aligned} \tag{3-20}$$

$$S = \begin{bmatrix} 1/E_1 & -\nu_{12}/E_1 & -\nu_{12}/E_1 & 0 & 0 & 0 \\ -\nu_{12}/E_1 & 1/E_2 & -\nu_{23}/E_2 & 0 & 0 & 0 \\ -\nu_{12}/E_1 & -\nu_{23}/E_2 & 1/E_2 & 0 & 0 & 0 \\ 0 & 0 & 0 & 1/G_{23} & 0 & 0 \\ 0 & 0 & 0 & 0 & 1/G_{12} & 0 \\ 0 & 0 & 0 & 0 & 0 & 1/G_{12} \end{bmatrix} \tag{3-21}$$

$$T_{\varepsilon} = \begin{bmatrix} c^2 & s^2 & 0 & 0 & 0 & cs \\ s^2 & c^2 & 0 & 0 & 0 & -cs \\ 0 & 0 & 1 & 0 & 0 & 0 \\ 0 & 0 & 0 & c & s & 0 \\ 0 & 0 & 0 & -s & c & 0 \\ -2cs & 2cs & 0 & 0 & 0 & c^2 - s^2 \end{bmatrix} \tag{3-22}$$

$$T_{\sigma} = \begin{bmatrix} c^2 & s^2 & 0 & 0 & 0 & 2cs \\ s^2 & c^2 & 0 & 0 & 0 & -2cs \\ 0 & 0 & 1 & 0 & 0 & 0 \\ 0 & 0 & 0 & c & s & 0 \\ 0 & 0 & 0 & -s & c & 0 \\ -cs & cs & 0 & 0 & 0 & c^2 - s^2 \end{bmatrix} \tag{3-23}$$

where S is the compliance matrix of lamina; $c = \cos(\theta)$ and $s = \sin(\theta)$; E_2=E_3; G_{12}=G_{13}.

Substituting the three-dimensional version of composites compliance matrix into CLT equations (Kaw, 2006), the three-dimensional version of [A], [B] and [D] matrices can be written as,

$$
\begin{aligned}
[A] &= \sum_{k=1}^{N} \left(\overline{C}_{ij}\right)_k \left(z_k - z_{k-1}\right) \\
[B] &= \frac{1}{2} \sum_{k=1}^{N} \left(\overline{C}_{ij}\right)_k \left(z_k^2 - z_{k-1}^2\right) \\
[D] &= \frac{1}{3} \sum_{k=1}^{N} \left(\overline{C}_{ij}\right)_k \left(z_k^3 - z_{k-1}^3\right)
\end{aligned}
\tag{3-24}
$$

Assembling the [A], [B] and [D] matrices for $\begin{bmatrix} A & B \\ B & D \end{bmatrix}$ matrix, and its inversed $\begin{bmatrix} a & b \\ b & d \end{bmatrix}$ matrix,

$$
\begin{bmatrix} N \\ M \end{bmatrix} = \begin{bmatrix} A & B \\ B & D \end{bmatrix} \begin{bmatrix} \varepsilon \\ \kappa \end{bmatrix} \tag{3-25}
$$

$$
[A, B; B, D] = \begin{bmatrix} A & B \\ B & D \end{bmatrix} \tag{3-26}
$$

$$
[a, b; b, d] = \begin{bmatrix} a & b \\ b & d \end{bmatrix} = \begin{bmatrix} A & B \\ B & D \end{bmatrix}^{-1} \tag{3-27}
$$

Once the three-dimensional $[a, b; b, d]$ matrix is assembled, the elastic properties of laminate can be evaluated by (Kaw, 2006),

$$
\begin{aligned}
&E_x = 1/(h * a_{11}), E_y = 1/(h * a_{22}), E_z = 1/(h * a_{33}) \\
&G_{xy} = 1/(t * a_{66}), G_{yz} = 1/(t * a_{44}), G_{xz} = 1/(h * a_{55}) \\
&\nu_{xy} = -a_{12} / a_{11}, \nu_{yx} = -a_{12} / a_{22}, \nu_{yz} = -a_{32} / a_{22}, \nu_{xz} = -a_{31} / a_{11} \\
&\eta_{xyx} = -a_{16} / a_{11}, \eta_{xyy} = -a_{26} / a_{22}
\end{aligned}
\tag{3-28}
$$

Consider a composite laminate with symmetric lay-up under three-point bending. The coupling matrix $[B] = 0$, so the moment about x axes can be written as,

$$
M_x = \frac{\kappa_x}{d_{11}} = \frac{FL}{4w} \tag{3-29}
$$

If it is assumed that the curvature through-thickness is a constant, the strain and longitudinal stress are determined by,

$$\varepsilon_x^z = z\kappa_x = \frac{zFLd_{11}}{4w}, \sigma_1^z = E_k \varepsilon_x^z = E_k \frac{zFLd_{11}}{4w} \tag{3-30}$$

and the apparent flexural properties (Kaw, 2006),

$$\begin{aligned} &E_x^f = \frac{12M_x}{\kappa_x h^3} = \frac{12}{h^3 d_{11}}, E_y^f = \frac{12}{h^3 d_{22}}, E_z^f = \frac{12}{h^3 d_{33}} \\ &G_{xy}^f = \frac{12}{h^3 d_{66}}, G_{yz}^f = \frac{12}{h^3 d_{44}}, G_{xz}^f = \frac{12}{h^3 d_{55}} \\ &\nu_{xy}^f = -\frac{d_{12}}{d_{11}}, \nu_{yx}^f = -\frac{d_{12}}{d_{22}}, \nu_{yz}^f = -\frac{d_{23}}{d_{22}}, \nu_{xz}^f = -\frac{d_{13}}{d_{11}} \end{aligned} \tag{3-31}$$

The maximum strain appears on the top and bottom surfaces $z = \pm h/2$. However, the maximum stress is dependent on both the through-thickness coordinate and the ply modulus.

With the 3D version of $[a,b;b,d]$ matrix, the interlaminar shear stress τ_{xz} and transverse shear stress τ_{yz} can be evaluated by the principle of continuum mechanics (Creemers, 2009),

$$\begin{aligned} \tau_{xz}^{(k)} &= \sum_{j=1}^{k-1} \int_{z_{j-1}}^{z_j} \left(\frac{\partial \tau_{xz}}{\partial z} \right)_{(j)} dz + \int_{z_{k-1}}^{z} \left(\frac{\partial \tau_{xz}}{\partial z} \right)_{(k)} dz \\ &= -\sum_{j=1}^{k-1} \left\{ \begin{array}{l} \left(\overline{C}_{11(j)} b_{11} + C_{12(j)} b_{21} + \overline{C}_{16(j)} b_{61}\right)\left(z_j - z_{j-1}\right) \\ + \frac{1}{2}\left(\overline{C}_{11(j)} d_{11} + \overline{C}_{12(j)} d_{21} + \overline{C}_{16(j)} d_{61}\right)\left(z_j^2 - z_{j-1}^2\right) \end{array} \right\} Q_x \\ &- \left\{ \begin{array}{l} \left(\overline{C}_{11(k)} b_{11} + \overline{C}_{12(k)} b_{21} + \overline{C}_{16(k)} b_{61}\right)\left(z - z_{k-1}\right) \\ + \frac{1}{2}\left(C_{11(k)} d_{11} + \overline{C}_{12(k)} d_{21} + \overline{C}_{16(k)} d_{61}\right)\left(z^2 - z_{k-1}^2\right) \end{array} \right\} Q_x \end{aligned} \tag{3-32}$$

$$\begin{aligned} \tau_{yz}^{(k)} &= \sum_{j=1}^{k-1} \int_{z_{j-1}}^{z_j} \left(\frac{\partial \tau_{yz}}{\partial z} \right)_{(j)} dz + \int_{z_{k-1}}^{z} \left(\frac{\partial \tau_{yz}}{\partial z} \right)_{(k)} dz \\ &= -\sum_{j=1}^{k-1} \left\{ \begin{array}{l} \left(\overline{C}_{61(j)} b_{11} + C_{62(j)} b_{21} + \overline{C}_{66(j)} b_{61}\right)\left(z_j - z_{j-1}\right) \\ + \frac{1}{2}\left(\overline{C}_{61(j)} d_{11} + \overline{C}_{62(j)} d_{21} + \overline{C}_{66(j)} d_{61}\right)\left(z_j^2 - z_{j-1}^2\right) \end{array} \right\} Q_x \\ &- \left\{ \begin{array}{l} \left(\overline{C}_{61(k)} b_{11} + \overline{C}_{62(k)} b_{21} + \overline{C}_{66(k)} b_{61}\right)\left(z - z_{k-1}\right) \\ + \frac{1}{2}\left(C_{16(k)} d_{11} + \overline{C}_{26(k)} d_{21} + \overline{C}_{66(k)} d_{61}\right)\left(z^2 - z_{k-1}^2\right) \end{array} \right\} Q_x \end{aligned} \tag{3-33}$$

The local interlaminar shear stress in the kth ply (along fibre orientation) is evaluated according to its orientation (Creemers, 2009),

$$\begin{aligned} \tau_{13}^{(k)} &= \tau_{xz}^{(k)} \cos\theta_{(k)} + \tau_{yz}^{(k)} \sin\theta_{(k)} \\ \tau_{23}^{(k)} &= -\tau_{xz}^{(k)} \sin\theta_{(k)} + \tau_{yz}^{(k)} \cos\theta_{(k)} \end{aligned} \tag{3-34}$$

Table 3-4 Material properties of the laminates. The flexural modulus is also listed in the Table

	UD([0]$_{16}$)	UT([90]$_{16}$)	CP([0/90]$_{4s}$)	CP([90/0]$_{4s}$)	AP([±45]$_{4s}$)
$E_x\ (GPa)$	139	8.8	74.2	74.2	16.7
$E_x^f\ (GPa)$	139	8.8	86.4	61.9	16.7
$E_y\ (GPa)$	8.8	139	74.2	74.2	16.7
$E_z\ (GPa)$	8.8	8.8	10.9	10.9	10.9
$G_{xy}\ (GPa)$	4.7	4.7	4.7	4.7	36.0
$G_{xz}\ (GPa)$	4.7	4.7	3.9	3.9	3.9
$G_{yz}\ (GPa)$	3.0	3.0	3.9	3.9	3.9
ν_{xy}	0.26	0.02	0.03	0.03	0.78
ν_{yz}	0.26	0.26	0.03	0.03	0.78
ν_{yz}	0.48	0.48	0.42	0.42	0.10

In order to solve these CLT formulae, a MATLAB programme was developed. The code and a snapshot of the Graphics User Interface (GUI) of this programme are shown in Appendix A, which include three sections: lamina, off-axial lamina and laminate.

As the extensional CLT formulae for the composite laminate have been well defined, substituting the material properties of lamina shown in **Table 3-3**, the mechanical properties of the five laminates used in this project (unidirectional [0]$_{16}$, unidirectional transverse [90]$_{16}$, cross-ply [0/90]$_{4s}$ cross-ply [90/0]$_{4s}$, and angle-ply [+45/-45]$_{4s}$) were then calculated, as shown in **Table 3-4**.

3.3.3 *Hygrothermal and thermal properties*

The prediction of CHE at lamina level has been discussed in section 2.4.1 showing as equation (2-23) and equation (2-24). Employing the extensional CLT formulae, the CHE in laminate level can be evaluated by (Gibson, 1994),

$$\beta = aN^C = a\sum_{k=1}^{n}\overline{C}^k \beta^k t^k \tag{3-35}$$

where a is the 'a' block of the 'abbd' matrix; N^C is force per unit length caused by free moisture expansion; $\overline{C}^k$ is the full 3D stiffness matrix of the kth ply; t^k is the thickness of the kth ply.

For the thermal expansion in a unidirectional lamina, the changes of dimensions differ in the two directions and the following equation using energy principles can be used to evaluate the CTE (Schapery, 1968),

$$\alpha_1 = \frac{\alpha_1^f E_1^f V_f + \alpha_m E_m (1 - V_f)}{E_1^f V_f + E_m (1 - V_f)} \tag{3-36}$$

$$\begin{aligned}\alpha_2 = \alpha_3 = &\left(\alpha_2^f - \frac{E_m}{E_1}\nu_{12}^f\left(\alpha_m - \alpha_1^f\right)\left(1 - V_f\right)\right)V_f \\ &+\left(\alpha_m + \frac{E_1^f}{E_1}\nu_m\left(\alpha_m - \alpha_1^f\right)V_f\right)(1 - V_f)\end{aligned} \tag{3-37}$$

Similar with the calculation of CHE, the CTE in laminate level can also be calculated by using the 3D CLT formulae,

$$\alpha = aN^T = a\sum_{k=1}^{N}\overline{C}^k \alpha^k t^k \tag{3-38}$$

3.4 Summary

The chapter has presented the manufacturing and characterisation of high strength HTS/977-2 CFRP composite which was used for the further tests throughout this project, as well as the optical microscopic inspection including void, fibre misalignment and fibre packing. An analytical model based on 3D CLT has also been developed to predict the mechanical/physical properties of the composite laminates, which is used for the further FEA models in this thesis.

CHAPTER 4 – BENDING TESTS AND MODELLING

The chapter is intended to understand how the fibre lay-up affects the initiation of failure of laminated composites in quasi-static bending. The specimens were tested in bending following ISO standards to measure the critical failure loads and to identify the failure modes. A 3D FEA model and an extended CLT model were then applied to examine the stress distribution under the measured failure loads. The stress distribution in critical areas of the laminates were examined and correlated with the observation of the initiation of failure in experiments.

4.1 Experiment setup

The experiment was conducted on a universal mechanical test machine (model: INSTRON 5582) according to ISO standards using three-point bending. The flexural modulus and flexural strength were evaluated by long-beam method (ISO14125, 1998) using an extension rate 5 mm/min, while the interlaminar shear strength was evaluated by short-beam method (ISO12130, 1998) using an extension rate 1 mm/min. **Figure 4.1** shows the schematics of the 3-point bending. Both of the radii of load cell and support rollers were 5 mm. At least five samples in each group were tested and the mean values were calculated.

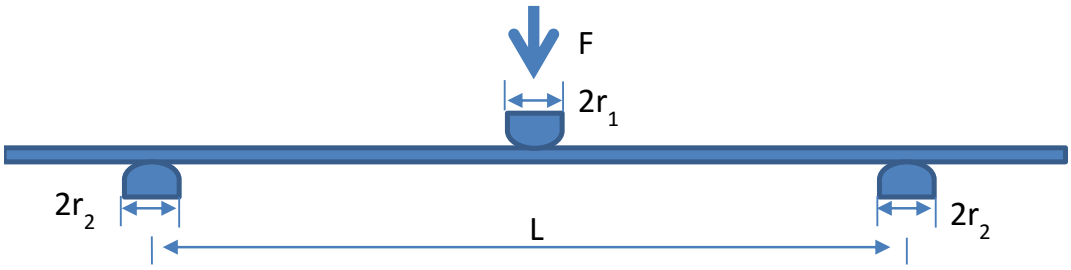

Figure 4.1 Illustration of the 3-point bending test

According to the ISO standards, the apparent flexural modulus, flexural strength and interlaminar shear strength were calculated by,

$$E_{app}^{f} = \frac{L^3}{4wh^3}\left(\frac{\Delta F}{\Delta D}\right) \qquad (4\text{-}1)$$

$$\sigma_x^{app} = \frac{3F_{\max}L}{2wh^2} \quad (4\text{-}2)$$

$$\tau_{xz}^{app} = \frac{3}{4} \times \frac{F_{\max}}{wh} \quad (4\text{-}3)$$

where L is the bending span, w, h are the width and thickness of the specimens respectively, $\Delta F, \Delta D$ are the differences in load and deflection between flexural strain at 0.05% and 0.25%, $F_{\max}$ is the maximum load.

The relation between flexural strain and deflection can be calculated by,

$$\varepsilon_x^{app} = \frac{6hD}{L^2} \quad (4\text{-}4)$$

Equations from (4-1) to (4-4) are based on an assumption that the load cell is exactly fixed at the mid-point of the span, however in practice the location of the load cell always has an offset. Therefore a parameter was introduced to compensate for this effect.

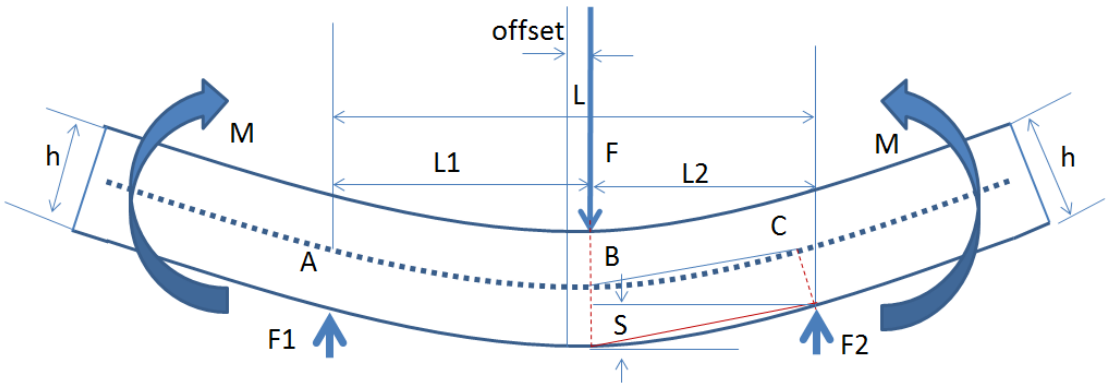

Figure 4.2 The offset of the 3-point bending

Considering simply supported Euler beam, as shown in **Figure 4.2**, the moments at AB and BC can be expressed as,

$$AB: M = F_1 x = \frac{L_2}{L} Fx \text{, and } m = \frac{L_2}{L} x \quad (4\text{-}5\text{-}1)$$

$$BC: M = F_2(L-x) = \frac{L_1}{L} F(L-x) \text{, and } m = \frac{L_1}{L}(L-x) \quad (4\text{-}5\text{-}2)$$

The virtual work is then calculated by the integration of the moment along AC,

$$
\begin{aligned}
D &= \int_A^C \frac{Mm}{EI}\,dx = \int_A^B \frac{L_2^2 F}{L^2 EI} x^2 dx + \int_B^C \frac{L_1^2 F}{L^2 EI}(L-x)^2 dx \\
&= \frac{L_2^2 F}{L^2 EI}\int_0^{L_1} x^2 dx + \frac{L_1^2 F}{L^2 EI}\int_{L_1}^{L}(L-x)^2 dx \\
&= \frac{F}{L^2 EI}\left(\frac{L_2^2 L_1^3 + L_1^2 L^3 - L_1^5}{3} - L L_1^3 L_2\right) \\
&= \frac{2\varepsilon_x^{app}}{3 L L_1 L_2 h}\left(L_2^2 L_1^3 + L_1^2 L^3 - L_1^5 - 3 L L_1^3 L_2\right)
\end{aligned}
\tag{4-6}
$$

Therefore, the flexural strain is then expressed as,

$$
\varepsilon_x^{app} = \frac{3 L L_1 L_2 h D}{2\left(L_2^2 L_1^3 + L_1^2 L^3 - L_1^5 - 3 L L_1^3 L_2\right)} \tag{4-7}
$$

In case of $L_1 = L_2$, this equation degenerates to equation (4-4).

The ISO standard provides a 'large-deflection criterion' (10%) (ISO14125, 1998) as a guideline that the apparent flexural strength should be calculated by a modified equation when the value $D_{\max}/L$ exceeds 10%,

$$
\left(\sigma_{\max}^{f}\right)_{cor} = \frac{3F_{\max}L}{2wh^2}\left(1 + 6\left(\frac{D_{\max}}{L}\right)^2 - 3\left(\frac{D_{\max}h}{L^2}\right)\right) \tag{4-8}
$$

The observation of the experiment showed that the two CP laminates had exceeded this criterion while the UD laminate was close to the criterion, therefore the apparent flexural strengths of both the CP and UD laminates were calculated by 'large-deflection correction', and the results are shown in **Table 4-1**.

The flexural modulus and apparent flexural strength of the angle-ply laminate are not presented in the table because the force-deflection curve of this type of laminate showed very strong nonlinear and high dependency on the extension rate which cannot represent any useful information. The interlaminar shear strengths of CP and UT laminates are not presented in the table because the CP laminate failed by plastic deformation while the UT laminate failed by tensile fracture rather than interlaminar shear.

Table 4-1 Experimental results from three-point bending tests and the Standard Deviations

laminate	UD $[0]_{16}$		UT$[90]_{16}$	CP$[0/90]_{4s}$		CP$[90/0]_{4s}$	AP$[\pm45]_{4s}$
Groups	**Long beam**	**Short beam**	**Long beam**	**Long beam**	**Short beam**	**Long beam**	**Short beam**
Length(mm)	100	20	100	100	20	100	20
Width(mm)	15.18±0.03	10.14±0.03	15.15±0.1	15.08±0.02	10.14±0.10	15.00±0.05	10.10±0.12
Height(mm)	2.09±0.06	2.13±0.07	2.09±0.01	1.93±0.01	1.94±0.02	1.93±0.02	1.93±0.01
Span(mm)	80	10	80	79	10	79	10
$F_{\max}$ **(N)**	853±32	2933±126	64±2.9	630±21	2257±83	606±31	1395±61
$D_{\max}$ **(mm)**	6.59±0.27	—	7.10±0.29	8.99±0.31	—	12.6±0.28	—
E_{app}^{f} **(GPa)**	120±3.1	—	8.4±0.3	79.7±0.8	—	55±2.2	—
σ_x^{app} **(MPa)**	1544±49	—	117±4.7	1328±39	—	1286±47	—
$(\sigma_x^{app})_{cor}$ **(MPa)**	1598±56	—	121±5.3	1421±48	—	1416±53	—
τ_{xz}^{app} **(MPa)**	—	101.9±3.5	—	—	86.1±4.0	—	53.7±2.8

$F_{\max}$ -maximum flexure load; $D_{\max}$ -maximum deflection; E_{app}^{f} -apparent flexural modulus; σ_x^{app} -apparent flexural strength; $(\sigma_x^{app})_{cor}$ -apparent flexural strength with 'large-deformation' correction; τ_{xz}^{app} -apparent interlaminar shear strength.

4.2 3D FEA modelling

A 3D solid FEA model was developed by COMSOL Multiphysics to examine the stress distribution under the measured failure loads. The stress distribution in critical areas of the laminated composites were examined and correlated with the observation of the initiation of failure in experiments.

4.2.1 *Model definition*

The technical term 'symmetry' includes symmetry in geometry, material and boundary condition. Although the lay-up sequence (as well as geometry) is symmetric for all specimens shown in **Table 3-1**, the angle-ply laminate has no through-thickness plane of symmetry in terms of material orientation.

All of the specimens were 'simply supported', which presents a linear relationship between flexure load and deflection when the deflection was relatively small. The loads applied in the FEA models (**Table 4-2**) were taken as the maximum measured loads in the three-point bending tests shown in **Table 4-1**.

Table 4-2 Loading forces in different groups of coupons

Orientation	UD $[0]_{16}$		CP$[0/90]_{4s}$		AP$[\pm45]_{4s}$
Groups	Long beam	Short beam	Long beam	Short beam	Short beam
Force (N)	853	2933	630	2257	1395

In the 3D FEA model, the boundary conditions are quite different from a 2D model, and some additional modelling techniques should be introduced because the 'simply supported' and loading boundary conditions might lead to inaccurate results due to the stress concentration at these boundaries. Additionally, the 'contact' boundary condition is not appropriate in the present work, so that these have been replaced by distributed loads with sinusoidal distribution, which includes an downward (negative) distributed load (P) in the middle area of top surface (load-point) and half of an upward (positive) distributed load ($P/2$) at the left and right ends of bottom surface, as shown in **Figure 4.3**. For the long-beam specimens, the spans (L) were set as 80 mm (longitudinal laminate) and 79 mm (cross-ply laminate), while the short-beam specimens had a span of 10 mm.

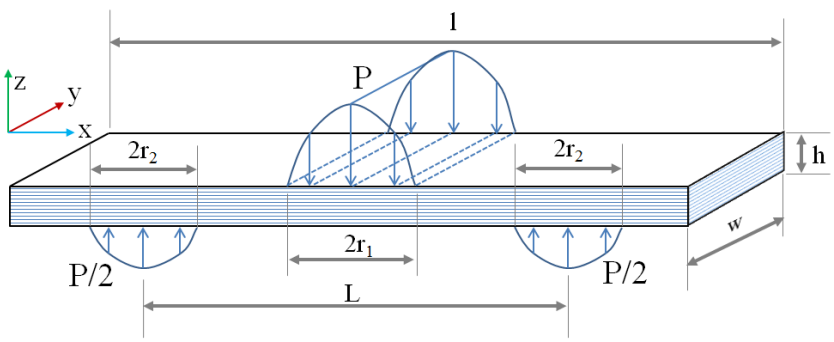

Figure 4.3 Modelling conditions were equal to testing conditions. The two 'simply supported' boundary conditions at two ends were replaced by positive distributed loads ($P/2$).

In order to avoid rigid movement, some additional boundary conditions were applied to eliminate the six degrees of freedom (DOF). With the natural symmetry of

unidirectional laminate and cross-ply laminate, two symmetric planes were applied to eliminate the DOFs of x, y, and the rotation about three axes. The two central points at each end of the laminate (z=h/2) were restrained as z=0 to eliminate the last DOF. However, the 'symmetric plane' boundary conditions do not exist in the angle-ply laminate, due to the asymmetric material properties. Two 'edge displacement' boundary conditions were applied to replace the symmetric planes for eliminating the DOFs. **Figure 4.4** shows the artificial boundary conditions for the DOFs elimination in unidirectional and cross-ply laminates (a), and angle-ply laminate (b).

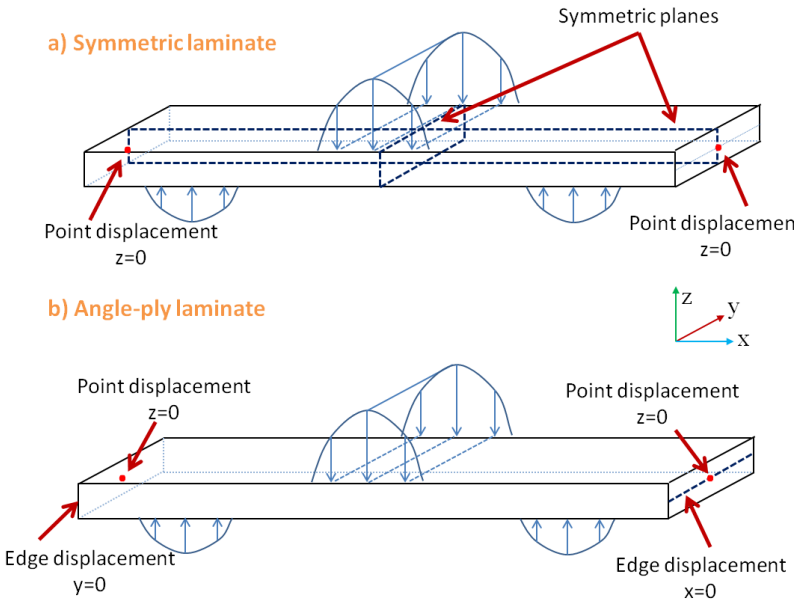

Figure 4.4 Boundary conditions applied in a) symmetric laminates and b) angle-ply laminate

The material properties for the FEA model have been given in **Table 3-2**. For the orthotropic material, such as a composite laminate, Tsai-Hill failure criterion (Tsai, 1968; Gibson, 1994) has shown a good fit to experiments, and this is used in the present work:

$$(G_2+G_3)\sigma_1^2+(G_1+G_3)\sigma_2^2+(G_1+G_2)\sigma_3^2- \\ 2(G_3\sigma_1\sigma_2+G_2\sigma_1\sigma_3+G_1\sigma_2\sigma_3-G_4\tau_{23}^2-G_5\tau_{13}^2-G_6\tau_{12}^2)<1 \tag{4-9}$$

$$G_1=\frac{1}{\left(\sigma_2^{ult}\right)^2}-\frac{1}{2\left(\sigma_1^{ult}\right)^2},G_2=G_3=\frac{1}{2\left(\sigma_1^{ult}\right)^2}, \\ G_4=\frac{1}{2\left(\tau_{23}^{ult}\right)^2},G_5=\frac{1}{2\left(\tau_{13}^{ult}\right)^2},G_6=\frac{1}{2\left(\tau_{12}^{ult}\right)^2} \tag{4-10}$$

There are six parameters of lamina strength in equations (4-9) and (4-10), however only four are independent (since $\sigma_2^{ult} = \sigma_3^{ult}$, $\tau_{12}^{ult} = \tau_{13}^{ult}$). The failure criterion must be applied in the local coordinate system. For example σ_x, σ_y and τ_{xy} are based on global coordinates, which should be transformed to the local coordinates (σ_1, σ_2 and τ_{12}) in accordance with the failure criterion.

Orthotropic material properties were applied in the simulation and every off-axis ply used a rotated coordinate,

$$\begin{pmatrix} x \\ y \end{pmatrix} = \begin{bmatrix} \cos\theta & -\sin\theta \\ \sin\theta & \cos\theta \end{bmatrix} \begin{pmatrix} X \\ Y \end{pmatrix} \tag{4-11}$$

where X and Y are the transformed variables in the rotated (θ) coordinate system. The elastic properties of the lamina (Young's modulus, shear modulus and Poisson's ratio) were transformed using equation (4-11) for the definition of FEA.

In FEA models, all of the 16 plies were built as 3D-solid element, and bonded together. Because the mesh quality could affect the 3D FEA results significantly, two methods for mesh quality control were employed: a) distributed mesh was defined near edge region; b) global elements were referred to 'q' factor, which was evaluated by (COMSOL, 2013),

$$q = \frac{24\sqrt{3}V}{\left(\sum_{i=1}^{12} h_i^2\right)^{3/2}} \tag{4-12}$$

where V is the volume, and h_i are the edge lengths. If $q > 0.1$, the mesh size should not affect the solution quality.

The through-thickness mesh density has a weak influence on the FEA results since the material properties within each ply are considered as homogeneous. However the mesh quality in the width direction has to be refined and the dimension of an individual element at the edge should be comparable to the ply thickness. In the present work, geometry near the edge was refined to be approximately one half-ply thickness along the width, and each ply was divided into 3 elements through-thickness, as shown in **Figure 4.5**. A finer mesh than this would not provide noticeable improvement of the

FEA solution, while demanding exponentially increasing computing resources. **Figure 4.6** shows the relationship between the mesh size (multiple of one-ply thickness) and the solution. The FEA models were solved by COMSOL Multiphysics (Version 4.4), with approximate one million DOFs in each laminate.

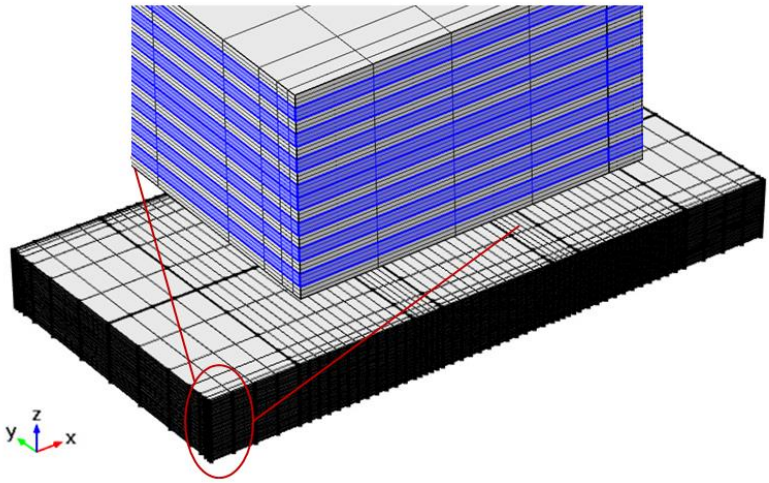

Figure 4.5 Mesh plot of $20mm \times 10mm$ laminate with local refinement. The edge area was refined to investigate the free edge effect.

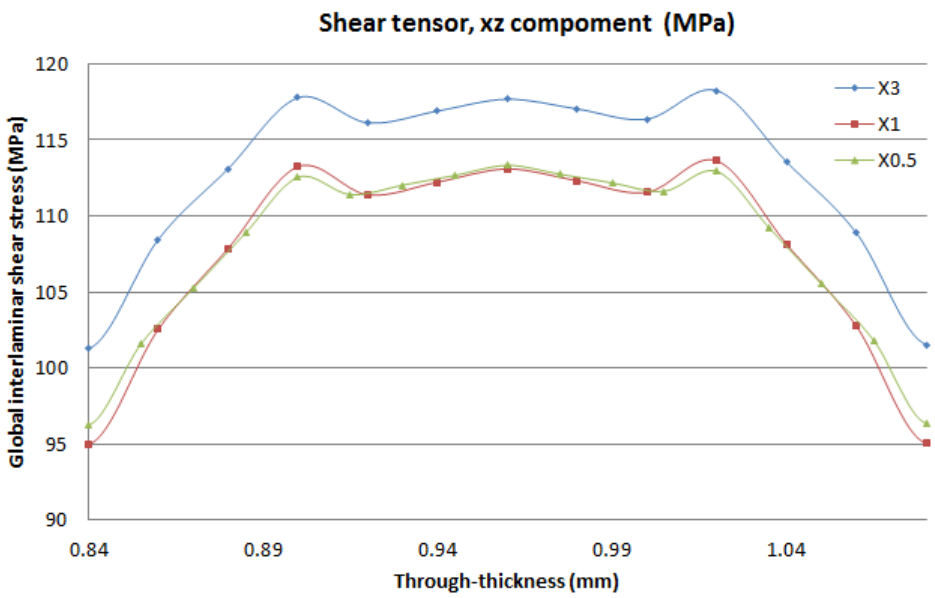

Figure 4.6 The effect of mesh size near the edge region on the distribution of global interlaminar shear stress in short-beam angle-ply laminate. The results show that 0.5 was sufficient to get mesh independency.

4.2.2 *Flexural strength and modulus*

Substituting the laminate dimensions, flexure loads and deflections in **Table 4-1** into 3D CLT formulae, the maximum ply normal stress and interlaminar shear stress can be obtained, as shown in **Table 4-3**.

Table 4-3 Maximum ply normal stress and interlaminar shear stress by 3D CLT

	UD $[0]_{16}$		CP $[0/90]_{4s}$		AP $[\pm45]_{4s}$	Notes
Groups	**Long beam**	**Short beam**	**Long beam**	**Short beam**	**Short beam**	
E_{CLT}^{f} (GPa)	139	—	86.5	—	—	Flexural modulus by CLT
$\sigma_1^{\max}$ (MPa)	1598±56	—	2157±78	—	—	Maximum ply normal stress
$\tau_{13}^{\max}$ (MPa)	—	101.9±3.5	—	83.3±2.6	40.6±2.1	Maximum ply interlaminar shear stress

For the long-beam method, the ISO standard considers the flexural stress in longitudinal direction by neglecting the other components. According to the 3D FEA model, the stress components σ_2 and σ_3 are very small compared with σ_1(about 2%) because of the 'simply supported' boundary condition. The flexural stress σ_1 shows a small increase (about 2%) near the free edge region, as shown in **Figure 4.7**. Although the maximum tensile stress is much lower than longitudinal tensile strength $(\sigma_1^{ult})^t$ (2.52 GPa), the compressive stress is very close to the compressive strength $(\sigma_1^{ult})^c$ (1.58 GPa), as shown in **Table 4-2**. Therefore, the long-beam unidirectional laminate failed in compression, rather than tension.

The microscope observation confirmed this hypothesis. **Figure 4.8** shows a typical failure image of long-beam unidirectional laminate, and **Figure 4.9** shows the deflection-load curves of long-beam unidirectional laminate. **Figure 4.8**(b) clearly shows the interface between tensile and compressive failures within a unidirectional laminate, while **Figure 4.8**(c) indicates that fibres in the upper half failed by compression. A survey of literature (Soutis, 1991; Budiansky and Fleck, 1993; Soutis, 1997; Liu, Fleck

et al., 2004) shows that the half-wavelength λ_0 of fibre microbuckling is typically 10-15 times of fibre diameter, which is in accordance with the kinking band shown in **Figure 4.8**(b).

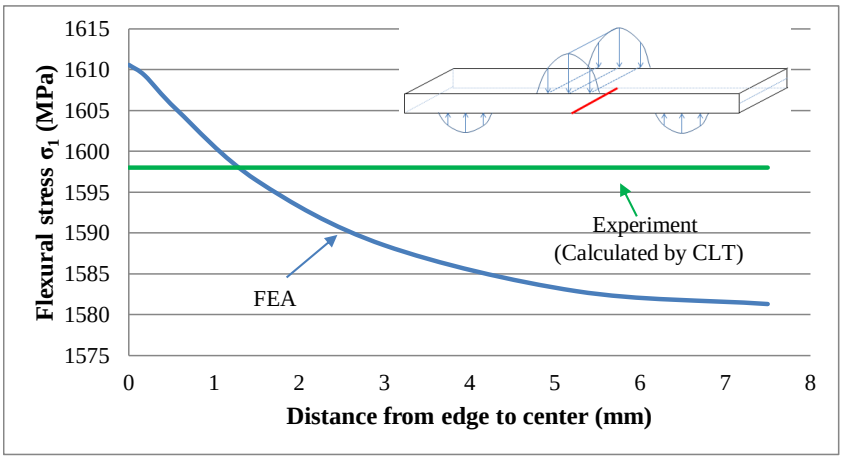

Figure 4.7 Distribution of tensile stress σ_1 on bottom surface of long-beam unidirectional laminate. The stress (FEA) shows a minor fluctuation about 2% between the free edge and central areas.

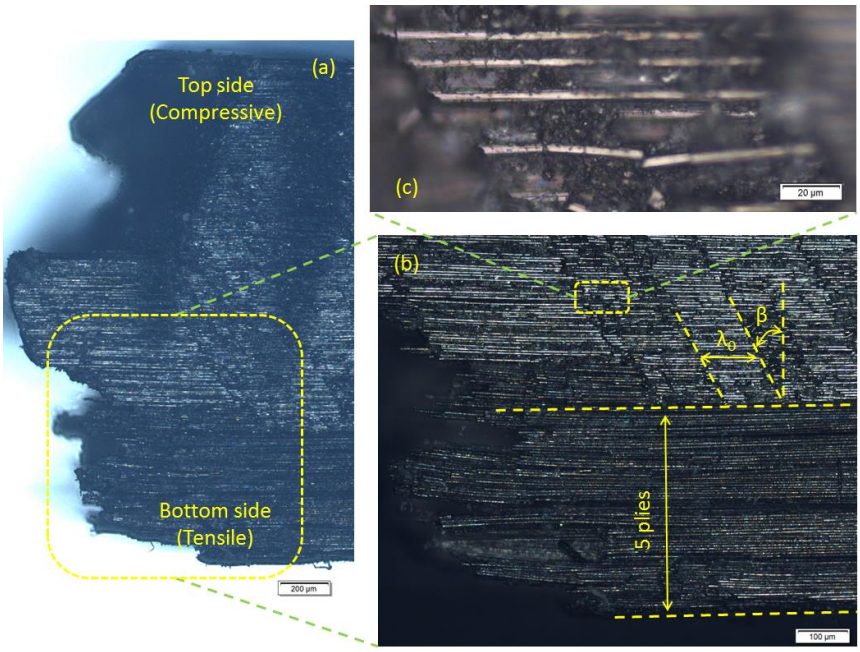

Figure 4.8 Microscope image of failure mode in a long-beam unidirectional laminate under three-point bending (side-view). Approximate 70% of the plies failed by compression, and fibre microbuckling could be observed on the compressive side. $\lambda_0 \approx 12 \times 2r$: half wavelength of fibre microbuckling; β=30°: orientation of microbuckling band.

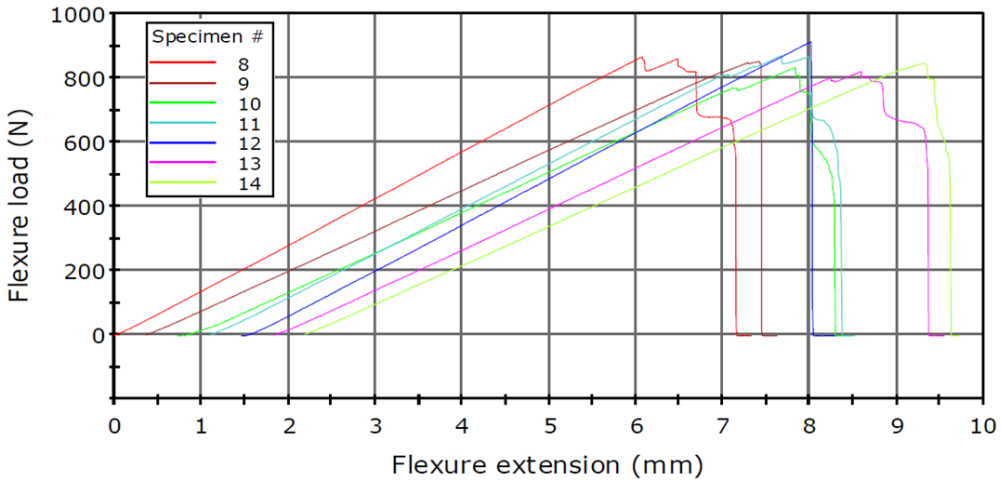

Figure 4.9 Deflection-load curves of long-beam unidirectional laminate under three-point bending. Laminate failed rapidly after the first 'stiffness losses' appeared.

The observed stiffness dropped in small steps when the flexure load reached the peak, and each step of 'stiffness losses' represents the failure of a single ply (compressive failure). The flexural stress re-distributed, and the lower plies withstood the maximum compressive stress but the tensile stress at bottom ply did not reach the tensile strength. As a consequence, more and more plies failed by compressive stress, and then the sample broke into two parts suddenly when the last 1/3 of the plies failed. Previous literature (Soutis, 1991; Budiansky and Fleck, 1993; Soutis, 1997; Lemanski, Wang et al., 2013) shows that the longitudinal compressive strength of unidirectional laminate is about 60%~70% of its tensile strength. One possible reason is that fibre misalignment causes fibre microbuckling. The discussion of the progressive failure is beyond the scope of this thesis.

Figure 4.10 is a schematic diagram to show the microbuckling in a long-beam unidirectional laminate. The carbon fibres are allowed to buckle into the weaker resin in lower plies and finally break under in-plane compressive stress. Because of the bidirectional lay-up sequence, the flexural stresses are not continuous through thickness in cross-ply laminates. **Figure 4.11** shows these discontinuities in the long-beam cross-ply laminate in local coordinate system, while **Figure 4.12** shows the through-thickness stress distribution at the centre.

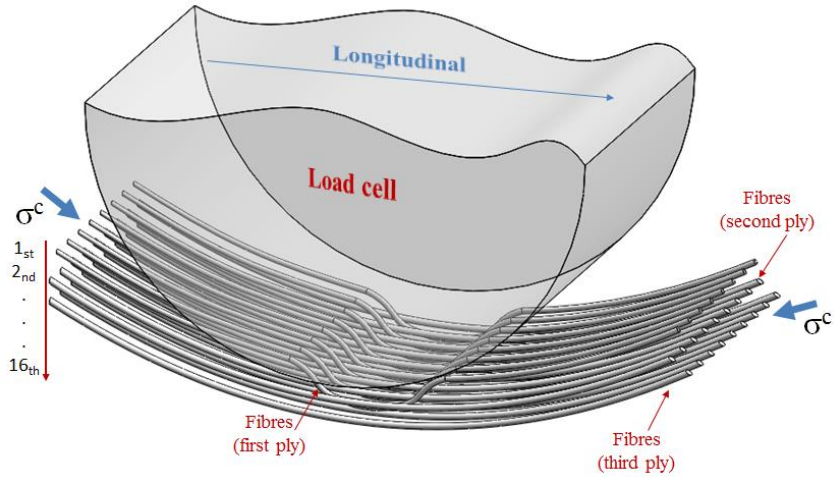

Figure 4.10 Schematic diagram of fibre microbuckling of long-beam unidirectional laminate. With the same fibre orientation, the second ply is likely to 'buckle' following the first ply by the compressive stress, and then followed by the third ply, and so on.

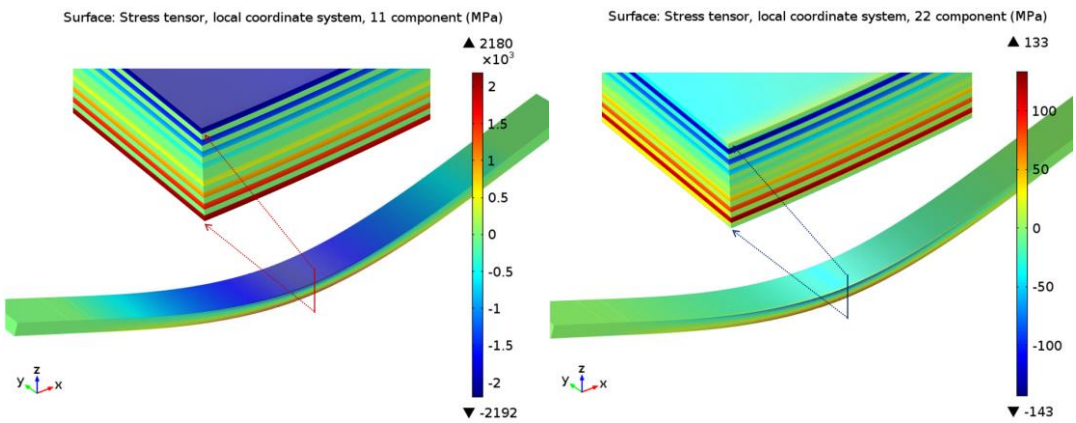

Figure 4.11 Distributions of stress components σ_1 (left) and σ_2 (right) in long-beam cross-ply laminate and their side-views

Figure 4.12 shows that the maximum σ_1 and σ_2 at the centre of laminate are about ±2.2GPa and ±140MPa respectively. A comparison of these values with the lamina strength shown in **Table 4-3** illustrates that the longitudinal compressive stress has exceeded the lamina compressive strength, while the longitudinal tensile stress is slightly lower than lamina tensile strength. In accordance with the experimental condition, the top ply could withstand such high value of compressive stress, because the microbuckling was constrained by the roller and supported by the transverse ply underneath it. In this condition, the top ply would be more difficult to 'buckle' compared to the situation in a unidirectional laminate (c.f. **Figure 4.8**). **Figure 4.13**

shows the schematics of fibre orientation in the long-beam cross-ply laminate. The out-of-plane buckling of fibres in the top ply is constrained by the roller and the transverse fibres in the adjacent ply. Therefore the compressive strength of the material is significantly improved.

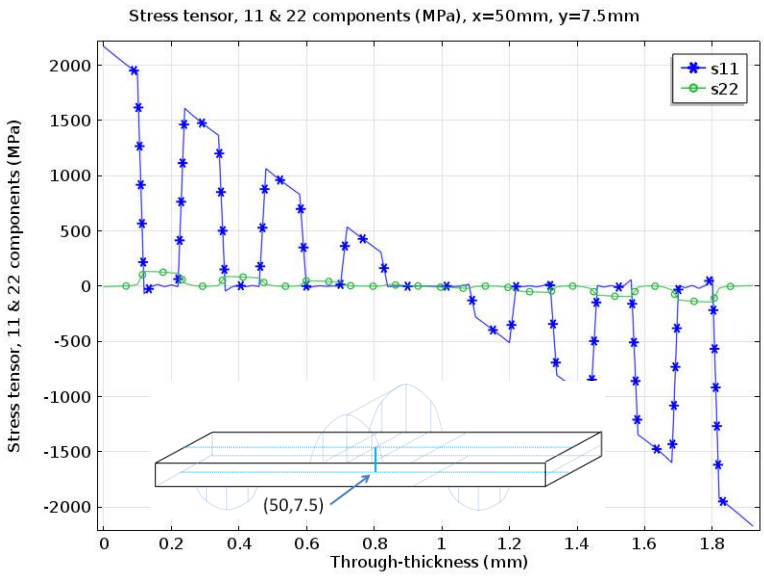

Figure 4.12 Through-thickness distributions of flexural stress σ_1 (s11) and σ_2 (s22) at central point of long-beam cross-ply laminate. The stresses jump rapidly at the interface between longitudinal and transverse plies.

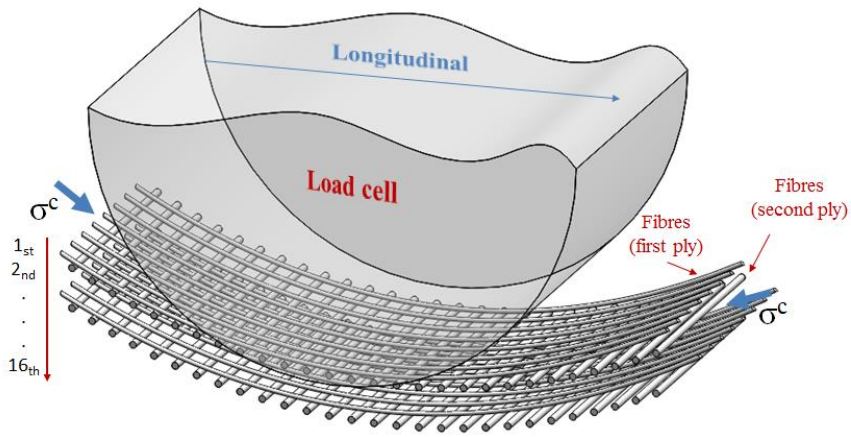

Figure 4.13 Schematics of fibre microbuckling of long-beam cross-ply laminate. With the support of the second ply, the first ply is more difficult to fail by microbuckling.

On the other hand, it is widely recognized that the plastic matrix could withstand higher compressive stress than tensile stress. Therefore, the 15th ply (90° orientation with low

stiffness) in the tensile region was more likely to fail than the second ply (90°) in the compressive region. Indeed, the tensile stress in the 15th ply had exceeded the transverse tensile strength of resin shown in **Table 4-2**. Therefore, the failure sequence of long-beam cross-ply laminate can be explained as, a) the 15th ply failed in tension and the stiffness had a tiny drop (90° ply failed), b) the 16th ply (0° orientation with high stiffness) delaminated and failed in tension, and then the stiffness shown a huge decrease, c) the delamination propagated inside the laminate and it failed. **Figure 4.14** shows a typical microscope failure image of long-beam cross-ply laminate, while **Figure 4.15** shows the deflection-load curves of long-beam cross-ply laminate.

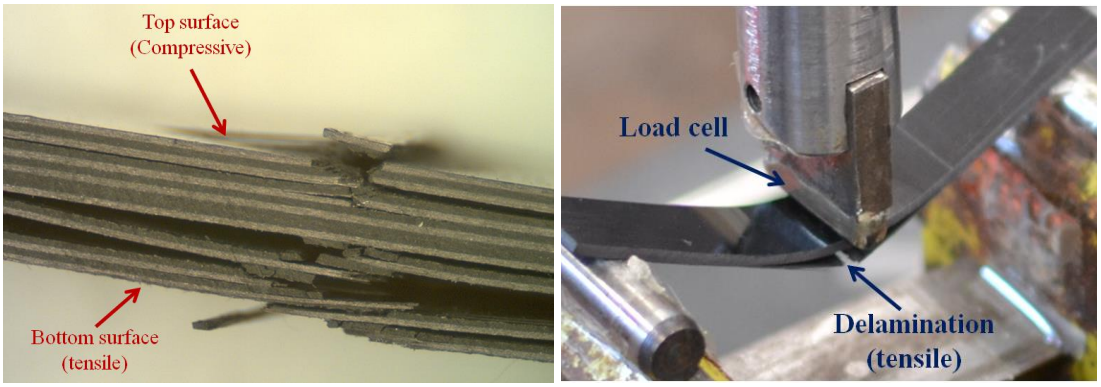

Figure 4.14 Typical microscope failure image of long-beam cross-ply laminate (left) and its tensile failure in 3-point bending (right).

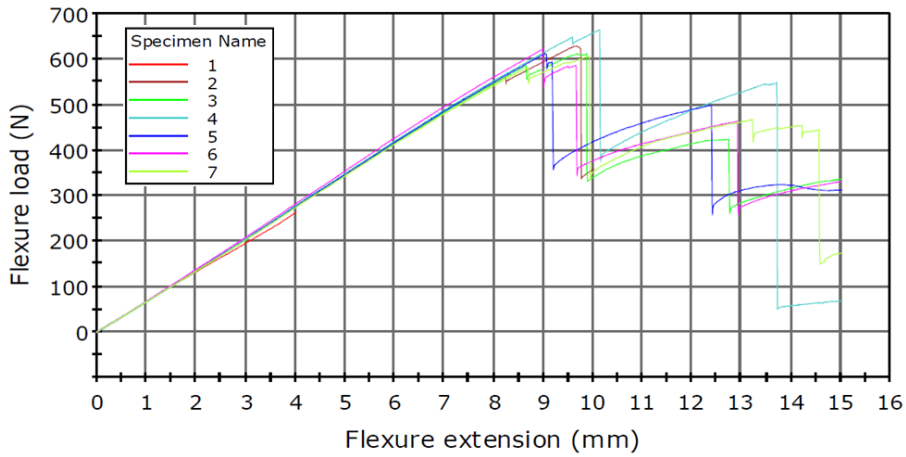

Figure 4.15 Deflection-load curves of long-beam cross-ply laminate. The small and large 'stiffness losses' represent the failure of transverse and longitudinal plies.

Applying the Tsai-Hill failure criterion to the FEA results of the long-beam cross-ply laminate, indicates that the interlaminar shear stress contributed about 4% to the

criterion. However, the stress component σ_2 contributes much more due to the lower transverse tensile strength $\left(\sigma_2^{ult}\right)^t$. **Figure 4.16** shows the distribution of the Tsai-Hill failure criterion in the long-beam cross-ply laminate. The maximum value appeared at the interfaces of the first and second plies corresponding to the maximum transverse stress σ_2, as shown in **Figure 4.11**. Delamination was also observed between the 1st and the 2nd ply in the experiment as shown in **Figure 4.14**.

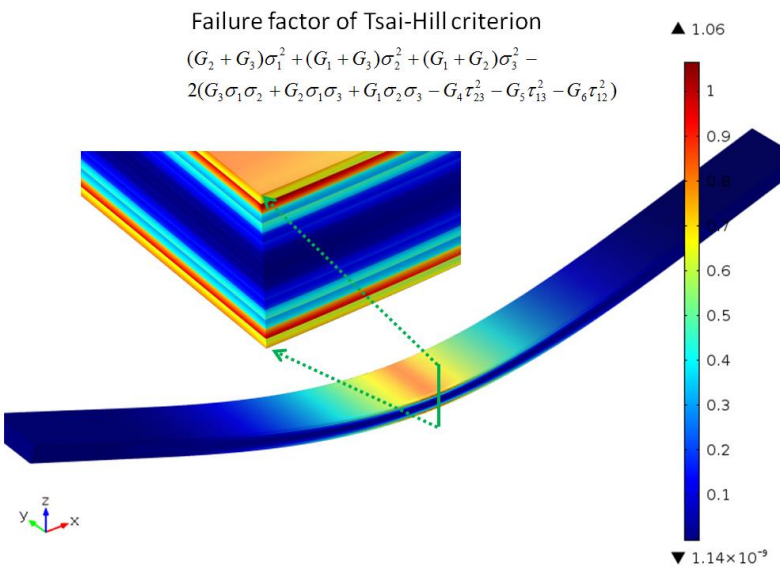

Figure 4.16 Distribution of Tsai-Hill 'failure factor' in long-beam cross-ply laminate. The transverse plies exceeded the failure criterion rather than the surface plies.

4.2.3 *Interlaminar shear strength*

For the short-beam laminate, the 3D FEA model shows a significant increase (15%) of the free edge effect on the interlaminar shear stress τ_{13}. However this value decays sharply inside the laminate and then converges to the CLT value (c.f. **Table 4-3**) in the central area, as shown in **Figure 4.17**.

This implies that the laminate failed initially from edge area. Additionally, due to the short span, the out-of-plane normal stress σ_3, which is neglected in the ISO standard, shows a relatively high value in the FEA model. Similarly, this value decays inside the laminate, and is located at the loading area. **Figure 4.18** shows the distribution of out-of-

plane normal stress σ_3 and images of typical failure for the short-beam unidirectional laminate. The maximum out-of-plane normal stress σ_3 is very close to the transverse tensile strength $\left(\sigma_2^{ult}\right)^t$ in **Table 4-3**. It also indicates that the ISO standard may underestimate the interlaminar shear strength of short-beam unidirectional laminate.

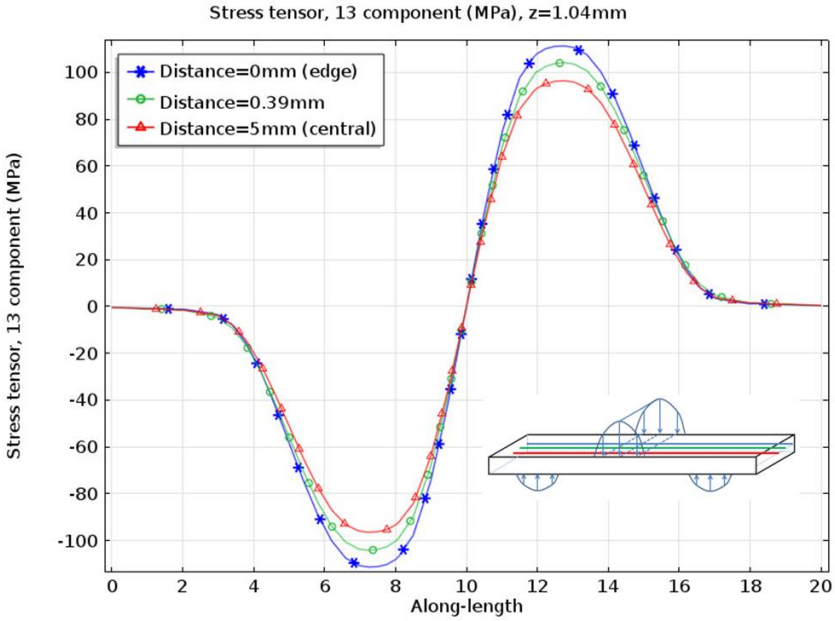

Figure 4.17 Distribution of interlaminar shear stress τ_{13} on middle plane of short-beam unidirectional laminate. The higher value at free edge region implies the crack could be initialized from this area.

For the short-beam cross-ply laminate, the interlaminar shear stress τ_{13} is not continuous due to the bidirectional lay-up sequence, and the maximum value appears at the interface between the 7th and 8th plies (z=1.08mm) rather than the mid-plane. This is different from the measured apparent interlaminar shear stress (shown in **Table 4-1**). **Figure 4.19** shows the distribution of interlaminar shear stress τ_{13} through-thickness at x=13mm. The coordinates are (13, 0), (13, 0.6) and (13, 5) respectively.

It can be seen from **Figure 4.19** that the maximum value of τ_{13} is lower than the interlaminar shear strength shown in **Table 4-3**. The transverse and out-of-plane components of normal stress, σ_2 and σ_3 are much higher, compared with the short-beam unidirectional laminate.

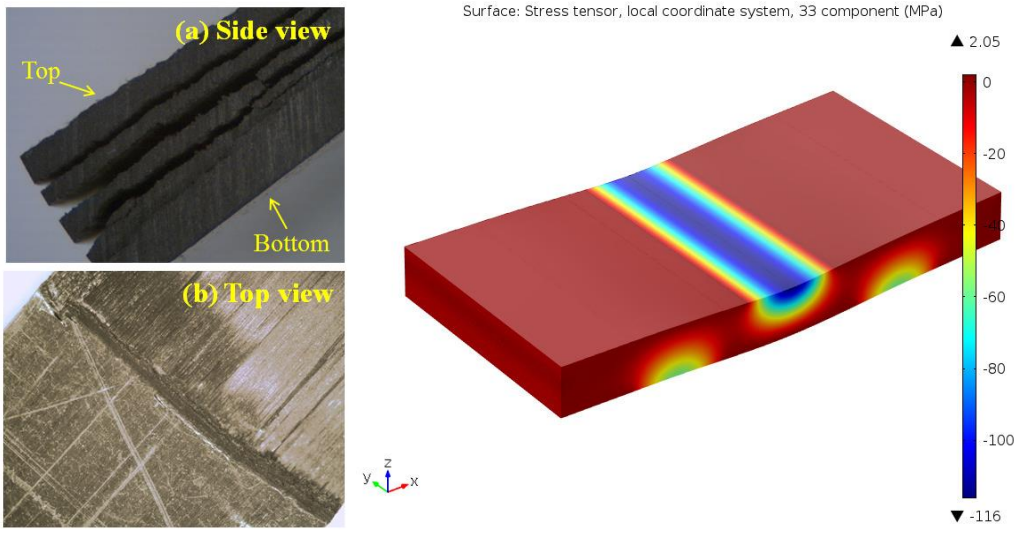

Figure 4.18 Typical failure images of short-beam unidirectional laminate and the distribution of out-of-plane normal stress σ_3. The combination of interlaminar shear stress τ_{13} and out-of-plane normal stress σ_3 leads to delamination at compressive (top) part of the laminate

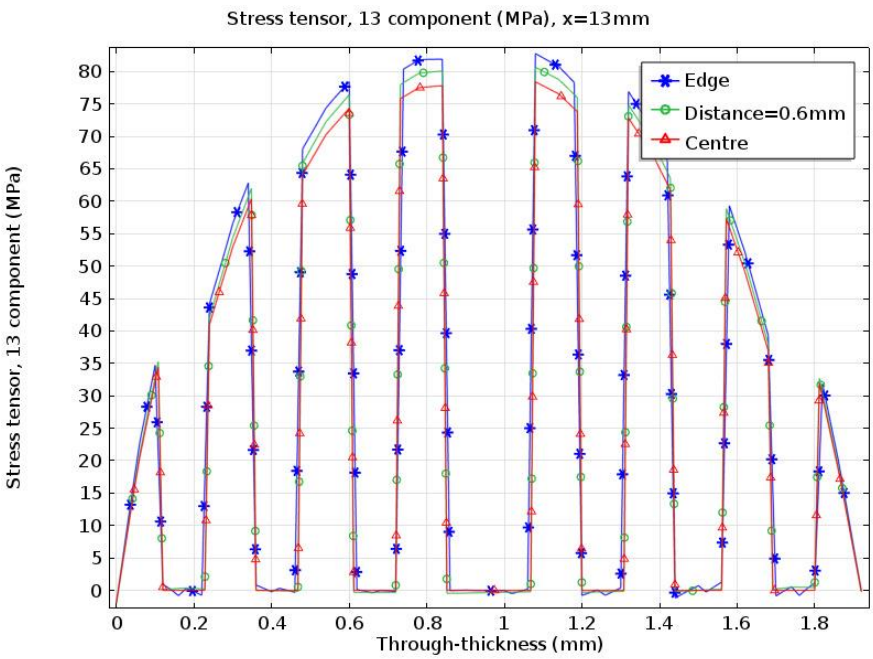

Figure 4.19 Distribution of interlaminar shear stress τ_{13} of short-beam cross-ply laminate. The free edge effect is slight, compared with short-beam unidirectional laminate.

Figure 4.20 shows the distributions of these two normal stress components in the short-beam cross-ply laminate. The maximum values of σ_2 and σ_3 are so high that they have exceeded the transverse tensile strength $\left(\sigma_2^{ult}\right)^t$. It indicates that the laminate failed in transverse compression initializing at the second ply. Following the 'stiffness losses' and stresses re-distribution, the maximum interlaminar shear stress τ_{13} exceeded the shear strength, and then the laminate failed. **Figure 4.21** shows a typical microscope image of interlaminar failure of short-beam cross-ply laminate.

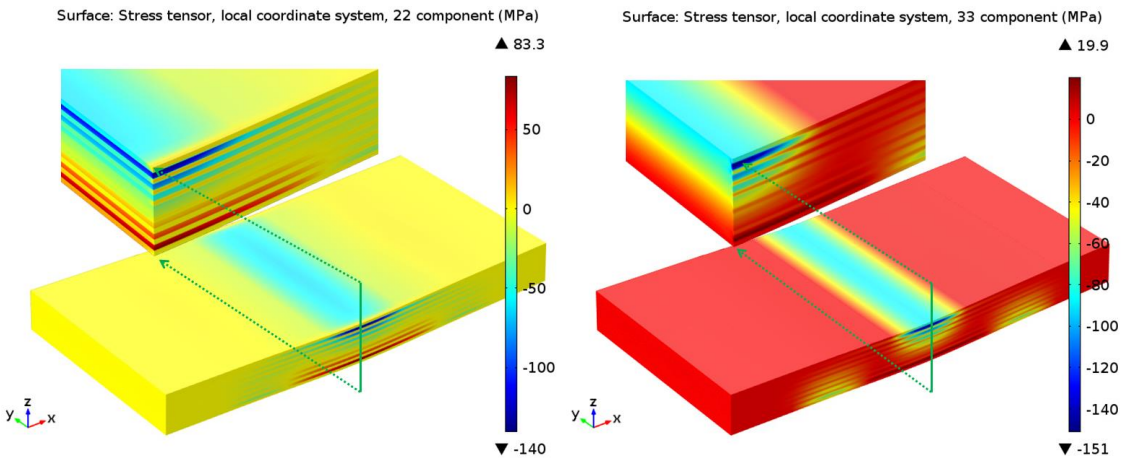

Figure 4.20 Distributions of normal stress σ_2 (left) and σ_3 (right) in short-beam cross-ply laminate and their side-views. The maximum stresses appeared at the second ply (90°), and strong free edge effect on σ_3 is observed.

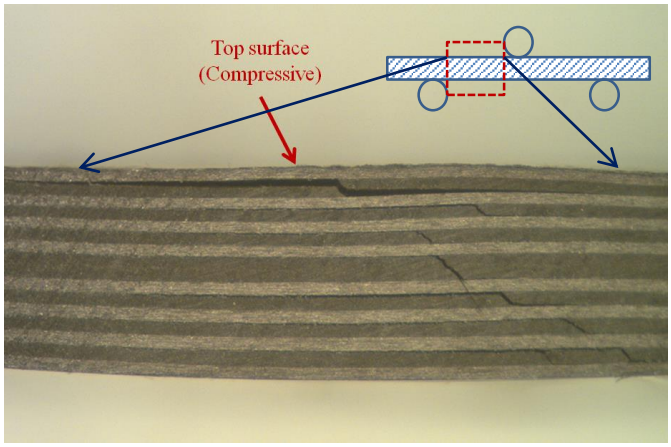

Figure 4.21 Typical microscope failure image of short-beam cross-ply laminate. The initial delamination began from the 2nd ply, corresponding to the maximum σ_2 and σ_3 in Figure 4.20.

For the angle-ply laminate, the distributions of these flexural stresses are quite different from the symmetric laminates. Moreover, the CLT and 3D FEA models present significantly different results. With the infinite plane hypothesis, the CLT method provides a relatively smooth distribution of stresses. **Figure 4.22** shows the distribution of interlaminar shear stress τ_{xz} (global) and τ_{13} (local) through-thickness in short-beam angle-ply laminate, evaluated by CLT method. It can be seen that both of the maximum value of τ_{xz} and τ_{13} appear at the mid-plane (z=0.92mm), and the shear stress τ_{13} in local coordinate system is not continuous because of the complicated lay-up sequence.

The curves extracted from the CLT method show that the local interlaminar shear stress τ_{13} is lower than the global value. Furthermore, these curves are so uniform that they provide no information about the free edge effects.

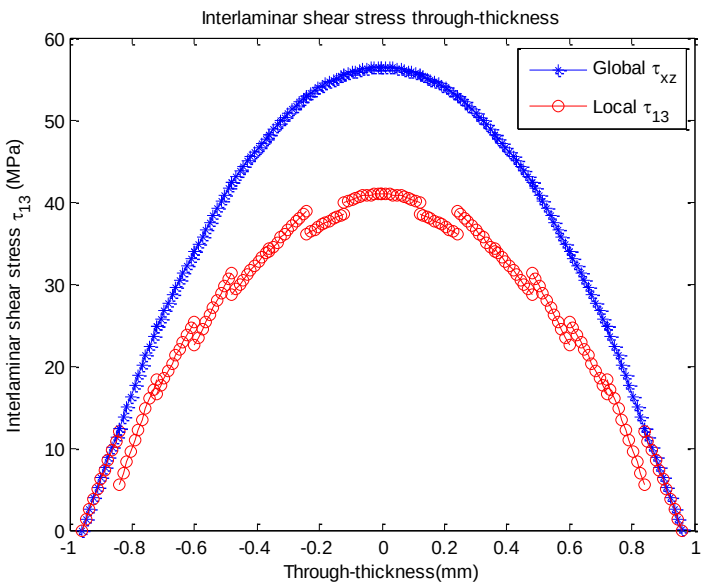

Figure 4.22 Interlaminar shear stress τ_{xz} and τ_{13} distribution through-thicknesses in short-beam angle-ply laminate (CLT). The discrete τ_{13} represents the complicated lamina orientation.

The early works of Pipes and Pagano (Pipes and Pagano, 1970; Pagano, 1978) had predicted the singularity of interlaminar shear stress near the free edge region of a $[\pm 45°]_2$ angle-ply laminate under axial load. 3D FEA models in the present work also

show the increase of interlaminar shear stress in the short-beam angle-ply laminate under bending.

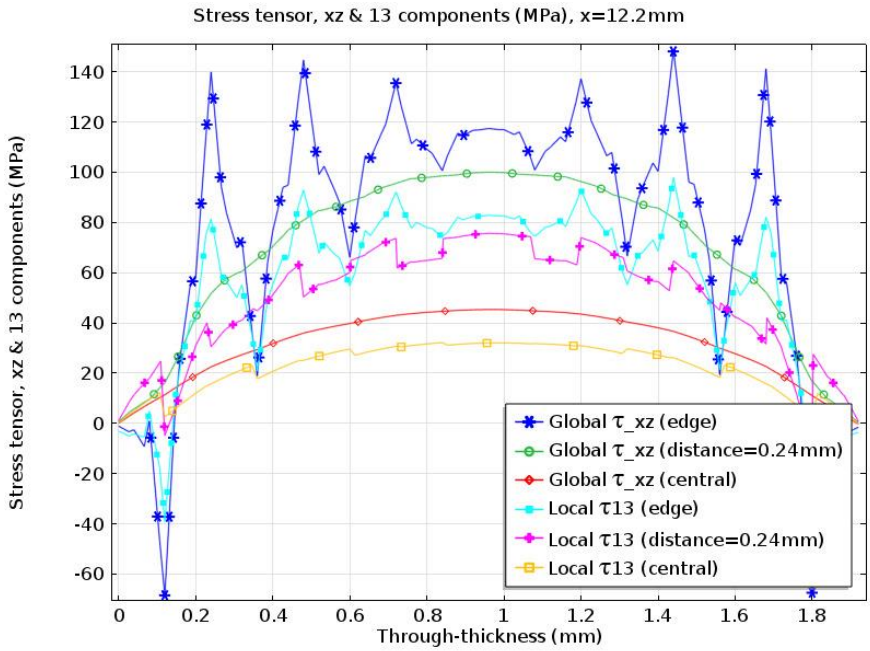

Figure 4.23 Distributions of interlaminar shear stress through-thicknesses in short-beam angle-ply (3D FEA model). The 'stress peaks' at edge area converge to CLT at centre, and the maximum value appears at z=1.44mm (interface of 4-5 plies)

Figure 4.23 shows the through-thickness distribution of interlaminar shear stress of the short-beam angle-ply laminate. It can be seen that both the τ_{xz} and τ_{13} near free edge area fluctuate remarkably. The maximum values appear at the interface between the 4th and 5th plies, instead of the mid-plane (8th and 9th plies, as predicted by CLT, shown in **Figure 4.22**). However, the distribution tends to be uniform inside the laminate. A small distance from the edge (2 ply-thicknesses, 0.24mm), the distribution of global shear stress τ_{xz} becomes a parabolic shape, while the maximum value of local shear stress τ_{13} at the mid-plane drops approximate 20%. Finally both of the global and local shear stresses converge to the CLT at central area.

This extremely high global shear stress τ_{xz} at the free edge located at the interface of two plies, which may lead to delamination, while the local shear stress τ_{13} at the corresponding location is very close to the shear strength τ_{13}^{ult} shown in **Table 4-3**.

Moreover, quite a few points with these 'extreme values' can be found at the interface of two plies, which are easier to induce the 'multi-crack' at the edge area. **Figure 4.24** shows the surface plot and slice plot of local shear stress τ_{13} of the short-beam angle-ply laminate, while **Figure 4.25** shows the diagram of the free edge effect.

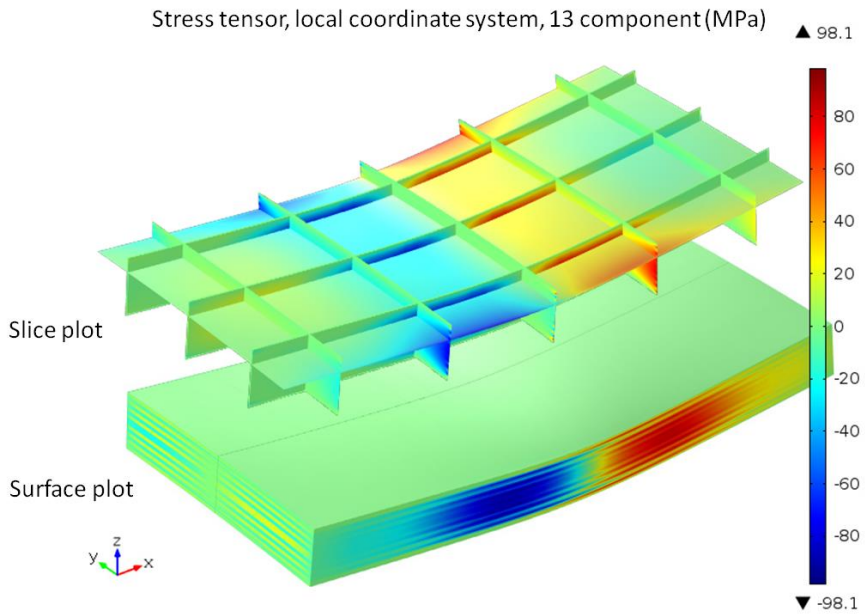

Figure 4.24 3D distribution of τ_{13} in short-beam angle-ply laminate. The slice plot reveals the distribution of τ_{13} in 3D scale, and the surface plot shows the variation of τ_{13} in different plies with particular fibre orientation.

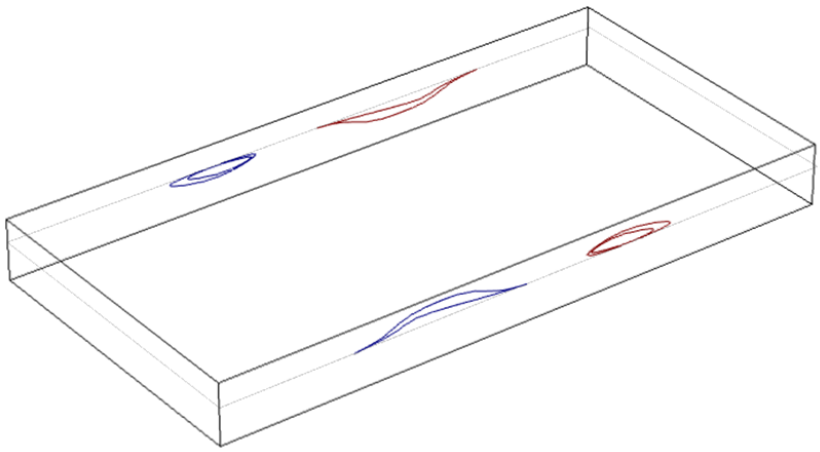

Figure 4.25 Contour curves of interlaminar shear stress τ_{13} in short-beam angle-ply laminate (z=1.44mm). The extremely high stress only appears near the edge area.

It should be noted that the interaction ratio (η_{xyx}) between normal stress σ_x and in-plane shear stress τ_{xy} is too high to be neglected in angle-ply laminates. According to 3D CLT, the transformed compliance matrix $\overline{S}$ of angle-ply laminate shows non-zero 'interaction' terms ($\overline{S_{16}}$ and $\overline{S_{26}}$), leading to a definition of interaction ratios:

$$\begin{aligned} \eta_{xyx} &= E_x \overline{S_{16}} \\ \eta_{xyy} &= E_x \overline{S_{26}} \end{aligned} \tag{4-13}$$

The interaction ratio (η_{xyx}) represents the ratio of the shear strain γ_{xy} induced by normal stress σ_x, to the normal strain ε_x induced by the same normal stress σ_x.

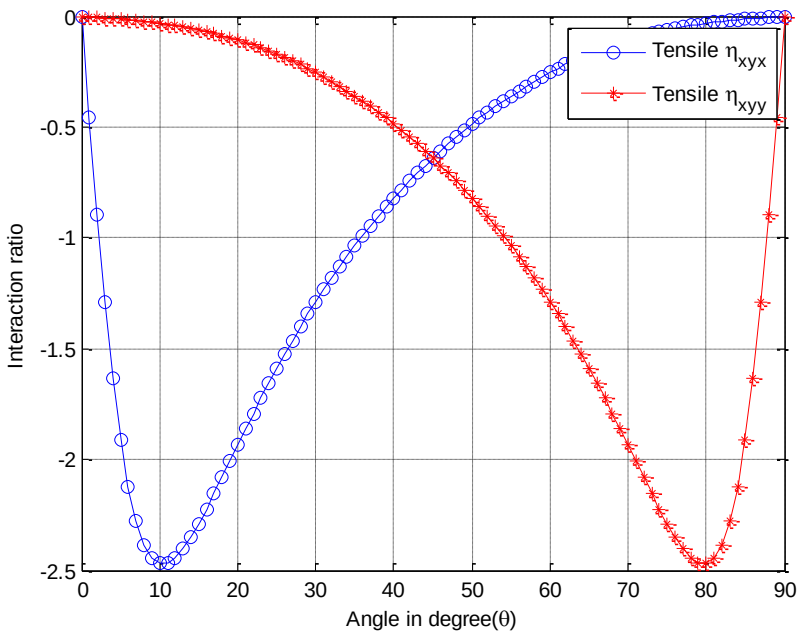

Figure 4.26 Interaction between axial stress and shear stress in off-axis laminate (according to CLT). The value of η represents the couple of normal stress to shear stress.

Figure 4.26 shows the relationship between interaction ratio η_{xyx} and the off-axis angle (predicted by CLT). The interaction ratio (η_{xyx}) evaluated by CLT predicted a value of about -0.7 in angle-ply lamina (45°). It illustrates the axial stress could induce rather high in-plane shear stress, which is happening in the present case of the short-beam angle-ply laminate. It was found that for many commercial CFRP composites, the

maximum value of interaction ratio appears around 10-13° off-axis angle. **Table 4-4** shows the maximum interaction ratio of ten commercial CFRP composites. In **Table 4-4**, there are ten different commercial CFRP composites and their maximum interaction ratios are very close. In fact, the coefficient of variation of off-axis angle is 1.3%.

Table 4-4 Engineering constants (Tsai and Melo, 2014) and the interaction ratio (CLT)

	$E_1(GPa)$	$E_2(GPa)$	ν_{12}	$G_{12}(GPa)$	$\lvert\eta_{xyx}^{\max}\rvert$	$\theta(°)$
IM7/977-3	191	9.94	0.35	7.79	2.259	12
T800/Cytec	162	9	0.4	5	2.622	10
T700 C-Ply 55	121	8	0.3	4.7	2.301	11
T700 C-Ply 64	141	9.3	0.3	5.8	2.224	12
AS4/H3501	138	8.96	0.3	7.1	1.970	13
IM6/epoxy	203	11.2	0.32	8.4	2.237	12
AS4/F937	148	9.65	0.3	4.55	2.625	10
T300/N5208	181	10.3	0.28	7.17	2.288	12
IM7/8552	171	9.08	0.32	5.29	2.629	10
IM7/MTM45	175	8.2	0.33	5.5	2.616	10
Average	163.1	9.363	0.32	6.13	2.377	11.2
SDs	25.85	0.96	0.03	1.37	0.23	1.14
Coeff var	15.9%	10.2%	10.7%	22.4%	9.7%	1.3%*

***Divided by 90°**

Due to the complex structure in angle-ply laminate, the interaction ratio (η) strongly affects the distribution of the in-plane shear stress τ_{xy} in 3D. Indeed, the value of in-plane shear stress τ_{xy} is much higher than the other two shear stress components τ_{xz} and τ_{yz}. Because of the nature of three-point bending, the maximum normal stress appears at the top and bottom plies. As a consequence, this 'induced' in-plane shear stress τ_{xy} may lead to strong twisting at the two surfaces of the laminate. **Figure 4.27** shows the slice plot and surface plot of in-plane shear stress τ_{12} in short-beam angle-ply laminate.

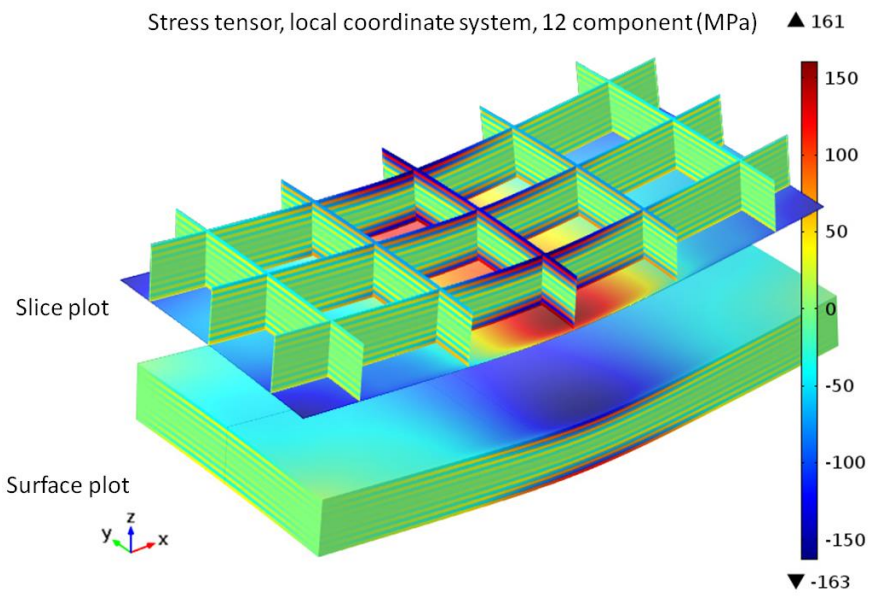

Figure 4.27 Slice plot (upper) and surface plot (lower) of in-plane shear stress in short-beam angle-ply laminate. The values of τ_{12} near the middle area of top and bottom surfaces are so high that strong distortion was observed in the bending test.

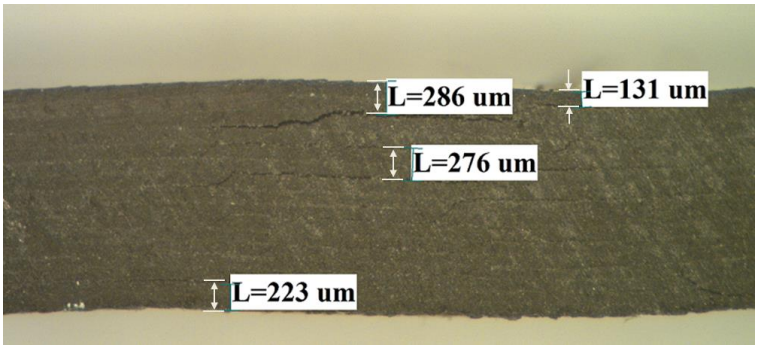

Figure 4.28 Typical failure image of angle-ply laminate under bending test condition. Cracks appeared at free edge area, but without penetrating inside the volume. The positions of cracks correspond to a peak of interlaminar shear stress, as shown in Fig.4-23. Specimen twisting induced by in-plane shear stress was observed.

The observation of microscope images confirmed the results from 3D FEA models. Instead of delamination failure (as likely occurred in unidirectional and cross-ply laminates), the failure mode in angle-ply laminate was the combination of in-plane shear stress τ_{12} and interlaminar shear stress τ_{13}. Consequently, the crack appeared

near the two free edge sides of specimen, but without propagating through the whole width. **Figure 4.28** gives a typical microscope failure image of short-beam angle-ply specimen under three-point bending, while **Figure 4.29** shows the deflection-load curves.

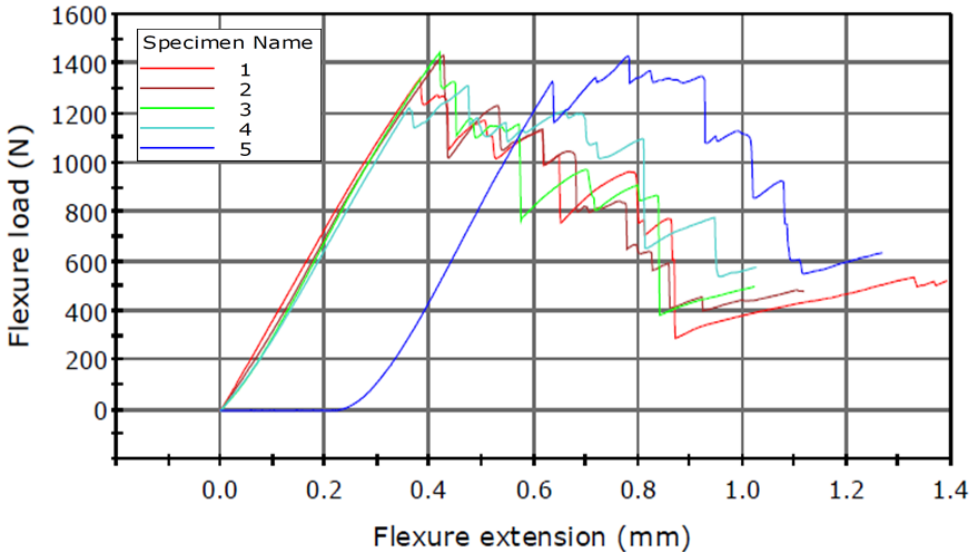

Figure 4.29 Deflection-load curves in angle-ply laminate from three-point bending test. Each crack represented a 'stiffness losses' in bending test.

4.3 Unequal compressive/tensile moduli

In practical composite structures, the composite materials are subjected to complicated loading conditions, such as bending, tension, compression and twisting. It has been demonstrated in section 4.2 that all of the six stress components (σ_i, τ_{ij}) contribute to the failure criterion of CFRP composites, particularly the initiation of failure in bending. However, most of the previous studies on composites are based on equal compressive/tensile moduli, which may lead to either overestimate or underestimate the composite strength. The effects of unequal compressive/tensile moduli on the failure criterion of composites have not been reported.

In this section, the compressive modulus is assumed to be a fraction lower than the tensile modulus based on the statistics of current commercial CFRP composites. The effects of unequal compressive/tensile moduli on composites are investigated: (a) the composite failure criterion, particularly Tsai-Wu failure criterion, (b) a modified CBT

for the flexural properties of unidirectional laminate and its failure mechanisms, (c) a modified CLT for the flexural properties of multi-directional laminate, and (d) fibre micro-buckling. Three approaches are used in parallel: (a) Finite Element Analysis (FEA) is employed to investigate the stress and strain distributions within the laminates for the identification of the maximum critical strains and stresses, (b) CLT is applied to extract the flexural modulus and strain/stress distributions of multi-directional laminate with different stacks, and (c) experiment is carried out to provide the sufficient evidence to support this study.

4.3.1 *Failure criteria*

It has been shown that unequal compressive/tensile moduli of the CFRP composites commonly exist and the average λ ($\lambda = E_1^c / E_1^t$) value is 0.9 with very small coefficient of variation. It means that the ultimate compressive strain of CFRP composites is underestimated by traditional failure criteria. Therefore, strain dominated failure criteria could more generally reflect the real conditions, and the failure envelope should be presented in strain space rather than stress space. Tsai-Wu failure criterion (Tsai, 2008), which includes compressive terms, is used in the present work to illustrate the effects of unequal compressive/tensile moduli of CFRP composites,

$$F_{ij}\sigma_i\sigma_j + F_i\sigma_i = 1 \tag{4-14}$$

$$\begin{aligned} F_{11} &= \frac{1}{\left(\sigma_1^t\right)_{ult}\left(\sigma_1^c\right)_{ult}}, F_1 = \frac{1}{\left(\sigma_1^c\right)_{ult}} - \frac{1}{\left(\sigma_1^t\right)_{ult}} \\ F_{22} &= \frac{1}{\left(\sigma_2^t\right)_{ult}\left(\sigma_2^c\right)_{ult}}, F_2 = \frac{1}{\left(\sigma_2^c\right)_{ult}} - \frac{1}{\left(\sigma_2^t\right)_{ult}} \\ F_{66} &= \left(\frac{1}{\tau_{12}^{ult}}\right)^2 \end{aligned} \tag{4-15}$$

The criterion is quadratic and is expressed in stress space. In fact, most of the current failure criteria are expressed in stress space. F_{12} is the interaction term which is nearly impossible to measure. In this thesis, the calculation was based on F_{12}=-0.5. The Tsai-Wu failure criterion can be transformed to strain space by applying the relationship of extensional stiffness matrix (Tsai, 2008),

$$U_{ij}\varepsilon_i\varepsilon_j + U_i\varepsilon_i = 1 \tag{4-16}$$

$$U_{ij} = F_{kl} Q_{ki} Q_{lj}$$
$$U_i = F_j Q_{ij} \tag{4-17}$$

$$Q_{11} = \frac{E_1}{1-\nu_{12}\nu_{21}}, Q_{22} = \frac{E_2}{1-\nu_{12}\nu_{21}}$$
$$Q_{12} = Q_{21} = \frac{\nu_{12}E_2}{1-\nu_{12}\nu_{21}}, Q_{66} = G_{12} \tag{4-18}$$

The Tsai-Wu failure criterion is fully defined in strain space by equations from (4-19) to (4-21). According to Tsai's invariant-based theory (Tsai and Melo, 2014), a transformation can be applied on the strain envelope to define the rotated strain envelopes of all ply orientations,

$$\begin{bmatrix} \overline{U_{11}} \\ \overline{U_{22}} \\ \overline{U_{12}} \\ \overline{U_{66}} \\ \overline{U_{16}} \\ \overline{U_{26}} \\ \overline{U_1} \\ \overline{U_2} \\ \overline{U_6} \end{bmatrix} = \begin{bmatrix} T_1 & T_2 & T_3 & 0 & 0 & 0 & 0 & 0 \\ T_1 & -T_2 & T_3 & 0 & 0 & 0 & 0 & 0 \\ T_4 & 0 & -T_3 & 0 & 0 & 0 & 0 & 0 \\ T_5 & 0 & -T_3 & 0 & 0 & 0 & 0 & 0 \\ 0 & 0 & 0 & \frac{T_2}{2} & T_3 & 0 & 0 & 0 \\ 0 & 0 & 0 & \frac{T_2}{2} & -T_3 & 0 & 0 & 0 \\ 0 & 0 & 0 & 0 & 0 & T_6 & T_7 & 0 \\ 0 & 0 & 0 & 0 & 0 & T_6 & -T_7 & 0 \\ 0 & 0 & 0 & 0 & 0 & 0 & 0 & T_7 \end{bmatrix} \begin{bmatrix} 1 \\ \cos 2\theta \\ \cos 4\theta \\ \sin 2\theta \\ \sin 4\theta \\ 1 \\ \cos 2\theta \\ \sin 2\theta \end{bmatrix} \tag{4-19}$$

$$\begin{bmatrix} T_1 \\ T_2 \\ T_3 \\ T_4 \\ T_5 \\ T_6 \\ T_7 \end{bmatrix} = \begin{bmatrix} \frac{3}{8} & \frac{3}{8} & \frac{1}{4} & \frac{1}{2} & 0 & 0 \\ \frac{1}{2} & -\frac{1}{2} & 0 & 0 & 0 & 0 \\ \frac{1}{8} & \frac{1}{8} & -\frac{1}{4} & -\frac{1}{2} & 0 & 0 \\ \frac{1}{8} & \frac{1}{8} & \frac{3}{4} & -\frac{1}{2} & 0 & 0 \\ \frac{1}{8} & \frac{1}{8} & -\frac{1}{4} & \frac{1}{2} & 0 & 0 \\ 0 & 0 & 0 & 0 & \frac{1}{2} & \frac{1}{2} \\ 0 & 0 & 0 & 0 & \frac{1}{2} & -\frac{1}{2} \end{bmatrix} \begin{bmatrix} U_{11} \\ U_{22} \\ U_{12} \\ U_{33} \\ U_1 \\ U_2 \end{bmatrix} \tag{4-20}$$

$$\overline{U_{11}}\varepsilon_1^2 + \overline{U_{22}}\varepsilon_2^2 + 2\overline{U_{12}}\varepsilon_1\varepsilon_2 + 2\overline{U_{16}}\varepsilon_1\varepsilon_6 +$$
$$2\overline{U_{26}}\varepsilon_2\varepsilon_6 + \overline{U_{66}}\varepsilon_6^2 + \overline{U_1}\varepsilon_1 + \overline{U_2}\varepsilon_2 + \overline{U_6}\varepsilon_6 = 1 \tag{4-21}$$

Figure 4.30 shows the failure envelopes of T800/Cytec in strain space with some particular ply orientations (0°, 15°, 30°, 45°, 60°, 75°, and 90°). The properties are given in **Table 4-5**.

In **Figure 4.30**, the failure envelopes were determined using equal compressive/tensile moduli (λ=1). The failure envelopes of different ply orientations construct a minimum shape, which was proposed as 'omni envelope' by Tsai's invariant theory (Tsai and Melo, 2014). It represents the first-ply-failure of a given composite for all ply orientations. Regardless of the ply orientation, the composite material is unlikely to fail when the strain inside into this omni envelope.

Table 4-5 Engineering constant of two CFRP composites and their strength (Tsai and Melo, 2014)

	E_1^t	E_2	G_{12}	ν_{12}	$(\sigma_1^t)_{ult}$	$(\sigma_1^c)_{ult}$	$(\sigma_2^t)_{ult}$	$(\sigma_2^c)_{ult}$	τ_{12}^{ult}
T800/Cytec	162	9.0	5.0	0.4	3.77	1.66	0.056	0.15	0.098
T700/C-Ply 55	121	8.0	4.7	0.3	2.53	1.70	0.066	0.22	0.093

***unit: GPa**

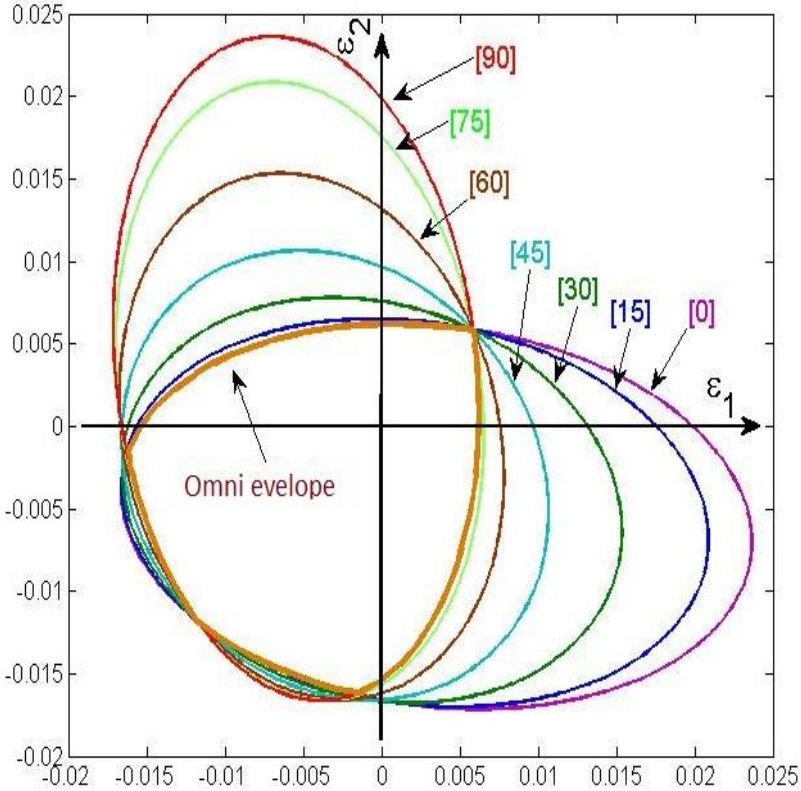

Figure 4.30 Failure envelopes of T800-Cytec CFRP composite in strain space

In **Table 2-3** and **Figure 2.3**, it has been shown that the λ value of most of the CFRP composites is between 0.8 and 1. **Figure 4.31** shows the omni envelopes of T800/Cytec and T700/C-Ply 55 with three λ values: 0.8, 0.9 and 1. It can be seen that, for both the two CFRP composites, the λ value has no effect on the omni envelope in the first quadrant $(\varepsilon_1 > 0, \varepsilon_2 > 0)$. For T800/Cytec, the λ value doesn't affect the omni envelope in the third quadrant $(\varepsilon_1 < 0, \varepsilon_2 < 0)$; however in the second $(\varepsilon_1 > 0, \varepsilon_2 < 0)$ and the fourth $(\varepsilon_1 < 0, \varepsilon_2 > 0)$ quadrants, the omni envelope enlarges with the decrease of the λ value. It means that the CFRP composites could withstand higher strain either when $\varepsilon_1 < 0$ or $\varepsilon_2 < 0$, and the traditional failure criterion has underestimated the composite strength. The experimental results of T800/Cytec also indicated this trend in the reference (Tsai and Melo, 2014).

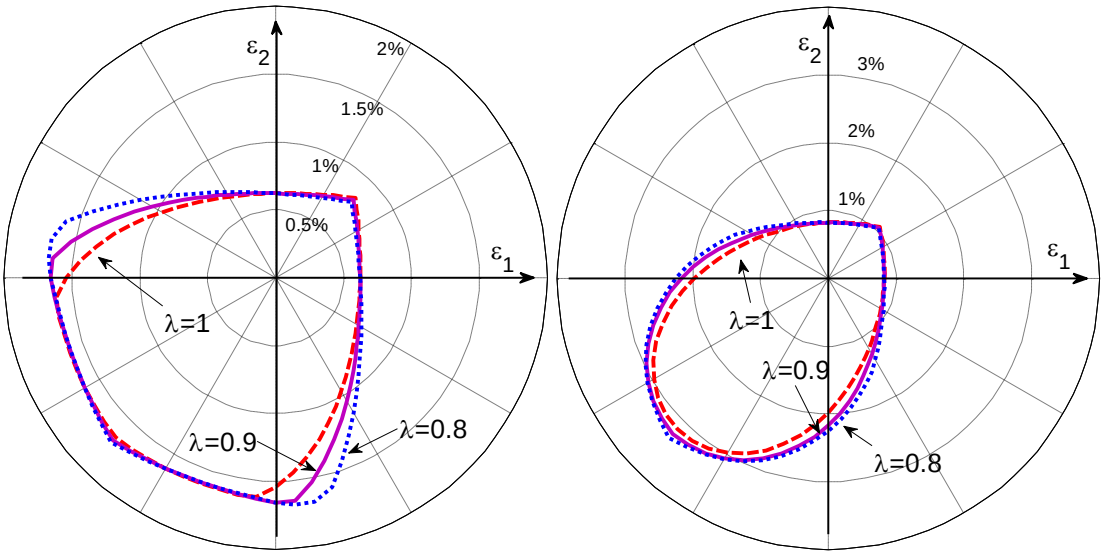

Figure 4.31 Omni envelopes of T800/Cytec (left) and T700/C-Ply 55 (right) with different λ values

4.3.2 *Unidirectional laminate*

The terms of compressive modulus can be introduced into a modified CBT to investigate the mechanical behaviour of unidirectional laminate. For a unidirectional laminate under bending, the neutral plane will have an offset to the bottom side due to the lower compressive modulus, as shown in **Figure 4.32**.

According to the principles of continuum mechanics (Lai, Rubin et al., 2009), the integration of the axial stress of an Euler beam in bending is zero, and the moment of normal stress (M_1) is equal to the moment (M_2) applied in the cross section:

$$\int_A \sigma_1 dA = \int_{-h_1}^{h_2} \sigma_1 w dz = w\int_{-h_1}^{0} E_1^t \varepsilon_1 dz + w\int_0^{h_2} E_1^c \varepsilon_1 dz = 0 \qquad (4\text{-}22)$$

$$M_1 = \int_A \sigma_1 z dA = w\int_{-h_1}^{0} E_1^t \kappa z^2 dz + w\int_0^{h_2} E_1^c \kappa z^2 dz \qquad (4\text{-}23)$$

$$M_2 = E^f I\kappa \qquad (4\text{-}24)$$

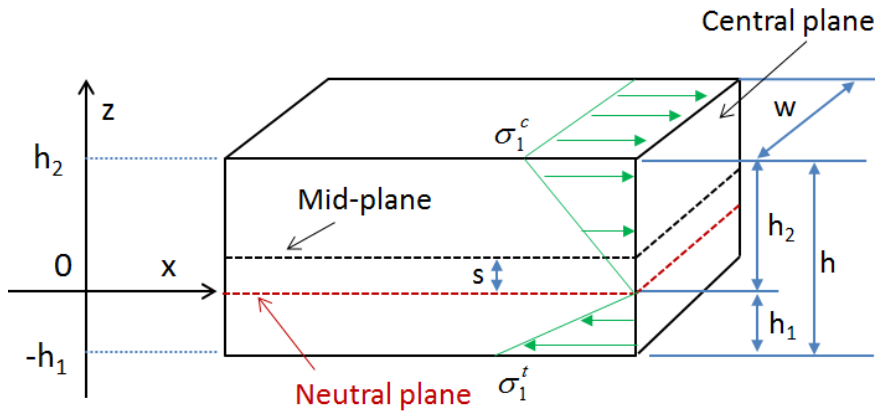

Figure 4.32 Unidirectional laminate under bending. The compressive stress and tensile stress re-distribute through-thickness due to the unequal compressive and tensile moduli.

If it is assumed that the specimen is long enough to neglect the out-of-plane strain, the longitudinal strain tensor is determined by:

$$\varepsilon_1 = \kappa z \qquad (4\text{-}25)$$

Substituting equations (4-24) and (4-25) into equations (4-22) and (4-23),

$$E_1^t h_1^2 = E_1^c h_2^2 \qquad (4\text{-}26)$$

$$E_1^t h_1^3 + E_1^c h_2^3 = \frac{E^f h^3}{4} \qquad (4\text{-}27)$$

As shown in Fig.4-32, the geometric relationship between h_1 and h_2 is governed by

$$h_1 + h_2 = h \qquad (4\text{-}28)$$

A parameter λ is introduced to identify the ratio of compressive modulus to tensile modulus:

$$\lambda = \frac{E_1^c}{E_1^t} \tag{4-29}$$

Combining equations (4-26), (4-27) and (4-28), one can get the relationship between compressive modulus, tensile modulus and flexural modulus of unidirectional laminate:

$$h_1 = \frac{h\sqrt{E_1^c}}{\sqrt{E_1^c} + \sqrt{E_1^t}} = \frac{\sqrt{\lambda}}{\sqrt{\lambda} + 1} h \tag{4-30}$$

$$h_2 = \frac{h\sqrt{E_1^t}}{\sqrt{E_1^c} + \sqrt{E_1^t}} = \frac{1}{\sqrt{\lambda} + 1} h \tag{4-31}$$

$$s = \frac{1 - \sqrt{\lambda}}{2\left(1 + \sqrt{\lambda}\right)} h \tag{4-32}$$

$$E^{app} = \frac{4E_1^c E_1^t}{(\sqrt{E_1^c} + \sqrt{E_1^t})^2} = \frac{4E_1^c}{\left(1 + \sqrt{\lambda}\right)^2} = \frac{4\lambda E_1^t}{\left(1 + \sqrt{\lambda}\right)^2} \tag{4-33}$$

Equations (4-30) to (4-33) indicate that the apparent flexural modulus falls in between the compressive modulus and tensile modulus, and the neutral plane shifts to the side with higher stiffness. It is convenient to obtain the tensile modulus either through tensile testing or calculation by rules of mixture, using fibre volume fraction, fibre tensile modulus and matrix modulus. However, the compressive modulus is much more dependent on the manufacturing process. The variation of compressive modulus may have different effects on different type of composites, which has been shown in the previous sections.

Equation (4-32) gives the offset (s) of the neutral plane to the mid-plane. For example, with the average λ value of CFRP composites (λ =0.9), the offset can be a quarter ply-thickness in a 16-ply unidirectional laminate or a half ply-thickness in a 32-ply laminate. The effects of unequal compressive/tensile moduli become more and more significant with the increase of laminate thickness.

If it is assumed that the bending curvature through-thickness is a constant, the ratio of maximum compressive strain on the top surface to maximum tensile strain on bottom surface can be evaluated as,

$$\frac{\left(\varepsilon_1^c\right)_{\max}}{\left(\varepsilon_1^t\right)_{\max}} = \frac{h_2}{h_1} = \frac{1}{\sqrt{\lambda}} \tag{4-34}$$

The ratio of maximum compressive stress on the top surface to maximum tensile stress on the bottom surface is given by:

$$\frac{\left(\sigma_1^c\right)_{\max}}{\left(\sigma_1^t\right)_{\max}} = \frac{\left(\varepsilon_1^c\right)_{\max} E_1^c}{\left(\varepsilon_1^c\right)_{\max} E_1^t} = \frac{\sqrt{E_1^c}}{\sqrt{E_1^t}} = \sqrt{\lambda} \tag{4-35}$$

Equations (4-34) and (4-35) indicate that the maximum compressive strain (top surface) is higher than tensile strain (bottom surface), but the maximum tensile stress is higher than maximum compressive stress. The higher compressive strain may lead to microbuckling and compressive failure, particular in thick laminates. For example, if λ=0.8, the maximum compressive strain may be 12% higher than the maximum tensile strain. Therefore, it is more reasonable to plot the failure criteria in strain space.

4.3.3 *Multi-directional laminate*

The terms of compressive modulus can also be introduced into a modified CLT to investigate the mechanical behaviour of multi-directional laminate. Multi-directional laminates have been used in complicated composite structures to provide variety of performance. In order to make the composite laminate self-balance for the thermal expansion, the most common multi-directional composite laminates are symmetric, and the middle two plies are the same ply orientations.

In the previous section, the offset of neutral plane is less than one ply-thickness. It is reasonable to simplify the multi-directional laminate as three layers. Consider a multi-directional laminate made of N plies (N is even number), the upper $(N/2-1)$ plies are treated as a compressive sheet, and the lower $(N/2-1)$ plies are treated as a tensile sheet, while the middle two plies are regarded as core material. **Figure 4.33** gives an illustration of this sandwich structure.

In such a sandwich structure, the compressive modulus is applied for the $(N/2-1)$ compressive plies, while the tensile modulus is applied for the $(N/2-1)$ tensile plies. Due to the symmetric geometry, the two core plies have the same ply orientations.

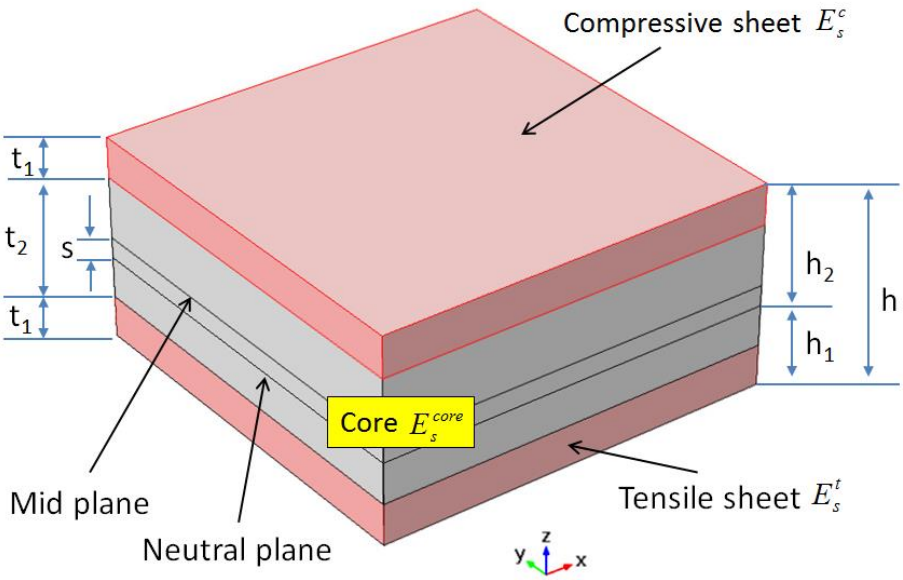

Figure 4.33 Sandwich structure representation of a multi-directional laminate: compressive sheet, core, and tensile sheet. Neutral plane shifts to the bottom side but is still located in the core area.

In order to estimate the elastic modulus of the compressive and tensile sheets, their stiffness matrices should be assembled first. The deviation of the CLT formulae has been shown in Chapter three. Once the ABBD matrix is assembled, inverting the matrix gives the compliance matrix:

$$[a,b;b,d]=\begin{bmatrix} a & b \\ b & d \end{bmatrix}=[A,B;B,D]^{-1} \tag{4-36}$$

Applying the compressive modulus into the abbd matrix of the compressive sheet, tensile modulus into the abbd matrix of tensile sheet, the apparent moduli in compressive sheet and tensile sheet can be obtained by:

$$E_s^c=\frac{12}{t_1^3 d_{11}^c}, E_s^t=\frac{12}{t_1^3 d_{11}^t} \tag{4-37}$$

where t_1 is the thickness of $(N/2-1)$ plies.

Because the core only contains two plies, it has a tiny effect on the total properties of the laminate. Its apparent modulus can be obtained by applying compressive modulus on the upper ply and tensile modulus on the lower ply,

$$E_s^{core} = \frac{12}{t_2^3 d_{11}^{core}} \tag{4-38}$$

For the purpose of comparison, the apparent flexural modulus of the whole laminate is also evaluated by CLT (Gibson, 1994),

$$E^{app} = \frac{12}{h^3 d_{11}} \tag{4-39}$$

Applying the bending moment, the curvature at a given point on the composite laminate can be obtained, and then the distribution of strain through-thickness can be calculated. For example, the 3-point bending curvature at loading point is calculated as,

$$\kappa = \frac{3FL}{E^{app} w h^3} \tag{4-40}$$

where F is the applied flexural force, L is the span and w is the width of the laminate.

The maximum value of compressive strain and tensile strain appear on the top and bottom surfaces at the loading point:

$$\begin{aligned} \left(\varepsilon_1^c\right)_{\max} &= \frac{FLd_{11}}{4w}\left(\frac{h}{2}+s\right) \\ \left(\varepsilon_1^t\right)_{\max} &= \frac{FLd_{11}}{4w}\left(\frac{h}{2}-s\right) \end{aligned} \tag{4-41}$$

where the offset of neutral plane is given by:

$$s = \frac{1}{8}\frac{\left(E_s^t - E_s^c\right)\left(h^2 - t_2^2\right)}{(E_s^c + E_s^t)t_1 + E_s^{core} t_2} \tag{4-42}$$

The maximum strains in the multi-directional laminate are determined by d_{11} and s, which depend on the layup sequence and the ratio of compressive modulus to tensile

modulus λ. Subsequently, the compressive stress and tensile stress of laminate are determined by the ply orientations at any particular area.

Table 4-6 gives the flexural properties (3-point bending) of HTS-12K/977-2 with two different λ values. The material properties have been given in **Table 3-3**.

The FEA and CBT/CLT models were built based on the geometry and boundary conditions shown in section 4.2 using shell element method. The FEA solution was solved by ANSYS ACP (ANSYS Composite Prepost) (ANSYS, 2013), while the CBT and CLT models were solved by MATLAB (MATWORKS, 2013). ANSYS ACP is a pre- and post-processor integrated in ANSYS Workbench, which defines the composite layup and transfers the material properties to the main ANSYS solver.

Table 4-6 Normalized flexural properties of two layups of HTS-12K/977-2 when λ=0.9 and λ=1

	CP $[0/90]_{4s}$				UD $[0]_{16}$			
	FEA	CLT	FEA	CLT	FEA	CBT	FEA	CBT
	λ=0.9		λ=1		λ=0.9		λ=1	
$\varepsilon^c_{\max} : \varepsilon^t_{\max}$	1.049	1.058	0.993	1.000	1.029	1.055	0.978	1.000
E^c_s / E^t_1	—	0.661	—	0.732	—	—	—	—
E^t_s / E^t_1	—	0.732	—	0.732	—	—	—	—
d_{11} ($N^{-1}m^{-1}$)	—	0.0206	—	0.0196	—	—	—	—
$s:t$*	—	0.23	0	0	0.47	0.21	0	0
$E^{app} : E^t_1$	1.126	1.110	1.178	1.166	0.932	0.950	0.979	1.000

***t: ply-thickness**

The apparent flexural modulus evaluated by CBT/CLT and FEA were quite different between unidirectional laminate and multi-directional laminate. This is because the top and bottom plies are longitudinal orientation in multi-directional laminate which withstand higher bending loads.

For the two laminate layups (16 plies), both the FEA and CBT/CLT models give a similar trend in that the maximum compressive strain is about 5% higher than tensile strain when λ=0.9, and the neutral plane has a quarter ply-thickness offset to the bottom

side. In the practical composite structures, the ply number might be more than 16 plies and these effects would be much more significant.

4.3.4 *Fibre microbuckling*

It has been shown in previous sections that the compressive strain is commonly higher than tensile strain when composites are subjected to bending. The higher compressive strain can increase the risk that the carbon fibres fail by microbuckling. Due to the manufacturing defects, the carbon fibres in unidirectional lamina (0°) are not perfectly aligned, typically a 2°-3° fibre misalignment, and the compressive failure is mostly due to fibre microbuckling (Soutis and Turkmen, 1997). Additionally, shear stress can also lead to fibre kinking and microbuckling (Liu, Fleck et al., 2004).

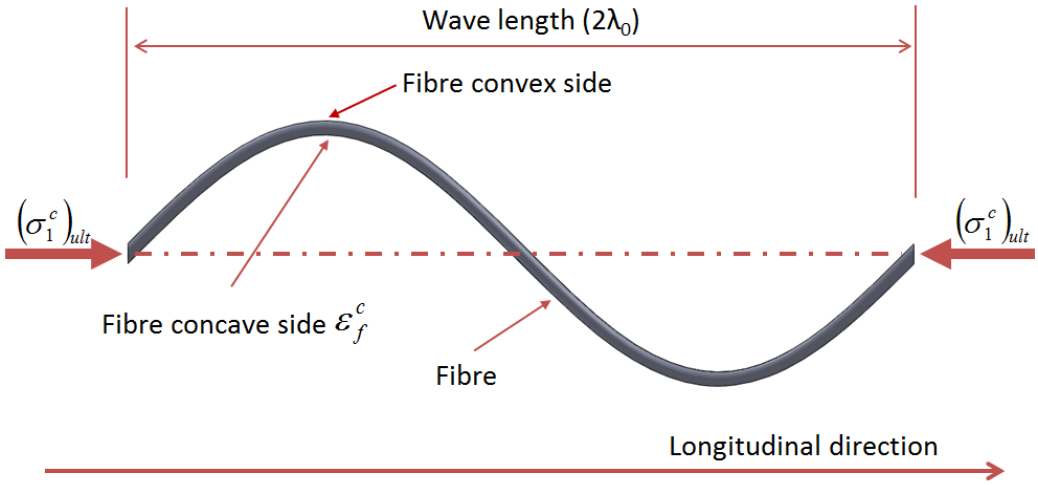

Figure 4.34 A schematic of a single fibre microbuckling in unidirectional lamina. On the fibre concave side, the fibre compressive strain is expected to be higher, and the fibre is more likely to break.

Figure 4.34 shows a schematic of a single fibre microbuckling. Because the carbon fibre is constrained by polymer within a lamina, the microbuckling is not only determined by the radius of fibre, but also the shear strength of matrix. A microbuckling term should therefore be added to the compressive strain on concave side of the fibre (Berbinau, Soutis et al., 1999):

$$\varepsilon_f^c = \frac{(\sigma_1^c)_{ult}}{E_1^c} + r\frac{\pi}{\lambda_0}\gamma_m \qquad (4\text{-}43)$$

where $(\sigma_1^c)_{ult}$ is the compressive strength of lamina, r is the radius of carbon fibre; λ_0 is the half wavelength of microbuckling wave; γ_m is the shear strain of matrix at failure point, for many epoxy matrices, it is in the order of 5% to 7% (Haberle and Matthews, 1994).

In terms of statistics, the value of microbuckling half wavelength λ_0 is typically 10-15 times of fibre diameter $2r$ (Soutis, 1991; Budiansky and Fleck, 1993; Soutis, 1997; Soutis and Turkmen, 1997; Liu, Fleck et al., 2004). Substituting the compressive strength $(\sigma_1^c)_{ult} = 1.58GPa$ of HTS/977-2 and intermediate value of matrix shear failure strain ($\gamma_m = 6\%$) into equation (4-43), the value of maximum compressive strain on fibre concave side ε_f^c can be evaluated, as shown in **Table 4-7**.

Table 4-7 Value of maximum fibre compressive strain on fibre concave side ε_f^c various to the λ_0 value and the maximum compressive strain on the top surface $(\varepsilon_1^c)_{\max}$

	λ_0=0.9		λ=1	
λ_0	$10\times 2r$	$15\times 2r$	$10\times 2r$	$15\times 2r$
$(\varepsilon_1^c)_{\max}$	1.26%	1.26%	1.14%	1.14%
ε_f^c	2.20%	1.89%	2.08%	1.76%

In **Table 4-7**, the fibre compressive strain ε_f^c shows a much higher value than the laminate compressive strain $(\varepsilon_1^c)_{\max}$ when the microbuckling term is introduced, and both the laminate and fibre compressive strains are amplified by the λ value. In the case of λ=0.9, the maximum fibre compressive strain is about 10% higher if compressive/tensile moduli are equal. Additionally, the half wavelength λ_0 of microbuckling also shows a significant effect on the fibre compressive strain. As a consequence, the fibres on the top surface tend to break rapidly once they are unstable.

The unequal compressive/tensile moduli have increased the risk of fibre microbuckling, which leads to a prediction that the unidirectional laminate fails by fibre microbuckling in 3-point bending test. **Figure 4.8** clearly shows the fibre kinking within a unidirectional laminate (HTS-12K/977-2). The top section of the fracture surface of

unidirectional laminate was smoother inferring a fracture by shear due to microbuckling and delamination followed by the crack penetrating through the whole compressive section. Then the tensile section endured the total flexure load and finally broke rapidly by tension and fibre pull-out resulting in a rougher surface on the bottom side.

With a lower compressive modulus, the failure mode is strain dominated. As a consequence, the apparent flexural strength of the unidirectional laminate is equal to the compressive strength. In fact, the apparent flexural strength ($\left(\sigma_1^f\right)_{ult} = 1.60GPa$) evaluated by the 3-point bending test is the very close to the compressive strength which was evaluated in compressive test ($\left(\sigma_1^c\right)_{ult} = 1.58GPa$)(Cytec, 2012).

4.4 Summary

This chapter presents a variety of failure modes of CFRP composite in the static mechanical behaviour in common environment. Compared with shell approximations, 3D FEA and CLT are capable of modelling laminated composites with arbitrary lay-ups, and provides more accurate results.

Study of the different failure mechanisms indicates ways in which laminate design might be improved, for example, inserting a transverse ply into a unidirectional laminate (such as $[0/90/0_n]$) could significantly improve the bending performance. This study also shows that the maximum interaction ratio appears at around 10°-13° off-axis, therefore suggesting that these orientations should be avoided in the surface plies of practical composite laminates. The FEA models demonstrated that the free edge effects, which are strongly dependent on the laminate lay-up and loading span, are responsible for the composite failure initiation.

The effects of unequal compressive/tensile moduli of composites have been systematically investigated in this chapter. This study has proposed modified CBT and CLT methods for investigating the flexural properties of unidirectional and multi-directional laminates respectively. It was proposed that strain dominated failure criteria should be used for composite design, testing and certification, considering the lower compressive modulus of CFRP composites.

This chapter has demonstrated the success of the combination of FEA, CLT and experiment for the investigation of the static mechanical properties of CFRP composite in common environment. With the same research method, the effects of marine environment exposure of the static and fatigue properties are presented in Chapter 5 and 6 respectively.

CHAPTER 5 – MOISTURE DIFFUSION MEASUREMENT AND MODELLING

In the marine environment, composites are subjected to continuous moisture exposure and temperature variation, as well as microorganisms and numerous ionic species present in seawater. These environmental conditions have important effects on the polymer matrix in particular, while the fibres are typically not affected as much by moisture or pressure; swelling or contraction of the polymer matrix is resisted by the fibre so that residual (hygrothermal) stress develops in composites. The increase of moisture content may not only cause a gradual reduction of the glass transition temperature, which is often a critical selection factor, but also change the stress distribution in the composite laminate. Since the moisture diffusion is time dependant, the hygrothermal stress should be investigated in the time domain. However, few of these topics have been found in the literature.

The aim of this chapter is to investigate the impact of sea water immersion on the failure mechanisms of FRP composites. Fresh water (tap water) and sea water were used for the diffusion measurements to investigate the effect of NaCl on the degradation of composite properties. After soaking the samples for one and three months respectively, both the interlaminar shear strength and flexural strength were measured and compared with un-soaked samples. A 3D solid FEA model was developed to simulate the moisture diffusion, hygrothermal expansion and the coupling of hygrothermal stress and bending in macro-scale (i.e. laminate), while a 2D FEA model was developed to simulate the moisture diffusion and stress/strain transfer at the micro-scale.

5.1 Experimental setup

The specimens for the bending test (presented in Chapter 4) and diffusion test were manufactured in different batches, therefore the laminate thickness showed a minor fluctuation. The specimens were divided into two sets after the moisture saturation in the diffusion test: one was tested in bending which is presented in this chapter; the other was kept for the fatigue and creep test which is presented in Chapter 6.

5.1.1 *Diffusion test*

Three chambers were used in the test, containing fresh water (tap water), sea water and sea water at 70 bar hydrostatic pressure (equivalent to a water depth of 700 m) respectively. In order to accelerate the water absorption, the chambers were placed in an oven at a constant temperature 50°C. This temperature is mainly for accelerating diffusion procedure, and the moisture diffusivity at the normal temperature can be calculated by the Arrhenius' relation (Gibson, 1994). Temperature from 36°C (Kotsikos, Evans et al., 2000) to 80°C (Ryan, Adams et al., 2009) was used for this acceleration. The ASTM standard (D5229/D5229M, 2004) provides a guideline of the maximum temperature for different epoxy systems, so that a moderate temperature (50°C) was chosen in order to compare with the open literatures.

Figure 5.1 shows the hydrostatic chamber which was used in the diffusion test. The hydrostatic chamber was made of stainless steel providing approximately 20 litres of cylindrical space, and the pressure was applied through the hose by a hydraulic pump. The specimens were constrained and separated by nylon breathe cloth before being immersed. The sea water was collected from the Atlantic Ocean near Plymouth harbour, and the water was refreshed every month during the tests. The salinity of the sea water varied by seasons and depth, and the values were in the range of 3.4%-3.5% in weight (provided by Marine Institute, Plymouth University). The salinity was similar to that used in literature, so that the chemical composition can be referred to the ASTM standard (D1141-98, 2008).

Figure 5.1 The hydrostatic chamber used in the diffusion test

The composite laminates were immersed into the three chambers for diffusion tests. The specimens were taken out of the chambers at intervals to measure the moisture content and hygrothermal expansion following the ASTM standard (D5229/D5229M, 2004) which suggests no more than five minutes for the measurement of each specimen and no more than thirty minutes for each group. Before being immersed into the water, all of the specimens were oven-dried at 70°C for 48 hours. The moisture content was measured by an electronic scale with 0.01 mg average precision, while the dimensions were measured by a vernier calliper with 0.01 mm nominal accuracy.

Since the carbon fibre is assumed not to absorb moisture, the composite's moisture diffusivity is mainly dependent on the polymer. A previous study (Gigliotti, Jacquemin et al., 2007) provides the reference parameters of the equation (2-13) (also known as Arrhenius relation) for 977-2 epoxy: $D_0 = 2\times10^{-9} m^2 s^{-1}$, $E_a / R = 2910 K^{-1}$. Therefore, the moisture diffusivity of HTS/977-2 can be roughly estimated of the order of $3\times10^{-13} m^2/s$ in the present case (50°C). According to ASTM standard (D5229/D5229M, 2004), the reference time period for each measurement is established by $0.02h^2/D$, giving an approximate interval of 5 days.

At least five specimens of each lay-up were measured, and the mean values were calculated. **Figure 5.2** shows the water absorption in UD, UT, CP and AP laminates vs. square root (time). It can be seen that, after 3 months accelerated water absorption, all of the specimens had become saturated. Within each lay-up, the saturated moisture content and the moisture diffusivity do not show noticeable differences between the sea water and tap water medium.

The time-dependent moisture diffusion curves of the four laminates in **Figure 5.2** present linear stage of the plot of moisture contents (M) to the square root of time ($\sqrt{t}$) at the beginning of diffusion, so that the apparent diffusivity can be calculated by equation (2-12). Like the orthotropic elastic properties in laminated composites, the previous study had reported that diffusion properties are also shown to be orthotropic. **Figure 5.3** shows an illustration of the longitudinal and transverse moisture diffusivities at both micro and macro scales.

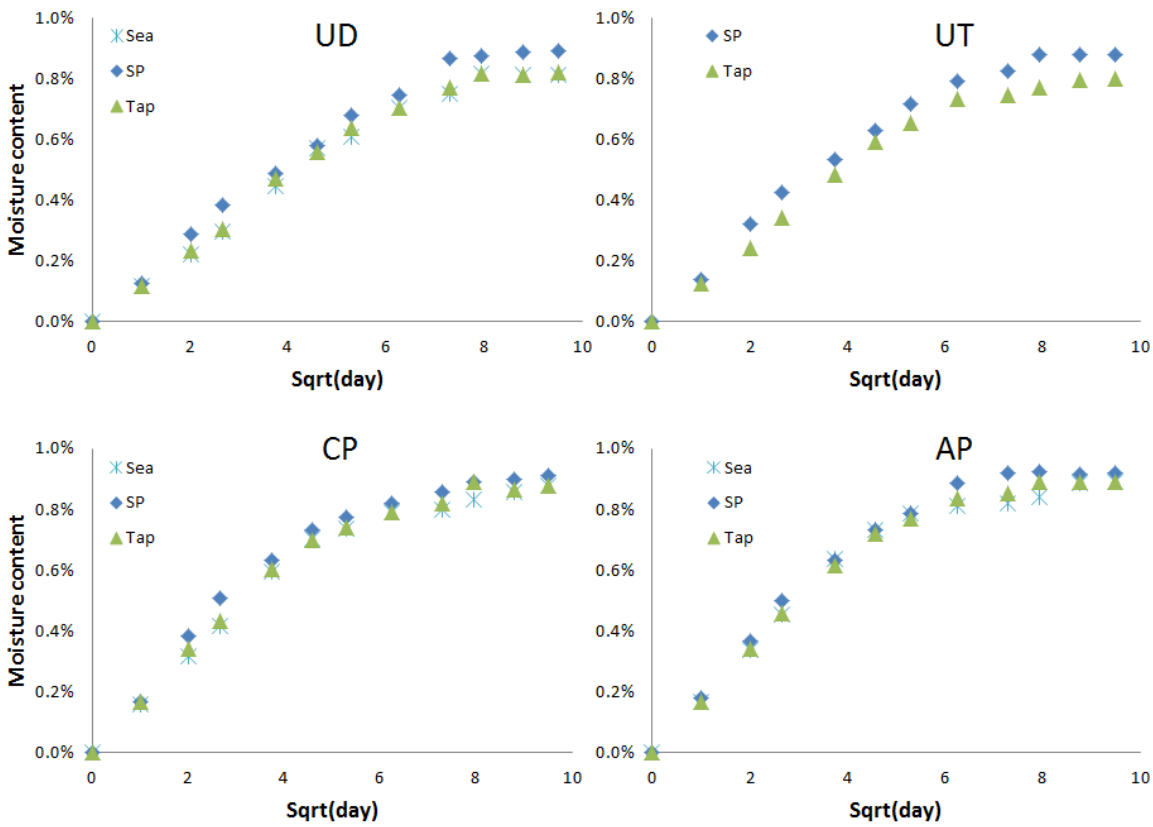

Figure 5.2 Moisture diffusion in UD/UT/CP/AP laminates immersed at 50°C sea water ('Sea'), tap water ('Tap') and sea water with 70bar hydrostatic pressure ('SP')

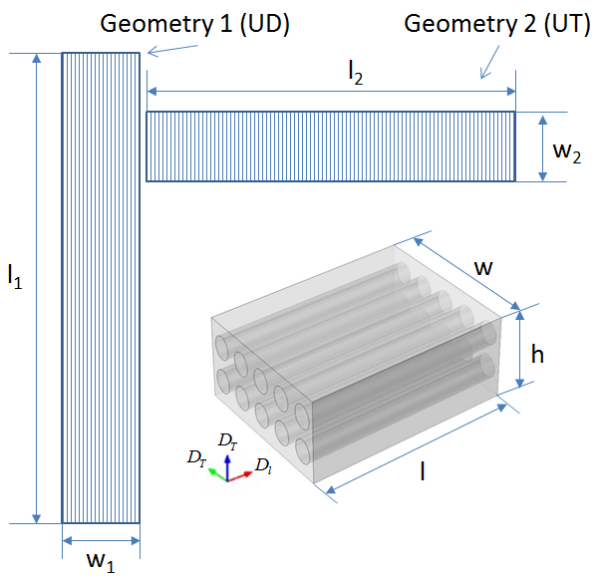

Figure 5.3 Orthotropic moisture diffusivity assumption and the two geometries for the calculation of longitudinal and transverse diffusivities

If the specimen dimension is finite (as in the present case), the longitudinal D_L and transverse D_T moisture diffusivities should be used to compensate the edge correction (Pomies, Carlsson et al., 1995), which has been discussed in Chapter 2 as equations from (2-14) to (2-19). Therefore, only UD and UT data were used to extract D_T and D_L for simplicity. The results are shown in **Table 5-1**, giving the saturated moisture content of each group of specimens and their apparent moisture diffusivities. It is shown that the moisture diffusion in fibre orientation (D_L) is about 60% faster than transverse direction (D_T).

Table 5-1 Accelerated diffusion test results (50°C)

	Immersion*	M_{max} (%)	Height (mm)	Length (mm)	Width (mm)	D^{app} ($10^{-13}m^2/s$)	D_T ($10^{-13}m^2/s$)	D_L ($10^{-13}m^2/s$)
UD	Sea	0.81	2.06	204	15	2.6	–	–
$[0]_{16}$	SP	0.89	2.06	204	15	2.6	2	3.6
	Tap	0.82	2.06	204	15	2.8	2.2	3.6
UT	SP	0.88	2.06	15	122	2.8	2	3.6
$[90]_{16}$	Tap	0.82	2.06	15	122	3	2.2	3.6
CP	Sea	0.89	1.95	286	15	2.8	–	–
$[90/0]_{4s}$	SP	0.92	1.95	286	15	3	–	–
	Tap	0.89	1.95	286	15	3	–	–
AP	Sea	0.89	1.95	100	20	2.8	–	–
$[\pm45]_{4s}$	SP	0.93	1.95	100	20	2.9	–	–
	Tap	0.89	1.95	100	20	2.9	–	–

*** 'Sea': sea water immersion; 'Tap': tap water immersion; 'SP': sea water immersion with 70 bar hydrostatic pressure**

Because the longitudinal elastic modulus of carbon fibre is much higher than epoxy, the longitudinal hygrothermal expansion of the UD laminate is expected to be very small. Indeed, the measured values of expansion in the CP and AP laminates were also smaller than the precision of vernier calliper, and hence only the specimen with a very long width w (UT laminate) could provide measureable expansion. The increase of hygrothermal expansion as a function of moisture content is shown in **Figure 5.4**. The hygrothermal expansion of the 'SP specimen' showed a smaller value compared with 'Tap specimen'.

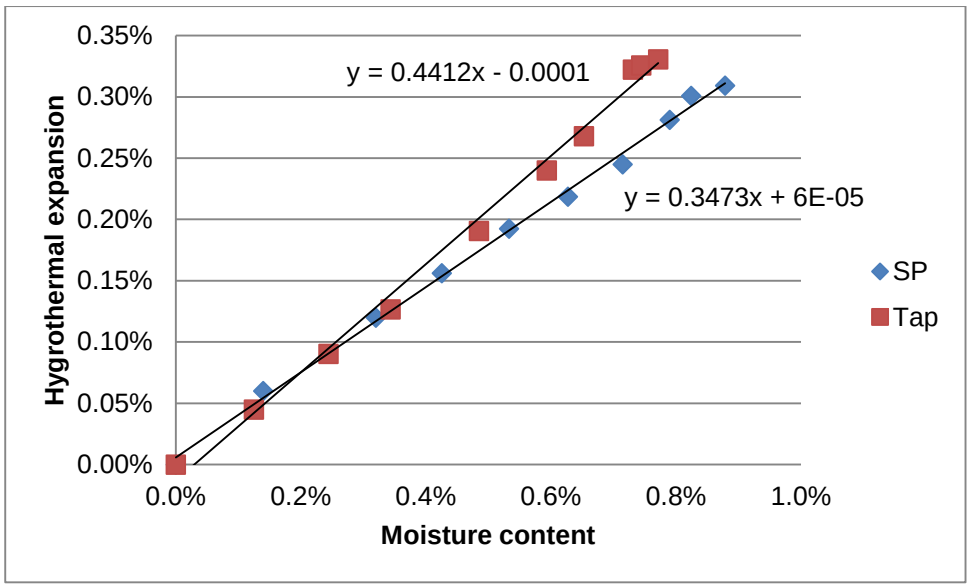

Figure 5.4 Hygrothermal expansion of UT $[90]_{16}$ laminate varying with moisture content

5.1.2 *Bending test*

The moisture content in composite laminates was saturated after 3 months of water immersion. In order to investigate the environmental effects on the mechanical properties in the time domain, bending tests were carried out after 1 month and 3 months of water immersion. The experiments were conducted using 3-point bending according to the ISO standards (ISO12130, 1998; ISO14125, 1998). Typical loading force and displacement curves for the UD/UT/CP laminates in both dry and 3-M SP conditions are plotted in **Figure 5.5**. The zigzag aspect can be seen in the curves of UD and CP laminates in dry condition; however the specimens showed a sudden break after immersion. The AP laminate was not considered because it showed significant nonlinear behaviour in the flexural test which could not represent the flexural modulus/strength.

At least five samples in each group were tested, and the apparent interlaminar shear strength τ_{xz}^{app} (shown in **Figure 5.6**), apparent flexural strength σ_x^{app} and apparent flexural modulus E_f^{app} (shown in **Table 5-2**) were calculated. The material properties at 0-Month (dry condition) were measured prior to immersion so that they are independent of medium. So are the theoretical calculations.

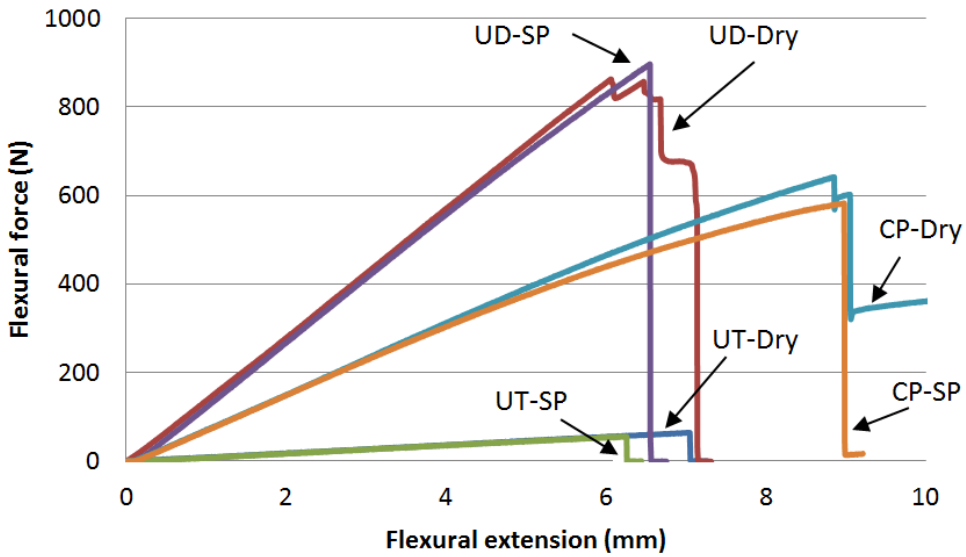

Figure 5.5 Typical flexural force-extension curves of UD/UT/CP laminates

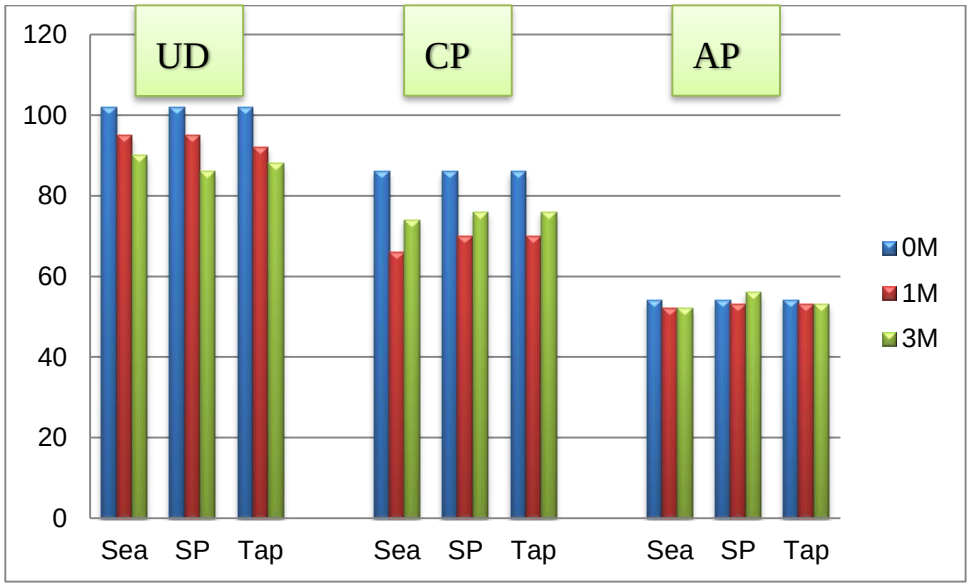

Figure 5.6 Measured ILSS (MPa) of UD/CP/AP laminates before (0M) and after moisture diffusion. 0-M: dry condition; 1-M: 1-month immersion; 3-M: 3-month immersion.

It should be noted that the deflections of the UD/UT laminates were close to the 'large-deflection criterion' (10%) and the deflection of CP laminate had exceeded the criterion, the flexural strength was then calculated by the 'large-deflection correction'. The

gradual degradation of interlaminar shear strength showed a similar trend with the work of (Ryan, Adams et al., 2009) whose specimens contained the same epoxy system.

Table 5-2 Bending test results and their Standard Deviations (SDs)

	Immersion	$\sigma_x^{app}(MPa)$ [b]		$E_f^{app}(GPa)$		
		0-M[a]	3-M	CLT[c]	0-M	3-M
UD	Sea	1598±56	1696±41	139	120±3	121±4
	SP		1780±122			121±4
	Tap		1688±137			122±2
UT	SP	117±5	99±6	8.8	8.4±0.3	9.1±0.1
	Tap		102±4			9.0±0.2
CP	Sea	1416±53	1441±40	62	56±2.2	58±0.4
	SP		1398±88			58±1.6
	Tap		1400±74			57±0.8

(a) 0-M: dry condition; 1-M: 1-month immersion; 3-M: 3-month immersion.

(b) The values of UD and CP laminates were calculated with the 'large-deflection correction'.

(c) Calculated by CLT with the elastic properties shown in Table 3-1.

5.2 Multi-scale FEA modelling

Two scales of FEA model were built to study the moisture diffusion within CFRP composite laminates and its coupling with external mechanical loading. At the micro scale, a 2D model was constructed according to the real distribution of fibres within one single ply to investigate the moisture diffusion behaviour. At the macro scale, a 3D model was developed based on the actual laminate lay-up to investigate the impact of moisture diffusion and external load on the interlaminar shear stresses. Both the two FEA models were solved by COMSOL Multiphysics.

5.2.1 *Definition of micro-model*

The aim of the micro-model is to investigate the moisture diffusion at micro-scale and the coupling effect between hygrothermal expansion and bending. This model mainly

focuses on the effects of moisture diffusion on the transverse properties of composite, particularly the role of the interphase between fibre and matrix.

The geometry of the micro scale model was taken directly from the optical microscope image to capture the real distribution of fibres within a single ply, but assuming that the fibres were perfectly circular, as shown in **Figure 5.7**. The FEA model contained two components: (a) species transport was used to simulate the moisture diffusion within the matrix and interphase, therefore the surface ply (ply 16) was extracted for the FEA geometry; (b) structural mechanics was employed to calculate the stress/strain transfer among the three phases, as well as the coupling between hygrothermal expansion and external loading.

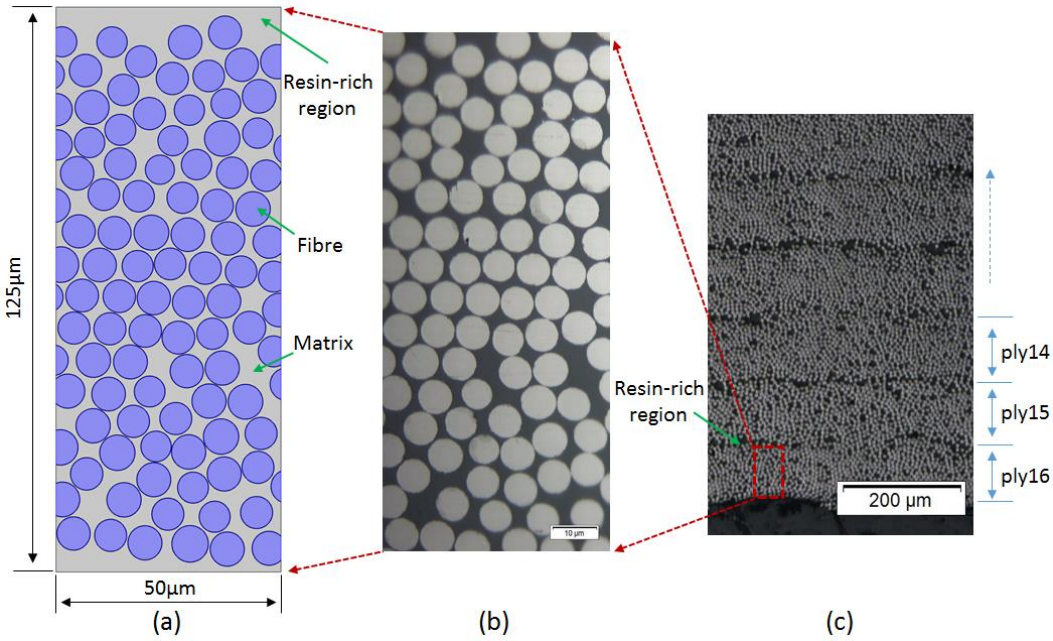

Figure 5.7 Optical microscopic image of a UT specimen and schematics of FEA model

It can be seen from **Figure 5.7**(c) that there was a resin-rich volume between two adjacent layers; therefore it is reasonable to extract a single ply for the modelling by applying the continuous boundary condition. For the species transport component, the lower surface could be defined as being at the saturated moisture concentration given by:

$$c_{\max} = \frac{\rho_m M_\infty^m}{18 \times 10^{-3}} \qquad (5\text{-}1)$$

where ρ_m is the density of matrix, and $18\times10^{-3}\ kg/mol$ is the molar mass of water. Substituting the matrix saturation (2.7%) into the equation, the boundary moisture concentration can be calculated as 1965 mol/m^3. This value is necessary for FEA boundary condition.

It can also be seen from **Figure 5.7**(a) that the fibres are very close to each other so that the stress concentration due to the barrier layer effect could be induced during moisture diffusion. It is well known that the moisture diffusivity of the interphase should be different from that of the matrix. Therefore, a sensitivity study of the interphase diffusivity was carried out to investigate this barrier effect.

Due to the bending moment applied to the laminate, the bottom surface of the laminate was under maximum tension, and the tensile stress at the 15th and 16th plies near the bottom was calculated to be 102 MPa and 117 MPa respectively. For the structural mechanics component, a distributed tensile stress was applied on the left side of the model while the right side was defined as symmetric plane. **Figure 5.8** shows the schematics of the boundary conditions for both species transport component and structural mechanics component.

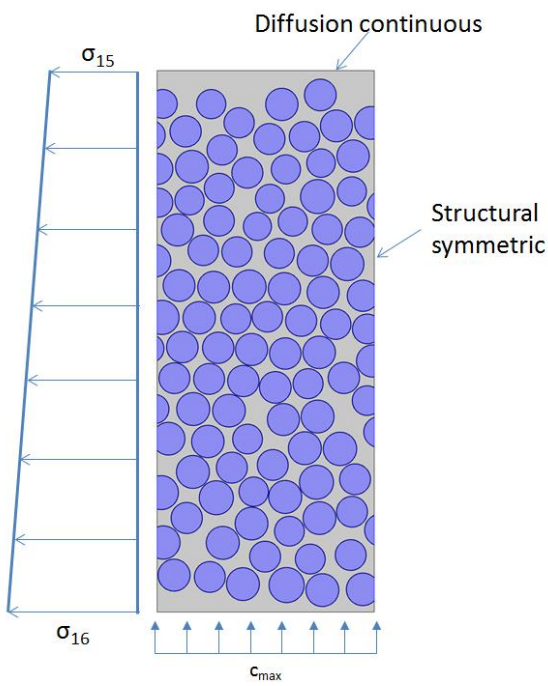

Figure 5.8 The boundary conditions for the multiphysics micro model: species transport and structural mechanics

The mechanical properties of the fibre and matrix were obtained from the product technical datasheet (Cytec, 2012), and the diffusion properties of the matrix was taken as the measured value in **Table 5-1**. **Table 5-3** gives the material properties used for the micro-model. The properties of the interphase shown in **Table 5-3** were for the baseline case, and these values were used for the parametric study.

Table 5-3 Mechanical and chemical properties of carbon fibre and epoxy

	E_1 (GPa)	$E_2 = E_3$ (GPa)	$\nu_{12} = \nu_{13}$	ν_{23}	D $(10^{-13} m^2/s)$	M_∞
Fibre	238	24	0.2	0.4	-	-
Matrix	3.5	3.5	0.34	0.34	6.0	2.7%
Interphase	2.6	2.6	0.34	0.34	6.0	2.7%

An area with dimensions of $125\mu m \times 50\mu m$ was considered with 125 μm being the thickness of each ply. There were three phases in the model including fibres, interphase and matrix. The diameter of the fibres varied with an average value of 7µm (Toho-Tenax-HTS), while the thickness of the interphase was 0.1µm as the baseline case, which is equivalent to approximately 4% of the weight of fibres. The calculated fibre volume fraction was 58% which was the same as the experimental value.

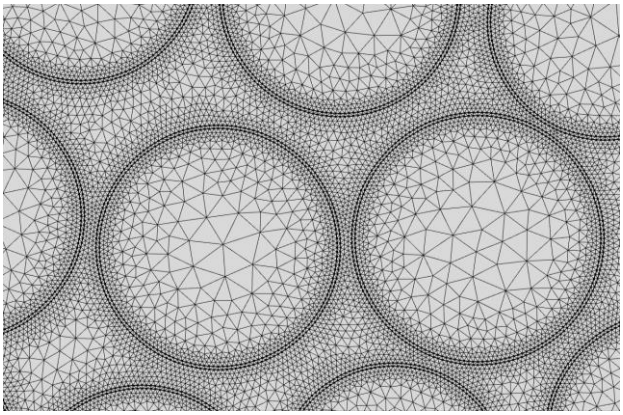

Figure 5.9 A local view of the mesh, showing the three phases in the micro model

The model was solved using COMSOL Multiphysics (COMSOL, 2013). The automatic meshing method of COMSOL was employed to generate the mesh. Approximately 250k triangular elements were created. **Figure 5.9** shows a magnified view of the mesh

which shows detailed meshes of the three phases within the composite. The interphase and the adjacent regions were refined to capture the stress concentration effect and the fibres barrier effect.

5.2.2 *Definition of macro-model*

It can be seen from **Table 5-1** that the moisture diffusivity in the fibre direction is different from that in the transverse direction, so are the mechanical properties (elastic modulus, shear modulus and Poisson's ratio). Based on this orthotropic assumption, the macro-model was built by using a rotated coordinate system to define the material properties of the off-axis plies which has been discussed in Chapter 4. The geometry and lay-up sequence of each group of laminates has been defined in **Table 5-1**.

In the experiments, the specimen was immersed into water, so all of the surfaces could be defined as being at the saturated moisture concentration. The saturated moisture concentration can be calculated by

$$c_{\max} = \frac{V\rho_c M_{\max}}{18\times10^{-3}V} = \frac{\rho_c M_{\max}}{18\times10^{-3}} \qquad (5\text{-}2)$$

where ρ_c is the density of composite laminate, 18×10^{-3} is the molar mass of water with the unit kg/mol.

Substituting the saturated content $M_{\max} = 0.9\%$ from Table 5-1, and the density of CFRP composite $\rho_c = 1.6\times10^3 kg/m^3$, the saturated moisture concentration can be calculated as $c_{\max} = 800 mol/m^3$.

The FEA solution gives the distribution of moisture concentration in 3D. Integration should be carried out to obtain the moisture content, and then hygrothermal expansion can be calculated by multiplying the coefficient of hygrothermal expansion with moisture content. Considering the inverse form of equation (5-2) in an infinite element, the expansion term can be expressed as

$$\varepsilon^{CHE} = \frac{18\times10^{-3}cV}{\rho_c V}\beta = \frac{18\times10^{-3}c\beta}{\rho_c} \qquad (5\text{-}3)$$

Equation (5-3) can be used to specify the coupling relation in the FEA model since the expansion term relates the moisture content (c) to mechanical expansion (ε^{CHE}). It should be noted that both the moisture content and the expansion are variable in time and space domains.

Table 5-4 Material properties for moisture diffusion modelling

Longitudinal modulus E_1(GPa)	139
Transverse modulus $E_2 = E_3$(GPa)	8.8
In-plane shear modulus $G_{12} = G_{13}$(GPa)	4.7
Transverse shear modulus G_{23}(GPa)	3.0
In-plane Poisson's ratio $\nu_{12} = \nu_{13}$	0.26
Transverse Poisson's ratio ν_{23}	0.48
Longitudinal diffusivity $D_1(m^2/s)$	3.6×10^{-13}
Transverse diffusivity $D_2 = D_3(m^2/s)$	2.2×10^{-13}
Longitudinal CHE β_1	0
Transverse CHE $\beta_2 = \beta_3$	0.49

The elastic properties are then introduced to calculate the hygrothermal stresses. The mechanical properties and diffusion properties used in the macro-model are shown in **Table 5-4**.

Due to the development of hygrothermal stresses after water absorption, the flexural stresses re-distribute when the composite laminates are subjected to bending. Therefore, the hygrothermal expansion was introduced as the initial strain in the mechanical model, and the diffusion/expansion were solved simultaneously. Since the diffusion (as well as the expansion) is time dependent, the mechanical model was solved in the time domain, although the applied load was static.

The geometries used in the FEA models were the same as the test condition, and the maximum static loads evaluated in dry condition were applied in the mechanical model.

The boundary condition used in the macro-model was the same as the one in Chapter 4. **Table 5-5** shows the dimensions and loading forces for different groups of coupons.

Once the FEA models were set up, the moisture distribution and the induced hygrothermal expansion inside laminate were investigated. The process of diffusion is very slow so that the moisture distribution varies in spatial and time domains. Additionally, the computing time (or DOFs) increased exponentially when the coupling term was introduced. Therefore, only 90 days of immersion were investigated. The macro-model was solved by COMSOL Multiphysics (COMSOL, 2013).

Table 5-5 Geometries and boundary conditions in different groups of coupons

	$UD[0]_{16}$		$CP[90/0]_{4s}$		$AP[\pm45]_{4s}$
	Long beam	Short beam	Long beam	Short beam	Short beam
Length(mm)	100	20	100	20	20
Width(mm)	15	10	15	10	10
Height(mm)	2.08	2.08	1.92	1.92	1.92
Span(mm)	80	10	79	10	10
Force(N)	853	2933	574	2223	1395
$r_1=r_2$ (mm)	2				
c_{max} (mol/m^3)	800				

5.3 Failure mechanisms

5.3.1 *Moisture diffusion*

After 3 months accelerated water absorption, all of the specimens had become saturated. **Table 5-1** has given the maximum moisture content of each group of specimens and their apparent moisture diffusivities. It is shown that the moisture diffusion along the fibre orientation (D_L) is about 60% faster than transverse direction (D_T), and these values were regardless of the water medium. The higher pressure induces a larger saturation in all four lay-ups. In the present case of 70 bar hydrostatic pressure, the saturation is 5% larger than that at ambient pressure. The diffusion slope $(M_2 - M_1)/\left(\sqrt{t_2} - \sqrt{t_1}\right)$ in the high pressure case was also larger. However, by substituting the diffusion slope and saturation into equation (2-12), it is found that the

moisture diffusivity in the high pressure environment was the same as the normal pressure, as shown in **Table 5-1**.

Because the fibres do not absorb the moisture, the saturation is mainly dependent on the matrix and the fibre volume fraction. It has been known that the saturation and diffusivity are varied for different polymer systems. The typical saturation of polymer is epoxy 1.5% (Cytec, 2012), vinyl ester 1.5% (Derakane, 2011), polyester 1.5% (Davallo, Pasdar et al., 2010), polyimide 4.4% (Cytec, 2012) and PEEK 0.5% (Victrex, 2012). The diffusion test results of (Ryan, Adams et al., 2009) gave a similar nominal saturation to the present work.

The CP/AP laminates were cut from one composite plate, while the UD/UT laminates were cut from another plate. Therefore, the CP/AP laminates show similar results, as well as the UD/UT laminates. Although the longitudinal and transverse diffusivities show apparently different values, as shown in **Table 5-1**, the macro-model presented a smooth distribution of moisture concentration throughout the whole laminate with both complex lay-up (such as AP and CP laminates) and simple lay-up (such as UD and UT laminates). This is because the moisture diffusion is time dependent and the procedure is very slow.

Figure 5.10 shows the FEA result for moisture distribution within an AP short beam laminate in slice-view after one month of immersion indicating different depths of water penetration in the longitudinal and transverse directions. It can be seen that the moisture concentration distributed smoothly in the slice-section of xz-plane and yz-plane. Specifically, the moisture distribution through-thickness was extracted to analyse the effect of the longitudinal and transverse diffusivities, as shown in **Figure 5.11**. **Figure 5.10** shows the moisture distribution on the mid-line of the AP laminate in the time domain, which indicates a smooth distribution through-thickness regardless of the ply-orientation at different times. It can also be seen that saturation occurs after 90 days of immersion.

As discussed in section 5.2.1, the barrier layer effect develops due to the narrow gap between fibres. The diffusion rate extracted from the micro-model was significantly lower than that observed in the experiment if the diffusivity of the interphase (D_{in}) was assumed to be the same as for the matrix in the FEA model. A parametric study was

carried out to investigate the sensitivity of the interphase diffusivity. **Figure 5.12** shows the comparison of the fit of the measurement to Fick's law and the predictions by the micro model for three levels of D_{in} : the same, five times, or ten times that of the matrix. The results suggested that the FEA prediction matched the experiment well when the D_{in} value was ten times that for the matrix. This is in agreement with the previous reports that the diffusivity of the interphase is much higher than that of the matrix.

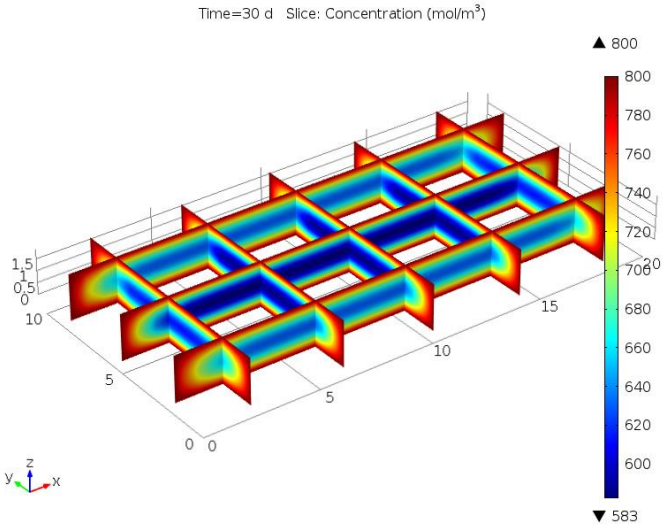

Figure 5.10 Moisture distribution according to FEA in AP short beam laminate after 30 days' water immersion. The slice plot shows a smooth distribution of moisture concentration regardless of the ply orientations.

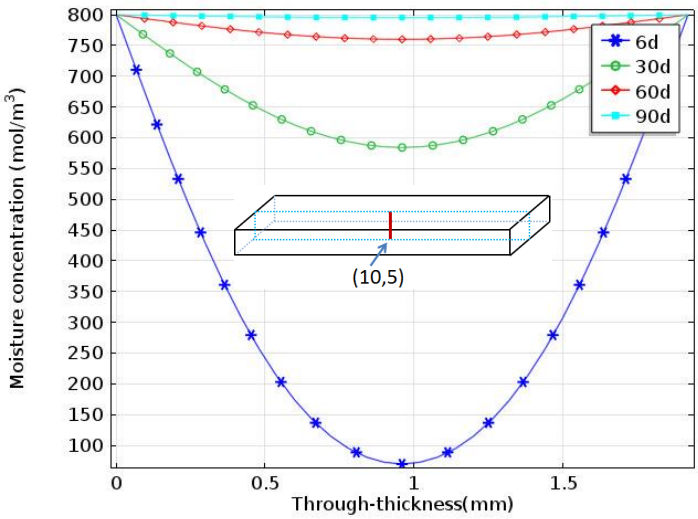

Figure 5.11 FEA moisture distribution of AP short beam laminate along the mid-line after 6/30/60/90 days' water immersion respectively. The moisture diffused smoothly inside the laminate, and converged to saturation.

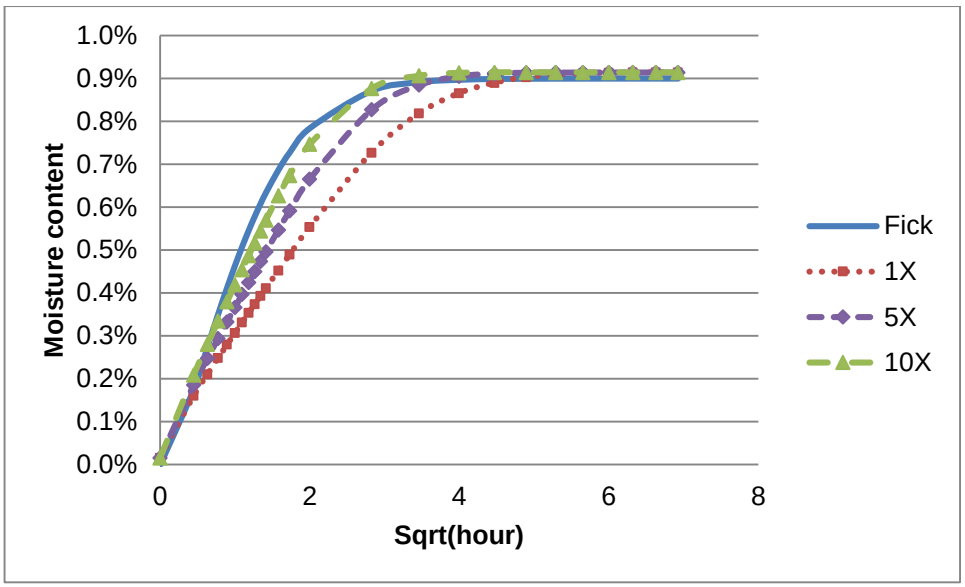

Figure 5.12 Comparison of mass gain: Fick's fit and FEA computation with various values of D_{in}

A previous study of the carbon fibres/epoxides reaction (Waltersson, 1985) has shown that the mechanical modulus of the interphase is a fraction lower than the matrix, which may lead to a higher capability to attract water molecules. This is one of the possible reasons that the moisture diffusivity of the interphase presents a higher value.

According to equation (2-12), the time to saturation is exponential to the thickness of the specimen. The moisture can penetrate one ply thickness with relatively low concentration within a short time of immersion. Indeed, the moisture concentration reached saturation after 24 hours in the micro-model, compared to 90 days for the whole (16 plies) experimental laminate. **Figure 5.13** shows the moisture distribution after one hour of immersion (D_{in} was 10 times that of the matrix). A magnified view of the interphase shows a smooth moisture distribution which indicates the moisture distribution was not affected by the difference of diffusivities of the two phases of resin (the bulk and interphase).

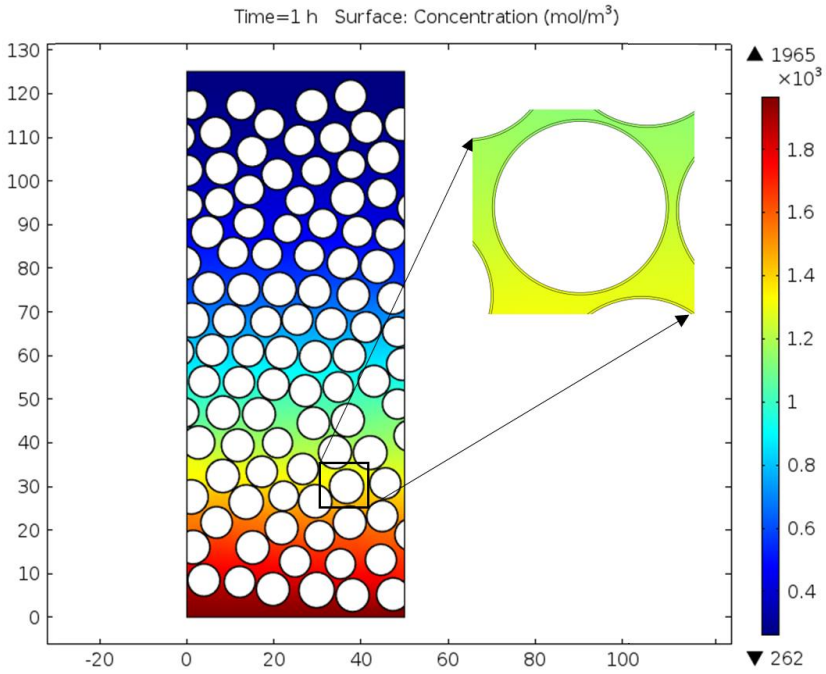

Figure 5.13 Moisture distribution in the micro model after one hour immersion (dimension unit: μm)

5.3.2 *Hygrothermal expansion*

The saturated hygrothermal expansion measured in the UT laminate showed a value of about 0.4% in tap water immersion (normalized to $M_{\max} = 0.9\%$), and a lower value (0.32%) in sea water with 70 bar hydrostatic pressure (SP), as shown in **Figure 5.4**. One possible reason is that the hydrostatic pressure reduced the hygrothermal expansion. However, no measureable expansion was observed in UD/CP/AP laminates.

Substituting the saturated concentration, CHE and composite density in equation (5-3), a reference transverse strain in an infinite unidirectional plate can be estimated to be

$$\varepsilon_T = \frac{18\times10^{-3} c_{\max}\beta_3}{\rho_c} = \frac{18\times10^{-3}\times800\times0.49}{1.6\times10^3} = 0.44\%$$

In order to compare with this reference value, the hygrothermal strains of three types of laminates were extracted from the macro-model. Since the specimen was under free expansion induced by hygrothermal effects, the apparent normal strains can be extracted from the average normal displacements on the surfaces,

$$\begin{cases} \varepsilon_x = u_x \left(\frac{l}{2}\right)^{-1} \\ \varepsilon_y = u_y \left(\frac{w}{2}\right)^{-1} \\ \varepsilon_z = u_z \left(\frac{h}{2}\right)^{-1} \end{cases} \tag{5-4}$$

where ε_x, ε_y and ε_z are the apparent normal strains; u_x, u_y and u_z are the average normal displacements of yz, xz and xy surfaces;. $\frac{l}{2}$, $\frac{w}{2}$ and $\frac{h}{2}$ are the half-length, half-width and half-height of specimen respectively.

Figure 5.14 shows the expansion curves of UD/UT/CP/AP short beam laminates as a function of square root of time from the macro-model. It can be seen that the curves of UD/UT laminates are overlapped, so are the CP/AP laminates. It is noted that the maximum hygrothermal expansion of UD/UT laminates is in line with the reference value (0.44%) but CP/AP laminates have significantly higher values.

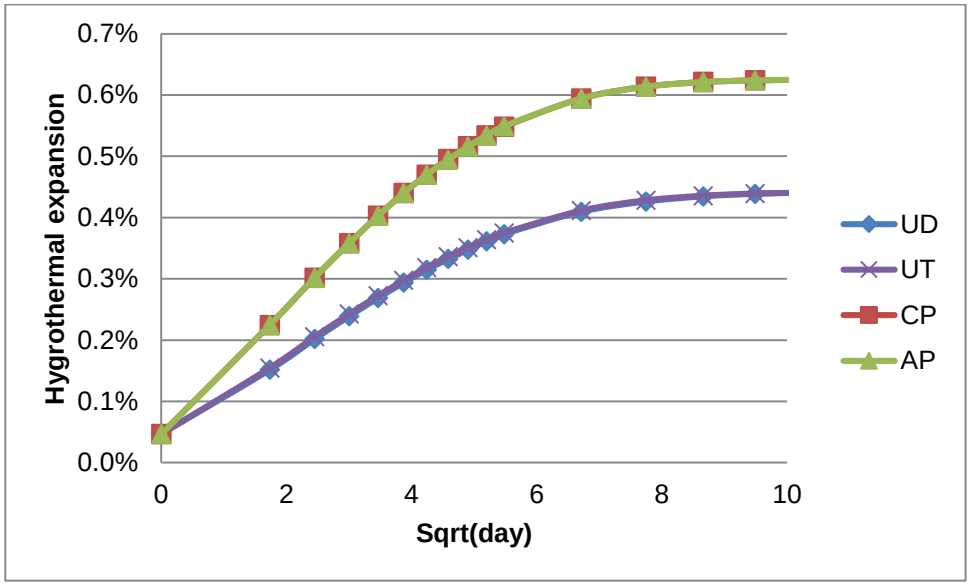

Figure 5.14 FEA out-of-plane hygrothermal expansion of UD/UT/CP/AP short beam laminates

The CLT calculation of laminate CHE can explain this increase of expansion in CP/AP laminates. According to the CLT, the apparent CHE of CP laminate can be calculated

giving $\beta_x = \beta_y = 0.04, \beta_z = 0.70$. The predicted out-of-plane CHE value (β_z) is in line with the maximum CHE extracted from FEA simulations shown in **Figure 5.14**.

In the macro-model, the concentration on all surfaces was constant during the entire diffusion process. The hygrothermal stresses were induced in 'free edge' region at the very beginning, and then the stresses propagated inside the specimen following the moisture diffusion. **Figure 5.15** shows the through-thickness distribution of interlaminar shear stress (τ_{13}) within the AP short beam laminate after one month's diffusion. It can be seen that the interlaminar shear stress induced by hygrothermal expansion could be as high as the 20% of the interlaminar shear strength. This high value of stress might induce the stress re-distribution when the laminate is subjected to mechanical loading. However, this induced interlaminar shear stress only appeared at the interfaces of plies and decayed rapidly inside the laminate and finally converged to zero in the centre. The coupling of the hygrothermal stress with bending will be discussed in the next section.

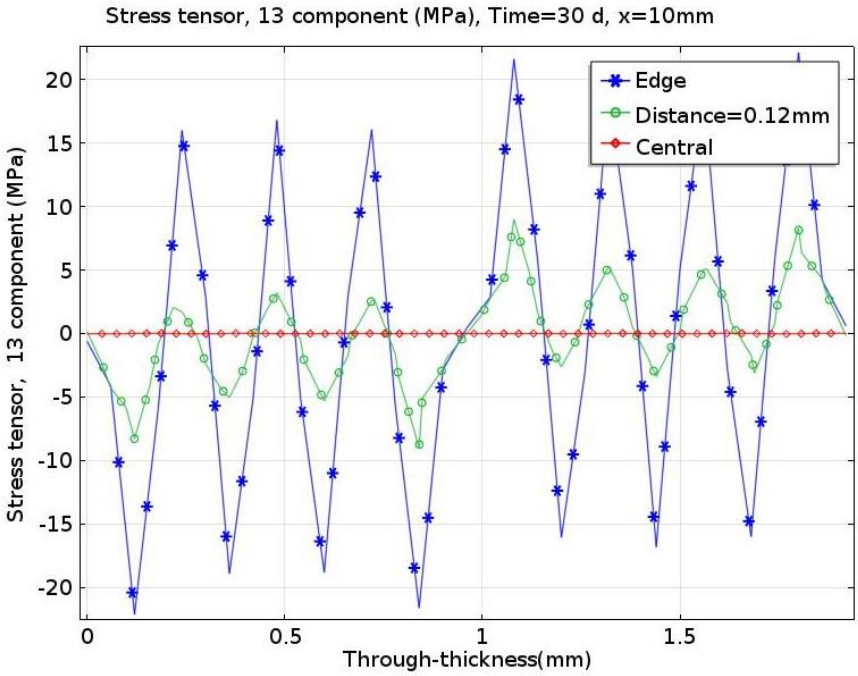

Figure 5.15 FEA result for interlaminar shear stress τ_{13} induced by hygrothermal effect in AP short beam laminate after one month's diffusion

Such a strong 'free edge' effect can also be found in the CP laminate. **Figure 5.16** shows the surface plot of interlaminar shear stress τ_{13} in the CP short beam laminate. Compared with the interlaminar shear strength measured in dry condition, this induced

stress τ_{13} was so high that it could not be neglected in the context of fracture or fatigue initiation. As will be discussed in the next section, this induced shear stress τ_{13} would reduce the measured interlaminar shear strength significantly.

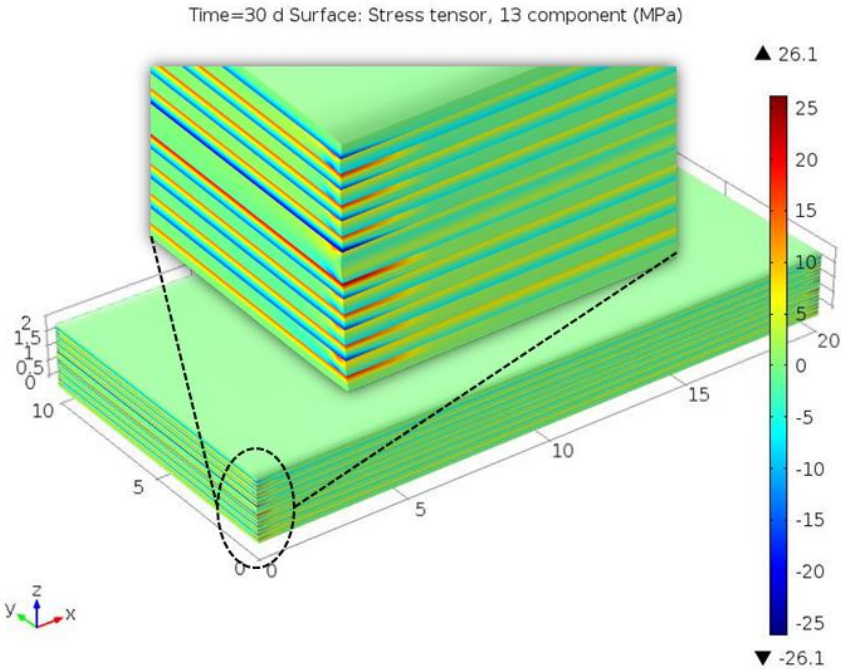

Figure 5.16 FEA result for interlaminar shear stress τ_{13} induced by hygrothermal expansion in CP short beam laminate from macro-model after one month's water absorption

5.3.3 *Interaction between bending and diffusion*

In the previous section, the 'free edge' effect induced by hygrothermal expansion was observed in the macro-model. It showed the induced interlaminar shear stress τ_{13} is of the order of 20 MPa in CP/AP laminate. Transverse normal stresses are also as high as: 30 MPa (σ_2 or σ_3) in CP/AP laminates and 10 MPa (σ_2 or σ_3) in UD/UT laminates. And this edge effect decayed rapidly inside the laminate within a couple of ply-thickness.

The FEA model introduced this hygrothermal expansion as the initial strain. When the bending condition was applied, this effect would be coupled with the bending stress leading to stress re-distribution. Due to the small deformation in FEA model, the diffusion and expansion could be considered as a one-way coupling problem: the effect

of structural deformation on moisture diffusion was not considered in FEA model. Therefore, the time dependent diffusion was the same as the case without bending. On the other hand, the hygrothermal stresses shown in the case of 'free expansion' were coupled with the bending stresses. **Figure 5.17** shows the time dependent distribution of transverse normal stress in CP short beam laminate. With the increase of moisture content in laminate, the hygrothermal stress showed an increasing trend with the concentration.

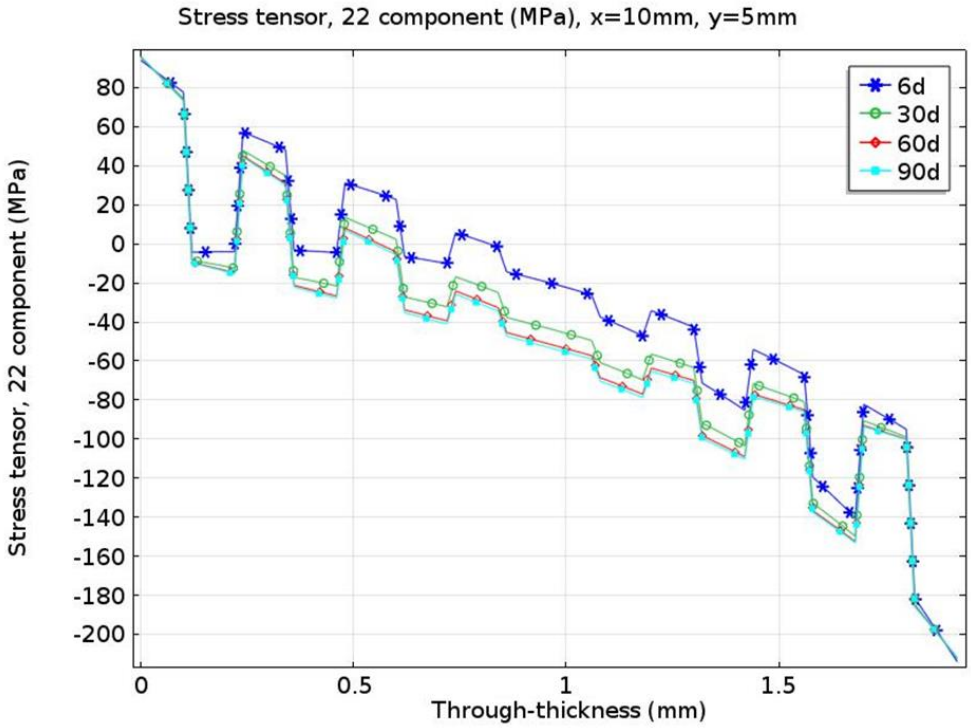

Figure 5.17 The through-thickness distribution of σ_2 at central point (x=10mm, y=5mm) of CP short beam laminate in the time domain from macro-model. The transverse stress shifts into compression.

Figure 5.18 shows the through-thickness distribution of interlaminar shear stress (τ_{13}) of the AP short beam laminate. Compared with the dry condition, the coupling had no effect on the maximum value of τ_{13}. However, the stress was asymmetric about the mid-plane, and the positions of peaks shifted to the bottom side.

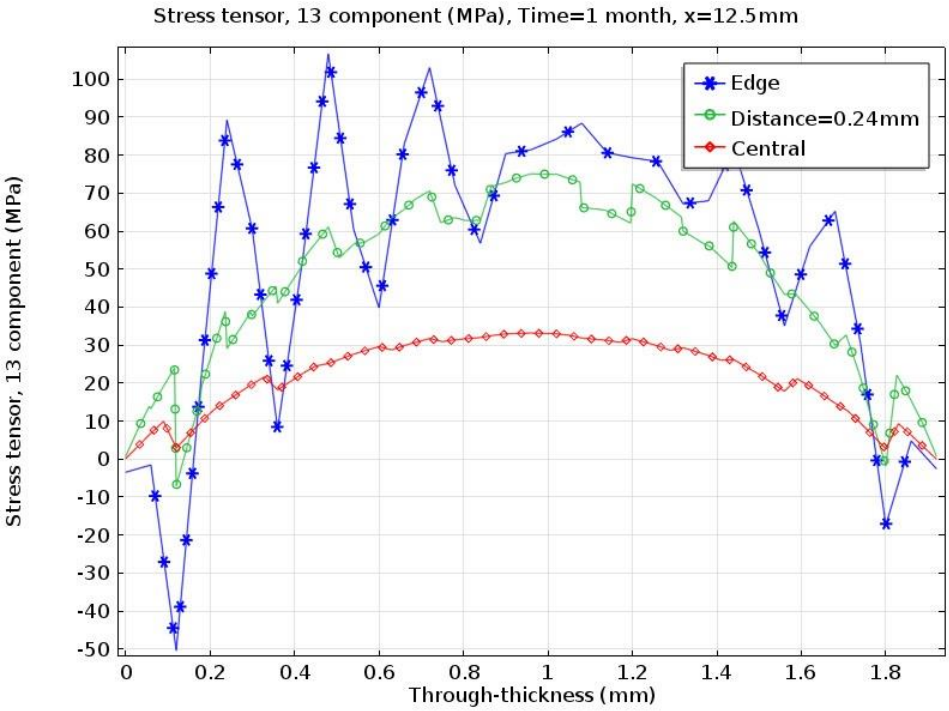

Figure 5.18 FEA through-thickness distribution of τ_{13} after one month's diffusion in AP short beam laminate from macro-model

Figure 5.19 gives a typical failure image of AP laminate from a bending test. The sample was immersed for one month in tap water. Compared with the dry condition, more cracks were found on the bottom side and the cracks propagated a longer distance inside the laminate. However, the interlaminar shear strength of the AP laminate showed a small variation due to the water immersion.

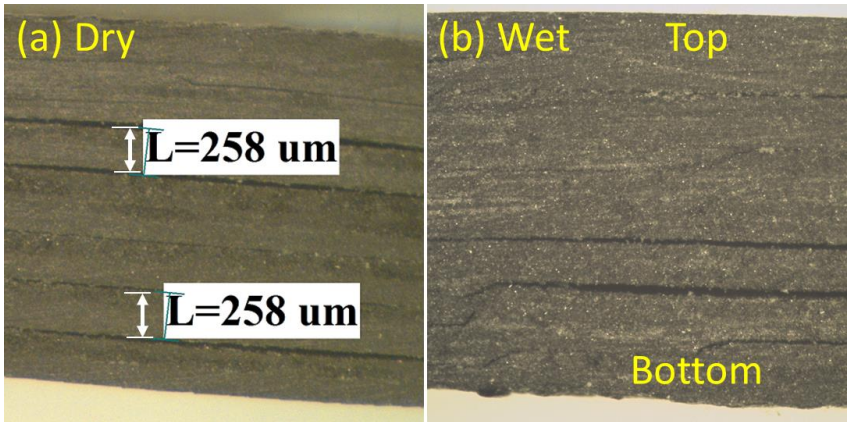

Figure 5.19 Typical failure image of AP short beam laminate in ILSS test (side view). (a) in dry condition; (b) after one month's tap water immersion.

Figure 5.6 has shown the measured ILSS after three kinds of water immersion. The samples were taken out of the chambers for bending test after 1 month or 3 months' immersion. The AP laminate showed a consistent value of ILSS for all the immersion conditions, and no degradation of this property was found. However, it showed quite a different failure mode from the dry condition, due to the hygrothermal expansion. Withstanding the same level of bending load, the AP laminate presented much larger cracks after water immersion, and more cracks appeared on the bottom side, as shown in **Figure 5.19**. This is because the peak values of interlaminar shear stress shift to the bottom side, which has been shown in the FEA results in **Figure 5.18**.

The ILSS of the CP laminate showed a sharp reduction (20%) after 1 month immersion and a slight increase after 3 months immersion. However, regardless of the three kinds of medium, the ILSS of CP laminate remained at the same level with respect to immersion time (0/1/3 month), which is similar to the UD and AP laminates.

The ILSS of the UD laminate showed a gradual decrease from 1 month to 3 months water absorption, but no significant difference among the three kinds of medium was observed. It was found that, compared with the interlaminar failure in dry condition, the UD laminate failed by the plastic deformation after water absorption. **Figure 5.20** shows a typical failure image of UD short beam laminate. The laminate was immersed in sea water for 1 month before being tested in bending. A large number of micro cracks were found in the optical microscope image.

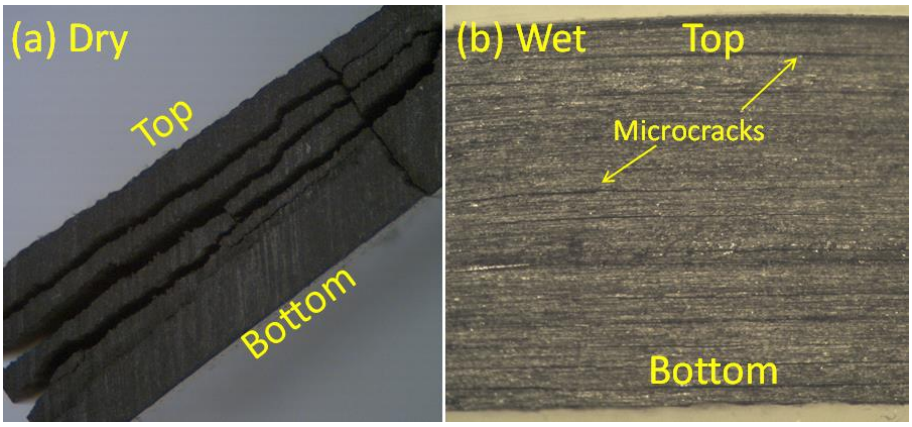

Figure 5.20 Typical failure image of UD short beam laminate in ILSS bending test (side view): (a) in dry condition, (b) after 1-month's water immersion. The delamination was uncompleted in wet condition (b).

According to Chapter 4, the UD laminate failed by compression in bending condition, and the flexural strength was the same as the laminate compressive strength in uniaxial compression. If the thermal residual stress is taken into account, the composite laminate was subjected to initial compression in the dry condition. When the composite laminates were immersed, the hygrothermal expansion should relax the thermal residual stress. As a consequence, the UD laminate showed a relatively higher flexural strength in bending after moisture absorption. **Figure 5.21** shows the normalized flexural strength of CP/UD/UT laminates in three kinds of water immersions. The flexural strength of UD laminate showed a 5%-10% increase (of the order of 100 MPa) compared to that in dry condition.

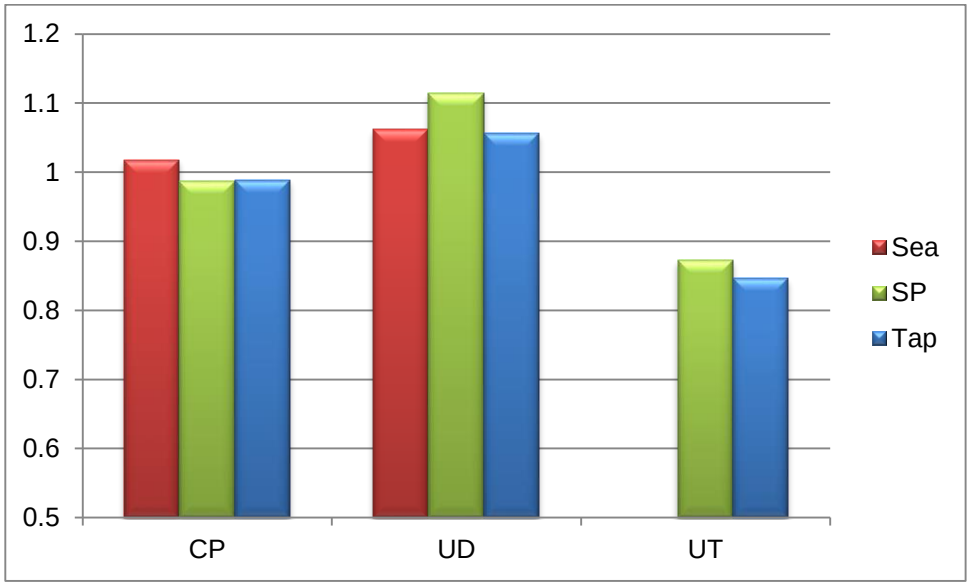

Figure 5.21 Flexural strength of CP/UD/UT laminates after 3-month's water absorption. The values were normalized by the measurement in dry condition.

Although many researchers have investigated the degradation due to the moisture ingress, most of them have focused on either tension or compression. Some researchers have reported that the tensile strength showed a gradual decrease with increasing immersion time (Kootsookos and Mouritz, 2004; Ryan, Adams et al., 2009; Zafar, Bertocco et al., 2012). In bending, composite laminates are subjected to tension, compression and shear, which is quite different from the uniaxial tension and

compression. Therefore, the bending test represents more a general condition, and the change of stress distribution contributed significantly to the failure mechanisms.

The increase of mode I delamination fracture toughness of unidirectional specimen after sea water immersion had been reported by (Sloan and Seymour, 1992), who suggested that the extended weakening of the fibre/matrix interfaces caused by sea water gives rise to fibre bridging across the crack surfaces. This is similar to the results shown in **Figure 5.21**. On the other hand, the flexural strength of UT laminate showed a dramatic decrease after moisture diffusion, while the CP laminate retained the flexural strength of the dry condition. Since the failure mechanism of UT laminate was matrix dominated, the flexural strength was strongly dependent on the bonded interface between the matrix and fibre, which will be discussed in the next section.

Figure 5.22 shows the normalized flexural moduli of CP/UD/UT laminates in three kinds of water immersions. It can be seen that the flexural modulus of CP/UD laminates had a small fluctuation after moisture absorption, however, the UT laminate showed an opposite trend to its strength. Compared to the decrease in flexural strength shown in **Figure 5.21**, the UT laminate became stiffer after moisture absorption. One possible reason is because the epoxy became stiffer when the water molecules diffuse inside the long molecular chain of polymer.

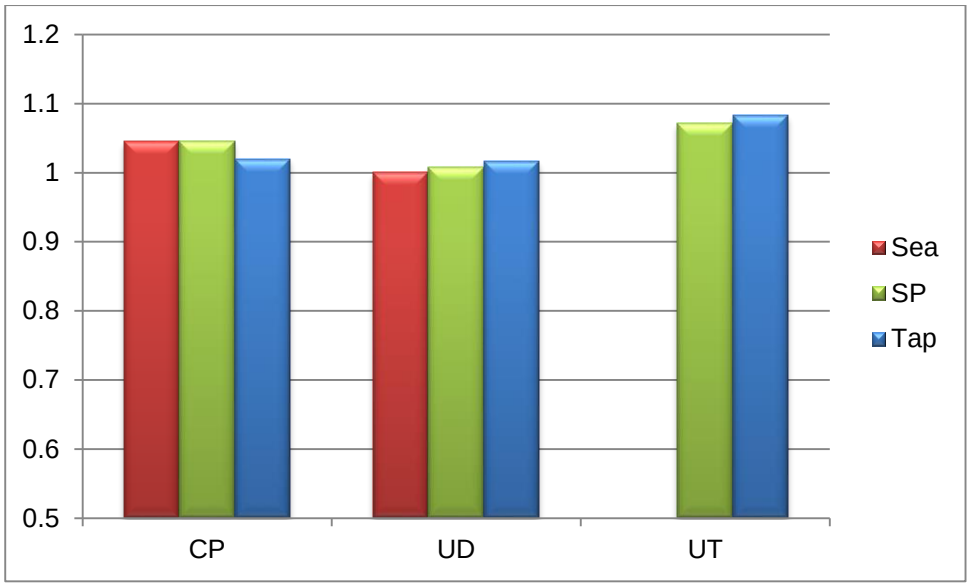

Figure 5.22 Flexural modulus of CP/UD/UT laminates after 3-month's water absorption. The values were normalized by the measurement in dry condition.

The chemical structure of epoxy resin has been shown in **Figure 3.1**. Due to the competition of sulfone bridge, the electron density of nitrogen-carbon bond between DDS and DGEBA is relatively low which leads to water resistance in DDS unit (EICHLER and MLEZIVA, 1971). According to (Korcek, Chenier et al., 1972), the propagation rate constant for hydrocarbon oxidation in the propanol unit is higher than the one in isopropyledene unit, which means that the hydroxyl radical in DGEBA is relatively more hydrophilic. As a consequence, the water molecule was mainly absorbed by the sub-branch (OH-) of DGEBA which had no effect on strength of the cross-link network but might slightly enhance the stiffness of the resin. Therefore, the decrease of strength observed in the UT laminate might be caused by the degradation of fibre/matrix interface which will be discussed in the next section.

The mechanism of stress transfer among the three phases can be evaluated from the FEA micro-model. The influence of the elastic modulus of the interphase was captured through a parametric study. Because of the random distribution of fibres, the first principal stress and strain along an arbitrarily chosen path through-thickness were extracted. **Figure 5.23** and **Figure 5.24** show the first principal stress and strain distributions respectively along a path at x=25μm for the cases of $E_{in} = E_m$ and $E_{in} = 0.75E_m$. Significant stress concentration can be seen in **Figure 5.23**(b), and the peaks correspond to the fibre barrier regions located near the fibre surface. Eventual fracture may initiate at these regions with the combination of fibre surface peeling, fibre/interphase delamination, and matrix fracture.

These peak stresses have exceeded the tensile strength of the matrix (81 MPa) and some of them even exceeded its flexural strength (197 MPa), according to the values given in the manufacturer's datasheet. The average value matched the applied load on the boundary (110 MPa). The sensitivity study of the interphase modulus showed that the two curves almost overlapped each other, which means that a lower value of E_{in} did not change the stress distribution among the three phases.

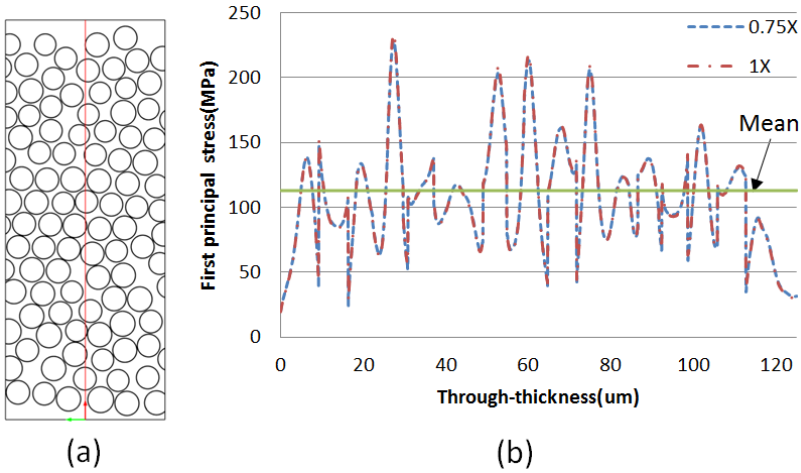

Figure 5.23 (a) Schematics of stress distribution and the chosen line for the stress plot; (b) First principal stress distribution along the chosen line. The mean value is also shown in the figure.

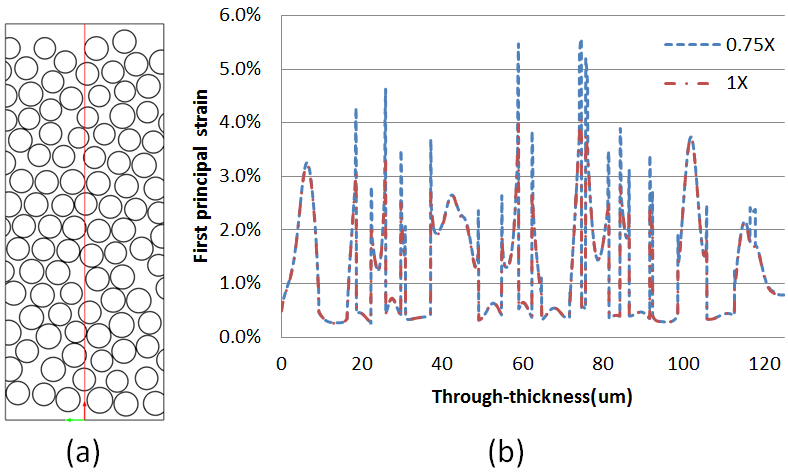

Figure 5.24 a) Schematics of the chosen line for the strain plot; (b) First principal strain distribution along the chosen line.

The strain distribution in **Figure 5.24** (b) gives a more typical plot for the interaction among the three phases. The relatively flat valleys show the strain in the fibres. Many extremely sharp peaks are evident at points where the chosen line crossed the fibre barrier regions. According to the previous studies, the ultimate failure strain of epoxy falls into the range of 5%-7% (Gibson, 1994), which is close to the peak strains extracted from the micro model. **Figure 5.25** is a local view of the strain distribution indicating that the stress concentration occurs at the narrow gaps between adjacent fibres.

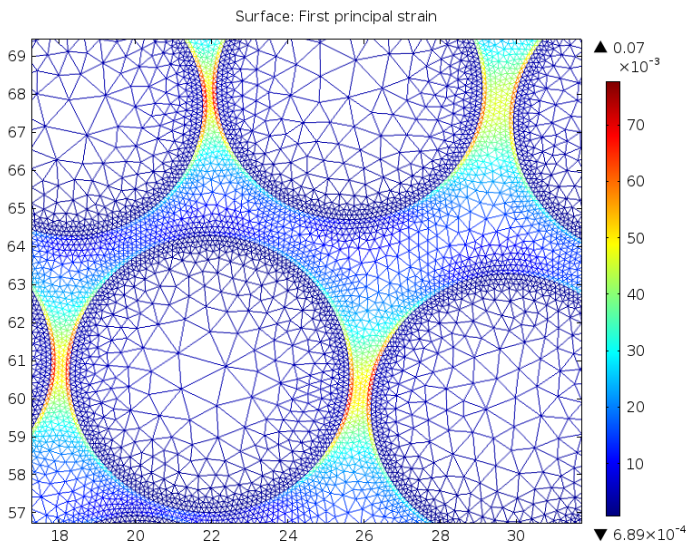

Figure 5.25 Distribution of the first principal strain. Peak values were found at interphases.

Figure 5.23 and **Figure 5.24** have illustrated the variation of mechanical behaviours of the first principal stress/strain in the sensitive study of the elastic modulus of the interphase. Since the first principal stress is independent of the value of E_{in}, stress distributions along five chosen paths near the centre were extracted to study the stress concentration in case of $E_{in} = E_m$, shown in **Figure 5.26**. Compared with **Figure 5.23** (x=25μm), **Figure 5.26** shows extremely high values of the stress concentration on each path at the fibre barrier region, indicating micro crack initiation.

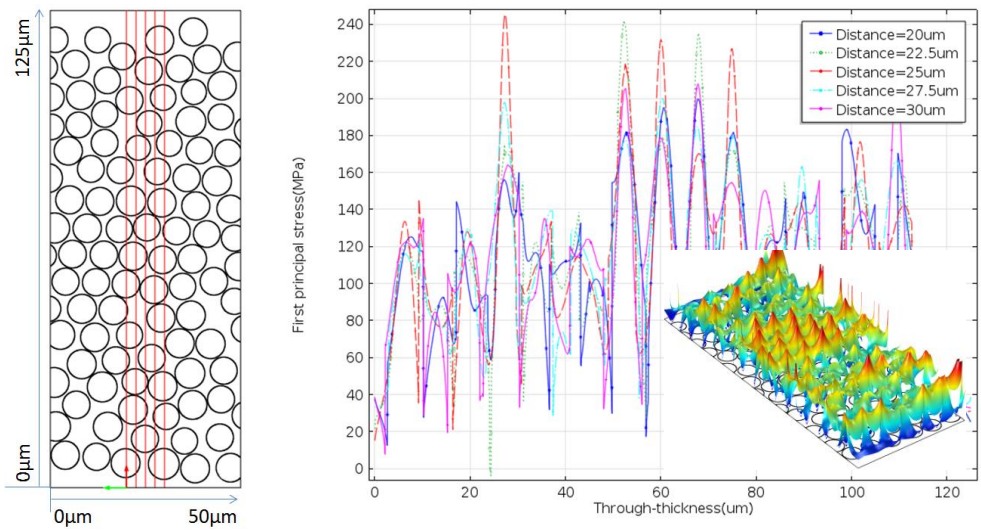

Figure 5.26 The distributions of the first principal stress along five chosen paths in the central

Figure 5.27 shows the distributions of interlaminar shear stress obtained from the macro-model along three chosen through-thickness lines in the angle-ply laminate. A significant edge effect can be seen in Figure 5.27(a) Figure 5.27(b), however the extremely high value of interlaminar shear stress decayed significantly inside the laminate within a distance of two ply thicknesses. It can also be seen that the coupling of hygrothermal expansion had changed the distribution of interlaminar shear stress so that the stress was asymmetric about the mid-plane, as shown in Figure 5.27(b). The positions of peaks shifted to the tensile side. The maximum value of interlaminar shear stress showed an increase of about 15% after water absorption, compared with the dry condition.

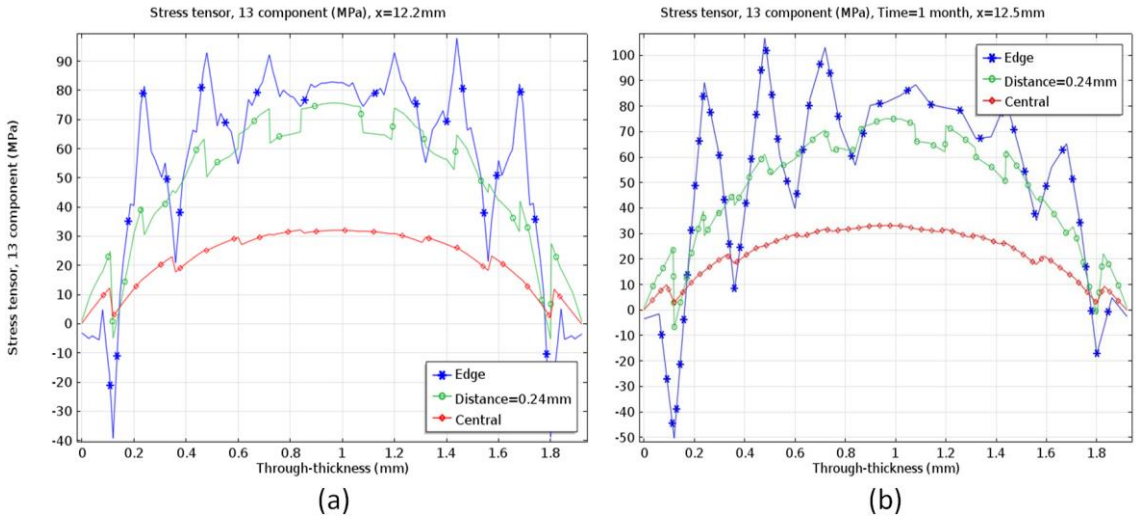

Figure 5.27 Through-thickness distribution of interlaminar shear stress of macro model for angle-ply laminate: (a) dry condition and (b) after one-month immersion.

5.4 SEM analysis

Scanning eletronic microscopy (SEM, model: JEOL-7001-FE-SEM) was used to examine the interface of fibre/epoxy at the fracture surface. The fracture debris was taken from UT laminate, and dry/tap/sea conditions were examined. The samples were coated with gold/paladium before being examined in SEM. Figure 5.28, Figure 5.29 and Figure 5.30 show the particular fracture surfaces of the three conditions. There are two magnifications in each figure, 500 and 4000.

Figure 5.28 illustrates the transverse fracture surface within a dry condition UT sample. The epoxy was still attached to the carbon fibre, so that the fractured polymer showed a

tough wave-like morphology. Without water ingression, the epoxy provided adequate adhesion to the carbon fibre, and the failure mode tended to be the tensile fracture of epoxy rather than the debonding of fibre/epoxy interphase.

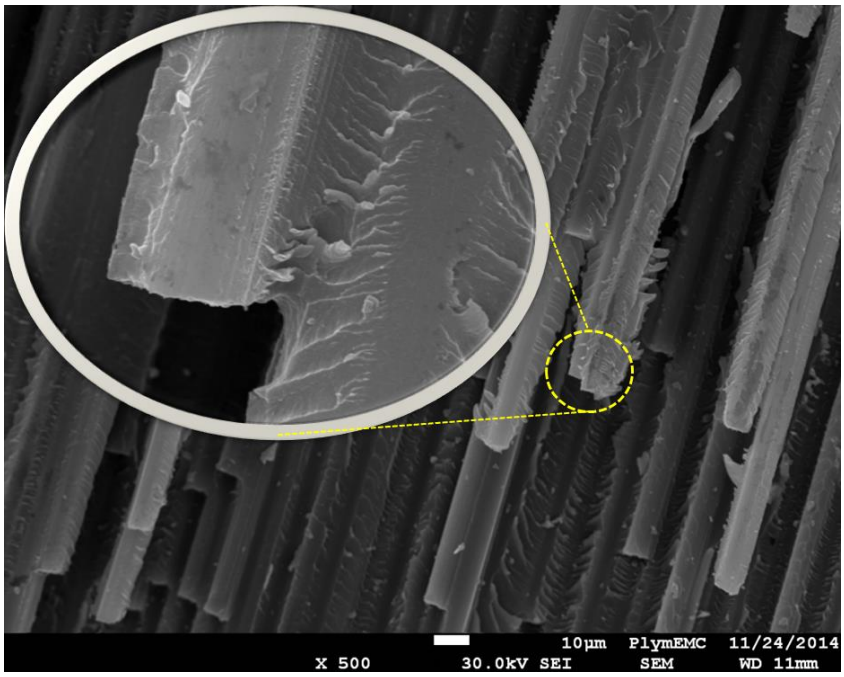

Figure 5.28 SEM image of dry sample with a local magnification

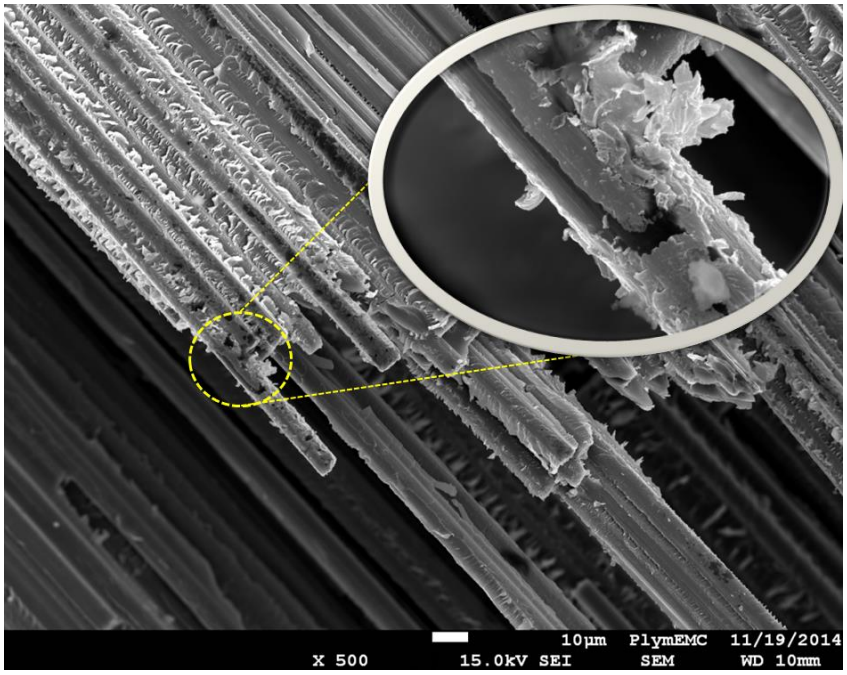

Figure 5.29 SEM image of tap water condition

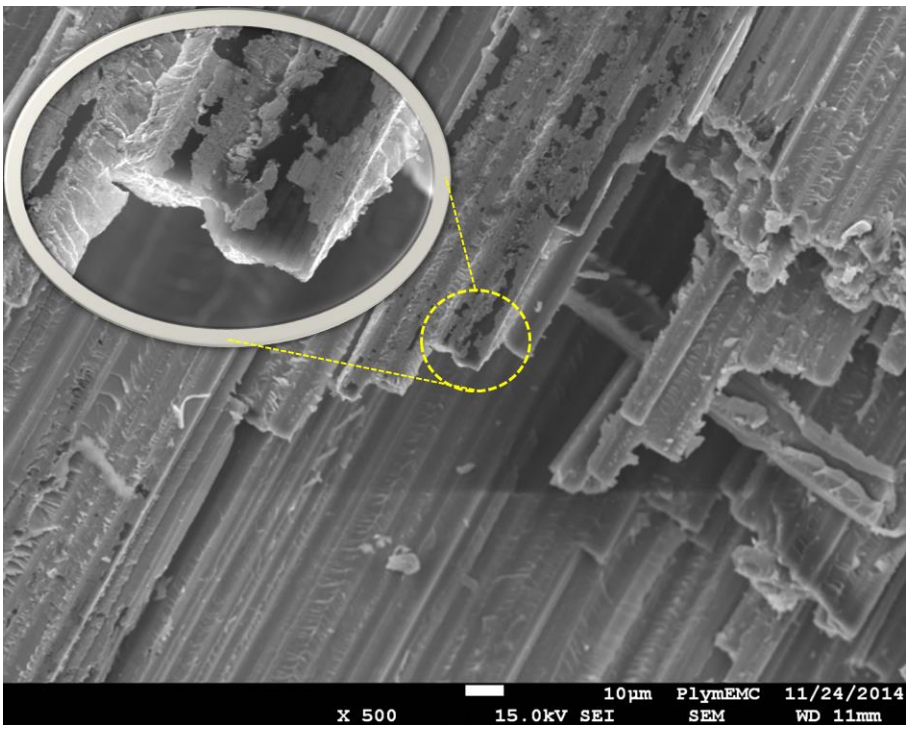

Figure 5.30 SEM image of sea water condition

Figure 5.29 and **Figure 5.30** show similar characters of transverse fracture surface of tap water and sea water conditions. At a lower magnification, it can be seen from **Figure 5.29** that the epoxy became porous; however the wave-like morphology was still observed which indicates that the failure mode was the tensile fracture of epoxy. At a higher magnification in **Figure 5.30**, the carbon fibre showed sections of bare surface which indicates that the adhesion of epoxy on carbon fibre had deteriorated after water absorption.

It should be noted that the SEM could only examine a local area under a relative high magnification. It was found that, in sea water condition, the number of bare fibres was higher than the tap water condition. Therefore, it is reasonable to believe that the degradation in sea water is more severe in long term exposure.

It is possible to extract the elemental content by energy dispersive spectroscopy (EDS) inside the SEM. It has been known that the carbon fibre is chemical stable which means that sea water immersion has no effect on the carbon fibre, therefore only the matrix was detected by the EDS. **Figure 5.31** shows the EDS elemental analysis (software: Oxford Instruments AZtecEnergy) of the specimen after sea water immersion.

There quite a few points were inspected as shown in **Figure 5.31**(a), which showed similar elemental content as shown in **Figure 5.31**(b). Plenty of carbon and oxygen were detected showing the main composition of the epoxy, while the content of sulphur represented the DDS radicals in the epoxide networks as shown in **Figure 3.1**. The small amount of the potassium, sodium, chlorine and magnesium indicated the diffusion of the ions from sea water. It is interesting to see a very high level of the energy dispersion of the calcium (shown about 37.5 wt%). One possible reason is the information interference because the dispersion energy of calcium is very close to that of carbon.

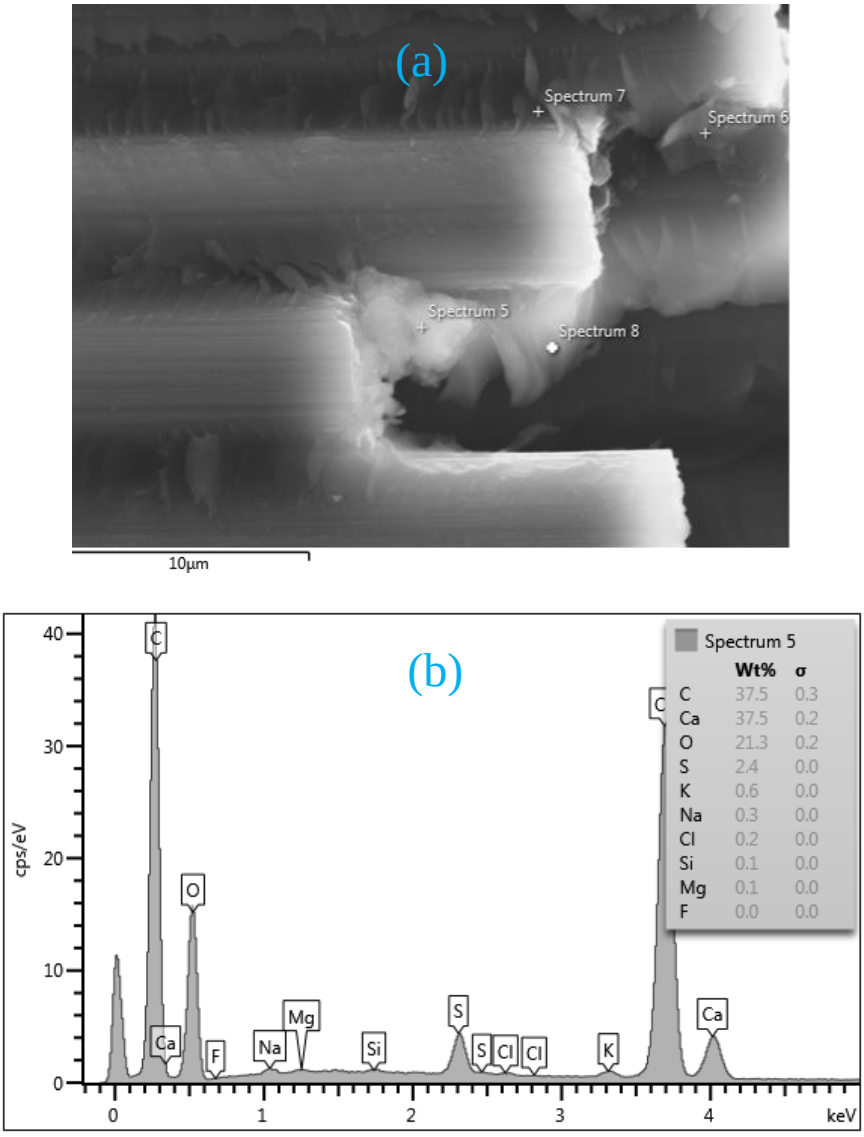

Figure 5.31 EDS analysis of the sea water condition: (a) analysis point; (b) elemental content

For the comparison, the EDS elemental analysis for the dry specimen is also plotted as **Figure 5.32**. It can be seen from **Figure 5.32**(b) that no ions were detected in the dry specimen. The specimen was coated by gold and palladium in prior to analyse by EDS, therefore a large amount of these two elements were detected.

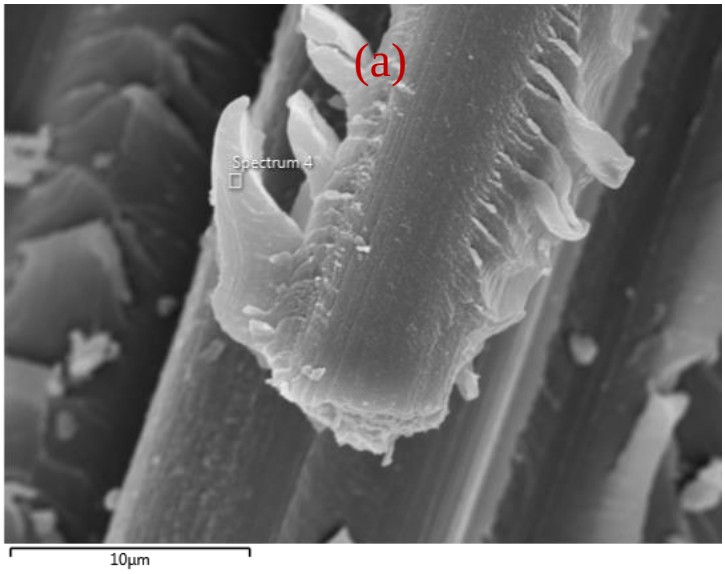

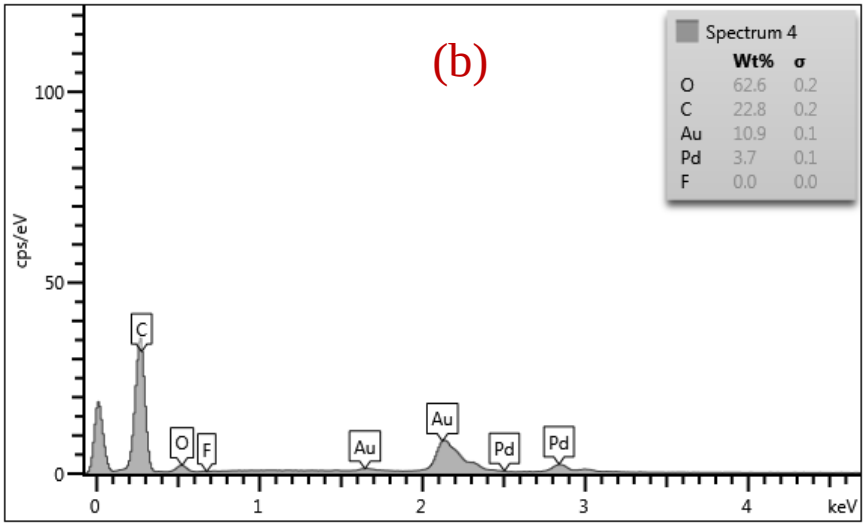

Figure 5.32 EDS analysis of the dry condition: (a) analysis point; (b) elemental content

5.5 Summary

This chapter has investigated the effects of water immersions on the CFRP composites. A macro-model (3D solid FEA), which inherited the mechanical component from the one presented in Chapter 4, has been developed to analyse the hygrothermal effects, and

a realistic micro-model (2D FEA) to analyse the moisture diffusion and stress/strain transfer between fibre and matrix at the micro-scale. The experimental results showed a good agreement with the FEA solutions, which has also been validated by CLT calculation.

The experimental work illustrated the variety of behaviour of moisture diffusion as well as the mechanical performance. In the Tap/Sea/SP water immersions, the moisture diffusivity showed negligible difference at the same temperature. It was found that the longitudinal moisture diffusivity presented a much higher value than the transverse diffusivity (60% in this study). Hygrothermal stresses could be induced at the very beginning of diffusion, and these stresses mainly appeared at the edge region (edge effect) which means that the laminate lay-up becomes a critical issue for the exposed surfaces. For interlaminar shear stress, the induced hygrothermal stress could be as high as 20% of the strength. Therefore, in the design of marine composites, it is desirable to avoid complicated lay-ups at the connection region of composite joints or notches in order to improve the fatigue properties.

The FEA simulation revealed details of moisture diffusion coupled with stress distribution in micro and macro scales. The micro-model suggests that the moisture diffusivity of the interphase must be about one order of magnitude higher than that of the matrix, in order to reproduce the fibre barrier effect. Meanwhile, significant stress concentration was found at the fibre barrier regions. The coupling effect of hygrothermal expansion induced a significant interlaminar shear stress edge effect at the interfaces of adjacent plies, and the study showed a decrease by about 15% in interlaminar shear strength when the CFRP composite is moisture-saturated.

The SEM analysis has shown a variety of matrix fracture morphologies and the effects of degradation of fibre/matrix interface on the failure mechanisms of CFRP composites in marine environment.

The model predictions described in this chapter have helped to understand the failure mechanisms of CFRP composites in the marine environment. In the next chapter, the FEA model is extended to cyclic load for the investigation of the environmental fatigue.

CHAPTER 6 – INTERATION BETWEEN WATER INGRESS AND FATIGUE

This chapter investigates the effects of water immersion on the fatigue failure of CFRP composites. Dry and wet specimens were tested in a variety of bending conditions following the ISO standard (ISO13003, 2003), and the failure mechanisms revealed by the previous chapters were then recalled to understand the fatigue failures. As a special type of fatigue, the creep phenomenon is also discussed (for the angle-ply laminate). A 2D FEA model was developed to simulate the fatigue crack propagation in bending, while a 3D FEA model was developed to examine the mechanisms of fatigue crack initiation and propagation when the terms of free edge effect and water ingress were introduced. Both the two FEA models were solved by ABAQUS/Standard.

6.1 Fatigue tests

6.1.1 *Machine setup*

The experiment was carried out on a universal fatigue testing machine (INSTRON E3000) which applied a sinusoidal cyclic load, as shown in **Figure 6.1**. The input parameters required include the control method, frequency of cyclic load, R ratio, loading level (amplitude and mean value) and the stop criterion.

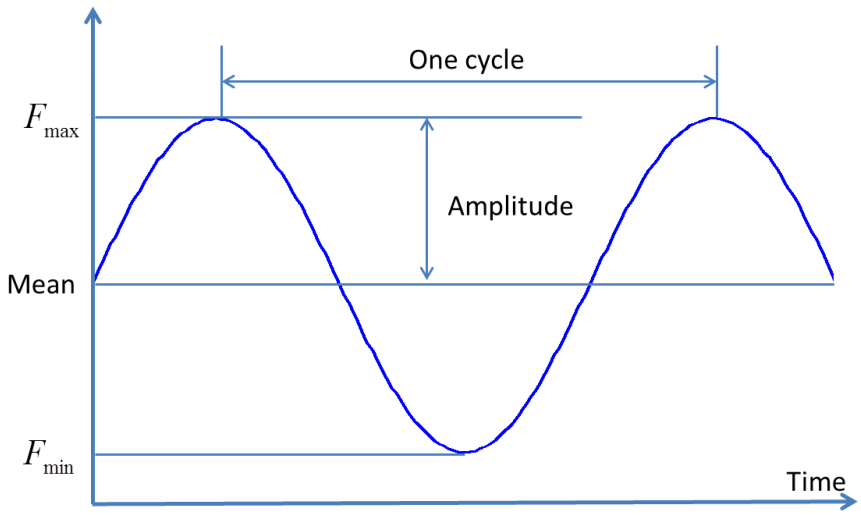

Figure 6.1 Sinusoidal cyclic loading condition of the fatigue test

There are two **control methods** commonly used for the bending fatigue test: force control and deflection control. The force control method applies constant maximum and minimum forces for each cycle during the fatigue test until the specimen breaks. Similarly, the deflection control method applied constant deflections; however the specimen cannot break since the maximum deflection is a fraction lower than the ultimate deflection. The specimen controlled by deflection method might have a drop of stiffness when cracks initiate and propagate. According to the standard (ISO13003, 2003), the specimen is considered to meet the fatigue limit when it loses 20% of the stiffness. Compared with glass fibre composites, carbon fibre composites present much better fatigue performance therefore much longer time is needed for a single CFRP specimen in deflection control. In order to expedite the specimen as soon as possible, the force control method was used in this project.

The main concern of the choice of **frequency** is the heat generation during the cyclic load and the thermal conductivity (associated with heat dispersion) of the specimen. As polymeric matrices are thermal insulating, the thermal conductivity of FRP composites is mainly dependent on the fibres. Since carbon fibres present a much higher value of thermal conductivity than the other kinds of fibres, a higher frequency can be applied on CFRP specimen. Many researchers employed 5Hz for GFRP composites while 10Hz for CFRP composites, however 30Hz for the CFRP composites was reported in some cases (Peters, 2013). According to the FEA simulation (ANSYS Workbench), the first mode of resonance frequency of the unidirectional and cross-ply laminates were calculated in the order of 600Hz and 900Hz respectively based on the material properties shown in the **Table 3-3**, therefore the resonance effect can be neglected when the loading frequency is in range of 5-30Hz. In this thesis, most of the specimens were tested at a frequency of 10Hz though a few were tested at 15 Hz for comparison.

The **R ratio** is the ratio of minimum load to the maximum load $R = F_{\min} / F_{\max}$. It is well known that at the same loading level, the lower the R ratio the lower the fatigue life presents. The ideal case is to apply R=-1; however this is not happened in bending fatigue. In order to avoid slipping, this project applied R=0.1 for the fatigue test.

The S-N curve, plotted as the **loading level** against the cycle count, is commonly used to compare the fatigue life for many materials such as metals; nevertheless it is not

appropriate for FRP composites particularly for CFRP composites because the curve might be a flat line due to the excellent fatigue performance. In this thesis, specimens were mainly tested at 80% and 90% UFS (ultimate flexural strength), though a few specimens were tested at 65% UFS for comparison. The ultimate flexural strengths of the unidirectional and cross-ply laminates were inherited from the bending test shown in Chapter 4. The mean value and amplitude are necessary for the machine setup which are calculated by,

$$F_{mean} = \frac{F_{\max}(1+R)}{2}$$
$$F_{amp} = \frac{F_{\max}(1-R)}{2} \qquad (6\text{-}1)$$

Table 6-1 shows the loading levels corresponding to the mean value and amplitude. The previous chapters have shown that the flexural strength of the dry and wet specimens were very close to each other, therefore the loading levels for both dry and wet specimens were the same in the fatigue tests.

Table 6-1 Loading levels of the UD and CP laminates for the fatigue test. The level '100%' represents the ultimate flexural strength which was tested in quasi-static bending.

	Bending	Level	F_{mean}(N)	F_{amp}(N)
UD $[0]_{16}$	3P	65%	305	250
		80%	375	307
		90%	422	345
		100%	853	–
	4P	65%	458	374
		80%	563	461
		90%	634	518
		100%	1280	–
CP $[90/0]_{4s}$	3P	65%	225	184
		80%	277	227
		90%	312	255
		100%	630	–
	4P	65%	338	276
		80%	416	340
		90%	468	383
		100%	945	–

Two **stop criteria** were applied: (a) the cycle count, corresponding to an infinite fatigue life; and (b) maximum deflection, corresponding to the fracture failure with a significant stiffness reduction. The default maximum cycle count of the INSTRON machine was defined as one billion cycles (approximately 11,574 days at 10Hz), but this is obvious impractical. Therefore the machine should be stopped manually if the cycle count exceeds a particular value and then the specimen is considered to have an infinite fatigue life. In this thesis, the maximum cycle count was defined as three million cycles. Once the force control method is chosen for the cyclic test, the fracture will propagate through the whole laminate rapidly once the crack initiated. Therefore a proper value of the maximum deflection was defined to be approximately a 20% stiffness reduction.

It should be noted that the 'tuning', which represents the loading stiffness for a particular condition, should be calibrated in advance of any other setup. According to the quasi-static bending test, the 'tuning' was in the order of 100N/mm which was used for all the laminates in this thesis.

UD ($[0]_{16}$) and CP ($[90/0]_{4s}$) laminates were tested at room temperature using 3-point and 4-point bending methods which inherited the specimen dimension from the quasi-static test discussed in Chapter 4. In order to simulate the condition of water immersion, the specimen was covered by a wet sponge on to which water was dropped by a tube regularly during the fatigue test. The specimen that was immersed in sea water was wetted by sea water, while tap water was used to wet those specimen immersed in tap water. **Figure 6.2** shows the three test conditions: Dry-3P, Dry-4P and Wet-4P.

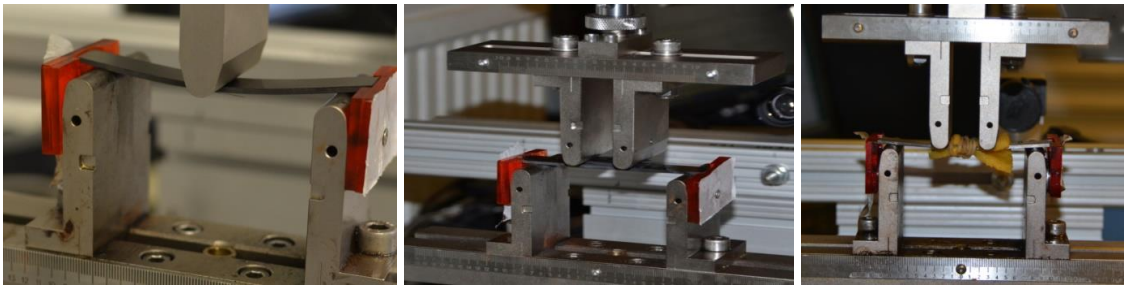

(a) **(b)** **(c)**

Figure 6.2 Fatigue test condition: (a) 3-point bending for specimen without immersion (Dry-3P); (b) 4-point bending for specimen without immersion (Dry-4P) and for immersed specimen without the cover of wet sponge (Wet2-4P); and (c) 4-point bending for immersed specimen covered by wet sponge (Wet1-4P).

The deflection and reaction force at the loading point were recorded. The machine applied a linear increasing force to the mean value for five seconds, after that a gradual ramp amplitude cyclic force was applied until the designated loading level. **Figure 6.3** shows the loading history at the beginning of the fatigue test. As can be seen the reaction force was unstable at the first few cycles therefore the stiffness calculated by this reaction force is expected to have a fluctuation during this period.

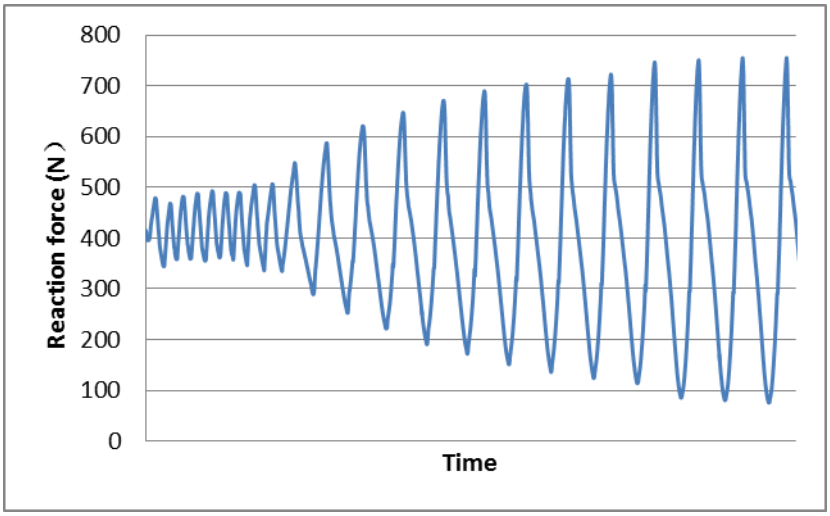

Figure 6.3 Loading history at the beginning of the fatigue test for the cross-ply laminate

The INSTRON machine showed a variety of responses for unidirectional and cross-ply laminates at the end of the fatigue test, indicating different failure modes. **Figure 6.4** shows the reaction force and deflection of a unidirectional laminate at the moment of fracture and then the criterion tripped the limit, leading to the machine stopping. The rapid drop of the reaction force to zero indicated that the specimen failed suddenly and broke into two parts.

Figure 6.5 shows the reaction force and deflection of a cross-ply laminate when it failed. Instead of zero reaction force at the failure status, the deflection increased gradually till the limit was tripped and then the machine stopped automatically while the reaction force remained at an intermediate value, indicating that the specimen suffered significant fracture but did not break into two parts.

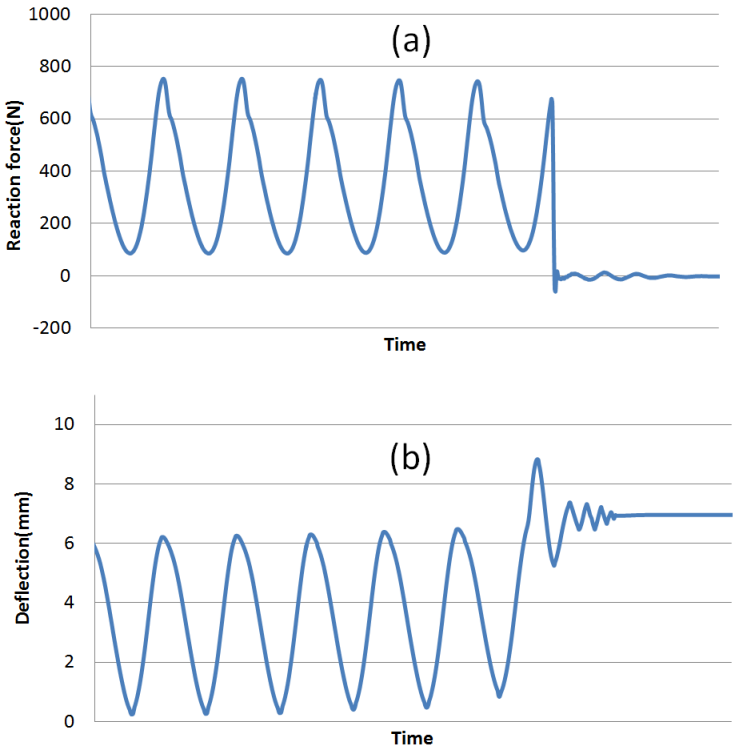

Figure 6.4 **The reaction force (a) and deflection (b) responses of a UD specimen at the moment when the specimen broke**

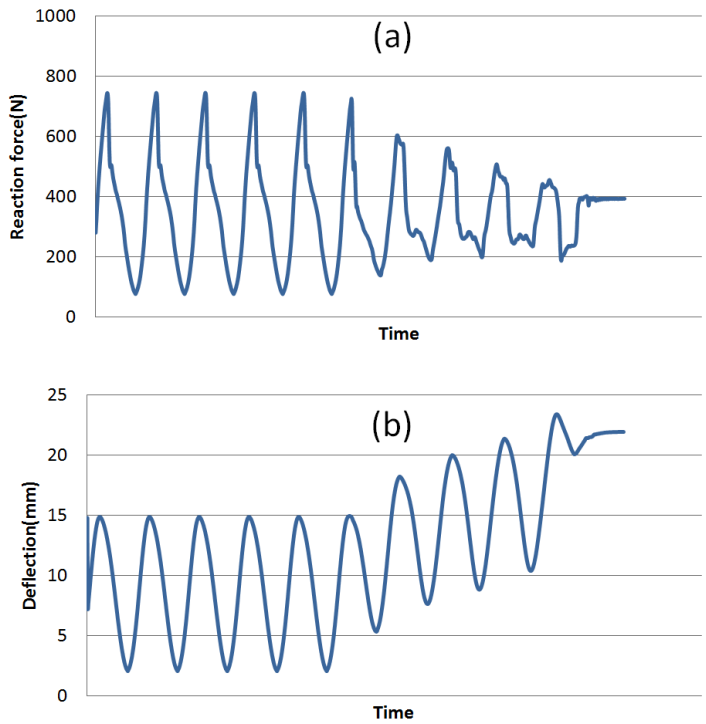

Figure 6.5 **The reaction force (a) and deflection (b) responses of a CP specimen at the stage when the specimen broke**

For comparison, the response of an 'infinite fatigue life' specimen was extracted, plotted as **Figure 6.6**, showing two oscillations of both reaction force and deflection at an intermediate value when the machine was forced down manually.

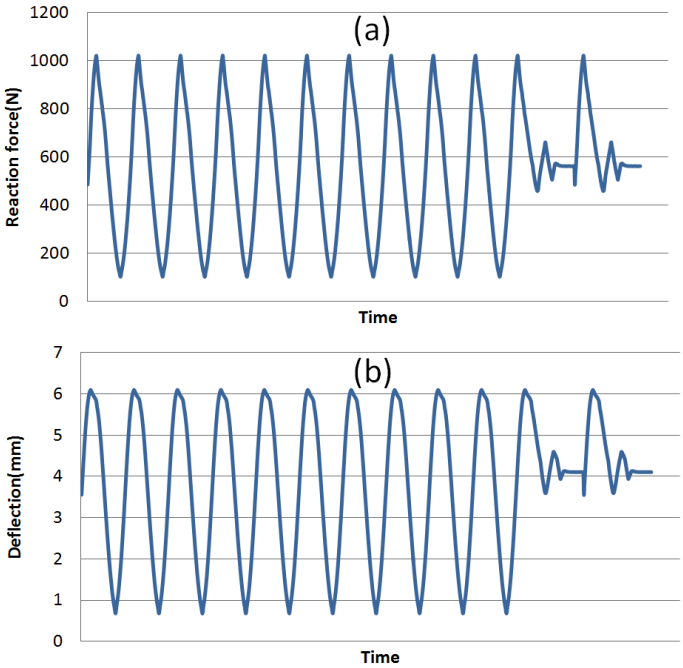

Figure 6.6 The reaction force (a) and deflection (b) responses when the machine was manually stopped

6.1.2 *Fatigue life*

The analysis of fatigue life was plotted as a graph with different loading levels. **Figure 6.7** shows the fatigue life of the cross-ply laminate in the four testing environments. Although the figure shows scatter of the distribution of the fatigue life at different loading levels and testing environments, there are still some observation that derived from these data.

At the highest loading level, 90% of the ultimate flexural strength (UFS), both wet and dry specimens were tested in 4-point bending condition and all of the specimens failed at no more than one million cycles. The immersed specimen showed relatively lower cycle count than those specimens without water immersion. At the intermediate loading level, 80% UFS, all the dry specimens presented infinite fatigue life, in contrast, all of the immersed specimens broke although one specimen still showed a relatively high level of fatigue cycle count (more than two million). The fatigue cycle counts for the

dry specimens distribute at 80% UFS loading level with a scatter in the figure because the tests were stopped manually when it was found that the fatigue cycle count had exceeded three million and such a specimen was labelled as having an infinite fatigue life. It is interesting to note that the immersed specimen which was tested in dry survived at this loading level, indicating that the fatigue behaviour was also affected by the testing environment. At the lowest loading level, 65% UFS, all of the specimens survived regardless of the laminate pre-conditions and testing environments.

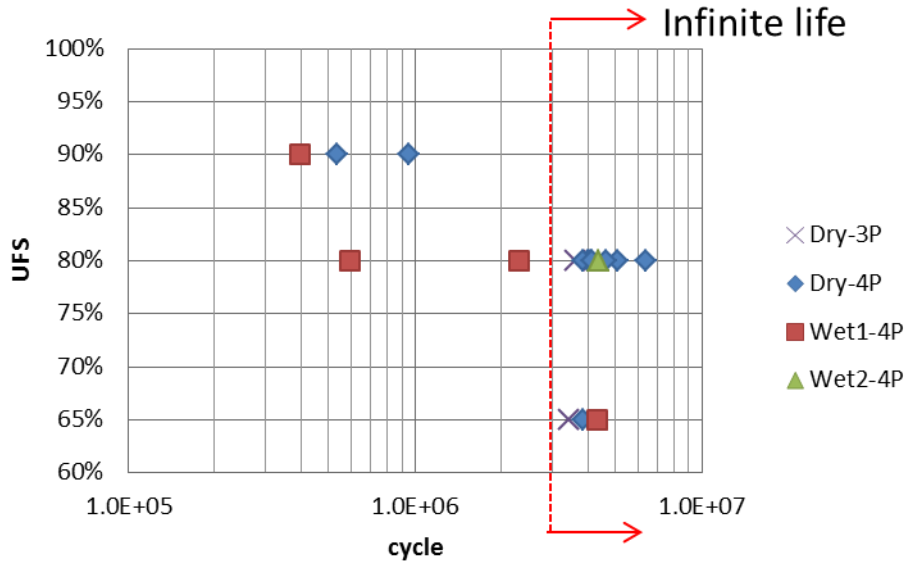

Figure 6.7 Fatigue life of CP laminate. The fatigue cycle is plotted as logarithm scale. Wet1-4P: immersed specimen, covered by wet sponge while 4-point bending fatigue testing; Wet2-4P: immersed specimen, without wet sponge cover while testing.

The unidirectional laminate showed a similar trend at the high loading levels, as plotted in **Figure 6.8**. At the 90% UFS loading level, no specimen could withstand as high as 3 million fatigue cycles. At the 80% UFS loading level, the dry specimen survived while all the immersed specimens broke. More specifically, as shown in the magnified chart for the immersed specimens at 80% UFS loading level, the cycle counts of the three kinds of water immersions showed such a large scatter that there was no evidence to identify the difference of the three kinds of water immersions. As discussed in the SEM analysis in Chapter 5, the sea water immersed specimens presented a larger number of bare fibres than the tap water condition, meaning that the sea water degradation was more severe than tap water. One possible explanation for this phenomenon is that the 3-

month period of water immersion was not long enough to see the obvious difference of the effects on the fatigue behaviour. Compared with the cross-ply laminate, the immersed unidirectional laminate failed at 65% UFS, indicating that the effects of water immersion on cut-off fatigue life depends on the laminate stacking.

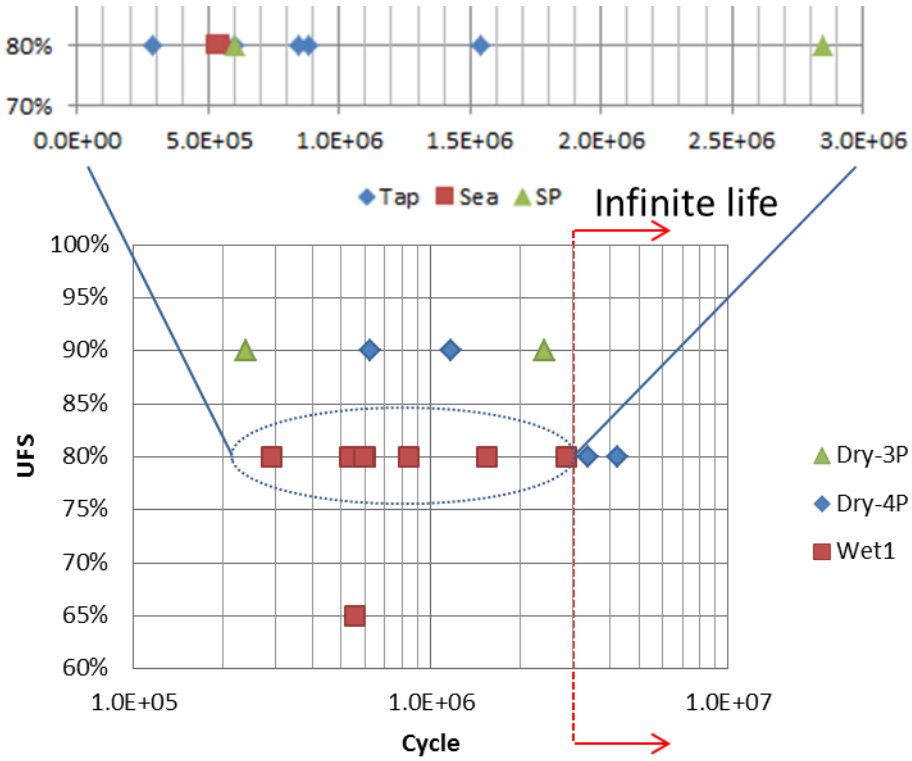

Figure 6.8 Fatigue life of UD laminate. Tap: tap water immersion; Sea: sea water immersion; SP: sea water immersion with 70 bars hydrostatic pressure.

The fatigue lives of the UD and CP laminates shown in the **Figure 6.7** and **Figure 6.8** share many common features, one of which is that the distribution of the ultimate fatigue cycles showed very large scatter. Additionally, these values were extremely high and strongly dependent on the laminate pre-conditions (dry or wet), testing environments as well as the ply stacking. In the later sections, it will be shown that these values are also dependent on the other factors, such as the bending condition. Therefore it is reasonable to believe that the traditional S-N curve, which is widely used to predict the fatigue of metals, is inappropriate to FRP composites, and the analysis of their fatigue failure requires consideration of the other directions, such as the durability of the stiffness during the fatigue test, crack initiation and propagation.

6.1.3 *Fatigue stiffness*

The quasi-static bending test had shown a perfect linear force-deflection curve for the simply supported laminate in 3-point and 4-point bending when the ratio of deflection to span was lower than 10%. The standard (ISO14125, 1998) provides an equation to calculated the apparent flexural modulus for 3-point and 4-point bending,

$$E_{3P}^{f} = \frac{L_{3P}^{3}}{4wh^{3}} \frac{F_{\max}}{D_{\max}}$$
$$E_{4P}^{f} = \frac{0.21L_{4P}^{3}}{wh^{3}} \frac{F_{\max}}{D_{\max}^{mid}} \qquad (6\text{-}2)$$

where L_{3P} is the span of 3-point bending, L_{4P} is the outer span of the 4-point bending (the inner span is 1/3 of the outer span), w, h are the width and thickness of the laminate respectively, $F_{\max}/D_{\max}$ is the slope of the force-deflection, and $D_{\max}^{mid}$ is the deflection at the middle point of the specimen.

For the case of 4-point bending, the maximum deflection $D_{\max}^{mid}$ shown in equation (6-2) was the deflection at the middle point of the laminate; however this is not appropriate to the present work because the INSTRON machine recorded the deflection at the loading point. Therefore, a formula should be derived to present the relation between the apparent flexural modulus and deflection at the loading point.

Considering an Euler beam under 4-point bending condition, the inner span is one third of the outer span, as shown in **Figure 6.9**.

In the zone AB, the moment is expressed as,

$$M = E_{4P}^{f} Iy'' = \frac{1}{2} Fx, 0 \le x \le \frac{L}{3} \qquad (6\text{-}3)$$

Integrating equation (6-3) twice,

$$E_{4P}^{f} Iy' = \frac{1}{4} Fx^{2} + C_{1}, E_{4P}^{f} Iy_{B}^{'} = \frac{1}{36} FL^{2} + C_{1}$$
$$E_{4P}^{f} Iy = \frac{1}{12} Fx^{3} + C_{1}x + C_{2}, E_{4P}^{f} Iy_{A} = 0, C_{2} = 0 \qquad (6\text{-}4)$$
$$E_{4P}^{f} Iy_{B} = \frac{1}{324} FL^{3} + \frac{1}{3} C_{1}L$$

where I is the moment of inertia, y_B, y_E are the deflections at the loading point and middle point respectively.

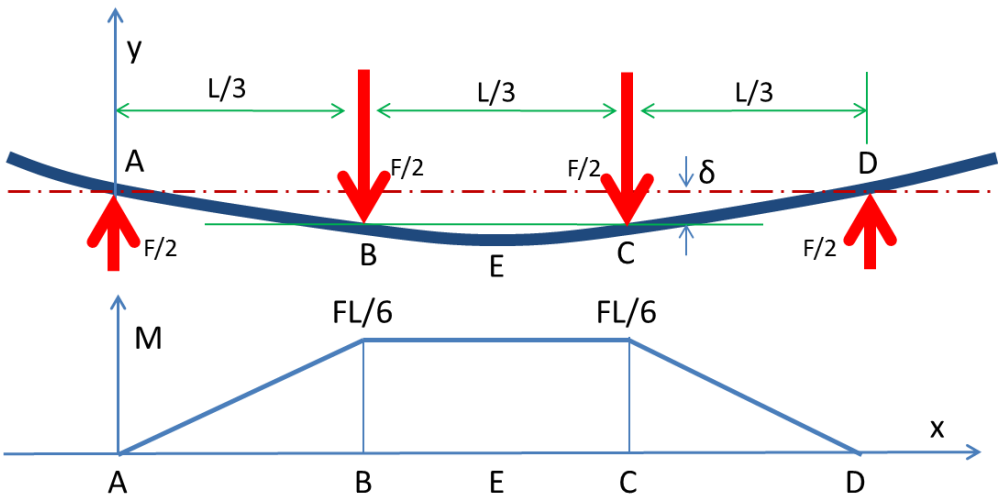

Figure 6.9 Schematics of 4-point bending and the distribution of moment

In the zone BC, the moment is expressed as,

$$M = E_{4P}^{f} Iy'' = \frac{1}{6} FL, \frac{L}{3} \le x \le \frac{2L}{3} \tag{6-5}$$

Integrating equation (6-5),

$$E_{4P}^{f} Iy' = \frac{1}{6} FLx + C_3 \tag{6-6}$$

The differential at the middle point is zero, leading to $y_E^{'} = 0$. Therefore,

$$\begin{aligned} E_{4P}^{f} Iy_E^{'} &= \frac{1}{12} FL^2 + C_3 = 0, C_3 = -\frac{1}{12} FL^2 \\ E_{4P}^{f} Iy_B^{'} &= -\frac{1}{36} FL^3 \end{aligned} \tag{6-7}$$

Integrating equation (6-7),

$$\begin{aligned} E_{4P}^{f} Iy &= \frac{1}{12} FLx^2 + \frac{1}{12} FL^2 x + C_4 \\ E_{4P}^{f} Iy_B &= \frac{1}{54} FL^3 + C_4 \end{aligned} \tag{6-8}$$

Combining equations (6-4) and (6-8),

$$C_1 = -\frac{1}{18}FL^2, C_4 = \frac{1}{324}FL^3 \qquad (6\text{-}9)$$

Substituting equation (6-9) and the moment of inertia $I = \frac{1}{12}wh^3$ into equations (6-7) and (6-8), the apparent flexural moduli at the loading point and mid-point are then calculated by,

$$E_{4P}^{f} = -\frac{5L^3}{27wh^3}\frac{F}{y_B} \qquad (6\text{-}10\text{-}1)$$

$$E_{4P}^{f} = -\frac{23L^3}{104wh^3}\frac{F}{y_E} \qquad (6\text{-}10\text{-}2)$$

Equation (6-10-2) is the same as the one in the ISO standard shown as equation (6-2) using the deflection at the middle point.

Figure 6.10 shows the hysteresis loops of a cross-ply laminate under 3-point bending in terms of deflection-reaction force. Two loops were plotted in the figure, showing the histories at the beginning (100 cycles) and the end (500,000 cycles) of the test. The reason to choose cycle 100, rather than cycle 1 to represent the 'beginning of the test' was because both the deflection and reaction force were unstable at the beginning of the test (as discussed for **Figure 6.3**.

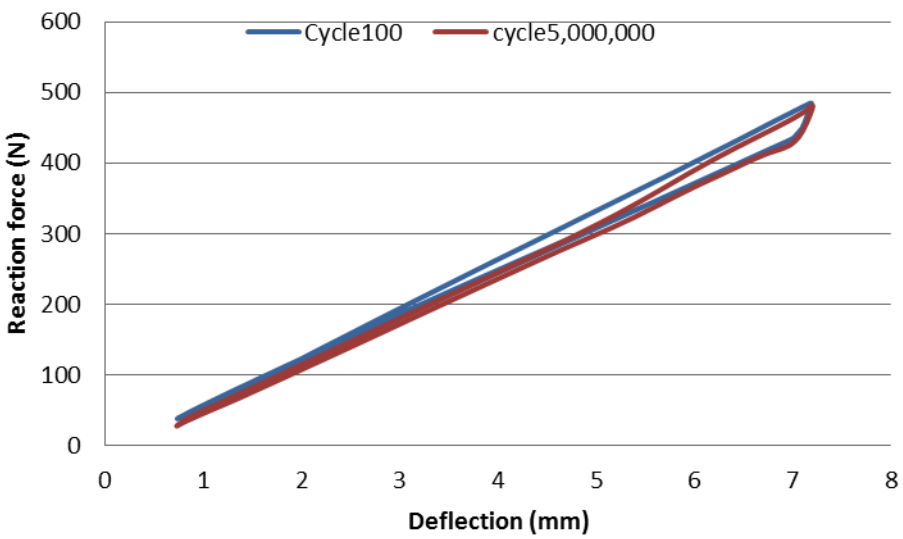

Figure 6.10 The typical hysteresis loops of the deflection-reaction force of CP-dry laminate in 3-point bending fatigue test at the 80% UFS loading level

Two loops were plotted in **Figure 6.10**. As can be seen they almost overlapped each other, indicating that this type of plot can only provide limited information on the change of specimen status. Therefore the reaction force was transformed to flexural modulus by introducing the specimen dimension and bending condition, as shown in **Figure 6.11**. The two hysteresis loops illustrated the loading sequence within one single cycle as shown by the coloured arrows in the figure and the degradation of the flexural stiffness by increasing the fatigue cycle.

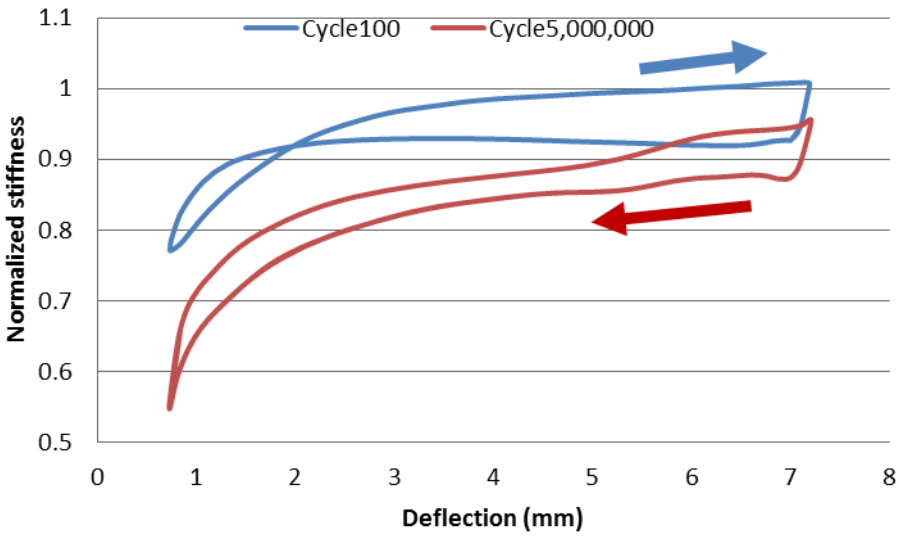

Figure 6.11 The typical hysteresis loops of the CP-dry laminate in 3-point bending fatigue test at the 80% UFS loading level in view of deflection-normalized stiffness. The stiffness was normalized to the value of dry condition. The directions of the hysteresis loops are also shown as two coloured arrows in the figure.

In terms of dynamic loading, the apparent reaction force is calculated from the sum of the specimen reaction force and the inertia force of the load cell. In sinusoidal cyclic loading, the acceleration decreases to zero at the maximum deflection and shifts to negative value when the load cell restores. Therefore, a sudden drop of the reaction force can be seen at the maximum deflection from **Figure 6.10**, and the amplified stiffness reduction from **Figure 6.11**. At the minimum deflection, the flexural modulus decreased significantly from cycle 100 to cycle 500,000, as can be seen in **Figure 6.11**, indicating that fracture appeared at the contact region on the compressive side. Additionally, based on the equation (6-10), the apparent flexural modulus at the

minimum deflection was more sensitive to the deflection than that at the maximum deflection.

Stiffness reduction was also observed in the 4-point bending fatigue test. A microscopic study of an 'infinite fatigue life' specimen, shown in **Figure 6.12**, reveals an explanation of this stiffness reduction at the minimum deflection observed in the fatigue test. First, the fracture initiated at the contact region between the load cell and the compressive surface of the specimen, due to the stress concentration, showing a clear damaged interface in the figure. Later on some of the material at the pure bending region (between the two load cells) on the compressive surface was peeled off due to the compression and delamination. The stiffness decreased gradually when the specimen was peeled off ply by ply. As the fatigue test was force controlled, the deflection increased while the stiffness decreased. It should be noted that this was a very slow and continuous process; thus it is unacceptable to test the specimen until failure, and it is reasonable to believe that the initial crack caused by contact or concentrated load is the cause of fatigue failure of FRP composites.

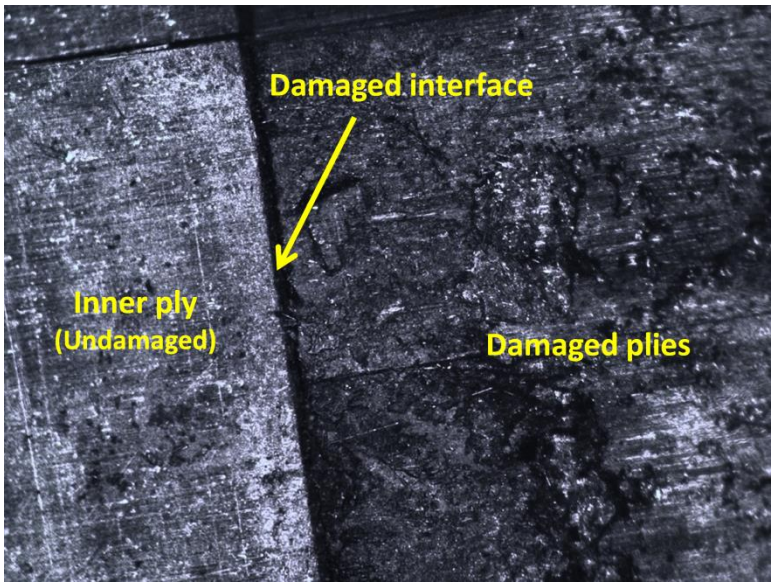

Figure 6.12 Typical fracture image of the CP laminate in 4-point bending fatigue test at the 80% UFS loading level. The specimen survived after withstanding more than five million cycles.

As has been discussed in Section 6.1.2, the fatigue failure of FRP composites is very complicated and is dependent on many aspects such as the testing conditions,

environments, and the laminate layups, so that any attempt to predict the fatigue behaviour by a universal formulation may lead to inaccurate result. In this thesis, the fatigue analysis of FRP composites for marine environment is based on the study of the fatigue stiffness which shows a variety of interactions among the fatigue behaviour, laminate layups, testing conditions and the environmental effects.

The fatigue stiffness unveiled the relation of fatigue and **loading levels** and the **bending conditions**, i.e. 3-point and 4-point bending. **Figure 6.13** shows the flexural stiffness of cross-ply laminate without water immersion (CP-dry) tested in 3-point and 4-point bending. Both the specimens survived after withstanding more than three million cycles at 80% UFS loading level in the fatigue test, and therefore were labelled as 'infinite fatigue life'. As can be seen from the figure, both the specimens showed nearly flat curves of the fatigue stiffness during the millions of cycles, demonstrating the perfect fatigue performance at this loading level. However, the curve of the 4-point case showed a downward trend at increasing fatigue cycle, due to the contact and delamination shown in **Figure 6.12**. As a contrast, the curve of the 3-point case remained flat because the fracture contact region was constrained by the load cell which prevented the propagation of the crack.

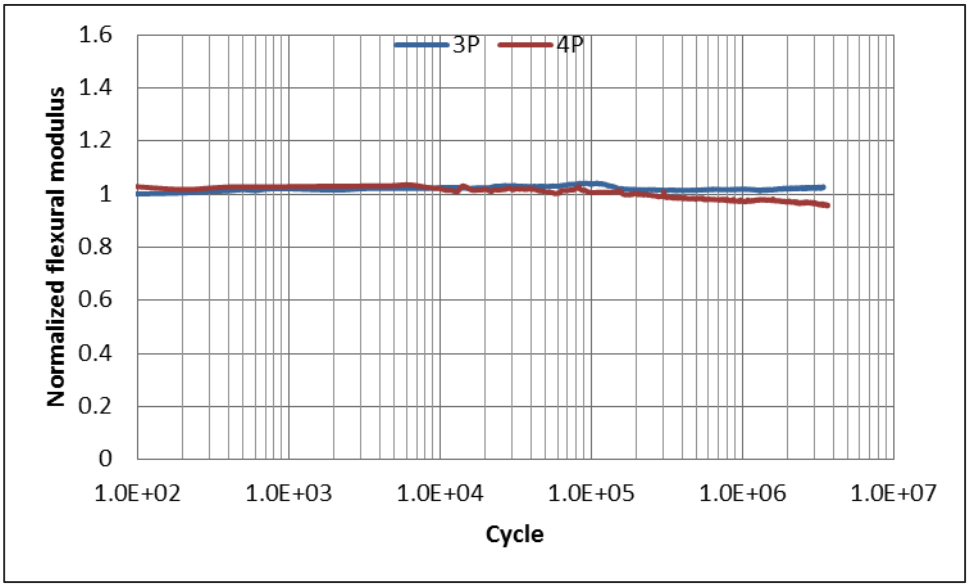

Figure 6.13 Typical fatigue stiffness of the CP-dry laminates with 'infinite fatigue life' in both 3-point and 4-point bending fatigue tests at the 80% UFS loading level. The fatigue stiffness was normalized to the flexural modulus which was tested in quasi-static bending.

For comparison, **Figure 6.14** shows the 'broken' cases of the CP-dry laminates tested in 3-point and 4-point bending. Both the specimens were tested at the highest loading level, 90% UFS, and both the fatigue lives were counted as no more than one million cycles. The 3-point case showed a flat curve of fatigue stiffness which was similar with the 80% UFS case; however it failed suddenly when the fracture accumulated to a critical value. The 4-point case presented an amplified stiffness reduction compared with the 80% UFS case until damaged plies accumulated to a critical value and then the specimen failed.

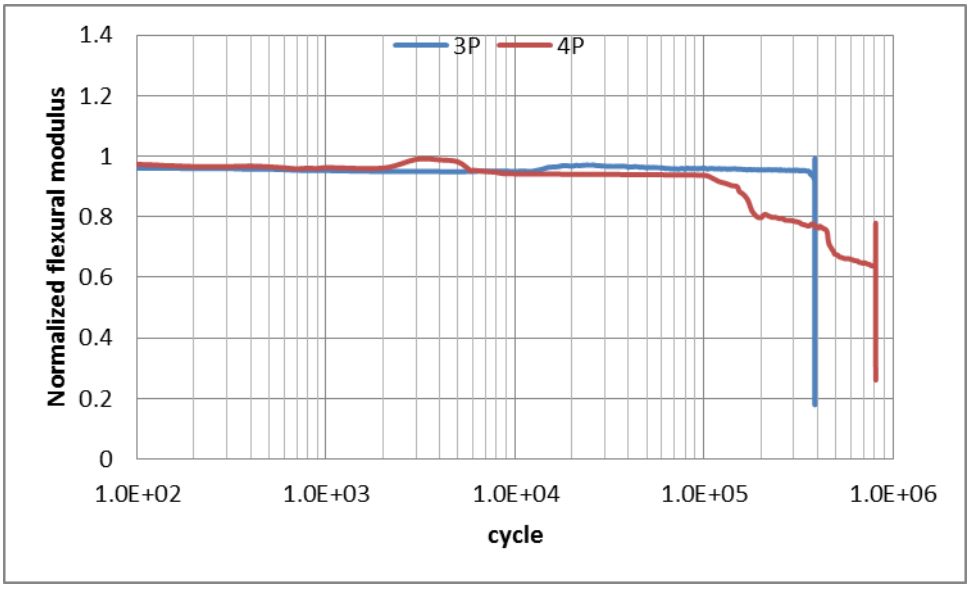

Figure 6.14 Typical fatigue stiffness of the CP-dry laminates in both 3-point and 4-point bending fatigue tests at 90% UFS loading level. Both the two specimens failed.

A similar trend can be seen from the fatigue stiffness of the UD-dry laminates, as shown in **Figure 6.15** and **Figure 6.16**. At the intermediate loading level, 80% UFS, the UD-dry specimen presented a flat curve of fatigue stiffness until the end of the test, regarded to be 'infinite fatigue life'. At the higher loading level, 90% UFS, the specimen failed suddenly in 3-point bending due to the fibre microbuckling which had been discussed for **Figure 4.8** and **Figure 4.10** in Chapter 4. Both the specimens failed after withstanding more than one million cycles. It is interesting to notice that the UD specimen failed and broke into two pieces rapidly in 4-point quasi-static bending test, and the fracture happened too quickly to be captured by a camera. However, in the fatigue test, the stiffness loss, shown step by step, can be seen clearly, as well as the delamination on the compressive surface of the specimen.

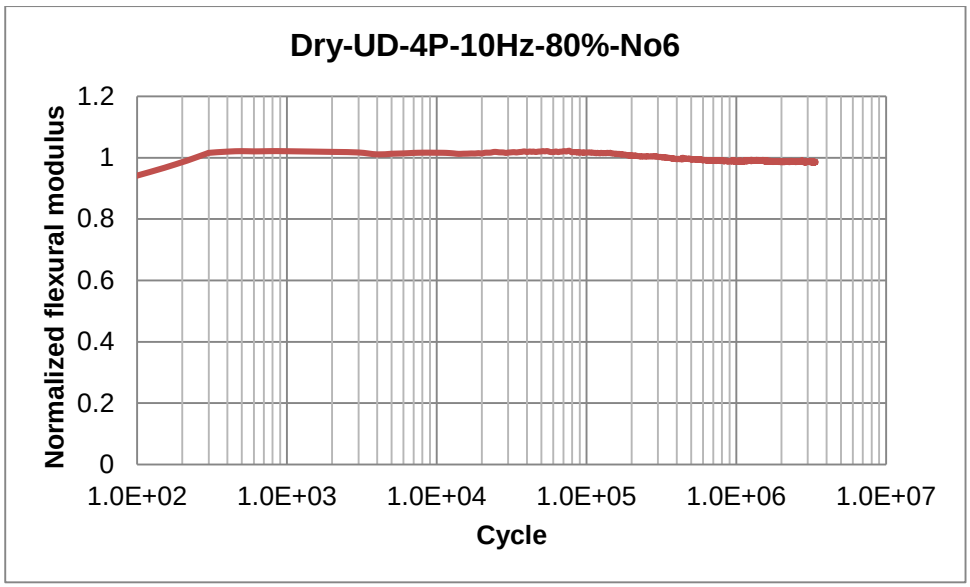

Figure 6.15 Typical fatigue stiffness of the UD-dry laminate in 4-point bending fatigue test at 80% UFS loading level. No UD-dry specimen was tested in 3-point bending at this loading level.

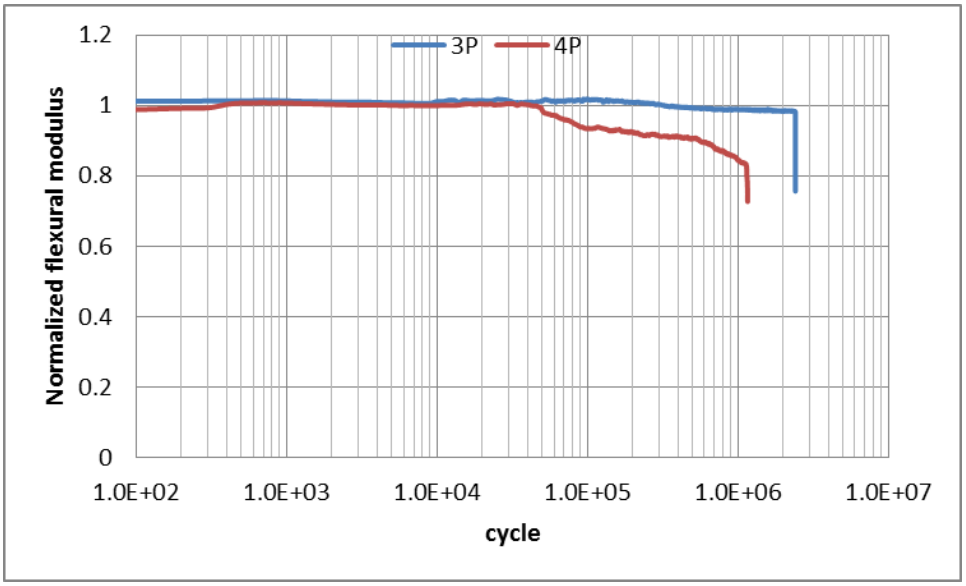

Figure 6.16 Typical fatigue stiffness of the UD-dry laminates in both 3-point and 4-point bending fatigue test at 90% UFS loading level

The fatigue stiffness unveiled the effects of **testing environments**, i.e. dry and wet conditions. **Figure 6.17** and **Figure 6.18** show the comparisons of the fatigue stiffness of the CP and UD laminates tested in dry and wet environments respectively. There are three curves of fatigue stiffness in each figure for the comparison: (a) CP-dry-90%, dry specimen tested at 90% UFS which failed in the end of the test; (b) CP-tap-80%, tap

water immersion specimen tested at 80% UFS which failed in the end of the test, and (c) CP-dry-80%, dry specimen tested at 80% UFS loading level which survived in the end of the test. No obvious difference can be found from the testing environments of the tap water, sea water and sea water with 70 bar hydrostatic pressure (specimen was immersed in the SP chamber until saturation, and was fatigue tested by wetting with sea water).

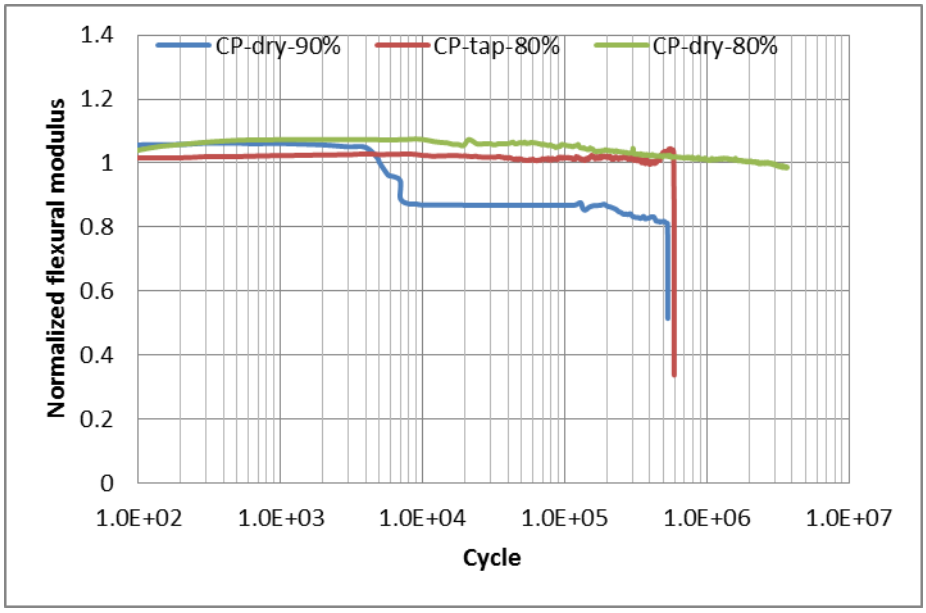

Figure 6.17 Typical fatigue stiffness of the CP laminates in 4-point bending fatigue test in dry and wet environments

As can be seen from **Figure 6.17**, the curves of fatigue stiffness, as well as the fatigue failure modes, depend on the loading levels and the testing environments. The CP-dry-90% specimen failed and showed similar fatigue life with the CP-tap-80% specimen, however the previous one was tested at the highest loading level while the wet specimen was tested at 80% UFS. Therefore, the water immersion degraded one level of the strength of FRP composites, and reduction in both crack initiation time and failure times were presented. On the other hand, no obvious stiffness loss can be seen from the CP-tap-80% specimen until it failed suddenly when the fracture accumulated to a critical value. This is different from the CP-dry-90% specimen which showed a step of approximate 10% stiffness reduction before it failed. The CP-dry-80% specimen survived in the end of the fatigue test although it showed a tiny stiffness reduction after

a couple of million cycles, which illustrated that there is a cut off strength for this kind of FRP composites for the fatigue behaviour.

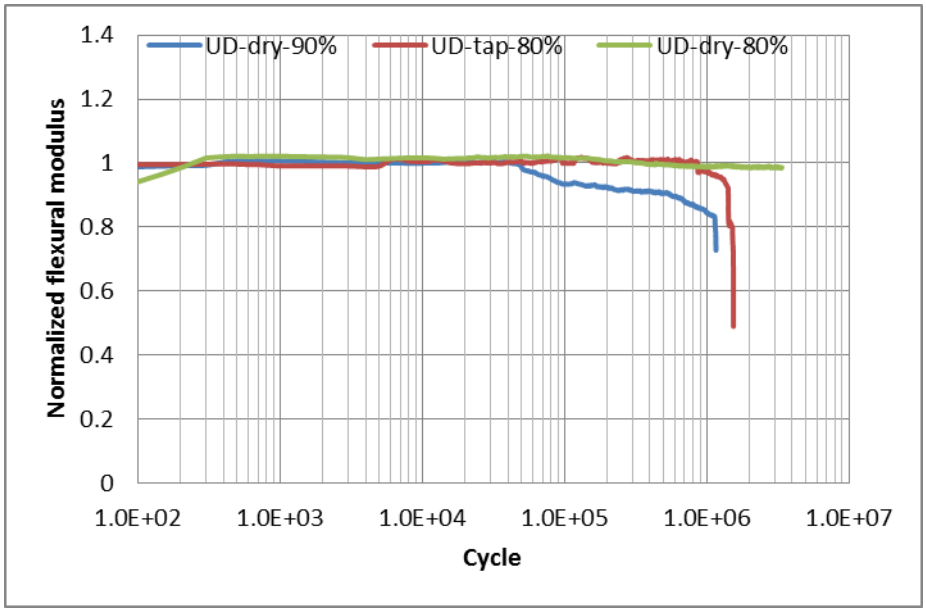

Figure 6.18 Typical fatigue stiffness of the UD laminates in 4-point bending fatigue test in dry and wet environments

The fatigue stiffness of UD laminates showed a similar trend although the failed specimens (UD-dry-90% and UD-tap-80%) withstood a higher fatigue cycle count. The comparison of the fatigue behaviour of these two layups demonstrates the high scatter of the composite fatigue. The observation that the fatigue failure process as well as the fatigue life of GFRP composites (Boller, 1964; Phillips, Scott et al., 1978; Yang, Kasamori et al., 1992) and CFRP composites (Sumsion, 1976; Morton, Kellas et al., 1988) are accelerated by water immersion had been reported.

Experimental evidence shows the fatigue failure was also affected by the **loading sequence**, i.e. quasi-static and cyclic (fatigue) loading. **Figure 6.19** and **Figure 6.20** provide the evidence of different failure modes of the CP laminate associated with different testing condition. In 3-point bending, as shown in **Figure 6.19**(a), the specimen failed by delamination caused by the maximum tensile stress at the bottom (tensile) surface. This failure mode had been discussed for **Figure 4.14** in Chapter 4. However, initial crack was found on the compressive surface of the CP specimen in the 3-point bending fatigue test, as shown in **Figure 6.19**(b). This initial crack did not cause the failure of the laminate immediately, but instead, it accumulated and then leading the

applied strength to a critical value until the laminate failed rapidly, as shown in **Figure 6.14**.

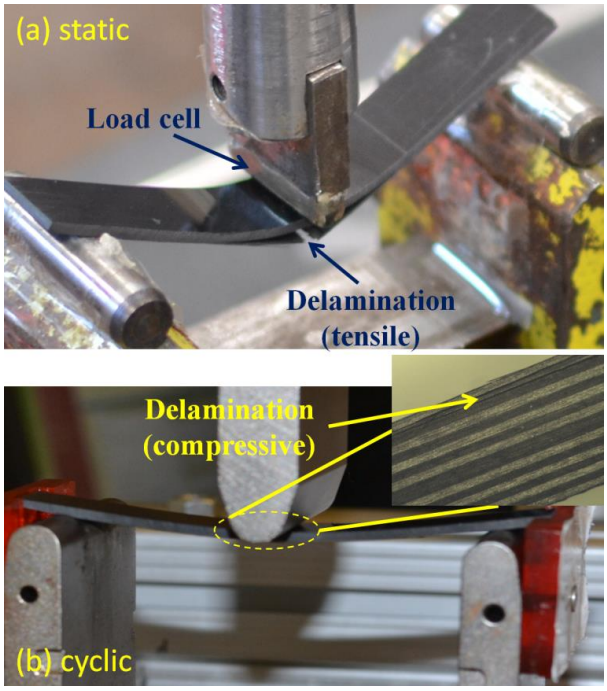

Figure 6.19 Comparison of the CP specimen failure mode in 3-point bending test: (a) quasi-static bending and (b) bending fatigue

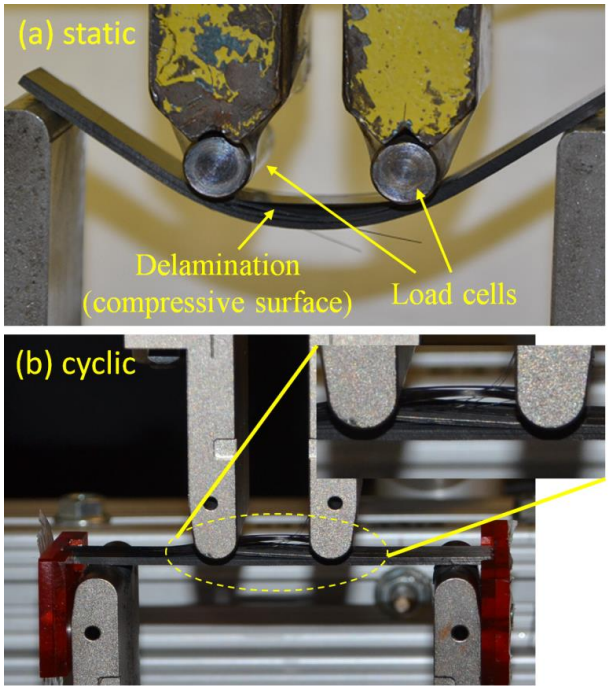

Figure 6.20 Comparison of the CP specimen failure mode in 4-point bending test: (a) quasi-static bending and (b) bending fatigue

Nevertheless, different failure modes were observed in 4-point bending cases. The specimens failed by delamination on the compressive surface regardless of the loading sequence (quasi-static or fatigue), as shown in **Figure 6.20**. This compressive delamination is regarded as **buckling-driven delamination** in this thesis, which is discussed in the later section on the FEA modelling in this chapter. It should be noted that, compressive delamination failure was also observed from the UD specimen in the 4-point bending fatigue test. The UD specimen, which was tested in 4-point quasi-static bending, broke into two parts too rapidly to be observed by a camera, however the fracture surface indicated the crack initialized at the contact region on the compressive surface, as shown in **Figure 6.21**.

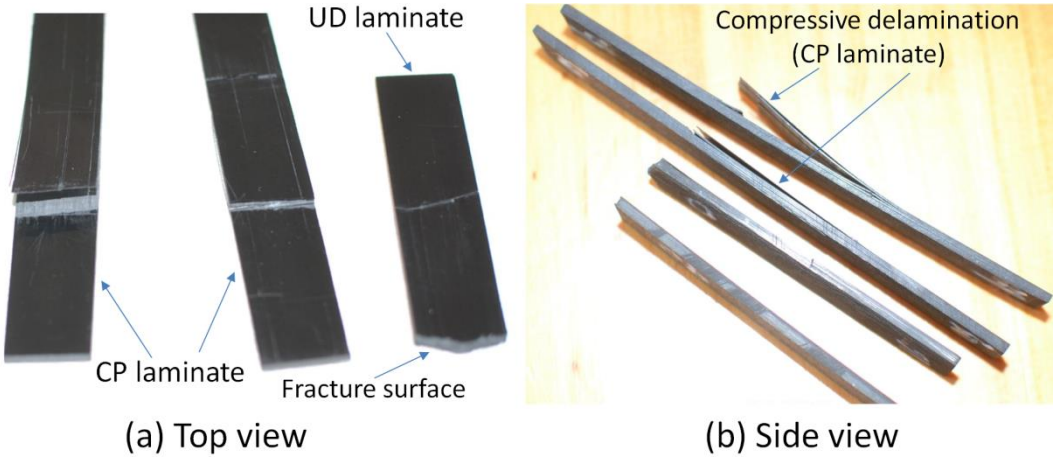

Figure 6.21 Typical failure modes of CP and UD laminates tested in 4-point quasi-static bending

6.2 Creep tests

6.2.1 *Machine setup*

Creep is also known as static fatigue, or stress corrosion. According to the open literature (Petermann and Schulte, 2002), the UD and CP laminates have no creep, therefore the angle-ply layup [±45] is widely used in composite structures combining with unidirectional plies whereas tensile loads are carried by the unidirectional plies, the shear loads are withstood by angle-ply layers (Reeder, Song et al., 2002). Only the angle-ply laminate was creep tested in this thesis, including the dry, tap, sea and SP

specimens. The creep test was carried out on a universal INSTRON machine at room temperature, conducted by ISO standard (ISO899-2:2003, 2003). **Figure 6.22** gives a snapshot of the angle-ply specimen mounted on the INSTRON machine for the creep test.

Figure 6.22 3-point bending creep test for the angle-ply laminate

The standard recommends a relation between the span and the specimen thickness,

$$L = (16 \pm 1)h \qquad (6\text{-}11)$$

In fact, the ASTM standard (D7264, 2007) also recommends this relation for the flexural test of FRP composites. Additionally the standard suggests 13mm for the width of specimen which was adopted in this thesis. The average thickness of the angle-ply laminates for the creep test was 1.95mm, which was the same as those used for diffusion test list in Chapter 5. Therefore, the 3-point bending span was defined as 32mm and the angle-ply laminate was sliced into dimension of $Length \times Width = 40mm \times 13mm$.

Based on the CLT formulae shown in Chapter 3 and the material properties list in **Table 3-3**, the flexural modulus of angle-ply laminate $[\pm 45]_{4s}$ was calculated as 16 GPa, which was a reference to compare the apparent flexural modulus in the creep test. In fact, the quasi-static 3-point bending test was carried out to investigate the specimen behaviour

prior to the creep test, using the same specimen dimension. The typical relation between deflection and flexural force is plotted in **Figure 6.23**.

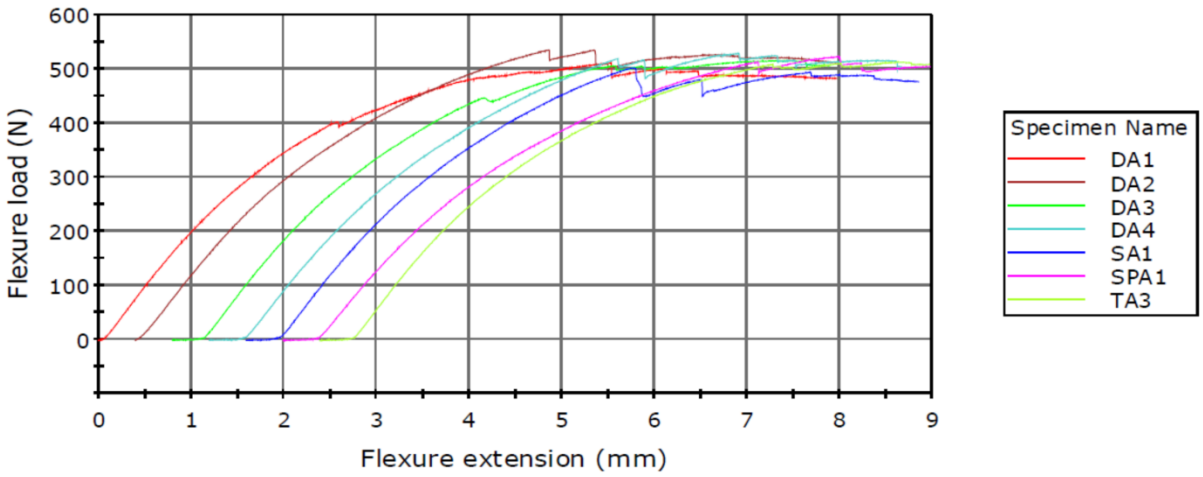

Figure 6.23 The loading curves of the angle-ply laminates in quasi-static 3-point bending test. DA: angle-ply laminate without immersion; SA: sea water immersion; SPA: sea water immersion with 70bar hydrostatic pressure; TA: tap water immersion. The 'DA1' specimen was tested at 1mm/min strain rate, while all the others were at 2mm/min.

As can be seen from the figure, the loading curves were nonlinear and also dependent on the loading sequence, i.e. the extension rate. The specimen 'DA1', who was tested at a relatively lower extension rate (1mm/min), presented a relatively smooth parabolic curve without obvious stiffness reduction at the maximum loading point. This is quite different from the others which were tested at 2mm/min shown in the same figure. Moreover there was no linear stage to calculate the flexural modulus. However, no obvious difference was found among the four specimen conditions, i.e. dry, tap water immersion, sea water immersion and sea water immersion with 70 bar hydrostatic pressure.

In the quasi-static 3-point bending test, an unidentified failure mode was observed, as shown in **Figure 6.24**. A periodic fibre break can be found to be parallel to the load cell at the contact area on the compressive surface. As can be estimated from the figure, the periodic distance of this fibre break was in range of 200-300μm. One possible reason is the surface ply failed by in-plane shear stress which was induced by the compressive

stress due to the nature of bending, since the maximum compressive stress appears at the top surface. According to the CLT formulation, the interaction ratio η_{xyx} of the angle-ply laminate $[\pm 45]_{4s}$ can be calculated as -0.5, which means that the in-plane shear strain γ_{xy} induced by the normal stress σ_x can be as high as half of the normal strain ε_x.

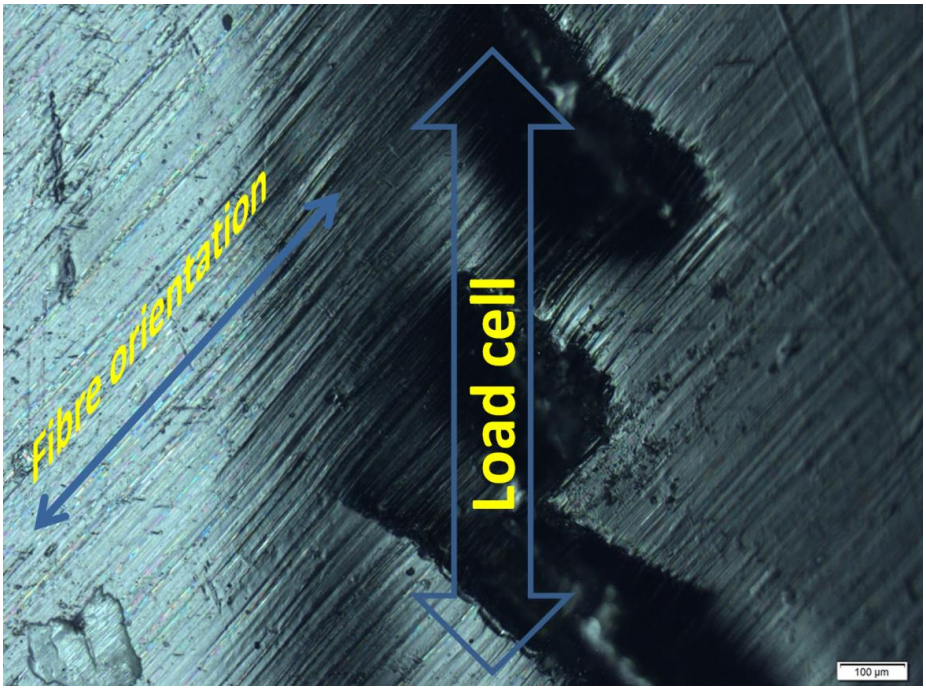

Figure 6.24 The failure mode of AP-dry specimen in 3-point bending quasi-static test

The apparent yield strength was estimated to be in the order of 500MPa (corresponding to approximately 500 N) and no significant stiffness loss was found under 400 N according to **Figure 6.23**, therefore three loading levels were applied for the creep test: 200N, 300N and 400N, corresponding to 194MPa, 291MPa and 388MPa with the given specimen dimension. A ramp rate of 100 N/min (approximately 0.5 mm/min) was applied until the pre-defined loading level, after that the loading cell was held at a constant force and the deflection was recoded every 5 seconds. At each loading level, only one specimen corresponding to the immersion condition (dry, tap water and sea water immersions) was tested.

The typical loading curve of an AP-dry specimen up to 300 N is potted in **Figure 6.25**, showing a good linear relation between the flexural force and deflection. The apparent

flexural modulus was a fraction lower than the CLT prediction; one possible reason is because of the short span in the 3-point bending.

Table 6-2 gives an overview of the flexural modulus of different immersion conditions according to the three loading levels. As can be seen from the table, at the same loading level, the flexural modulus extracted from the linear stage provided a lower value for the dry specimen than those of the other immersions, which is quite similar to the matrix dominated laminate (i.e. UT $[90]_{16}$ laminate). One possible reason is that the matrix became stiffer after the water immersion. However, the information shown in the table cannot provide sufficient evidence to distinguish the effects of the three types of water immersions on the apparent flexural modulus.

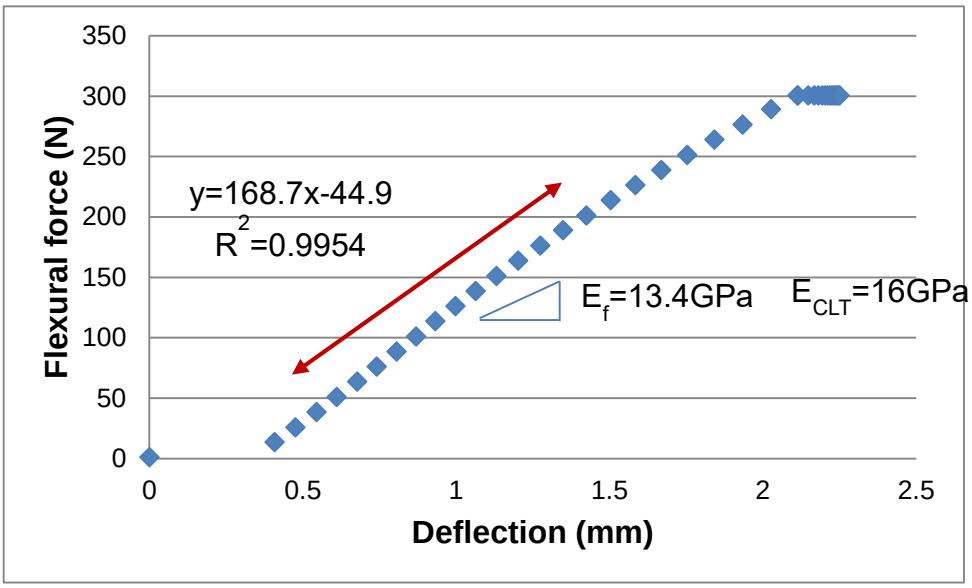

Figure 6.25 The typical loading curve of an AP-dry specimen in 3-point bending creep test, showing linear relationship between load and deflection

Table 6-2 Flexural modulus of AP laminate at different loading level and immersions

	200N	300N	400N
AP-dry	13.4GPa	13.4GPa	13.6GPa
AP-sea	14.2GPa	13.4GPa	14.1GPa
AP-SP	14.0GPa	13.7GPa	14.2GPa
AP-tap	14.3GPa	13.1GPa	14.3GPa

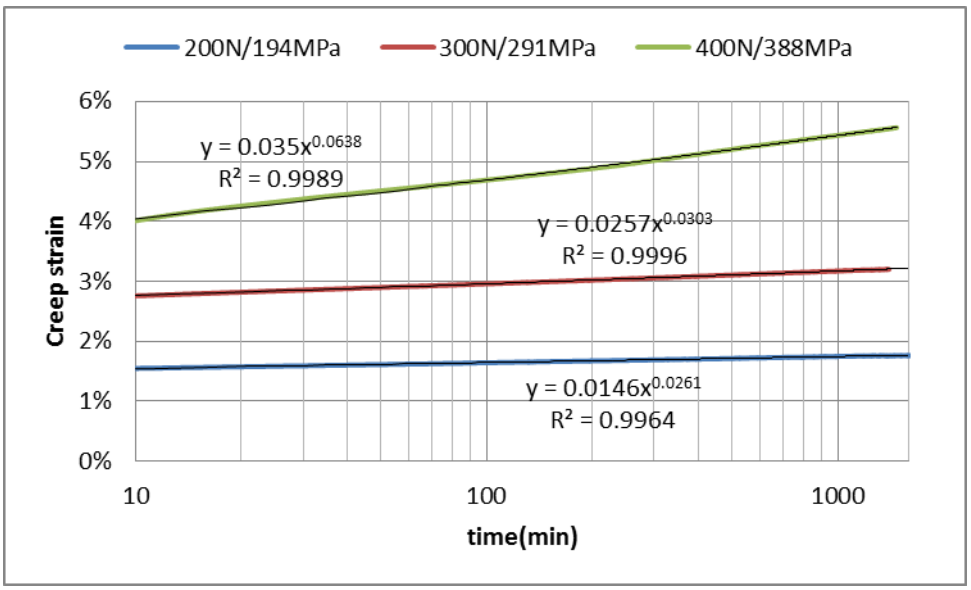

Figure 6.26 The typical deflection curve of an AP-dry specimen in 3-point bending creep test at the creep deformation stage, showing a perfect power law by the loading time. The power law fitting results are also shown in the figure.

6.2.2 *Creep stiffness*

In the previous section, it has been shown that the flexural force was proportional to the deflection at the increasing loading stage and later on the deflection was exponential to the creep time at the constant loading stage. Due to the relatively short span, the flexural modulus extracted from the increasing loading stage showed relatively high variation. The apparent flexural modulus was also highly dependent on the extension rate. The flexural force was proportional to the deflection in case of very low extension rate, i.e. 0.5 mm/min. Therefore, the creep of the angle-ply laminate is to be investigated by both the creep strain and stiffness.

According to the ISO standard (ISO899-2:2003, 2003), the creep strain and creep stiffness (flexural-creep modulus) can be calculated by,

$$\varepsilon_t = \frac{6D_t h}{L^2}$$
$$E_t = \frac{L^3 F}{4wh^3 D_t} \qquad (6\text{-}12)$$

where D_t is the deflection at the loading point at time t; w and h are the width and thickness of the specimen respectively; F is the applied force; and L is the span. The equation has no terms to represent the creep deformation at the increasing loading stage. (Nutting, 1921) proposed a more general function which includes the terms of loading level and the deformation at both the increasing loading stage and constant loading stage (creep deformation),

$$\varepsilon(\sigma,t)=\varepsilon_0(\sigma,t)+\varepsilon_t(\sigma,t) \tag{6-13}$$

In case of very slow extension rate and intermediate stress level, for example 0.5 mm/min and 388 MPa (the yield stress was approximate 486 MPa) in this thesis, the first term of the equation $\varepsilon_0(\sigma)$ is linear to the loading time. The second term $\varepsilon_t(\sigma,t)$ should contain an exponential expression. (Nutting, 1921) proposed an empirical expression for the second term,

$$\varepsilon_t(\sigma,t)=K\sigma^m t^n \tag{6-14}$$

According to experimental observation (Findley and Davis, 2013), the exponential parameter of time is independent on the temperature.

Therefore, equation (6-13) has a form like this,

$$\varepsilon(\sigma,t)=\begin{cases} C_1 t, t\le F/R_F \\ C_2\sigma^{C_3}t^{C_4}, t>F/R_F \end{cases} \tag{6-15}$$

where C_1, C_2, C_3 and C_4, are the material properties, F, R_F are the target loading level in N and the loading rate in N/min respectively.

The first parameter C_1 can be fitted by the relation of the strains at the four loading levels (0N, 200N, 300N and 400N), while the others were fitted by MATLAB toolbox 'CFTOOL'. For the fitting of the three parameters of the exponential terms, the fitting tool returned a value with small deviation for the last parameter C_4 at different loading levels; however the other parameters compete to each other at different loading levels. Therefore, the value fitted from the intermediate loading level (300N, 291MPa) was used to represent the corresponding immersion condition. **Table 6-3** lists the fitting results of the four parameters for the four immersions.

Table 6-3 The fitting results of the four parameters for equation (6-15). The R^2 value is also given in the table (the unit of stress: MPa; time: minute).

	C_1	C_2	C_3	C_4	R^2
Dry	0.0089	0.0017	0.48	0.03	0.9996
Sea	0.0081	0.002	0.45	0.029	0.9987
SP	0.0083	0.0017	0.45	0.03	0.9936
Tap	0.0081	0.002	0.43	0.04	0.9995

After the water immersion, the specimen became stiffer and the maximum deflection of dry specimen was higher than those of water immersions, which has been discussed in the previous section. It has been known that the viscoelastic response of polymers and polymeric composites is strongly coupled with the moisture content (Weitsman, 1977; Weitsman, 1987; Cai and Weitsman, 1994); however there was no obvious evidence summarized to identify the effects of water immersion on the creep deformation according to the four parameters shown in **Table 6-3**. One possible reason is that those immersion specimens were not tested in wet environment (e.g. covered by a wet sponge). This is similar with the phenomenon observed from the fatigue test, which suggests that the effects of water immersion on the creep deformation are more likely to be a physical process (invertible) in short time of marine environment exposure rather than chemical process. (Kibler, 1980) showed similar results, reporting that the creep compliance of AS/3502 $[\pm 45]_{2s}$ specimen showed only a tiny fluctuation in different levels of humidity but a huge shift due to the elevated temperature. At the meantime, the degradation of fibre/matrix interphase from the SEM study, shown in **Figure 5.29** and **Figure 5.30**, indicates that the creep response might be different for long exposure time.

Figure 6.27, **Figure 6.28** and **Figure 6.29** show the creep stiffness of the angle-ply laminate in the four immersion conditions at 200 N, 300 N and 400 N loading levels respectively. Since the same loading rate, 100 N/min was applied for all specimens; the time of the increasing loading stages were 2, 3 and 4 minutes for the three cases corresponding to the different onsets of the creep deformation shown in the figures. The common characteristics which can be seen from the three figures are that the specimen became stiffer after water immersion and the creep stiffness curves plotted in the three figures suggest a power law for the history.

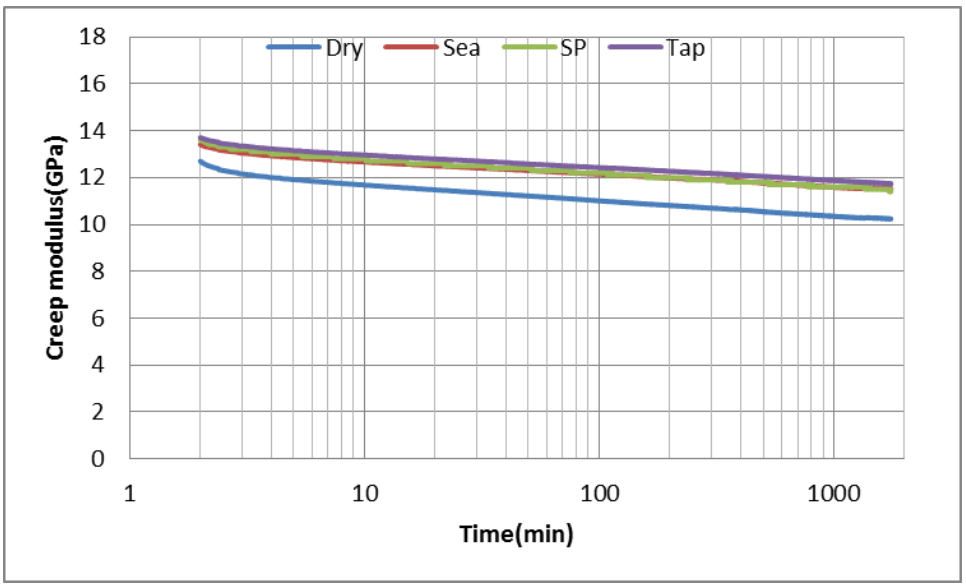

Figure 6.27 Creep stiffness of AP specimen at 200N

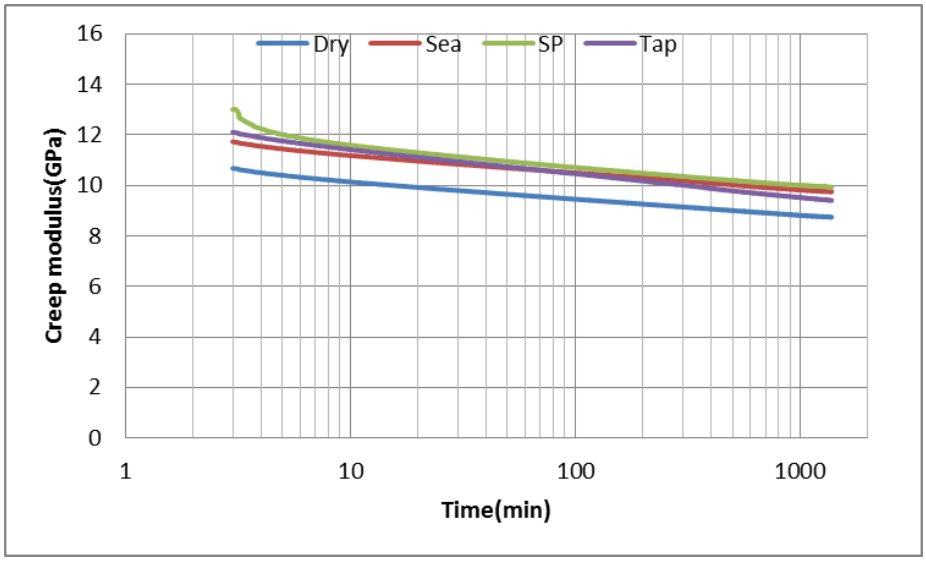

Figure 6.28 Creep stiffness of AP specimen at 300N

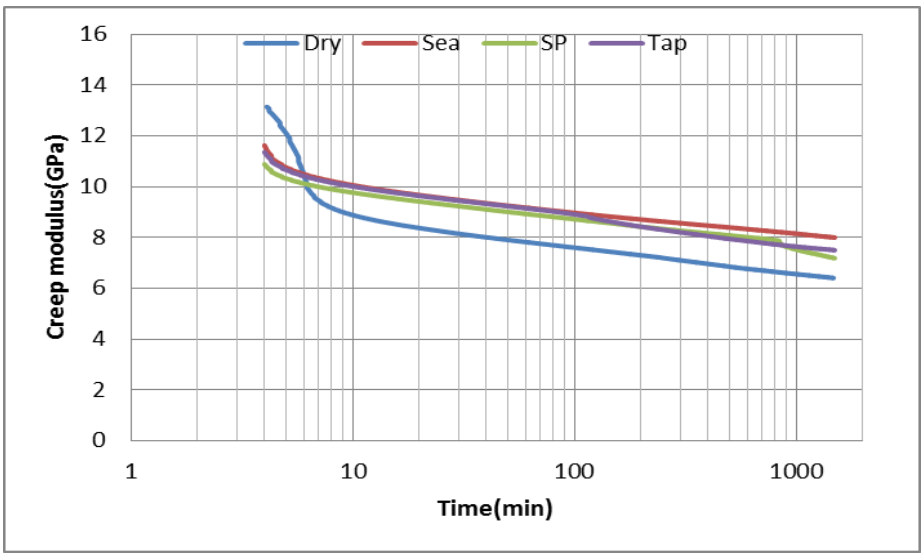

Figure 6.29 Creep stiffness of AP specimen at 400N

6.3 Buckling-driven delamination

The previous section has shown that compressive delamination was the main failure mode of bending fatigue. Compressive delamination is called buckling-driven delamination in this thesis. A comparative study of the bending fatigue was conducted using FEA method. Only the CP laminate was modelled for the study, and the investigation of the other laminate layups can be extended using the same technique.

6.3.1 *Virtual crack closure technique*

VCCT uses linear elastic fracture mechanics (LEFM) concepts based on the strain energy release rate of crack tip deformation, and compares the strain energy release rate to interlaminar fracture toughness (Rybicki and Kanninen, 1977). For the pure mode I, as shown in **Figure 6.30**, nodes 2 and 5 will start to release when,

$$\frac{1}{2}\frac{v_{1,6}F_{v,2,5}}{wd} = G_I \geq G_{IC} \qquad (6\text{-}15)$$

where G_I and G_{IC} are mode I energy release rate and the critical energy release rate; w is the width; $F_{v,2,5}$ is the vertical force between nodes 2 and 5; $v_{1,6}$ is the vertical displacement between nodes 1 and 6. Mode II can be treated similarly.

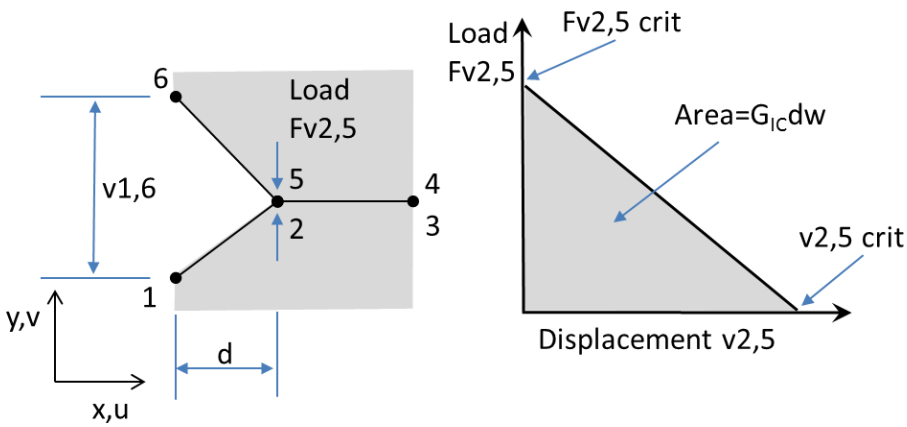

Figure 6.30 Configuration of the virtual crack closure technique

The calculated G value must exceed the critical G_c before the crack propagates, and mixed mode should be taken into account to evaluate the equivalent energy release rate. Compared with the power law which requires three parameters corresponding to the three modes, the Benzeggagh-Kenane criterion by (Benzeggagh and Kenane, 1996), also known as BK law, is easier to implement (ABAQUS, 2015),

$$G_{equivC} = G_{IC} + \left(G_{IIC} - G_{IIIC}\right)\left(\frac{G_{IIC} + G_{IIIC}}{G_{IC} + G_{IIC} + G_{IIIC}}\right)^{\eta} \qquad (6\text{-}16)$$

where η is the BK law fitting parameter. This criterion was used in the present work.

The onset and fatigue delamination growth at the interfaces are characterized by using the Paris law, which relates crack growth rate da/dN to the relative strain energy release rate, as shown in **Figure 6.31**. The fatigue crack growth initiation criterion and the crack growth rate are defined as (ABAQUS, 2015),

$$\frac{N}{c_1 \Delta G^{c_2}} \geq 1 \qquad (6\text{-}17\text{-}1)$$
$$\Delta G = G_{max} - G_{min}$$

$$\frac{da}{dN} = c_3 \Delta G^{c_4} \qquad (6\text{-}17\text{-}2)$$

where N is fatigue cycle; a is the crack length; c_1, c_2, c_3, c_4 are material constants; G_{max} and G_{min} correspond to the strain energy release rates when the structure is loaded up to F_{max} and F_{min} respectively.

The interface elements at the crack tips will not be released unless the equation (6-17-1) and $G_{max}>G_{thress}$ are satisfied; and then the crack propagates at an exponential stage (so called Paris regime); after that the crack will grow catastrophically when the G_{max} is higher than the strain energy release rate upper limit G_{pl}.

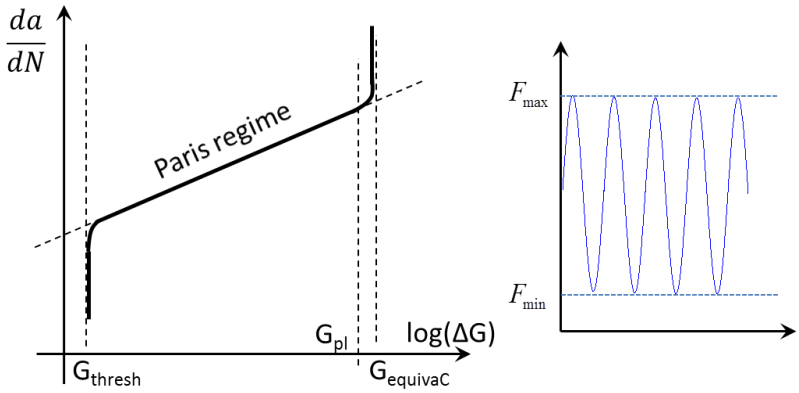

Figure 6.31 Schematics of fatigue crack growth relative to the Paris law. There is no fatigue crack initiation or growth when the strain energy release rate is lower than G_{thress}.

6.3.2 *FEA implementation*

In 4-point bending, the cross-ply laminate is symmetric in geometry, material properties and the boundary condition, therefore the model was simplified to half geometry and the crack was defined at the interface between ply15 (unidirectional transverse lamina, thickness 0.12mm) and ply16 (unidirectional lamina, thickness 0.12mm). The lower section ($[0/90]_{3s}90/0$, thickness 1.68mm), ply1-14 was considered as homogeneous orthotropic, whose material properties (flexural elastic properties) were calculated by CLT formula. **Figure 6.32** illustrates the FEA model including three layers. The two rollers were considered as rigid body, and contact boundary condition was applied for the interaction between the rollers and the specimen.

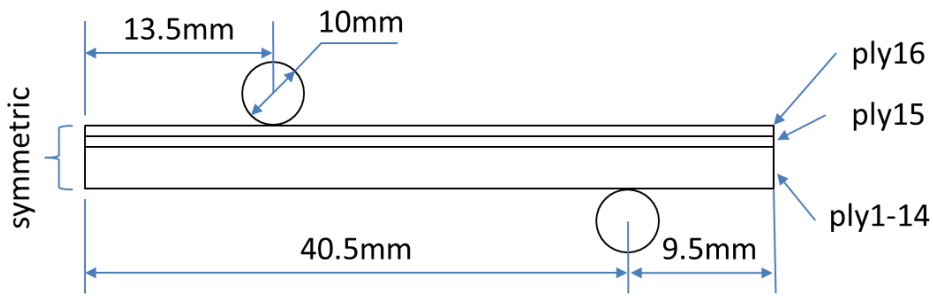

Figure 6.32 Schematics of the three layers FEA model

According to (Liu and Nairn, 1992; Hottengada, 2006), the 977-2 epoxy based composites have G_C in the range of 600-2400 J/m^2. Therefore, an intermediate value, G_c=1500J/m^2 was applied on the FEA model. **Table 6-4** gives the material properties, including elastic and fracture properties.

Table 6-4 Material properties for FEA simulation. The out-of-plane direction in 3D corresponds to the transverse direction in 2D model, i.e. E_y=E_3. For the comparison, the properties of CP $[0/90]_{4s}$ laminate are also shown in the table.

Elastic properties					Fracture properties	
	ply16	ply15	ply1-14	$[0/90]_{4s}$	G_{IC}(J/m^2)	1500
E_x(GPa)	139	8.8	88	86	G_{IIC}(J/m^2)	1500
E_y(GPa)	8.8	8.8	11	11	G_{IIIC}(J/m^2)	1500
ν_{xy}	0.26	0.02	0.04	0.04	*η	1.75
ν_{yz}	0.48	0.26	0.44	0.43	c_1	0.5
ν_{xz}	0.26	0.48	0.41	0.41	c_2	-0.1
G_{xy}(GPa)	4.7	4.7	4.7	4.7	c_3	4.88E-06
G_{xz}(GPa)	4.7	3	4	4	c_4	1.15

***The fitting parameter η for BK law and the four parameters $c_{1,2,3,4}$ for Paris law were estimated based on reference (ABAQUS, 2015).**

To the VCCT, an initial crack should be embedded into the interfacial elements and the crack path should be predefined. It is reasonable to assume that the crack was initialized under the load cell due to the stress concentration. According to the 3D solid modelling of quasi-static bending, presented in Chapter 4, the solution was mesh independent when each ply was divided into three elements through thickness, however the contact region should be refined to capture the stress concentration due to the contact. For the fatigue modelling, the loading history was simplified to a triangular function instead of the sinusoidal shape. **Figure 6.33** plots the mesh of the FEA model and the schematics of loading history. The FEA model was solved by ABAQUS/Standard.

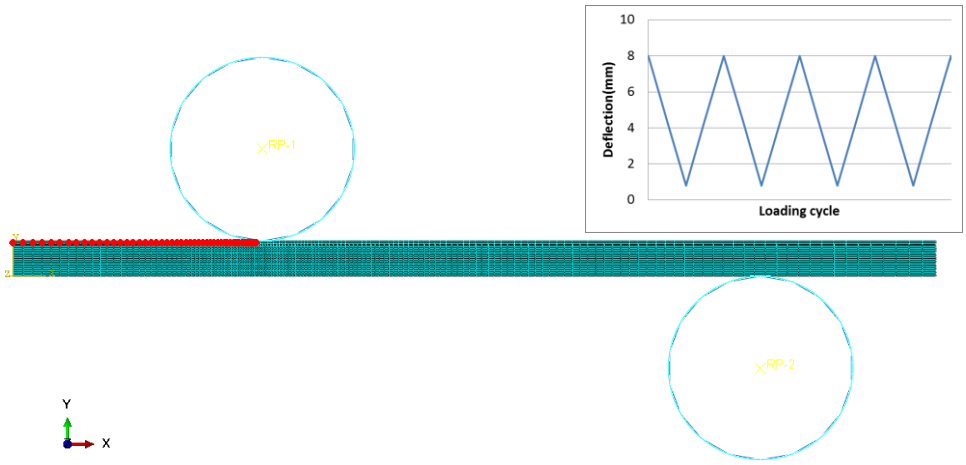

Figure 6.33 Mesh plot of the three layer FEA model and the loading history. An initial crack (0.2 mm) was embedded at the interface between ply15 and ply16 under the load cell. The crack path (shown as red dots) is also shown in the figure.

It should be noted that the maximum deflection had exceeded the 'large-deflection criterion'; therefore nonlinear behaviour must be taken into account. **Figure 6.34** presents the stress distribution of the whole model. The buckling-driven delamination is clearly shown in the figure. Multi cracks are not allowed to cross each other according to the current FEA technique (ABAQUS, 2015); therefore ply16 still withstood part of the compressive stress and the stiffness reduction was not as significant as the experimental observation after the buckling.

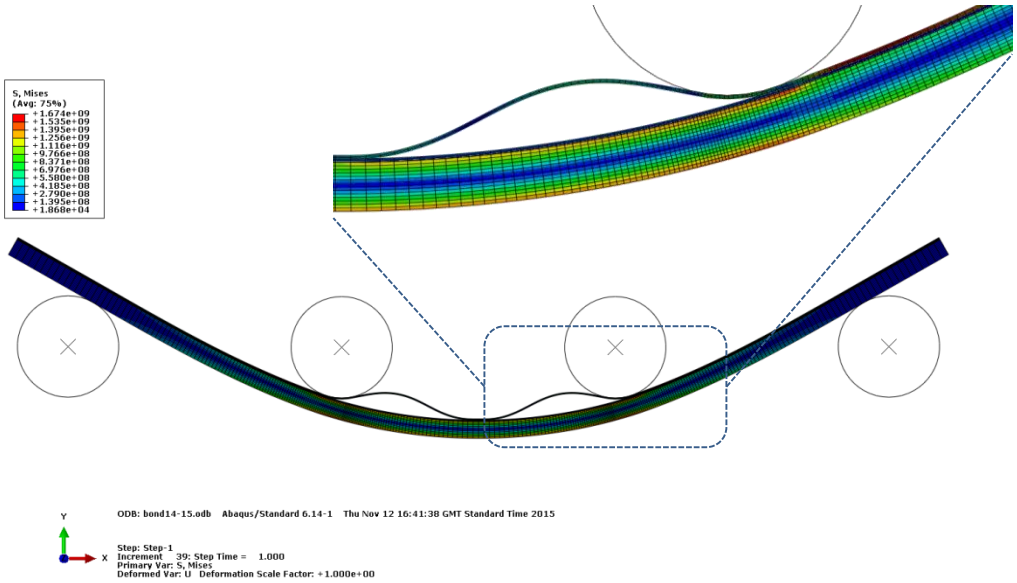

Figure 6.34 Stress distribution in the bending fatigue. A magnified view of the delamination is also shown in the figure.

Figure 6.35 compares the flexural force-deflection curves of the five cases. For the case (a), FEA simulation without initial crack, the reaction force simultaneously increased with the increase of deflection and the curve was linear until the deflection was close to about 10% of the bending span (large deflection criterion). According to the CLT formula, the apparent flexural modulus of CP laminate ($[0/90]_{4s}$) is calculated as 86 GPa, shown in **Table 6-3**, which is a higher than the experimental data (measured as 80 GPa), therefore the reaction force in the FEA simulation showed a higher value than the experiment (case b) at the same deflection. For the cases (c-e), where FEA simulation is with 0.2mm initial crack and $G_{IC} = 1200J/m^2, 1500J/m^2, 1800J/m^2$ respectively, the curve showed zigzag aspect at the linear stage indicating the debonding of the interfacial elements. With the growth of the crack length and the increase of deflection as well as the compressive stress, the part of ply16 above the crack buckled when the loading was increased to approximately 90% of the ultimate flexural strength, leading to a catastrophic delamination, therefore the curve showed a significant oscillation. In FEA, ply16 still withstood compressive stress after it buckled; therefore the stiffness was relatively high. As a contrast, the experiment observation showed that ply16 failed after it buckled and the stiffness reduced significantly.

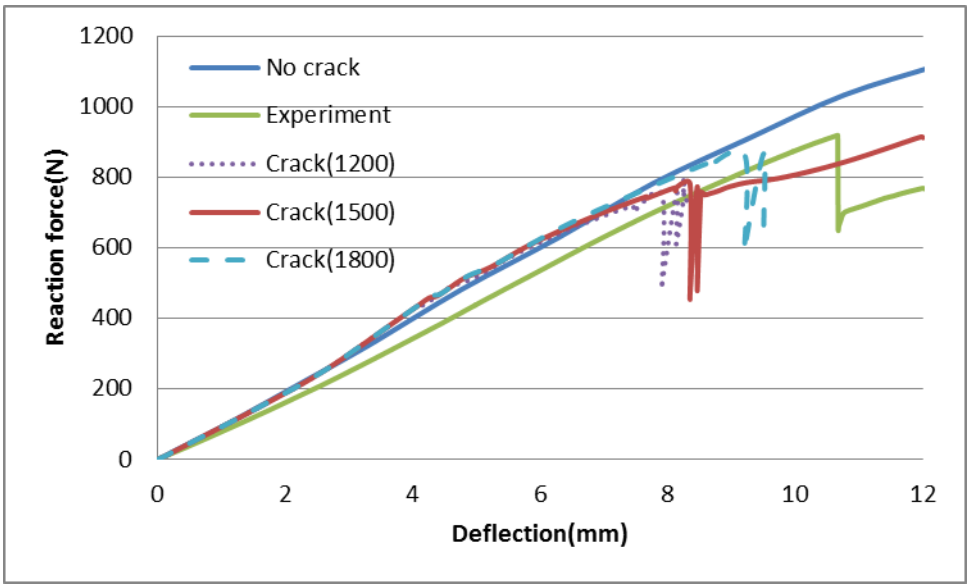

Figure 6.35 Relation between reaction force and deflection for five cases: (a) FEA simulation without initial crack; (b) a typical experimental curve of CP-dry specimen; and (c-e) FEA simulation with 0.2mm initial crack.

Figure 6.36 and Figure 6.37 present the distributions of mode I and mode II strain energy release rates along the crack path at the onset of buckling and after catastrophic delamination. It is apparent that the crack propagated in a single direction due to the constraint of the load cell. It can be seen from Figure 6.36 that the onset of buckling was associated with the mode I; however the mode I strain energy release rate reduced to zero exponentially when the buckling initialized, after that the delamination was driven by mode II according to Figure 6.37. Therefore, the onset of the buckling was mode I dominated while the crack propagation was mode II dominated.

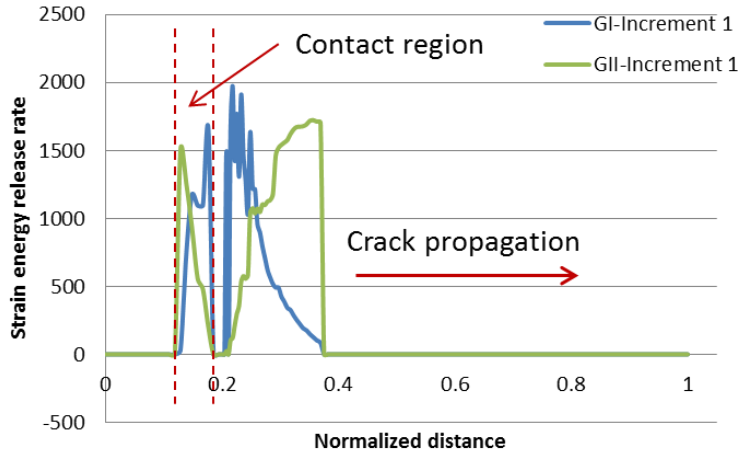

Figure 6.36 Distributions of mode I and mode II strain energy release rates along the crack path when the buckling initialized. The crack path was normalized.

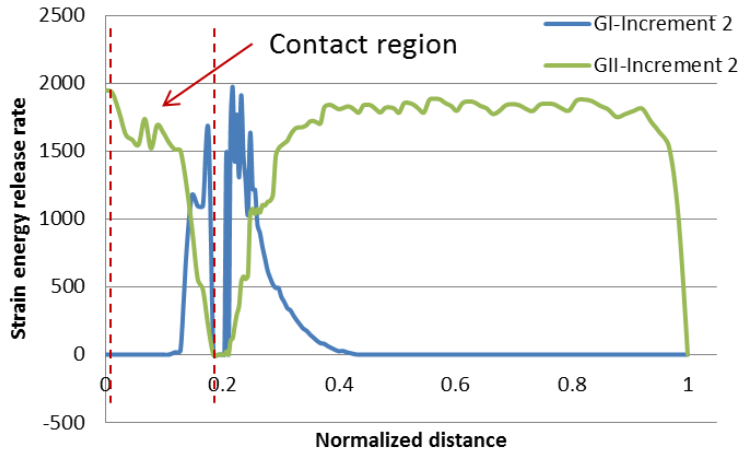

Figure 6.37 Distributions of mode I and mode II strain energy release rates along the crack path after the catastrophic delamination. The contact region enlarged due to the tangential slide of the specimen/load cell and the buckling deformation of ply16.

It was observed that the initial crack length had no effect on the onset of the buckling if it was shorter than a critical length. Once the buckling initialized, the crack propagated rapidly, corresponding to a very narrow band of time increment in FEA. The parametric study on the critical strain energy release rate showed that the buckling initialized at a larger deflection in the case of higher critical strain energy release rate, as shown in **Figure 6.35**. However the deflection at buckling was not as large as that observed in the experiment due to the artificial initial crack in the FEA. Therefore, the initial crack must be critical to the flexural strength and the fatigue life. Since the initial crack is caused by the stress concentration, the apparent flexural strength is expected to be significantly higher if the stress concentration is reduced, for instance, by increasing the radius of the load arm.

Recalling the fatigue stiffness of the CP specimen from Fig.6-14, the initial crack was induced by the stress concentration at relatively low cycle count at the highest loading level. Since this loading level was very close to the criterion of buckling shown in **Figure 6.35**, ply16 failed by the buckling-driven delamination rapidly, corresponding to the stiffness reduction shown in **Figure 6.14**. Since the onset of the buckling is associated with the mode I strain energy release rate, this may lead to an assumption that those FRP composites with higher mode I strain energy release rate are expected to have better fatigue life at the highest loading level.

The 2D FEA model has no transverse information; therefore a comprehensive 3D solid model was built to compare with the 2D model. The 3D solid model was similar with the 2D, containing a three-layer structure. Taking advantage of the symmetry it is sufficient to consider a quarter of the region. The 3D FEA model suffered convergent problem if the load cells were defined as rigid body, therefore they were designated to be steel. The mesh near the transverse edge was refined in order to capture the edge effect. Due to the limits of the computing resource, the through-thickness mesh of ply15 and ply16 was only divided into two layers. **Figure 6.38** shows the similar buckling-driven delamination in the 3D solid model.

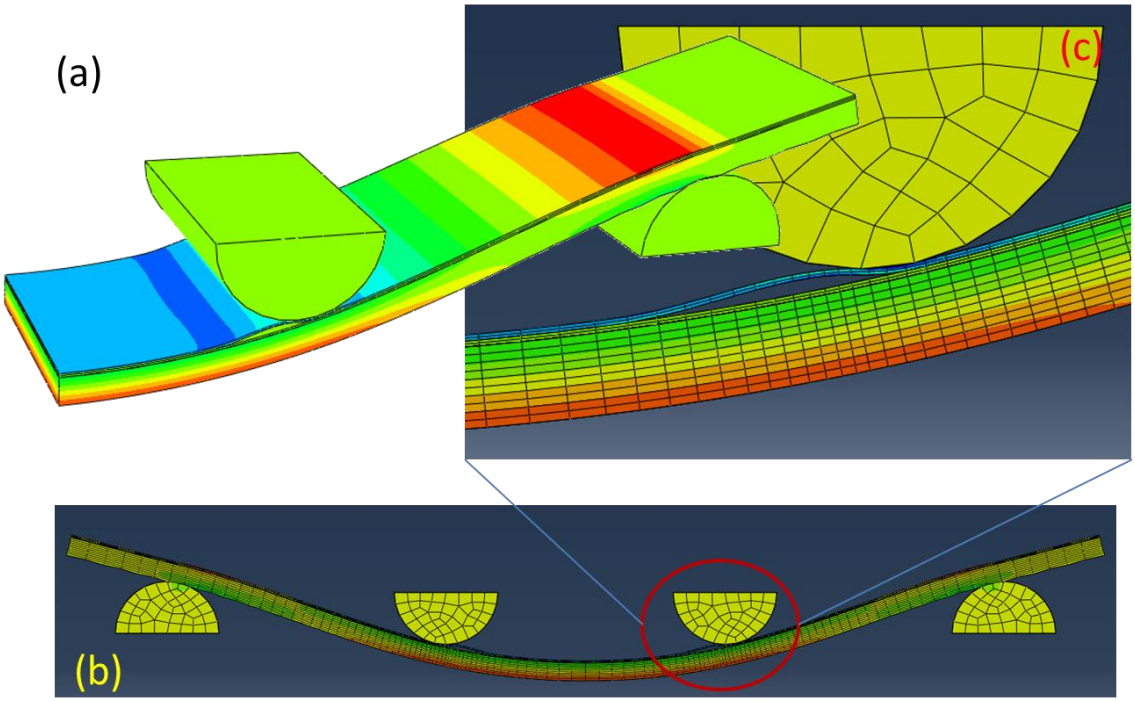

Figure 6.38 Distribution of longitudinal stress component (s11) of the 3D solid FEA model: (a) isotropic view; (b) side view; and (c) a magnified side view.

Figure 6.39 presents the progressive bonding state of 3D solid model. Although an initial crack was embedded underneath the load cell, it was found that the foregoing debonding elements were formed at the edge during the fatigue crack propagation, as shown in increment 2, and then the crack propagated through the transverse direction, as shown in increment 3. For an intact specimen in the experiment, it is reasonable to state that the crack is induced at the two edges underneath the load cell by the combination of the stress concentration and edge effect.

Therefore, the buckling-driven delamination in fatigue was formed at four steps, as shown in **Figure 6.40**: (a) the edge cracks were induced underneath the load cell; (b) the edge cracks penetrated inside the laminate to form the initial crack (which was embedded in the FEA model); (c) the edge cracks lead the foregoing fracture during fatigue; until (d) the crack length met the criterion of buckling and then the buckling drove a catastrophic delamination. After the first compressive ply (top surface) failed by the buckling-driven delamination, the second ply repeated the same process, and then the third ply (as shown in **Figure 6.12**) … until the whole specimen failed.

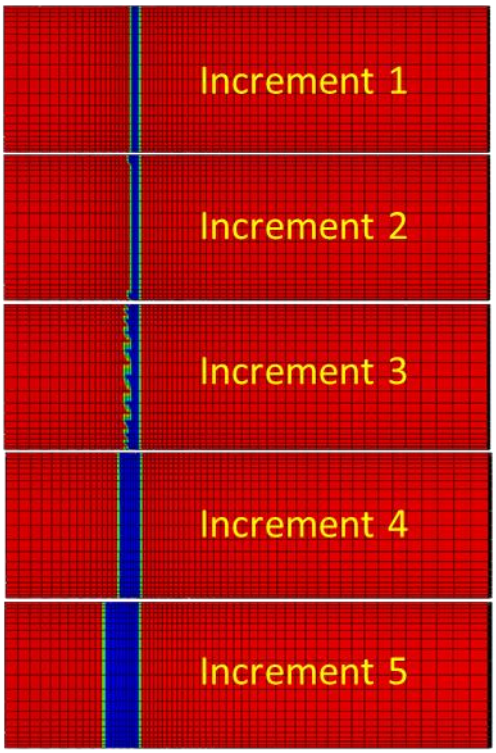

Figure 6.39 Bonding state of the interfacial elements as the fatigue crack propagating (top view). The blue elements denote debonding state while the red elements denote bonding state.

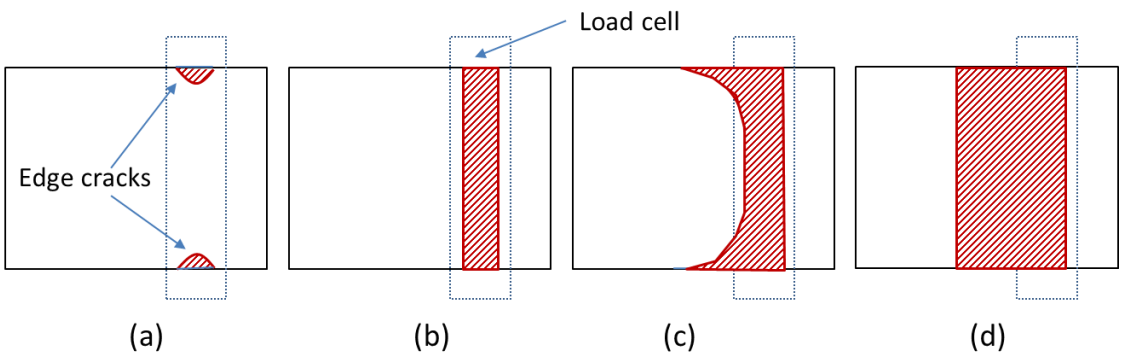

Figure 6.40 Development of the buckling-driven delamination in bending fatigue: (a) edge cracks initialized; (b) edge cracks penetrated through width; (c) foregoing edge cracks; (d) buckling and buckling-driven delamination

In case of those specimens fatigue tested in the wet environment (i.e. covered by a wet sponge), it is apparent that water penetrated the cracks due to the capillary effect. (Smith and Weitsman, 1990) used X-ray to investigate the capillary effect of the immersed fatigue response of CFRP composites and found that the speed of capillary climb was

approximately 7 mm/min regardless of stress levels. Compared with the moisture diffusivity of polymer composites, the rate of capillary climb is one million times faster; therefore it is reasonable to assume that the foregoing mass of water is preserved during the loading cycle. As a consequence, the water prevented the crack closure when the specimen was unloaded, and then the crack propagation was accelerated, leading to a much shorter fatigue life.

6.4 Summary

Following the diffusion measurements presented in Chapter 5, this chapter performed the fatigue study of dry specimens in dry environment, and moisture saturated specimens (tap water immersion, sea water immersion, and sea water immersion with 70bar hydrostatic pressure) in both dry and wet environments. Bending fatigue (both 3-point and 4-point bending) was carried out at three loading levels to investigate the fatigue performance of the UD and CP laminates while bending creep (3-point bending) was carried out at three loading levels for the AP laminate. FEA models, based on VCCT, were conducted to investigate the fatigue crack propagation as well as the fatigue failure mechanisms.

The experimental study showed that composite fatigue were associated with bending condition (3-point and 4-point bending), loading level, loading sequence, stacking sequence and the loading environments (dry and wet). Any attempt to analyse the fatigue failure mechanisms without the loading conditions may lead to inaccurate results. No evidence was found to identify the effects of the three different immersions on the fatigue performance. It was found that water ingress during the fatigue significantly accelerated the crack initiation and fatigue crack propagation, therefore a short fatigue life was expected. The use of the traditional S-N curve was inappropriate to predict the fatigue of CFRP composites and the fatigue analysis must be associated with the practical conditions.

The study of creep test showed that the matrix hardened after water immersion: immersed coupons presented higher creep stiffness compared with the dry specimen at all of the three loading levels. It was found that the relation between creep strain and

creep time was perfectly governed by power law. Again, no evidence was found to identify the different effects of the three immersions on the creep performance.

Both the UD and CP laminates failed by the so-called buckling-driven delamination in the 4-point bending fatigue. FEA based on VCCT performed the buckling-driven delamination in both 2D and 3D. It was found that the buckling initiation was mode I dominated while the fatigue crack propagation was mode II dominated.

The FEA modelling unveiled the development of the 4-step buckling-driven delamination, in which the edge effect played its important role in the fatigue crack propagation. Besides, the water ingress due to the capillary phenomenon significantly accelerated the progress of crack initiation and propagation.

CHAPTER 7 – CONCLUSIONS

7.1 Summary of findings

The aim of this thesis was to investigate the fatigue failure mechanisms of CFRP composites used in the marine environment. Fatigue is a process of the accumulation of material damage, thus the analysis of fatigue failure is to study the failure modes as well as its accumulating mechanisms. From this point of view, this thesis considered both quasi-static and cyclic fatigue loading. Among many aspects of the marine environmental effects, the main concern was the effect of water ingress on the fatigue performance of laminated composites. Since aerospace structures are also subjected to moisture diffusion, the findings of this thesis can be extended to their applications.

The structure of this thesis was based on two aspects: composite fatigue and its interaction with environmental effects. Firstly, coupons made up of pre-preg CFRP composite with some typical layups were manufactured, and the manufacturing quality was inspected by optical microscope and scanning electric microscope. A series of MATLAB tools based on CLT were developed to predict the material properties of those layups, and the codes are also attached in the Appendix A-D. Secondly, quasi-static bending tests were carried out, and a variety of composite failure modes were identified. CLT and FEA were employed to study these failure mechanisms. Later on, composite coupons were immersed into a simulated marine environment, and the environmental effects on the composite failure modes were investigated. Finally, a series of bending fatigue tests, both in air and while immersed, had been conducted on dry and immersed coupons, and the crack accumulation mechanisms as well as the effects of water ingress were studied. Based on the four steps above, the main findings can be summarised as follows:

Composite manufacturing:

1) The statistics of fibre misalignment angles within unidirectional lamina followed a normal distribution (Gaussian distribution), and the average angle was in range of 2°-3°. The distribution of fibre misalignment was important in understanding some aspects of composite behaviour, such as the lower compressive strength compared to tensile strength due to the fibre microbuckling.

2) The statistics of fibre separation within unidirectional lamina followed a Weibull distribution, and the average distance was lower than the one predicted either by hexagonal or square packing. The statistics of fibre packing was an important aspect in understanding the fibre barrier effects, such as the stress concentration and moisture diffusion at the micro scale.
3) A new formulation based on hydrostatic pressure was derived to predict the transverse Poisson's ratio (ν_{23}) of unidirectional lamina.
4) The traditional 2D CLT formulae were extended to 3D by introducing the 3D stress/strain transformation matrix. The 3D CLT was necessary to extract some stress/strain components which were ignored in 2D. The distributions of these ignored stress/strain components were important to understand the composite failure mechanisms in bending.
5) A MATLAB tool was developed to predict the material properties (elastic properties and diffusion properties) of composite laminates based on the 3D CLT. The codes are shown as Appendix A.

Quasi-static bending tests:

1) A new formulation was derived to correlate the deflection due to misalignment of load cell in 3-point bending.
2) The statistics of the interaction ratio η of the current commercial CFRP composites suggested that the orientation of the surface ply of a composite structure should avoid 10°-13°.
3) It was found that the failure modes of unidirectional and cross-ply laminates were different in 3-point bending: unidirectional laminate failed by compression due to fibre micro buckling while the cross-ply laminate failed by tension. Based on the different failure modes, it was suggested that for practical composite structures, inserting a transverse ply into a unidirectional laminate (such as [0/90/0n]) could significantly improve the bending performance.
4) It was found that edge effects were associated with the laminate layup. For a laminate with complex stacking sequence, e.g. angle-ply laminate, the edge effects significantly changed the stress distribution within a half ply thickness

from the edge. The edge effects were intensively investigated by a 3D solid FEA model, which was an important tool to understand the fatigue crack propagation.

5) The effects of unequal compressive/tensile moduli of composites had been systematically investigated. It was proposed that the strain dominated failure criterion should be applied for composite design, manufacturing and certification.
6) Some new formula based on classical beam theory and classical laminate theory has been derived to predict the flexural stress/strain distribution of different laminate layups. It was found that the traditional methods had underestimated the maximum compressive strain by about 5% when the composite laminates were subjected to bending.
7) The term of unequal compressive/tensile moduli was introduced into the failure criterion (Tsai-Wu), and was used to predict the failure envelopes in strain space. The MATLAB codes for the prediction of failure envelope are attached in the Appendix B.

Diffusion tests:

1) Temperature did not change the saturated moisture concentration but accelerated the moisture diffusion process. As a contrast, hydrostatic pressure did not change the moisture diffusion process but increased the saturated moisture concentration.
2) The moisture diffusivity of the interphase between fibre and matrix was found to be one order of magnitude higher than that of the matrix.
3) The moisture diffusivity along fibre orientation was about 60% higher than in the transverse direction.
4) Hygrothermal stress, which was induced by free expansion after moisture absorption, showed edge effects. For the angle-ply laminate, the interlaminar shear stress near edge could be as high as 20% of the strength. It was observed that the failure mode was changed due to the coupling between the edge effects of hygrothermal stress and external loading.
5) The effects of water absorption on mechanical properties were different in different composite layups. For the fibre dominated UD laminate, the flexural

modulus had no change but the flexural strength increased. In contrast, in the matrix dominated transverse laminate, the flexural modulus increased but the flexural strength decreased.

6) The SEM study revealed various matrix fracture morphologies in different water immersions, corresponding to the different failure mechanisms of CFRP composites. A variety of ions were found from sea water immersed coupons based on the EDS (energy dispersion) study. It was suggested that the mechanical properties were reduced after short term immersion due to the edge effects, while the damage to the fibre/polymer interface became more significant in laminate degradation after longer-term immersion.
7) A MATLAB tool, based on CLT, was developed to predict the hygrothermal expansion after moisture diffusion. The codes are shown in the Appendix C and D.

Bending fatigue tests:

1) The fatigue behaviour of CFRP composites is so different from the other kinds of materials that it was suggested to avoid employing the traditional S-N curve to plot the fatigue performance of CFRP composites.
2) It was found that the fatigue stiffness could describe most aspects of fatigue behaviour, and the fatigue failure modes were dependent on bending condition (3-point and 4-point bending), loading level, loading sequence, composite stacking sequence and the loading environments (dry and wet). Any attempt to analyse the fatigue failure mechanisms without knowledge of the practical conditions may lead to inaccurate results.
3) The degradation due to water ingress reduced the loading level for the desired fatigue performance, i.e. from 90% UFS to 80% UFS. No evidence was found to identify the different effects of the three immersions on the fatigue and creep performance.
4) Matrix hardening was found after water immersion. A new formulation was derived to predict the creep strain. The fitting curves at different loading levels showed a perfect power law relation between the creep strain and time.

5) Buckling-driven delamination was intensively studied by means of 2D and 3D solid FEA. It was found that the buckling initiation was mode I dominated while the fatigue crack propagation was mode II dominated. A 4-step theory was proposed to predict the development of fatigue cracks.
6) It was found that the acceleration mechanism of fatigue failure for wet environment was the prevention of crack closure due to the water capillary.

7.2 Contributions to knowledge

This thesis has contributed to an improved understanding of the failure modes of CFRP composites in both normal and marine environments, which leads to some suggestions for optimization of the design of composite structures. Apart from the findings listed above, the most notable contribution of this thesis is that it has successfully demonstrated the advantage of the methodology which could be applicable to other disciplines, such as aerospace composites.

The contributions to knowledge made in this thesis include:

- Visual and quantitative studies of fibre misalignment and fibre packing, leading to a better understanding of composite behaviour.
- A recommendation to avoid fibre orientations between 10°-13° as the surface ply in composite structures.
- Insertion of a transverse ply into a unidirectional laminate to improve the bending performance of composite structures.
- A new formulation to predict the transverse Poisson's ratio ν_{23} of unidirectional lamina.
- The recommendation to use strain-based failure criteria for composite design, manufacturing and certification, instead of stress-based failure criteria.
- Visual and quantitative results describing time-dependent moisture degradation of FRP composites.
- A new formulation to predict the creep strain of angle-ply laminates.
- A 4-step buckling-driven delamination theory to study the fatigue failure mechanisms of FRP composites in bending.

- A new algorithm and the coding for 3D classical laminate analysis.

7.3 Future research

The main findings and contributions described above have addressed the objective of this project. Some suggestions for future research extended in this direction are given below:

1) An unidentified failure mode was found on the compressive surface of angle-ply laminate in bending (i.e. Figure 6-24), which is worthy for further investigation.
2) Non-destructive sensing techniques can be employed to monitor morphology fracture during the fatigue test, such as ultrasonic sensing, optical fibre sensing and CT scanning. For example, with the manufacturing technique of semiconductor industry, it is possible to embed the MEMS sensor/actuator into a composite laminate.
3) The accelerated diffusion test presented in this thesis has simulated a period of water immersion of approximately one year. Longer exposure is recommended to examine the long term behaviour, either by increasing the immersed temperature or extending the immersion time.
4) The study of this project is based on carbon fibre – epoxy (continuous fibre composite) which is normally used in thin structures. For the short fibre composites which are formed in bulk structures and joints, the fatigue failure mechanisms could be different and worthy of investigation.
5) At the current stage (till January 2016), ABAQUS is one of the best commercial software for the modelling of fatigue crack propagation; however the VCCT technique used in FEA meets the limit to model the crossing of multi cracks. It is worthy to track the latest modelling technique and to simulate the development of multi cracks in fatigue.

REFERENCES

ABAQUS (2015). "ABAQUS reference manual."

Abdelaziz, Y. and A. Hamouine (2008). "A survey of the extended finite element." Computers & Structures **86**(11–12): 1141-1151.

ABS (2001). "Guide for building classing high-speed craft." American Bureau of Shipping

ACMA (2015). "www.acmanet.org." American Composites Manufacturers Association.

Adamson, M. J. (1980). "Thermal expansion and swelling of cured epoxy resin used in graphite/epoxy composite materials." Journal of Materials Science **15**(7): 1736-1745.

Alias, M. and R. Brown (1992). "Damage to composites from electrochemical processes." Corrosion **48**(5): 373-378.

Allred, R. E. (1981). "The Effect of Temperature and Moisture Content on the Flexural Response of Kevlar/Epoxy Laminates: Part I.[0/90] Filament Orientation*." Journal of Composite Materials **15**(2): 100-116.

ANSYS (2013). "ANSYS reference manual."

Ashbee, K. H. (1993). Fundamental principles of fiber reinforced composites, CRC Press.

ASTM-D2734 (2009). "Standard Test Methods for Void Content of Reinforced Plastics."

Basu, S., A. Waas and D. Ambur (2006). "Compressive failure of fiber composites under multi-axial loading." Journal of the Mechanics and Physics of Solids **54**(3): 611-634.

Belytschko, T., R. Gracie and G. Ventura (2009). "A review of extended/generalized finite element methods for material modeling." Modelling and Simulation in Materials Science and Engineering **17**(4): 043001.

Benzeggagh, M. and M. Kenane (1996). "Measurement of mixed-mode delamination fracture toughness of unidirectional glass/epoxy composites with mixed-mode bending apparatus." Composites Science and Technology **56**(4): 439-449.

Berbinau, P., C. Soutis and I. Guz (1999). "Compressive failure of 0 unidirectional carbon-fibre-reinforced plastic (CFRP) laminates by fibre microbuckling." Composites Science and technology **59**(9): 1451-1455.

Birger, S., A. Moshonov and S. Kenig (1989). "The effects of thermal and hygrothermal ageing on the failure mechanisms of graphite-fabric epoxy composites subjected to flexural loading." Composites **20**(4): 341-348.

Bledzki, A., R. Spaude and G. Ehrenstein (1985). "Corrosion phenomena in glass fibers and glass fiber reinforced thermosetting resins." Composites science and technology **23**(4): 263-285.

Boller, K. (1964). "Fatigue characteristics of RP laminates subjected to axial loading." Modern Plastics **41**(10): 145-150.

Bowles, D. E. and S. S. Tompkins (1989). "Prediction of coefficients of thermal expansion for unidirectional composites." Journal of Composite Materials **23**(4): 370-388.

Brandrup, J., E. H. Immergut, E. A. Grulke, A. Abe and D. R. Bloch (1999). Polymer handbook, Wiley New York.

Brintrup, H. (1975). Beitrag zum zeitabhängigen Verformungsverhalten und zur Rißbildung orthotro¨glasfaserverstärkter ungesättigter Polyesterharze unter ebener Normalbeanspruchung/vorgelegt von Hugo Brintrup.

Budiansky, B. and N. A. Fleck (1993). "Compressive failure of fibre composites." Journal of the Mechanics and Physics of Solids **41**(1): 183-211.

Cai, L.-W. and Y. Weitsman (1994). "Non-Fickian moisture diffusion in polymeric composites." Journal of composite materials **28**(2): 130-154.

Cairns, D. and D. Adams (1984). "Moisture and thermal expansion properties of unidirectional composite materials and the epoxy matrix." Environmental Effects on Composite Materials **2**: 300-316.

Cairns, D. S. and D. F. Adams (1981). "Moisture and thermal expansion of composite materials." U,S. ARMY RESEARCH OFFICE Report **UWME-DR-101-104-1**.

Carbajal, N. and F. Mujika (2009). "Determination of compressive strength of unidirectional composites by three-point bending tests." Polymer Testing **28**(2): 150-156.

Chamis, C. (1987). "Simplified composite micromechanics equations for mechanical, thermal, and moisture-related properties." Engineers' guide to composite materials: 3-8.

Chamis, C. C. (1969). Failure Criteria for Filamentary Composites, DTIC Document.

Chamis, C. C. (1972). Design Properties of Randomly Reinforced Fiber Composites, DTIC Document.

Chamis, C. C. (1974). Analysis of the three-point-bend test for materials with unequal tension and compression properties, National Aeronautics and Space Administration.

Chamis, C. C. (1984). Simplified Composite Micromechanics Equations for Strength, Fracture Toughness, Impact Resistance and Environmental Effects, DTIC Document.

Chateauminois, A., B. Chabert, J. Soulier and L. Vincent (1993). "Hygrothermal ageing effects on the static fatigue of glass/epoxy composites." Composites **24**(7): 547-555.

Chiou, P. and W. Bradley (1993). "The Effect of Seawater Exposure on the Fatigue Edge Delamination Growth of a Carbon/Epoxy Composite." University of Zaragoza(Spain): 516-523.

Chowdhury, S. R. and R. Narasimhan (2000). "A cohesive finite element formulation for modelling fracture and delamination in solids." Sadhana **25**(6): 561-587.

Colledge, J. J. and B. Warlow (2003). Ships of the Royal Navy: The Complete Record of All Fighting Ships of the Royal Navy, Greenhill.

COMSOL (2013). "COMSOL Multiphysics reference manual."

Creemers, R. (2009). "Interlaminar shear strength criteria for composites."

Cytec (2012). "CYCOM 977-2 Epoxy resin system. www.cytec.com." Technical data sheet.

Cytec (2012). "CYCOM 2237 Polyimide resin system. www.cytec.com." Technical data sheet.

D1141-98, A. (2008). Standard Practice for the Preparation of Substitute Ocean Water, ASTM International West Conshohocken, PA.

D5229/D5229M, A. (2004). Standard Test Method for Moisture Absorption Properties and Equilibrium Conditioning of Polymer Matrix Composite Materials. ASTM. **ASTM D5229:** 13.

D6115, A. (2011). "Standard test method for mode I fatigue delamination growth onset of unidirectional fiber-reinforced polymer matrix composites."

D7264, A. (2007). Standard Test Method for Flexural Properties of Polymer Matrix Composite Materials, ASTM International.

Daniel, I. M. and O. Ishai (1994). "Engineering mechanics of composite materials." Oxford university press(ISBN 0-19-507506-4).

Davallo, M., H. Pasdar and M. Mohseni (2010). "Mechanical Properties of Unsaturated Polyester Resin." International Journal of ChemTech Research **2**(4): 2113-2117.

De Morais, A. B. (1996). "Modelling lamina longitudinal compression strength of carbon fibre composite laminates." Journal of composite materials **30**(10): 1115-1131.

Dept. of defense, U. (1997). "V2 Polymer matrix composites material handbook." Composite handbook **2**.

Derakane (2011). "Derakane 411-45 Epoxy Vinyl Ester resin. www.ashland.com." Technical data sheet.

Downing, S. D. and D. Socie (1982). "Simple rainflow counting algorithms." International Journal of Fatigue **4**(1): 31-40.

E1049-85, A. (1994). Standard Practices for Cycle Counting in Fatigue Analysis. ASTM.

EICHLER, J. and J. MLEZIVA (1971). "STUDY ON REACTIVITY OF AROMATIC DIAMINES WITH EPOXIDE RESINS." ANGEWANDTE MAKROMOLEKULARE CHEMIE **19**(NSEP): 31-&.

Ellyin, F. and R. Maser (2004). "Environmental effects on the mechanical properties of glass-fiber epoxy composite tubular specimens." Composites Science and Technology **64**(12): 1863-1874.

Findley, W. N. and F. A. Davis (2013). Creep and relaxation of nonlinear viscoelastic materials, Courier Corporation.

Fox, D. J., G. F. Sykes Jr and C. T. Herakovich (1987). "Space environmental effects on graphite-epoxy compressive properties and epoxy tensile properties."

Foye, R. and D. Baker (1970). Design of orthotropic laminates. 11th Annual AIAA Structures, Structural Dynamics, and Materials Conference, Denver, Colorado.

French, M. and G. Pritchard (1993). "The fracture surfaces of hybrid fibre composites." Composites science and technology **47**(3): 217-223.

Furge, L. L. (2010). Giant molecules: From nylon to nanotubes, Wiley Online Library.

Gibson, R. F. (1994). "Principles of composite materials mechanics." McGraw-Hill(ISBN O-07-023451-5).

Gigliotti, M., F. Jacquemin, J. Molimard and A. Vautrin (2007). Modelling and experimental characterisation of hygrothermoelastic stress in polymer matrix composites. Macromolecular Symposia, Wiley Online Library.

Gordon, J. E. (1976). The new science of strong materials: or why you don't fall through the floor, Penguin UK.

Gough, H. and H. Pollard (1935). "The strength of metals under combined alternating stresses." Proceedings of the institution of mechanical engineers **131**(1): 3-103.

Greene, E. (1999). Marine composites, Eric Greene Associates.

Griffis, C., J. Nemes, F. Stonesifer and C. Chang (1986). "Degradation in strength of laminated composites subjected to intense heating and mechanical loading." Journal of Composite Materials **20**(3): 216-235.

Grogan, D. M. (2015). Damage and permeability in linerless composite cryogenic tanks.

Haberle, J. and F. Matthews (1994). "A micromechanics model for compressive failure of unidirectional fibre-reinforced plastics." Journal of composite materials **28**(17): 1618-1639.

Hahn, H. T. and J. G. Williams (1986). "Compression failure mechanisms in unidirectional composites." Composite Materials: Testing and Design: 115-139.

Hajianmaleki, M. and M. S. Qatu (2011). "Mechanics of Composite Beams." Advances in Composite Materials - Analysis of Natural and Man-Made Materials **22**(ISBN 978-953-307-449-8).

Halpin, J. C. and J. Kardos (1976). "The Halpin-Tsai equations: a review." Polymer engineering and science **16**(5): 344-352.

Halpin, J. C. and J. L. Kardos (1976). "The Halpin-Tsai equations: A review." POLYMER ENGINEERING AND SCIENCE **16**(5): 9.

Hammerfest, A. H. (2011). "www.hammerfeststrom.com."

Harper, B. and Y. Weitsman (1985). "On the effects of environmental conditioning on residual stresses in composite laminates." International Journal of Solids and Structures **21**(8): 907-926.

Hashin, Z. (1980). "Failure criteria for unidirectional fiber composites." Journal of applied mechanics **47**(2): 329-334.

Hashin, Z. (1981). "Fatigue failure criteria for combined cyclic stress." International Journal of Fracture **17**(2): 101-109.

Hashin, Z. (1981). "Fatigue failure criteria for unidirectional fiber composites." Journal of Applied Mechanics **48**(4): 846-852.

Hottengada, B. (2006). "Investigation of Microcracking and Damage Propagation in Cross-Ply Composite Laminates."

Hughes, J. D. H. (1991). "The carbon fibre/epoxy interface—A review." Composites Science and Technology **41**(1): 13-45.

Hull, D. and T. Clyne (1996). An introduction to composite materials, Cambridge university press.

Hyer, M. W. (2009). Stress analysis of fiber-reinforced composite materials, DEStech Publications, Inc.

INSEAN. (2007). "Technical report."

Irwin, G. R. (1997). "Analysis of stresses and strains near the end of a crack traversing a plate." SPIE MILESTONE SERIES MS **137**: 167-170.

ISO899-2:2003 (2003). Plastics -- Determination of creep behaviour -- Part 2: Flexural creep by three-point loading.

ISO12130 (1998). "14130-1998." Fiber-reinforced Plastic Composites-De-termination of Apparent Interlaminar Shear Strength by Short Beam Method.

ISO13003 (2003). "13003. Fibre-reinforced plastics–determination of fatigue properties under cyclic loading conditions." British Standards International.

ISO14125 (1998). Fibre-reinforced plastic composites— Determination of flexural properties. ISO standard. **BS EN ISO 14125:1998**.

JCMA (2014). "http://www.carbonfiber.gr.jp/english/material/feature.html." The Japan Carbon Fibre Manufacturers Association.

Jing, H.-S. and K.-G. Tzeng (1993). "Refined shear deformation theory of laminated shells." AIAA journal **31**(4): 765-773.

Johnson, D. (1987). "Structure-property relationships in carbon fibres." Journal of Physics D: Applied Physics **20**(3): 286.

Jones, R. M. (1976). "Apparent flexural modulus and strength of multimodulus materials." Journal of Composite Materials **10**(4): 342-354.

Jones, R. M. (1978). Mechanics of Composite Materials with Different Moduli in Tension and Compression, DTIC Document.

Jumahat, A., C. Soutis, F. R. Jones and A. Hodzic (2010). "Fracture mechanisms and failure analysis of carbon fibre/toughened epoxy composites subjected to compressive loading." Composite Structures **92**(2): 295-305.

Kant, T. and K. Swaminathan (2000). "Estimation of transverse/interlaminar stresses in laminated composites–a selective review and survey of current developments." Composite structures **49**(1): 65-75.

Kardos, J. (1985). The role of the interface in polymer composites—some myths, mechanisms, and modifications. Molecular characterization of composite interfaces, Springer**:** 1-11.

Kassapoglou, C. (1990). "Determination of interlaminar stresses in composite laminates under combined loads." Journal of reinforced plastics and composites **9**(1): 33-58.

Kaw, A. K. (2006). "Mchanics of composite materials (second edition)." Taylor & Francis Group(ISBN 0-8493-1343-0).

Kelly, A. and G. Davies (1965). "The principles of the fibre reinforcement of metals." Metallurgical Reviews **10**(1): 1-77.

Khan, L. A., A. Nesbitt and R. J. Day (2010). "Hygrothermal degradation of 977-2A carbon/epoxy composite laminates cured in autoclave and Quickstep." Composites Part A: Applied Science and Manufacturing **41**(8): 942-953.

Kibler, K. (1980). Time-dependent environmental behavior of graphite/epoxy composites, DTIC Document.

Kootsookos, A. and A. P. Mouritz (2004). "Seawater durability of glass- and carbon-polymer composites." Composites Science and Technology **64**(10–11): 1503-1511.

Korcek, S., J. Chenier, J. Howard and K. Ingold (1972). "Absolute rate constants for hydrocarbon autoxidation. XXI. Activation energies for propagation and the correlation of propagation rate constants with carbon-hydrogen bond strengths." Canadian Journal of Chemistry **50**(14): 2285-2297.

Kotsikos, G., J. Evans, A. Gibson and J. Hale (2000). "Environmentally enhanced fatigue damage in glass fibre reinforced composites characterised by acoustic emission." Composites Part A: Applied Science and Manufacturing **31**(9): 969-977.

Kumar, S. B., I. Sridhar and S. Sivashanker (2008). "Influence of humid environment on the performance of high strength structural carbon fiber composites." Materials Science and Engineering: A **498**(1–2): 174-178.

Kyriakides, S., R. Arseculeratne, E. J. Perry and K. M. Liechti (1995). "On the compressive failure of fiber reinforced composites." Int. J. Solid & Strucrtures **32**(6/7): 50.

Lai, W. M., D. H. Rubin, D. Rubin and E. Krempl (2009). Introduction to continuum mechanics, Butterworth-Heinemann.

Lee, C. and J. Chen (1996). "Interlaminar shear stress analysis of composite laminate with layer reduction technique." International journal for numerical methods in engineering **39**(5): 847-865.

Lekhnitskiĭ, S. (1963). Theory of elasticity of an anisotropic elastic body, Holden-Day.

Lemanski, S. L. and M. P. F. Sutcliffe (2012). "Compressive failure of finite size unidirectional composite laminates with a region of fibre waviness." Composites Part A: Applied Science and Manufacturing **43**(3): 435-444.

Lemanski, S. L., J. Wang, M. P. F. Sutcliffe, K. D. Potter and M. R. Wisnom (2013). "Modelling failure of composite specimens with defects under compression loading." Composites Part A: Applied Science and Manufacturing **48**(0): 26-36.

Liu, D., N. Fleck and M. Sutcliffe (2004). "Compressive strength of fibre composites with random fibre waviness." Journal of the Mechanics and Physics of Solids **52**(7): 1481-1505.

Liu, S. and J. A. Nairn (1992). "The formation and propagation of matrix microcracks in cross-ply laminates during static loading." Journal of reinforced plastics and composites **11**(2): 158-178.

Livingstone, D. A. (1963). Chemical composition of rivers and lakes, US Government Printing Office.

Loos, A. C. and G. S. Springer (1979). "Moisture absorption of graphite-epoxy composites immersed in liquids and in humid air." Journal of Composite Materials **13**(2): 131-147.

Lubin, G. (2013). Handbook of composites, Springer Science & Business Media.

Marsh, G. (2004). "A new start for marine propellers?" Reinforced Plastics **48**(11): 34-38.

Matsuishi, M. and T. Endo (1968). "Fatigue of metals subjected to varying stress." Japan Society of Mechanical Engineers, Fukuoka, Japan: 37-40.

MATWORKS (2013). "MATLAB reference manual."

Melenk, J. M. and I. Babuška (1996). "The partition of unity finite element method: Basic theory and applications." Computer Methods in Applied Mechanics and Engineering **139**(1–4): 289-314.

Meng, M., H. R. Le, M. J. Rizvi and S. M. Grove (2015a). "3D FEA modelling of laminated composites in bending and their failure mechanisms." Composite Structures **119**(0): 693-708.

Meng, M., H. R. Le, M. J. Rizvi and S. M. Grove (2015b). "The effects of unequal compressive/tensile moduli of composites." Composite Structures **126**(0): 207-215.

Meng, M., M. J. Rizvi, S. M. Grove and H. R. Le (2015c). "Effects of hygrothermal stress on the failure of CFRP composites." Composite Structures **133**: 1024-1035.

Meng, M., M. J. Rizvi, H. R. Le and S. M. Grove (2016). "Multi-scale modelling of moisture diffusion coupled with stress distribution in CFRP laminated composites." Composite Structures **138**: 295-304.

Mijovic, J. (1985). "Interplay of physical and chemical aging in graphite/epoxy composites." Journal of composite materials **19**(2): 178-191.

Milewski, J. V. and D. V. Rosato (1981). "History of Reinforced Plastics." Journal of Macromolecular Science: Part A - Chemistry **15**(7): 1303-1343.

Mohan, M. (2008). "The advantages of composite materials in marine renewable energy structures." RINA Marine Renewable Energy Conference 2008

Morton, J., S. Kellas and S. Bishop (1988). "Damage characteristics in notched carbon fiber composites subjected to fatigue loading—Environmental effects." Journal of composite materials **22**(7): 657-673.

Mujika, F., N. Carbajal, A. Arrese and I. Mondragon (2006). "Determination of tensile and compressive moduli by flexural tests." Polymer testing **25**(6): 766-771.

Murthy, P. L. and C. C. Chamis (1987). "Free-edge delamination: laminate width and loading conditions effects."

Naik, N. and R. S. Kumar (1999). "Compressive strength of unidirectional composites: evaluation and comparison of prediction models." Composite structures **46**(3): 299-308.

Nutting, P. G. (1921). "A Study of Elastic Viscous Deformation." ASTM Proceeding 1921 **21**: 10.

Olabisi, O. and K. Adewale (1997). Handbook of thermoplastics, CRC press.

Pagano, N. (1978). "Stress fields in composite laminates." International Journal of Solids and Structures **14**(5): 385-400.

Paris, P. C., M. P. Gomez and W. E. Anderson (1961). "A rational analytic theory of fatigue." The trend in engineering **13**(1): 9-14.

Park, K. and G. H. Paulino (2011). "Cohesive zone models: a critical review of traction-separation relationships across fracture surfaces." Applied Mechanics Reviews **64**(6): 060802.

Petermann, J. and K. Schulte (2002). "The effects of creep and fatigue stress ratio on the long-term behaviour of angle-ply CFRP." Composite Structures **57**(1–4): 205-210.

Peters, S. T. (2013). Handbook of composites, Springer Science & Business Media.

Phillips, D., J. Scott and N. Buckley (1978). "The effects of moisture on the shear fatigue of fibre composites." ICCM/2: 1544-1559.

Piggott, M. R. (1995). "The effect of fibre waviness on the mechanical properties of unidirectional fibre composites: a review." Composites science and technology **53**(2): 201-205.

Pipes, R. B. (1980). "Boundary layer effects in composite laminates." Fibre Science and Technology **13**(1): 49-71.

Pipes, R. B. and N. J. Pagano (1970). "Interlaminar Stresses in Composite Laminates Under Uniform Axial Extension." Journal of Composite Materials **4**: 11.

Pomies, F., L. Carlsson and J. Gillespie (1995). "Marine environmental effects on polymer matrix composites." ASTM SPECIAL TECHNICAL PUBLICATION **1230**: 283-303.

Raju, I. (1987). "Calculation of strain-energy release rates with higher order and singular finite elements." Engineering Fracture Mechanics **28**(3): 251-274.

Rasoldier, N., X. Colin, J. Verdu, M. Bocquet, L. Olivier, L. Chocinski-Arnault and M. Lafarie-Frenot (2008). "Model systems for thermo-oxidised epoxy composite matrices." Composites Part A: Applied Science and Manufacturing **39**(9): 1522-1529.

Reeder, J. R., K. Song, P. Chunchu and D. R. Ambur (2002). Postbuckling and growth of delaminations in composite plates subjected to axial compression. The 43rd AIAA/ASME/ASCE/AHS/ASC Structures, Structural Dynamics, and Materials Conference.

Reifsnider, K., W. Stinchcomb and T. O'brien (1977). "Frequency effects on a stiffness-based fatigue failure criterion in flawed composite specimens." Fatigue of Filamentary Composite Materials, ASTM STP **636**: 171-184.

Ryan, J., R. Adams and S. Brown (2009). Moisture ingress effect on properties of CFRP. Proceedings of the 17th International Conference on Composite Materials (ICCM’09).

Rybicki, E. F. and M. Kanninen (1977). "A finite element calculation of stress intensity factors by a modified crack closure integral." Engineering Fracture Mechanics **9**(4): 931-938.

Schapery, R. A. (1968). "Thermal expansion coefficients of composite materials based on energy principles." Journal of Composite Materials **2**(3): 380-404.

Schluter, L. (1991). Programmer's Guide for LIFE 2's Rainflow Counting Algorithm, Sandia National Laboritories.

Schultheisz, C. R. and A. M. Waas (1996). "Compressive failure of composites, part I-Testing and micromechanical theories." Progress in Aerospace Sciences **32**(1): 42.

Schwartz, M. M. (1984). Composite materials handbook, McGraw-Hill.

Selvaraju, S. and S. Ilaiyavel (2011). "Applications of composites in marine industry." J. Eng. Res. Stud., II: 89-91.

Shen, C.-H. and G. S. Springer (1976). "Moisture absorption and desorption of composite materials." Journal of Composite Materials **10**(1): 2-20.

SIEMENS (2008). "www.siemens.com."

Sloan, F. E. and R. J. Seymour (1992). "The effect of seawater exposure on mode I interlaminar fracture and crack growth in graphite/epoxy." Journal of composite materials **26**(18): 2655-2673.

Smith, C. (1991). "Design of submersible pressure hulls in composite materials." Marine structures **4**(2): 141-182.

Smith, L. and Y. Weitsman (1990). "The immersed fatigue response of polymer composites." International journal of fracture **82**(1): 31-42.

Smith, W. F. and J. Hashemi (2006). Foundations of materials science and engineering, Mcgraw-Hill Publishing.

Soutis, C. (1991). "Measurement of the static compressive strength of carbon-fibre/epoxy laminates." Composites science and technology **42**(4): 373-392.

Soutis, C. (1997). "Compressive strength of unidirectional composites: measurement and prediction." ASTM special technical publication **1242**: 168-176.

Soutis, C. and D. Turkmen (1997). "Moisture and temperature effects of the compressive failure of CFRP unidirectional laminates." Journal of Composite Materials **31**(8): 832-849.

Springer, G. S. (1981). Environmental effects on composite materials, Technomic Pennsylvania.

Springer, G. S. (1983). "Effects of temperature and moisture on sheet molding compounds." Journal of reinforced plastics and composites **2**(2): 70-89.

Strong, A. B. (2008). Fundamentals of composites manufacturing: materials, methods and applications, Society of Manufacturing engineers.

Summerscales, J. (2014). Durability of Composites in the Marine Environment. Durability of Composites in a Marine Environment. P. Davies and Y. D. Rajapakse, Springer**:** 1-13.

Sumsion, H. (1976). "Environmental effects on graphite-epoxy fatigue properties." Journal of Spacecraft and Rockets **13**(3): 150-155.

Sutcliffe, M. (2013). "Modelling the effect of size on compressive strength of fibre composites with random waviness." Composites Science and Technology **88**: 142-150.

Tang, S. (1975). "A boundary layer theory-Part I: Laminated composites in plane stress." Journal of composite materials **9**(1): 33-41.

Tang, S. and A. Levy (1975). "A boundary layer theory-part II: extension of laminated finite strip." Journal of Composite Materials **9**(1): 42-52.

Toho-Tenax-HTS. "Technical data sheet."

Toho-Tenax "Toho Tenax HTS. www.tohotenax-eu.com." Technical data sheet.

Tsai, S. W. (1968). "Strength theories of filamentary structures." Fundamental aspects of fiber reinforced plastic composites: 3-11.

Tsai, S. W. (2008). Theory of composites design, Think composites Dayton.

Tsai, S. W. and J. D. D. Melo (2014). "An invariant-based theory of composites." Composites Science and Technology **100**: 237-243.

Tucker, W. (1991). "Degradation of Graphite/Polymer Composites in Seawater." Journal of Energy Resources Technology **113**(4): 264-267.

Tucker, W. C. and R. Brown (1989). "Moisture absorption of graphite/polymer composites under 2000 feet of seawater." Journal of composite materials **23**(8): 787-797.

Victrex (2012). "Victrex PEEK polymer. www.victrex.com." Technical data sheet.

Vinson, J. R. (1978). Advanced composite materials-environmental effects, ASTM International.

Voyiadjis, G. Z. and P. I. Kattan (2005). "Mechanics of Composite Materials with MATLAB." (Springer).

Wagner, P. A., B. J. Little, K. R. Hart and R. I. Ray (1996). "Biodegradation of composite materials." International biodeterioration & biodegradation **38**(2): 125-132.

Walrath, D. E. and D. F. Adams (1980). Fatigue Behavior of Hercules 3501-6 Epoxy Resin, DTIC Document.

Waltersson, K. (1985). "ESCA studies of carbon fibres: Part II—Surface reactions of carbon fibres with epoxides." Composites Science and Technology **22**(3): 223-239.

Wang, A. and F. W. Crossman (1977). "Some new results on edge effect in symmetric composite laminates." Journal of Composite Materials **11**(1): 92-106.

Wang, S. and I. Choi (1982). "Boundary-layer effects in composite laminates: Part 2—free-edge stress solutions and basic characteristics." Journal of Applied Mechanics **49**(3): 549-560.

Weeton, J. W., K. L. Thomas and D. M. Peters (1987). Engineers' guide to composite materials, American Society of Metals.

Weitsman, Y. (1977). "Stresses in adhesive joints due to moisture and temperature." Journal of Composite Materials **11**(4): 378-394.

Weitsman, Y. (1987). "Stress assisted diffusion in elastic and viscoelastic materials." Journal of the Mechanics and Physics of Solids **35**(1): 73-94.

Whitney, J. and N. Pagano (1970). "Shear deformation in heterogeneous anisotropic plates." Journal of Applied Mechanics **37**(4): 1031-1036.

Wolff, E. G. (1993). "Moisture effects on polymer matrix composites." SAMPE Journal(USA) **29**(3): 11-19.

Wood, C. A. and W. L. Bradley (1997). "Determination of the effect of seawater on the interfacial strength of an interlayer E-glass/graphite/epoxy composite by in situ observation of transverse cracking in an environmental SEM." Composites Science and Technology **57**(8): 1033-1043.

Yang, B.-X., M. Kasamori and T. Yamamoto (1992). The effect of water on the interlamina delamination growth of composite laminates. The Second International Symposium on Composite Materials and Structures.

Yang, P. C., C. H. Norris and Y. Stavsky (1966). "Elastic wave propagation in heterogeneous plates." International Journal of Solids and Structures **2**(4): 665-684.

Zafar, A., F. Bertocco, J. Schjødt-Thomsen and J. C. Rauhe (2012). "Investigation of the long term effects of moisture on carbon fibre and epoxy matrix composites." Composites Science and Technology **72**(6): 656-666.

Zhang, Y., Y. Li, H. Ma and T. Yu (2013). "Tensile and interfacial properties of unidirectional flax/glass fiber reinforced hybrid composites." Composites Science and Technology **88**(0): 172-177.

Zhou, G. and G. Davies (1995). "Characterization of thick glass woven roving/polyester laminates: 1. Tension, compression and shear." Composites **26**(8): 579-586.

Zhou, G. and G. Davies (1995). "Characterization of thick glass woven roving/polyester laminates: 2. Flexure and statistical considerations." Composites **26**(8): 587-596.

PUBLICATIONS

1. Meng, M., H. R. Le* and S. M. Grove, M. J. Rizvi (2016). "Moisture effects on the bending fatigue of laminated composites." Composite Structures, DIO: 10.1016/j.compstruct.2016.06.078.
2. Meng, M., M. J. Rizvi, H. R. Le* and S. M. Grove (2016). "Multi-scale modelling of moisture diffusion coupled with stress distribution in CFRP laminated composites." Composite Structures 138: 295-304.
3. Meng, M., M. J. Rizvi, S. M. Grove and H. R. Le* (2015). "Effects of hygrothermal stress on the failure of CFRP composites." Composite Structures 133: 1024-1035.
4. Meng, M.*, H. R. Le, M. J. Rizvi and S. M. Grove (2015). "The effects of unequal compressive/tensile moduli of composites", Composite Structures 126: 207–215.
5. Meng, M.*, H. R. Le, M. J. Rizvi and S. M. Grove (2015). "3D FEA modelling of laminated composites in bending and their failure mechanisms." Composite Structures 119(0): 693-708.

*corresponding author

CONFERENCE PRESENTATIONS

1. Maozhou Meng*, Huirong Le, Stephen Grove, MD Jahir Rizvi. Environmental effects on the bending fatigue of laminated composites: experimental and modelling approaches. 17th European Conference on Composite Materials, Munich, Germany, 26th - 30th June 2016.
2. Maozhou Meng*, Huirong Le, Stephen Grove, Md. Jahir Rizvi. Multi-scale modelling of hygrothermal effects in CFRP composites. N8 HPC Network Event- Multiscale Computational Mechanics, Sheffield, UK, 30 October 2015.
3. Maozhou Meng*, Huirong Le, Stephen Grove, Md. Jahir Rizvi. Multi-scale analysis of moisture diffusion coupled with stress distribution in CFRP composites. 18th International Conference of Composite Structures, Lisbon, Portugal, 15-18 June 2015.
4. Maozhou Meng*, Huirong Le, Ming Dai. Design of a straight blade Darrieus tidal current turbine using composite-composite joint. 10th European Symposium of International Network on Offshore Renewable Energy, Naples, Italy, 23-29 May 2015.
5. Maozhou Meng*. 3D modelling of composites in marine environment: moisture and thermal effects. Presented to the US Office of Naval Research, Plymouth University, 30 July 2014.
6. Maozhou Meng*. Modelling laminated composites in bending: shell and solid strategies. Engineering Research Seminars, Plymouth University, 18 June 2014.

*presenting author

APPENDIX A: MATLAB CODE FOR 3D CLT

This tool was designed to predict mechanical properties of laminated composites, and the formulae have been shown in the main context of chapter 3. The graphic user interface (GUI), shown in the Figure A1, provides three sessions: (a) session one for the lamina using local coordinate system (1, 2, and 3); (b) session two for the off-axis lamina using global coordinate system (x, y, and z); and (c) session three for the laminate using global coordinate system (x, y, and z).

There is an add-on function that user can calculate the coefficient of thermal expansion (alpha). Each session provides various plots. For example, Figure A2 shows the Young's modulus and shear modulus of a cross-ply laminate ([0/90]) various to rotated angle (theta).

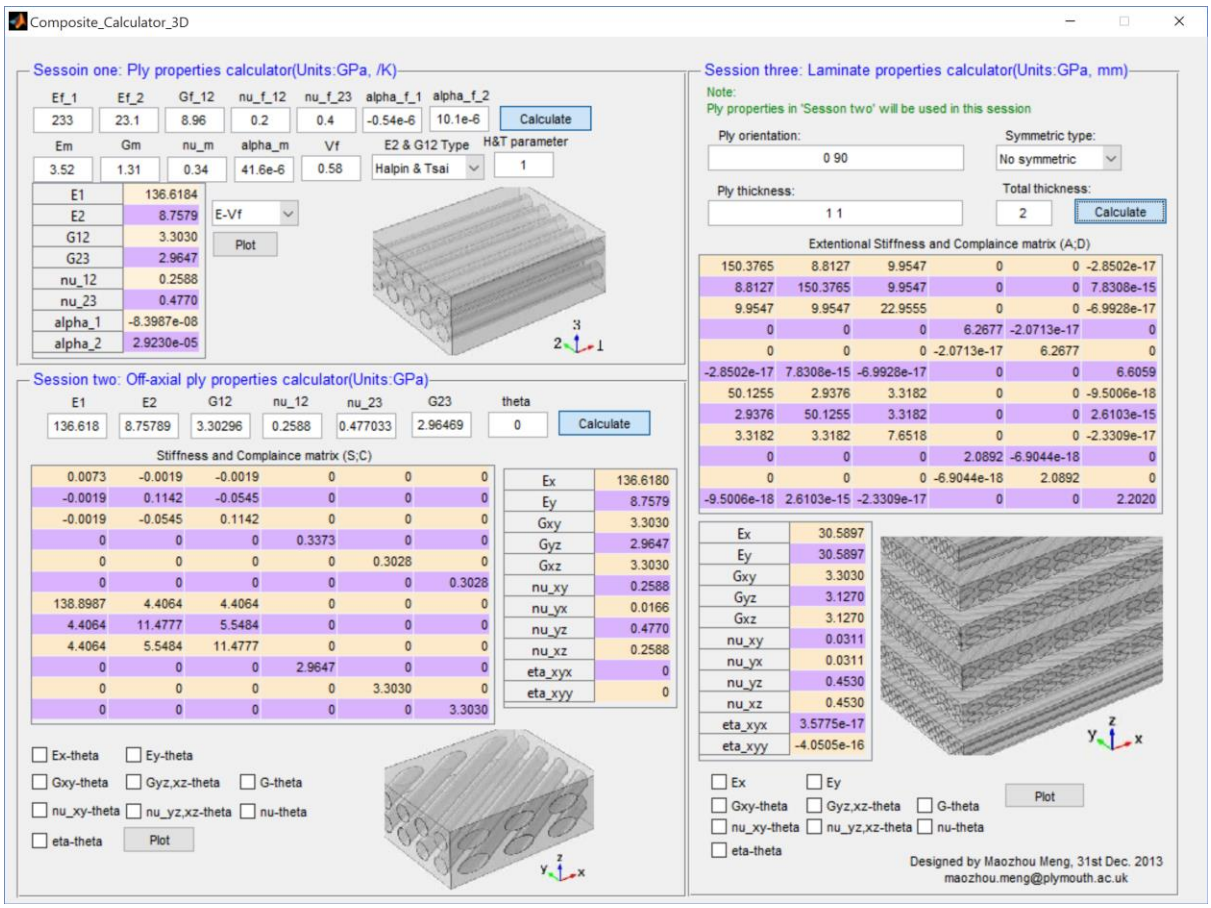

Figure A1. The GUI of composite calculator 3D

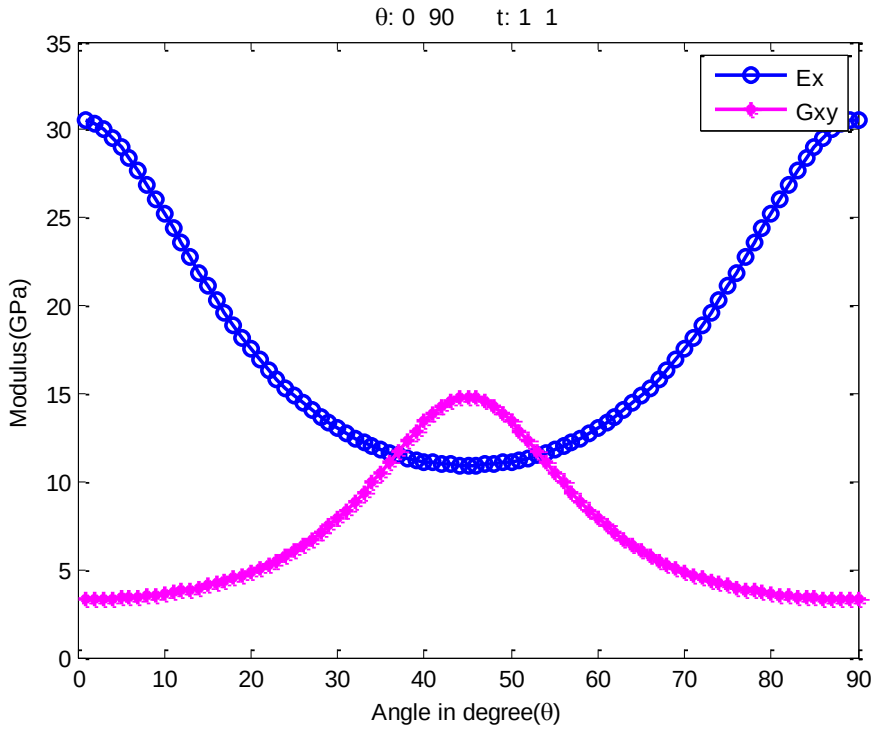

Figure A2. Young's modulus and shear modulus various to rotated angle

In the book 'Engineering Mechanics of Composite Materials', Daniel and Ishai gave overall laminate properties for [45] ply and a $[\pm 45]_s$ made of Carbon/Epoxy (AS4/3501-6, E_1 = 142 GPa, E_2 = 10.3 GPa, G_{12} = 7.2 GPa, and ν_{12} = 0.27). The results are given in Table A1. Figure A3 gives the results calculated by 'composite calculator 2D' with the same input properties as those in literature.

Table A1 Laminate properties in literature

	[45]			$[\pm 45]_s$		
Property	Approximation formula	Approximate value	Exact value	Approximation formula	Approximate value	Exact value
$\bar{E}_x$, GPa (Msi)	$\frac{4\,G_{12}\,E_2}{G_{12}+E_2}$	17.0 (2.46)	16.7 (2.43)	$4\,G_{12}$	28.7 (4.16)	24.4 (3.54)
$\bar{G}_{xy}$, GPa (Msi)	E_2	10.4 (1.50)	9.3 (1.34)	$E_1/4$	35.5 (5.15)	36.9 (5.35)
$\bar{\nu}_{xy}$	$\frac{E_2-G_{12}}{E_2+G_{12}}$	0.18	0.16	$\frac{E_1-4\,G_{12}}{E_1+4\,G_{12}}$	0.66	0.69
$\bar{\eta}_{xx}$	$-\frac{2\,G_{12}}{E_2+G_{12}}$	− 0.82	− 0.75	0	0	0
$\bar{\eta}_{sx}$	− 0.50	− 0.50	− 0.42	0	0	0

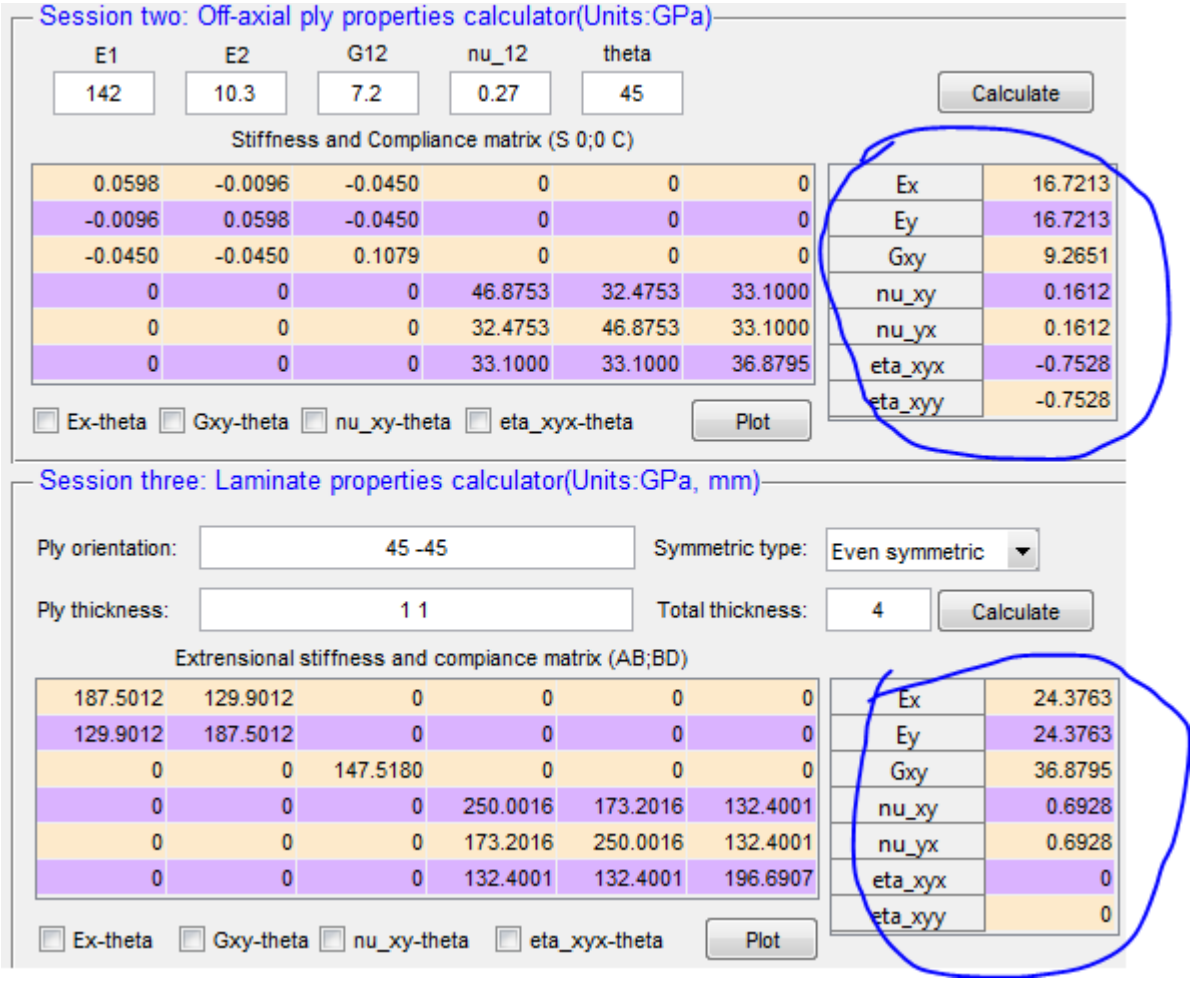

Figure A3. Carbon/Epoxy (AS4/3501-6) with 45 off-axis and 45 even symmetry

```
function varargout = Composite_Calculator_3D(varargin)
% COMPOSITE_CALCULATOR_3D MATLAB code for Composite_Calculator_3D.fig
% This program is built by Maozhou Meng on 29th,Dec.2013, Plymouth University
% Last Modified by GUIDE v2.5 27-Mar-2014 09:11:05
% Begin initialization code - DO NOT EDIT
gui_Singleton = 1;
gui_State = struct('gui_Name',       mfilename, ...
                   'gui_Singleton',  gui_Singleton, ...
                   'gui_OpeningFcn', @Composite_Calculator_3D_OpeningFcn, ...
                   'gui_OutputFcn',  @Composite_Calculator_3D_OutputFcn, ...
                   'gui_LayoutFcn',  [] , ...
                   'gui_Callback',   []);
if nargin && ischar(varargin{1})
    gui_State.gui_Callback = str2func(varargin{1});
end

if nargout
    [varargout{1:nargout}] = gui_mainfcn(gui_State, varargin{ISO899-2:2003,  #140});
else
    gui_mainfcn(gui_State, varargin{ISO899-2:2003,  #140});
```

```
end
% End initialization code - DO NOT EDIT

% --- Executes just before Composite_Calculator_3D is made visible.
function Composite_Calculator_3D_OpeningFcn(hObject, ~, handles, varargin)
% This function has no output args, see OutputFcn.
% Choose default command line output for Composite_Calculator_3D
handles.output = hObject;
% Update handles structure
guidata(hObject, handles);
axes(handles.axes_123);
imshow('m_123.jpg');
axes(handles.axes_xyz);
imshow('m_xyz.jpg');
axes(handles.axes_laminar);
imshow('m_laminar.jpg');

% --- Outputs from this function are returned to the command line.
function varargout = Composite_Calculator_3D_OutputFcn(hObject, eventdata, handles)
varargout{1} = handles.output;
% =====START OF INPUT ARGUMENTS=====

function Input_Ef_1_Callback(hObject, eventdata, handles)
function Input_Ef_1_CreateFcn(hObject, eventdata, handles)
if ispc && isequal(get(hObject,'BackgroundColor'), get(0,'defaultUicontrolBackgroundColor'))
    set(hObject,'BackgroundColor','white');
end

function Input_Ef_2_Callback(hObject, eventdata, handles)
function Input_Ef_2_CreateFcn(hObject, eventdata, handles)
if ispc && isequal(get(hObject,'BackgroundColor'), get(0,'defaultUicontrolBackgroundColor'))
    set(hObject,'BackgroundColor','white');
end

function Input_Gf_12_Callback(hObject, eventdata, handles)
function Input_Gf_12_CreateFcn(hObject, eventdata, handles)
if ispc && isequal(get(hObject,'BackgroundColor'), get(0,'defaultUicontrolBackgroundColor'))
    set(hObject,'BackgroundColor','white');
end

function Input_nu_f_12_Callback(hObject, eventdata, handles)
function Input_nu_f_12_CreateFcn(hObject, eventdata, handles)
if ispc && isequal(get(hObject,'BackgroundColor'), get(0,'defaultUicontrolBackgroundColor'))
    set(hObject,'BackgroundColor','white');
end

function Input_nu_f_23_Callback(hObject, eventdata, handles)
function Input_nu_f_23_CreateFcn(hObject, eventdata, handles)
if ispc && isequal(get(hObject,'BackgroundColor'), get(0,'defaultUicontrolBackgroundColor'))
    set(hObject,'BackgroundColor','white');
end

function Input_Alphaf_1_Callback(hObject, eventdata, handles)
function Input_Alphaf_1_CreateFcn(hObject, eventdata, handles)
if ispc && isequal(get(hObject,'BackgroundColor'), get(0,'defaultUicontrolBackgroundColor'))
    set(hObject,'BackgroundColor','white');
```

```
end

function Input_Alphaf_2_Callback(hObject, eventdata, handles)
function Input_Alphaf_2_CreateFcn(hObject, eventdata, handles)

if ispc && isequal(get(hObject,'BackgroundColor'), get(0,'defaultUicontrolBackgroundColor'))
    set(hObject,'BackgroundColor','white');
end

function Input_Em_Callback(hObject, eventdata, handles)
function Input_Em_CreateFcn(hObject, eventdata, handles)
if ispc && isequal(get(hObject,'BackgroundColor'), get(0,'defaultUicontrolBackgroundColor'))
    set(hObject,'BackgroundColor','white');
end


function Input_Gm_Callback(hObject, eventdata, handles)
function Input_Gm_CreateFcn(hObject, eventdata, handles)
if ispc && isequal(get(hObject,'BackgroundColor'), get(0,'defaultUicontrolBackgroundColor'))
    set(hObject,'BackgroundColor','white');
end

function Input_nu_m_Callback(hObject, eventdata, handles)
function Input_nu_m_CreateFcn(hObject, eventdata, handles)
if ispc && isequal(get(hObject,'BackgroundColor'), get(0,'defaultUicontrolBackgroundColor'))
    set(hObject,'BackgroundColor','white');
end

function Input_Alpham_Callback(hObject, eventdata, handles)
function Input_Alpham_CreateFcn(hObject, eventdata, handles)
if ispc && isequal(get(hObject,'BackgroundColor'), get(0,'defaultUicontrolBackgroundColor'))
    set(hObject,'BackgroundColor','white');
end

function Input_Vf_Callback(hObject, eventdata, handles)
function Input_Vf_CreateFcn(hObject, eventdata, handles)
if ispc && isequal(get(hObject,'BackgroundColor'), get(0,'defaultUicontrolBackgroundColor'))
    set(hObject,'BackgroundColor','white');
end

function Input_Hadjust_Callback(hObject, eventdata, handles)
function Input_Hadjust_CreateFcn(hObject, eventdata, handles)
if ispc && isequal(get(hObject,'BackgroundColor'), get(0,'defaultUicontrolBackgroundColor'))
    set(hObject,'BackgroundColor','white');
end


function E2_type_Callback(hObject, eventdata, handles)
function E2_type_CreateFcn(hObject, eventdata, handles)
if ispc && isequal(get(hObject,'BackgroundColor'), get(0,'defaultUicontrolBackgroundColor'))
    set(hObject,'BackgroundColor','white');
end
```

```
% --- Executes on button press in Calculate_Off_axial_ply.
function Calculate_ply_Callback(hObject, eventdata, handles)
% Get input data
Ef_1 = str2double(get(handles.Input_Ef_1,'String'));
Ef_2 = str2double(get(handles.Input_Ef_2,'String'));
Em = str2double(get(handles.Input_Em,'String'));
Gf_12 = str2double(get(handles.Input_Gf_12,'String'));
%Gf_23 = str2double(get(handles.Input_Gf_23,'String'));
Gm = str2double(get(handles.Input_Gm,'String'));
nu_f_12 = str2double(get(handles.Input_nu_f_12,'String'));
nu_f_23 = str2double(get(handles.Input_nu_f_23,'String'));
nu_m = str2double(get(handles.Input_nu_m,'String'));
Alphaf_1 = str2double(get(handles.Input_Alphaf_1,'String'));
Alphaf_2 = str2double(get(handles.Input_Alphaf_2,'String'));
Alpham = str2double(get(handles.Input_Alpham,'String'));
Vf = str2double(get(handles.Input_Vf,'String'));
HT = str2double(get(handles.Input_Hadjust,'String'));
% Mechanics of Composite Materials with Matlab, George Z. Voyiadjis and Peter I. Kattan
E1 = Vf*Ef_1+Em*(1-Vf);
nu_12 = Vf*nu_f_12+nu_m*(1-Vf);
Alpha1 = (Alphaf_1*Ef_1*Vf+Alpham*Em*(1-Vf))/(Ef_1*Vf+Em*(1-Vf));
Alpha2 = (Alphaf_2-Em*nu_f_12*(Alpham-Alphaf_1)*(1-Vf)/E1)*Vf+(Alpham+Ef_1*nu_m*(Alpham-
Alphaf_1)*Vf/E1)*(1-Vf);
% select the E2 calculating type from Halpin&Tsai and equal stress
kf = Ef_1*Ef_2/(2*Ef_1*(1-nu_f_12*Ef_2/Ef_1-nu_f_23)+Ef_2*(1-2*nu_f_12));
km = Em/3/(1-2*nu_m);
switch get(handles.E2_type,'Value')
   case 1
      etaE = (Ef_2/Em-1)/(Ef_2/Em+HT);
      E2 = Em*(1+HT*etaE*Vf)/(1-etaE*Vf);
      etaG = (Gf_12/Gm-1)/(Gf_12/Gm+HT);
      G12 = Gm*(1+HT*etaG*Vf)/(1-etaG*Vf);
      etaK = (kf/km-1)/(kf/km+HT);
      K = km*(1+HT*etaK*Vf)/(1-etaK*Vf);
   case 2
      E2 = 1/(Vf/Ef_2+(1-Vf)/Em);
      G12 = 1/(Vf/Gf_12+(1-Vf)/Gm);
      K = 1/(Vf/kf+(1-Vf)/km);
end
% calculate poisson ratio and shear modulus of 23 direction
% An Introduction to Composite Materials, D. Hull and T.W. Clyne
%kf = Ef_2/3/(1-nu_f_23-nu_f_12*Ef_2/Ef_1);
%K = 1/(Vf/kf+(1-Vf)/km);
nu_21 = nu_12*E2/E1;
nu_23 = 1-nu_21-E2/2/K+E2*(1-2*nu_12)/2/E1;
%nu_23 = 1-nu_21-E2/3/K;
%nu_23 = 1-nu_12*Em/Ef_2-E2*((3*Vf*(1-2*nu_f_12))/Ef_2+(3*(1-Vf)*(1-2*nu_m))/Em)/3;
G23 = E2/2/(1+nu_23);
% Output composite properties in table
Matrix_output = [E1 E2 G12 G23 nu_12 nu_23 Alpha1 Alpha2]';
set(handles.Ply_table,'data',Matrix_output);
set(handles.Input_E1,'string',E1);
set(handles.Input_E2,'string',E2);
set(handles.Input_G12,'string',G12);
set(handles.Input_G23,'string',G23);
set(handles.Input_nu_12,'string',nu_12);
set(handles.Input_nu_23,'string',nu_23);
guidata(hObject, handles);
```

```
function Input_E1_Callback(hObject, eventdata, handles)
function Input_E1_CreateFcn(hObject, eventdata, handles)
if ispc && isequal(get(hObject,'BackgroundColor'), get(0,'defaultUicontrolBackgroundColor'))
    set(hObject,'BackgroundColor','white');
end


function Input_E2_Callback(hObject, eventdata, handles)
function Input_E2_CreateFcn(hObject, eventdata, handles)
if ispc && isequal(get(hObject,'BackgroundColor'), get(0,'defaultUicontrolBackgroundColor'))
    set(hObject,'BackgroundColor','white');
end


function Input_nu_12_Callback(hObject, eventdata, handles)
function Input_nu_12_CreateFcn(hObject, eventdata, handles)
if ispc && isequal(get(hObject,'BackgroundColor'), get(0,'defaultUicontrolBackgroundColor'))
    set(hObject,'BackgroundColor','white');
end


function Input_G12_Callback(hObject, eventdata, handles)
function Input_G12_CreateFcn(hObject, eventdata, handles)
if ispc && isequal(get(hObject,'BackgroundColor'), get(0,'defaultUicontrolBackgroundColor'))
    set(hObject,'BackgroundColor','white');
end


function Input_Theta_Callback(hObject, eventdata, handles)
function Input_Theta_CreateFcn(hObject, eventdata, handles)
if ispc && isequal(get(hObject,'BackgroundColor'), get(0,'defaultUicontrolBackgroundColor'))
    set(hObject,'BackgroundColor','white');
end


% --- Executes on button press in Calculate_Off_axial_ply.
function Calculate_Off_axial_ply_Callback(hObject, eventdata, handles)
% Get input data
E1 = str2double(get(handles.Input_E1,'String'));
E2 = str2double(get(handles.Input_E2,'String'));
G12 = str2double(get(handles.Input_G12,'String'));
G23 = str2double(get(handles.Input_G23,'String'));
nu_12 = str2double(get(handles.Input_nu_12,'String'));
nu_23 = str2double(get(handles.Input_nu_23,'String'));
Theta = str2double(get(handles.Input_Theta,'String'));
% define transfering matrix
% Mechanics of composite materials. R.M. Christensen.
c = cos(Theta*pi/180);
s = sin(Theta*pi/180);
T = [c^2 s^2 0 0 0 2*c*s;
    s^2 c^2 0 0 0 -2*c*s;
    0 0 1 0 0 0;
    0 0 0 c s 0;
```

```
    0 0 0 -s c 0;
    -c*s c*s 0 0 0 c^2-s^2];
T1 = [c^2 s^2 0 0 0 c*s;
    s^2 c^2 0 0 0 -c*s;
    0 0 1 0 0 0;
    0 0 0 c s 0;
    0 0 0 -s c 0;
    -2*c*s 2*c*s 0 0 0 c^2-s^2];
% An Introduction to Compostie Materials. T, D. Hull, T. W. Clyne
S11 = 1/E1;
S12 = -nu_12/E1;
S22 = 1/E2;
S23 = -nu_23/E2;
S44 = 1/G23;
S66 = 1/G12;
S = [S11 S12 S12 0 0 0;
    S12 S22 S23 0 0 0;
    S12 S23 S22 0 0 0;
    0 0 0 S44 0 0;
    0 0 0 0 S66 0;
    0 0 0 0 0 S66];
Sbar = T1\S*T;
Cbar=inv(Sbar);
Ex=1/Sbar(1,1);
Ey=1/Sbar(2,2);
Gxy=1/Sbar(6,6);
Gyz=1/Sbar(4,4);
Gxz=1/Sbar(5,5);
nu_xy=-Ex*Sbar(2,1);
nu_yx=-Ey*Sbar(2,1);
nu_yz=-Ey*Sbar(3,2);
nu_xz=-Ex*Sbar(3,1);
eta_xyx=Ex*Sbar(1,6);
eta_xyy=Ey*Sbar(2,6);

set(handles.Stiffness_Complaince_ply_table,'data',[Sbar;Cbar]);
Matrix_elastic_off_axial_ply = [Ex Ey Gxy Gyz Gxz nu_xy nu_yx nu_yz nu_xz eta_xyx eta_xyy]';
set(handles.Off_axial_ply_table,'data',Matrix_elastic_off_axial_ply);
guidata(hObject, handles);


function Plot_Off_axial_Ply_Callback(hObject, eventdata, handles)
% Get input data
E1 = str2double(get(handles.Input_E1,'String'));
E2 = str2double(get(handles.Input_E2,'String'));
G12 = str2double(get(handles.Input_G12,'String'));
nu_12 = str2double(get(handles.Input_nu_12,'String'));
nu_23 = str2double(get(handles.Input_nu_23,'String'));
G23 = str2double(get(handles.Input_G23,'String'));
% An Introduction to Compostie Materials. T, D. Hull, T. W. Clyne
S11 = 1/E1;
S12 = -nu_12/E1;
S22 = 1/E2;
S23 = -nu_23/E2;
S44 = 1/G23;
S66 = 1/G12;
S = [S11 S12 S12 0 0 0;
```

```
    S12 S22 S23 0 0 0;
    S12 S23 S22 0 0 0;
    0 0 0 S44 0 0;
    0 0 0 0 S66 0;
    0 0 0 0 0 S66];

    theta = 1:90;
for i=1:length(theta);
    c = cos(i*pi/180);
    s = sin(i*pi/180);
T = [c^2 s^2 0 0 0 2*c*s;
    s^2 c^2 0 0 0 -2*c*s;
    0 0 1 0 0 0;
    0 0 0 c s 0;
    0 0 0 -s c 0;
    -c*s c*s 0 0 0 c^2-s^2];
T1 = [c^2 s^2 0 0 0 c*s;
    s^2 c^2 0 0 0 -c*s;
    0 0 1 0 0 0;
    0 0 0 c s 0;
    0 0 0 -s c 0;
    -2*c*s 2*c*s 0 0 0 c^2-s^2];
Sbar = T1\S*T;
Ex(i)=1/Sbar(1,1);
Ey(i)=1/Sbar(2,2);
Gxy(i)=1/Sbar(6,6);
Gyz(i)=1/Sbar(4,4);
Gxz(i)=1/Sbar(5,5);
nu_xy(i)=-Ex(i)*Sbar(2,1);
nu_yx(i)=-Ey(i)*Sbar(2,1);
nu_yz(i)=-Ey(i)*Sbar(3,2);
nu_xz(i)=-Ex(i)*Sbar(3,1);
eta_xyx(i)=Ex(i)*Sbar(1,6);
eta_xyy(i)=Ey(i)*Sbar(2,6);
i=i+1;
end

%select plot items
switch get(handles.PlyEx,'Value')+get(handles.PlyEy,'Value')
    case 1
        figure;
        if get(handles.PlyEx,'Value')
            plot(theta,Ex,'b-o','linewidth',2); hold on;
            legend('Ex'); hold on;
            xlabel('Angle in degree(\theta)');
            ylabel('Modulus(GPa)');
        else
            plot(theta,Ey,'m-*','linewidth',2); hold on;
            legend('Ey'); hold on;
            xlabel('Angle in degree(\theta)');
            ylabel('Modulus(GPa)');
        end
    case 2
        figure;
        plot(theta,Ex,'b-o',theta,Ey,'m-*','linewidth',2); hold on;
        legend('Ex','Ey'); hold on;
        xlabel('Angle in degree(\theta)');
```

```
        ylabel('Modulus(GPa)');
end

switch get(handles.PlyGxy,'Value')
   case 1
        figure;
            plot(theta,Gxy,'b-o'); hold on;
            legend('Gxy'); hold on;
            xlabel('Angle in degree(\theta)');
            ylabel('Modulus(GPa)');
end

switch get(handles.PlyGyz,'Value')
   case 1
                figure;
            plot(theta,Gyz,'r-+',theta,Gxz,'g-*'); hold on;
            legend('Gyz','Gxz'); hold on;
            xlabel('Angle in degree(\theta)');
            ylabel('Modulus(GPa)');
end

switch get(handles.PlyGxz,'Value')
   case 1
                figure;
            plot(theta,Gxy,'b-o',theta,Gyz,'g-*',theta,Gxz,'r-+'); hold on;
            legend('Gxy','Gyz','Gxz'); hold on;
            xlabel('Angle in degree(\theta)');
            ylabel('Modulus(GPa)');
end

switch get(handles.Plynu_xy,'Value')
   case 1
        figure;
            plot(theta,nu_xy,'b-o'); hold on;
            legend('nu_x_y'); hold on;
            xlabel('Angle in degree(\theta)');
            ylabel('Poisson ratio(\nu)');
end

switch get(handles.Plynu_yz,'Value')
   case 1
        figure;
            plot(theta,nu_yz,'b-o',theta,nu_xz,'r-+'); hold on;
            legend('nu_y_z','nu_x_z'); hold on;
            xlabel('Angle in degree(\theta)');
            ylabel('Poisson ratio(\nu)');
end

switch get(handles.Plynu_xz,'Value')
   case 1
        figure;
            plot(theta,nu_xy,'b-o',theta,nu_yz,'g-*',theta,nu_xz,'r-+'); hold on;
            legend('nu_x_y','nu_y_z','nu_x_z'); hold on;
            xlabel('Angle in degree(\theta)');
            ylabel('Poisson ratio(\nu)');
end
```

```
switch get(handles.Plyeta,'Value')
   case 1
      figure;
         plot(theta,eta_xyx,'r-*',theta,eta_xyy,'b-o'); hold on;
         legend('\eta_x_y_x','\eta_x_y_y'); hold on;
         xlabel('Angle in degree(\theta)');
         ylabel('Interaction ratio(\eta_X_y_x)');
end

function PlyEx_Callback(hObject, eventdata, handles)
function PlyGxy_Callback(hObject, eventdata, handles)


function Plynu_xy_Callback(hObject, eventdata, handles)
function Plyeta_Callback(hObject, eventdata, handles)


function Input_ply_thickness_Callback(hObject, eventdata, handles)
function Input_ply_thickness_CreateFcn(hObject, eventdata, handles)
if ispc && isequal(get(hObject,'BackgroundColor'), get(0,'defaultUicontrolBackgroundColor'))
   set(hObject,'BackgroundColor','white');
end


function Input_ply_orientation_Callback(hObject, eventdata, handles)
function Input_ply_orientation_CreateFcn(hObject, eventdata, handles)
if ispc && isequal(get(hObject,'BackgroundColor'), get(0,'defaultUicontrolBackgroundColor'))
   set(hObject,'BackgroundColor','white');
end


function Symmetric_type_Callback(hObject, eventdata, handles)

function Symmetric_type_CreateFcn(hObject, eventdata, handles)

if ispc && isequal(get(hObject,'BackgroundColor'), get(0,'defaultUicontrolBackgroundColor'))
   set(hObject,'BackgroundColor','white');
end


function Calculate_laminar_Callback(hObject, eventdata, handles)
% Get input data
E1 = str2double(get(handles.Input_E1,'String'));
E2 = str2double(get(handles.Input_E2,'String'));
G12 = str2double(get(handles.Input_G12,'String'));
G23 = str2double(get(handles.Input_G23,'String'));
nu_12 = str2double(get(handles.Input_nu_12,'String'));
nu_23 = str2double(get(handles.Input_nu_23,'String'));
Ply_angle = str2num(get(handles.Input_ply_orientation,'String'));
Ply_thickness = str2num(get(handles.Input_ply_thickness,'String'));
numcount = numel(Ply_thickness);
vector_length = numel(Ply_angle)-numcount;
if vector_length ~= 0;
errordlg('The length of orientation and thickness vector not consistent','Input Error');
```

```
return
end
% get the real matrix of ply angle and ply thickness
Ply_angle2 = zeros(1,numcount-1);
Ply_angle3 = zeros(1,numcount);
Ply_thickness2 = zeros(1,numcount-1);
Ply_thickness3 = zeros(1,numcount);
switch get(handles.Symmetric_type,'Value')
   case 1
      rPly_angle = Ply_angle;
      rPly_thickness = Ply_thickness;
      rnumcount = numcount;
   case 2
      for j = 1:numcount-1
         Ply_thickness2(j) = Ply_thickness(numcount-j);
         Ply_angle2(j) = Ply_angle(numcount-j);
      end
      rnumcount = numcount*2-1;
      rPly_thickness = [Ply_thickness Ply_thickness2];
      rPly_angle = [Ply_angle Ply_angle2];
   case 3
      for k = 1:numcount;
         Ply_thickness3(k) = Ply_thickness(numcount+1-k);
         Ply_angle3(k) = Ply_angle(numcount+1-k);
      end
      rnumcount = numcount*2;
      rPly_thickness = [Ply_thickness Ply_thickness3];
      rPly_angle = [Ply_angle Ply_angle3];
end
set(handles.Output_total_thickness,'String',sum(rPly_thickness));
% define the complaince matrix
S11 = 1/E1;
S12 = -nu_12/E1;
S22 = 1/E2;
S23 = -nu_23/E2;
S44 = 1/G23;
S66 = 1/G12;
S = [S11 S12 S12 0 0 0;
   S12 S22 S23 0 0 0;
   S12 S23 S22 0 0 0;
   0 0 0 S44 0 0;
   0 0 0 0 S66 0;
   0 0 0 0 0 S66];
% calculate the stiffness matrix of laminar
A = zeros(6,6);
B = zeros(6,6);
D = zeros(6,6);
h=zeros(1,rnumcount+1);
for j=1:rnumcount+1;
   if j==1
      h(j)=-sum(rPly_thickness)/2;
   else
      h(j)=h(j-1)+rPly_thickness(j-1);
   end
end
for i = 1:rnumcount
   c = cos(rPly_angle(i)*pi/180);
   s = sin(rPly_angle(i)*pi/180);
```

```
T = [c^2 s^2 0 0 0 2*c*s;
   s^2 c^2 0 0 0 -2*c*s;
   0 0 1 0 0 0;
   0 0 0 c s 0;
   0 0 0 -s c 0;
   -c*s c*s 0 0 0 c^2-s^2];
T1 = [c^2 s^2 0 0 0 c*s;
   s^2 c^2 0 0 0 -c*s;
   0 0 1 0 0 0;
   0 0 0 c s 0;
   0 0 0 -s c 0;
   -2*c*s 2*c*s 0 0 0 c^2-s^2];
Sbar = T1\S*T;
Cbar=inv(Sbar);
   for m = 1:6
      for n = 1:6
         A(m,n) = A(m,n)+Cbar(m,n)*(h(i+1)-h(i));
         B(m,n) = B(m,n)+Cbar(m,n)*((h(i+1))^2-(h(i))^2)/2;
         D(m,n) = D(m,n)+Cbar(m,n)*(h((i+1))^3-(h(i))^3)/3;
      end
   end
end
ABBD = [A B;B D];
abbd=inv(ABBD);
a=abbd(1:6,1:6);

%lCbar = lCbar/sum(rPly_thickness);
%lSbar = inv(lCbar);
% define the output matrix for the table
Matrix_stiffness_complaince_laminar = [A;D];
set(handles.Stiffness_Complaince_laminar_table,'data',Matrix_stiffness_complaince_laminar);
% get the elastic matrix and other parameters for output table

lEx=1/a(1,1)/sum(rPly_thickness);
lEy=1/a(2,2)/sum(rPly_thickness);
lGxy=1/a(6,6)/sum(rPly_thickness);
lGyz=1/a(4,4)/sum(rPly_thickness);
lGxz=1/a(5,5)/sum(rPly_thickness);

lnu_xy = -a(1,2)/a(1,1);
lnu_yx = -a(1,2)/a(2,2);
lnu_yz = -a(3,2)/a(2,2);
lnu_xz = -a(3,1)/a(1,1);
leta_xyx = a(1,6)/a(1,1);
leta_xyy = a(2,6)/a(2,2);

%lnu_xy=-lEx*lSbar(2,1);
%lnu_yx=-lEy*lSbar(2,1);
%lnu_yz=-lEy*lSbar(3,2);
%lnu_xz=-lEx*lSbar(3,1);
%leta_xyx=lEx*lSbar(1,6);
%leta_xyy=lEy*lSbar(2,6);

Matrix_elastic_laminar = [lEx lEy lGxy lGyz lGxz lnu_xy lnu_yx lnu_yz lnu_xz leta_xyx leta_xyy]';
set(handles.Laminar_table,'data',Matrix_elastic_laminar);
guidata(hObject, handles);
```

```
function Output_total_thickness_Callback(hObject, eventdata, handles)
function Output_total_thickness_CreateFcn(hObject, eventdata, handles)
if ispc && isequal(get(hObject,'BackgroundColor'), get(0,'defaultUicontrolBackgroundColor'))
    set(hObject,'BackgroundColor','white');
end


% --- Executes on button press in Plot_Vf.
function Plot_Vf_Callback(hObject, eventdata, handles)
% Get input data
Ef_1 = str2double(get(handles.Input_Ef_1,'String'));
Ef_2 = str2double(get(handles.Input_Ef_2,'String'));
Em = str2double(get(handles.Input_Em,'String'));
Gf_12 = str2double(get(handles.Input_Gf_12,'String'));
%Gf_23 = str2double(get(handles.Input_Gf_23,'String'));
Gm = str2double(get(handles.Input_Gm,'String'));
nu_f_12 = str2double(get(handles.Input_nu_f_12,'String'));
nu_f_23 = str2double(get(handles.Input_nu_f_23,'String'));
nu_m = str2double(get(handles.Input_nu_m,'String'));
Alphaf_1 = str2double(get(handles.Input_Alphaf_1,'String'));
Alphaf_2 = str2double(get(handles.Input_Alphaf_2,'String'));
Alpham = str2double(get(handles.Input_Alpham,'String'));
HT = str2double(get(handles.Input_Hadjust,'String'));
Vf = 0:0.01:1;
% calculate E1,nu_12,Alpha
pE1 = Ef_1*Vf+Em*(1-Vf);
pnu_12 = nu_f_12*Vf+nu_m*(1-Vf);
pAlpha1 = (Alphaf_1*Ef_1*Vf+Alpham*Em*(1-Vf))./(Ef_1*Vf+Em*(1-Vf));
pAlpha2 = Alphaf_2*Vf+Alpham*(1-Vf);
% Halpin & Tsai E2,G12
etaE = (Ef_2/Em-1)/(Ef_2/Em+HT);
etaG = (Gf_12/Gm-1)/(Gf_12/Gm+HT);
phE2 = Em*(1+HT*etaE*Vf)./(1-etaE*Vf);
phG12 = Gm*(1+HT*etaG*Vf)./(1-etaG*Vf);
% Equal stress E2,G12
peE2 = 1./(Vf/Ef_2+(1-Vf)/Em);
peG12 = 1./(Vf/Gf_12+(1-Vf)/Gm);
% Calculate nu_23,G23
kf = Ef_1*Ef_2/(2*Ef_1*(1-nu_f_12*Ef_2/Ef_1-nu_f_23)+Ef_2*(1-2*nu_f_12));
%kf = Ef_2/3/(1-nu_f_23-nu_f_12*Ef_2/Ef_1);
km = Em/3/(1-2*nu_m);
etaK = (kf/km-1)/(kf/km+HT);
K = km.*(1+HT*etaK*Vf)./(1-etaK*Vf);
Ke = 1./(Vf/kf+(1-Vf)/km);
%K = 1./(Vf/kf+(1-Vf)/km);
phnu_21 = pnu_12.*phE2./pE1;
%phnu_23 = 1-phnu_21-phE2/3./K;
phnu_23 = 1-phnu_21-phE2/2./K+phE2.*(1-2*pnu_12)/2./pE1;
penu_21 = pnu_12.*peE2./pE1;
penu_23 = 1-penu_21-peE2/2./Ke+peE2.*(1-2*pnu_12)/2./pE1;
%penu_23 = 1-penu_21-peE2/3./K;
%phnu_23 = 1-pnu_12*Em/Ef_2-phE2.*((3*Vf*(1-2*nu_f_12))/Ef_2+(3*(1-Vf)*(1-2*nu_m))/Em)/3;
phG23 = phE2./2./(1+phnu_23);
%penu_23 = 1-pnu_12*Em/Ef_2-peE2.*((3*Vf*(1-2*nu_f_12))/Ef_2+(3*(1-Vf)*(1-2*nu_m))/Em)/3;
peG23 = peE2./2./(1+penu_23);
```

```
switch get(handles.Volumn,'Value');
   case 1
      figure;
      plot(Vf,pE1,'r-*',Vf,phE2,'g-o',Vf,peE2,'b-+','LineWidth',2);hold on;
      legend('E1','E2 in Halpin&Tsai','E2 in Equal stress'); hold on;
      xlabel('Volume fraction');
      ylabel('Modulus(GPa)');
%        axis([0,1,0,50]);
   case 2
      figure;
      plot(Vf,phG12,'r-*',Vf,peG12,'r-o',Vf,phG23,'g-*',Vf,peG23,'g-o');
      legend('G12 in Halpin&Tsai','G12 in Equal stress','G23 in Halpin&Tsai','G23 in Equal stress'); hold
on;
      xlabel('Volume fraction');
      ylabel('Modulus(GPa)');
   case 3
      figure;
      plot(Vf,pnu_12,'r-*',Vf,phnu_21,'b-+',Vf,penu_21,'b-o',Vf,phnu_23,'c-+',Vf,penu_23,'c-o');
      legend('\nu_1_2','\nu_2_1 in Halpin&Tsai','\nu_2_1 in Equal stress','\nu_2_3 in
Halpin&Tsai','\nu_2_3 in Equal stress'); hold on;
      xlabel('Volume fraction');
      ylabel('Poisson ratio(\nu)');
   case 4
      figure;
      plot(Vf,pAlpha1,'r-o',Vf,pAlpha2,'b-*');
      legend('\alpha_1','\alpha_2'); hold on;
      xlabel('Volume fraction');
      ylabel('Thermal coefficient of expansion(\alpha /K)');
   case 5
      figure;
      plot(Vf,K,'r-o',Vf,Ke,'b-*');
      legend('K in Halpin & Tsai','K in Equal stress'); hold on;
      xlabel('Volume fraction');
      ylabel('Bulk modulus(GPa)');
end




function Input_nu_23_Callback(hObject, eventdata, handles)

function Input_nu_23_CreateFcn(hObject, eventdata, handles)
if ispc && isequal(get(hObject,'BackgroundColor'), get(0,'defaultUicontrolBackgroundColor'))
   set(hObject,'BackgroundColor','white');
end



function Input_G23_Callback(hObject, eventdata, handles)

function Input_G23_CreateFcn(hObject, eventdata, handles)
if ispc && isequal(get(hObject,'BackgroundColor'), get(0,'defaultUicontrolBackgroundColor'))
   set(hObject,'BackgroundColor','white');
end
```

```
function PlyEy_Callback(hObject, eventdata, handles)
function PlyGxz_Callback(hObject, eventdata, handles)
function Plynu_yz_Callback(hObject, eventdata, handles)
function Plynu_xz_Callback(hObject, eventdata, handles)
function PlyGyz_Callback(hObject, eventdata, handles)
function Volumn_Callback(hObject, eventdata, handles)
function Volumn_CreateFcn(hObject, eventdata, handles)
if ispc && isequal(get(hObject,'BackgroundColor'), get(0,'defaultUicontrolBackgroundColor'))
    set(hObject,'BackgroundColor','white');
end


function LEx_Callback(hObject, eventdata, handles)

function LEy_Callback(hObject, eventdata, handles)

function LGxy_Callback(hObject, eventdata, handles)

function LGyz_Callback(hObject, eventdata, handles)

function LGxz_Callback(hObject, eventdata, handles)

function Lnu_xy_Callback(hObject, eventdata, handles)

function Lnu_yz_Callback(hObject, eventdata, handles)

function Lnu_xz_Callback(hObject, eventdata, handles)

function Leta_Callback(hObject, eventdata, handles)


% --- Executes on button press in Plot_laminate.
function Plot_laminate_Callback(hObject, eventdata, handles)
E1 = str2double(get(handles.Input_E1,'String'));
E2 = str2double(get(handles.Input_E2,'String'));
G12 = str2double(get(handles.Input_G12,'String'));
G23 = str2double(get(handles.Input_G23,'String'));
nu_12 = str2double(get(handles.Input_nu_12,'String'));
nu_23 = str2double(get(handles.Input_nu_23,'String'));
Ply_angle = str2num(get(handles.Input_ply_orientation,'String'));
Ply_thickness = str2num(get(handles.Input_ply_thickness,'String'));
numcount = numel(Ply_thickness);
Ply_angle2 = zeros(1,numcount-1);
Ply_angle3 = zeros(1,numcount);
Ply_thickness2 = zeros(1,numcount-1);
Ply_thickness3 = zeros(1,numcount);
switch get(handles.Symmetric_type,'Value')
    case 1
        rPly_angle = Ply_angle;
        rPly_thickness = Ply_thickness;
        rnumcount = numcount;
    case 2
        for j = 1:numcount-1
            Ply_thickness2(j) = Ply_thickness(numcount-j);
```

```
        Ply_angle2(j) = Ply_angle(numcount-j);
      end
      rnumcount = numcount*2-1;
      rPly_thickness = [Ply_thickness Ply_thickness2];
      rPly_angle = [Ply_angle Ply_angle2];
   case 3
      for k = 1:numcount;
        Ply_thickness3(k) = Ply_thickness(numcount+1-k);
        Ply_angle3(k) = Ply_angle(numcount+1-k);
      end
      rnumcount = numcount*2;
      rPly_thickness = [Ply_thickness Ply_thickness3];
      rPly_angle = [Ply_angle Ply_angle3];
end

% An Introduction to Compostie Materials. T, D. Hull, T. W. Clyne
S11 = 1/E1;
S12 = -nu_12/E1;
S22 = 1/E2;
S23 = -nu_23/E2;
S44 = 1/G23;
S66 = 1/G12;
S = [S11 S12 S12 0 0 0;
   S12 S22 S23 0 0 0;
   S12 S23 S22 0 0 0;
   0 0 0 S44 0 0;
   0 0 0 0 S66 0;
   0 0 0 0 0 S66];

h=zeros(1,rnumcount+1);
for j=1:rnumcount+1;
   if j==1
      h(j)=-sum(rPly_thickness)/2;
   else
      h(j)=h(j-1)+rPly_thickness(j-1);
   end
end
theta = 1:90;
for L = 1:length(theta)
   A = zeros(6,6);
B = zeros(6,6);
D = zeros(6,6);
for i = 1:rnumcount
   c = cos((theta(L)+rPly_angle(i))*pi/180);
   s = sin((theta(L)+rPly_angle(i))*pi/180);
T = [c^2 s^2 0 0 0 2*c*s;
   s^2 c^2 0 0 0 -2*c*s;
   0 0 1 0 0 0;
   0 0 0 c s 0;
   0 0 0 -s c 0;
   -c*s c*s 0 0 0 c^2-s^2];
T1 = [c^2 s^2 0 0 0 c*s;
   s^2 c^2 0 0 0 -c*s;
   0 0 1 0 0 0;
   0 0 0 c s 0;
   0 0 0 -s c 0;
   -2*c*s 2*c*s 0 0 0 c^2-s^2];
```

```
Sbar = T1\S*T;
Cbar=inv(Sbar);
   for m = 1:6
      for n = 1:6
         A(m,n) = A(m,n)+Cbar(m,n)*(h(i+1)-h(i));
         B(m,n) = B(m,n)+Cbar(m,n)*((h(i+1))^2-(h(i))^2)/2;
         D(m,n) = D(m,n)+Cbar(m,n)*(h((i+1))^3-(h(i))^3)/3;
      end
   end
end
ABBD = [A B;B D];
abbd=inv(ABBD);
a=abbd(1:6,1:6);
Ex(L)=1/a(1,1)/sum(rPly_thickness);
Ey(L)=1/a(2,2)/sum(rPly_thickness);
Gxy(L)=1/a(6,6)/sum(rPly_thickness);
Gyz(L)=1/a(4,4)/sum(rPly_thickness);
Gxz(L)=1/a(5,5)/sum(rPly_thickness);
nu_xy(L) = -a(1,2)/a(1,1);
nu_yx(L) = -a(1,2)/a(2,2);
nu_yz(L) = -a(3,2)/a(2,2);
nu_xz(L) = -a(3,1)/a(1,1);
eta_xyx(L) = a(1,6)/a(1,1);
eta_xyy(L) = a(2,6)/a(2,2);
end
% Plot the title
rPly_angle = num2str(rPly_angle);
rPly_thickness = num2str(rPly_thickness);
G{1} = '\theta: ';
G{2} = rPly_angle;
G{3} = '      t: ';
G{4} = rPly_thickness;
angle_thickness = [G{ISO899-2:2003,  #140}];
%select plot items
switch get(handles.LEx,'Value')+get(handles.LEy,'Value')
   case 1
      figure;
      if get(handles.LEx,'Value')
         plot(theta,Ex,'b-o','linewidth',2); hold on;
         legend('Ex'); hold on;
         xlabel('Angle in degree(\theta)');
         ylabel('Modulus(GPa)');
                  title(angle_thickness);
      else
         plot(theta,Ey,'m-*','linewidth',2); hold on;
         legend('Ey'); hold on;
         xlabel('Angle in degree(\theta)');
         ylabel('Modulus(GPa)');
                  title(angle_thickness);
      end
   case 2
      figure;
      plot(theta,Ex,'b-o',theta,Ey,'m-*','linewidth',2); hold on;
      legend('Ex','Ey'); hold on;
      xlabel('Angle in degree(\theta)');
      ylabel('Modulus(GPa)');
               title(angle_thickness);
end
```

```
switch get(handles.LGxy,'Value')
   case 1
      figure;
         plot(theta,Gxy,'b-o'); hold on;
         legend('Gxy'); hold on;
         xlabel('Angle in degree(\theta)');
         ylabel('Modulus(GPa)');
                  title(angle_thickness);
end

switch get(handles.LGyz,'Value')
   case 1
            figure;
         plot(theta,Gyz,'r-+',theta,Gxz,'g-*'); hold on;
         legend('Gyz','Gxz'); hold on;
         xlabel('Angle in degree(\theta)');
         ylabel('Modulus(GPa)');
                  title(angle_thickness);
end

switch get(handles.LGxz,'Value')
   case 1
            figure;
         plot(theta,Gxy,'b-o',theta,Gyz,'g-*',theta,Gxz,'r-+'); hold on;
         legend('Gxy','Gyz','Gxz'); hold on;
         xlabel('Angle in degree(\theta)');
         ylabel('Modulus(GPa)');
                  title(angle_thickness);
end

switch get(handles.Lnu_xy,'Value')
   case 1
      figure;
         plot(theta,nu_xy,'b-o'); hold on;
         legend('nu_x_y'); hold on;
         xlabel('Angle in degree(\theta)');
         ylabel('Poisson ratio(\nu)');
                  title(angle_thickness);
end

switch get(handles.Lnu_yz,'Value')
   case 1
      figure;
         plot(theta,nu_yz,'b-o',theta,nu_xz,'r-+'); hold on;
         legend('nu_y_z','nu_x_z'); hold on;
         xlabel('Angle in degree(\theta)');
         ylabel('Poisson ratio(\nu)');
                  title(angle_thickness);
end

switch get(handles.Lnu_xz,'Value')
   case 1
      figure;
         plot(theta,nu_xy,'b-o',theta,nu_yz,'g-*',theta,nu_xz,'r-+'); hold on;
         legend('nu_x_y','nu_y_z','nu_x_z'); hold on;
```

```
        xlabel('Angle in degree(\theta)');
        ylabel('Poisson ratio(\nu)');
                title(angle_thickness);
end

switch get(handles.Leta,'Value')
   case 1
      figure;
        plot(theta,eta_xyx,'r-*',theta,eta_xyy,'b-o'); hold on;
        legend('\eta_x_y_x','\eta_x_y_y'); hold on;
        xlabel('Angle in degree(\theta)');
        ylabel('Interaction ratio(\eta_X_y_x)');
                title(angle_thickness);
end
```

APPENDIX B: MATLAB CODE FOR FAILURE ENVELOPES

Trace, the sum of the diagonal components of the stiffness matrix of composites, is an invariant of stress tensor transformation. The invariant theory was first proposed by Tsai and Melo (2014). This tool was originally developed to duplicate the work shown in literature 'An invariant-based theory of composites' and to draw the failure envelopes in stain space. Furthermore, it was used to investigate the effects of unequal compressive/tensile moduli.

For the convenience, the first session was designed to be the same as the 'composite calculator 3D', which can be used for the ply properties calculation. The user would need to provide material properties including the tensile, compressive and share strengths. Ten common carbon/epoxy composites are included in the database. Figure B2 shows the failure envelopes in strain space extracted from the tool.

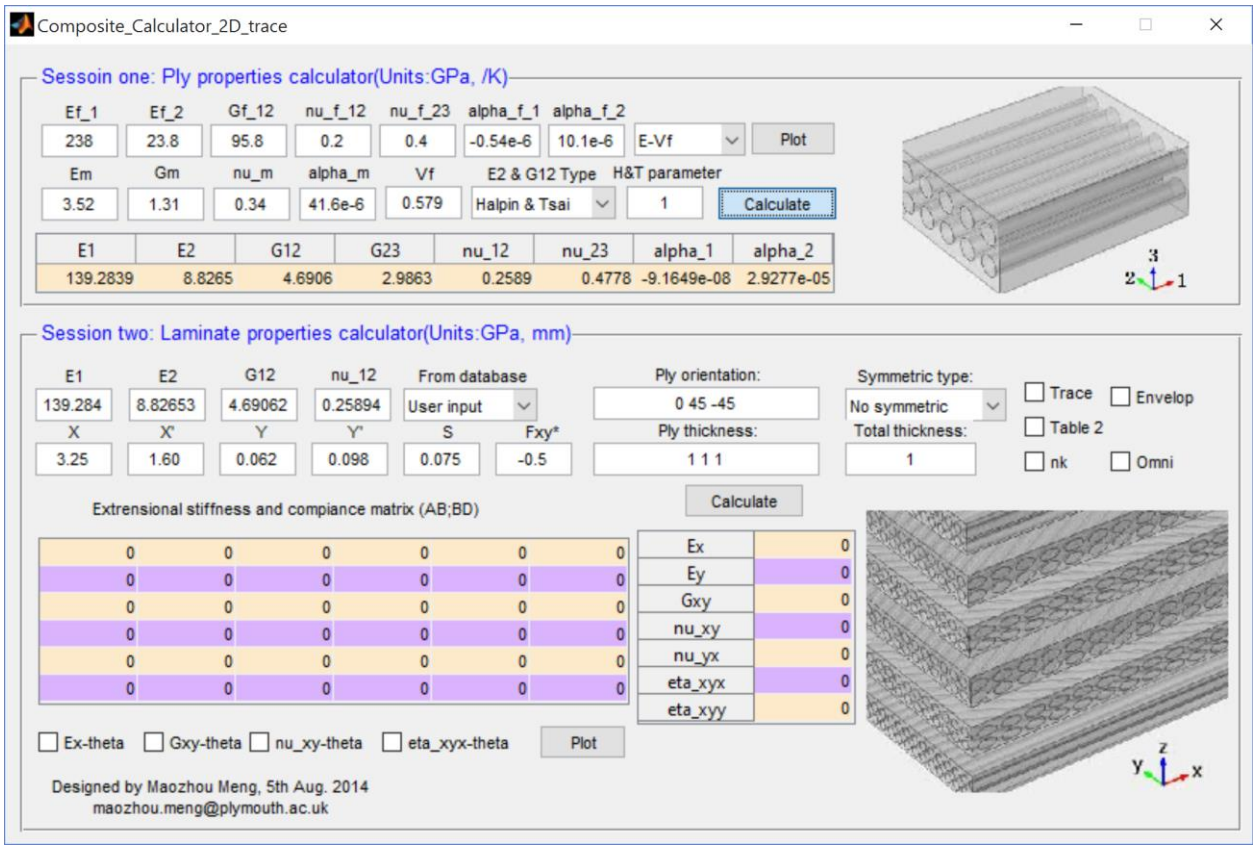

Figure B1. The GUI of trace calculator

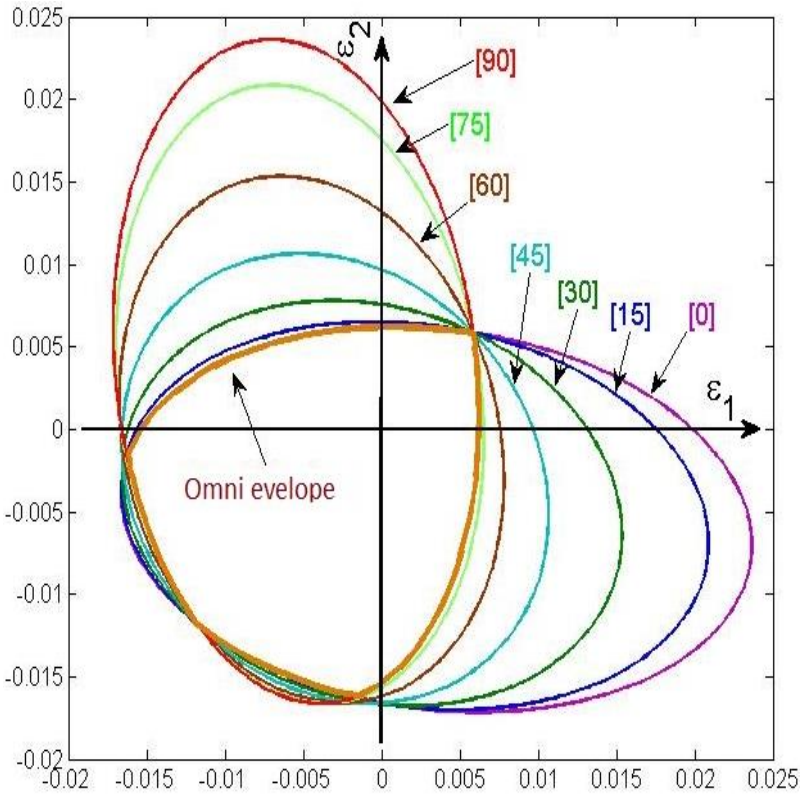

Figure B2. Failure envelopes and the omni envelope of T800/cytec carbon fibre-epoxy composite

```
function varargout = Composite_Calculator_2D_trace(varargin)
% COMPOSITE_CALCULATOR_2D_TRACE MATLAB code for Composite_Calculator_2D_trace.fig
% This program is built by Maozhou Meng on 29th,Dec.2013, Plymouth University
% Last Modified by GUIDE v2.5 05-Aug-2014 19:01:43
% Begin initialization code - DO NOT EDIT
gui_Singleton = 1;
gui_State = struct('gui_Name',       mfilename, ...
                   'gui_Singleton',  gui_Singleton, ...
                   'gui_OpeningFcn', @Composite_Calculator_2D_trace_OpeningFcn, ...
                   'gui_OutputFcn',  @Composite_Calculator_2D_trace_OutputFcn, ...
                   'gui_LayoutFcn',  [] , ...
                   'gui_Callback',   []);
if nargin && ischar(varargin{1})
   gui_State.gui_Callback = str2func(varargin{1});
end

if nargout
   [varargout{1:nargout}] = gui_mainfcn(gui_State, varargin{ISO899-2:2003,  #140});
else
   gui_mainfcn(gui_State, varargin{ISO899-2:2003,  #140});
end
% End initialization code - DO NOT EDIT
% --- Executes just before Composite_Calculator_2D_trace is made visible.
function Composite_Calculator_2D_trace_OpeningFcn(hObject, ~, handles, varargin)
```

```
% This function has no output args, see OutputFcn.
% Choose default command line output for Composite_Calculator_2D_trace
handles.output = hObject;
% Update handles structure
guidata(hObject, handles);
axes(handles.axes_123);
imshow('m_123.jpg');
axes(handles.axes_laminar);
imshow('m_laminar.jpg');
% --- Outputs from this function are returned to the command line.
function varargout = Composite_Calculator_2D_trace_OutputFcn(hObject, eventdata, handles)
varargout{1} = handles.output;
% =====START OF INPUT ARGUMENTS=====
function Input_Ef_1_Callback(hObject, eventdata, handles)
function Input_Ef_1_CreateFcn(hObject, eventdata, handles)
if ispc && isequal(get(hObject,'BackgroundColor'), get(0,'defaultUicontrolBackgroundColor'))
    set(hObject,'BackgroundColor','white');
end

function Input_Em_Callback(hObject, eventdata, handles)
function Input_Em_CreateFcn(hObject, eventdata, handles)
if ispc && isequal(get(hObject,'BackgroundColor'), get(0,'defaultUicontrolBackgroundColor'))
    set(hObject,'BackgroundColor','white');
end

function Input_Gm_Callback(hObject, eventdata, handles)
function Input_Gm_CreateFcn(hObject, eventdata, handles)
if ispc && isequal(get(hObject,'BackgroundColor'), get(0,'defaultUicontrolBackgroundColor'))
    set(hObject,'BackgroundColor','white');
end

function Input_nu_f_12_Callback(hObject, eventdata, handles)
function Input_nu_f_12_CreateFcn(hObject, eventdata, handles)
if ispc && isequal(get(hObject,'BackgroundColor'), get(0,'defaultUicontrolBackgroundColor'))
    set(hObject,'BackgroundColor','white');
end

function Input_nu_m_Callback(hObject, eventdata, handles)
function Input_nu_m_CreateFcn(hObject, eventdata, handles)
if ispc && isequal(get(hObject,'BackgroundColor'), get(0,'defaultUicontrolBackgroundColor'))
    set(hObject,'BackgroundColor','white');
end

function Input_Gf_12_Callback(hObject, eventdata, handles)
function Input_Gf_12_CreateFcn(hObject, eventdata, handles)
if ispc && isequal(get(hObject,'BackgroundColor'), get(0,'defaultUicontrolBackgroundColor'))
    set(hObject,'BackgroundColor','white');
end

function Input_Vf_Callback(hObject, eventdata, handles)
function Input_Vf_CreateFcn(hObject, eventdata, handles)
if ispc && isequal(get(hObject,'BackgroundColor'), get(0,'defaultUicontrolBackgroundColor'))
    set(hObject,'BackgroundColor','white');
end

function E2_type_Callback(hObject, eventdata, handles)
```

```
function E2_type_CreateFcn(hObject, eventdata, handles)
if ispc && isequal(get(hObject,'BackgroundColor'), get(0,'defaultUicontrolBackgroundColor'))
    set(hObject,'BackgroundColor','white');
end

function Input_Ef_2_Callback(hObject, eventdata, handles)
function Input_Ef_2_CreateFcn(hObject, eventdata, handles)
if ispc && isequal(get(hObject,'BackgroundColor'), get(0,'defaultUicontrolBackgroundColor'))
    set(hObject,'BackgroundColor','white');
end

function Input_nu_f_23_Callback(hObject, eventdata, handles)
function Input_nu_f_23_CreateFcn(hObject, eventdata, handles)
if ispc && isequal(get(hObject,'BackgroundColor'), get(0,'defaultUicontrolBackgroundColor'))
    set(hObject,'BackgroundColor','white');
end

function Input_Alphaf_1_Callback(hObject, eventdata, handles)
function Input_Alphaf_1_CreateFcn(hObject, eventdata, handles)
if ispc && isequal(get(hObject,'BackgroundColor'), get(0,'defaultUicontrolBackgroundColor'))
    set(hObject,'BackgroundColor','white');
end

function Input_Alphaf_2_Callback(hObject, eventdata, handles)
function Input_Alphaf_2_CreateFcn(hObject, eventdata, handles)

if ispc && isequal(get(hObject,'BackgroundColor'), get(0,'defaultUicontrolBackgroundColor'))
    set(hObject,'BackgroundColor','white');
end

function Input_Alpham_Callback(hObject, eventdata, handles)
function Input_Alpham_CreateFcn(hObject, eventdata, handles)
if ispc && isequal(get(hObject,'BackgroundColor'), get(0,'defaultUicontrolBackgroundColor'))
    set(hObject,'BackgroundColor','white');
end

% --- Executes on button press in Calculate_ply.
function Calculate_ply_Callback(hObject, eventdata, handles)
% Get input data
Ef_1 = str2double(get(handles.Input_Ef_1,'String'));
Ef_2 = str2double(get(handles.Input_Ef_2,'String'));
Em = str2double(get(handles.Input_Em,'String'));
Gf_12 = str2double(get(handles.Input_Gf_12,'String'));
%Gf_23 = str2double(get(handles.Input_Gf_23,'String'));
Gm = str2double(get(handles.Input_Gm,'String'));
nu_f_12 = str2double(get(handles.Input_nu_f_12,'String'));
nu_f_23 = str2double(get(handles.Input_nu_f_23,'String'));
nu_m = str2double(get(handles.Input_nu_m,'String'));
Alphaf_1 = str2double(get(handles.Input_Alphaf_1,'String'));
Alphaf_2 = str2double(get(handles.Input_Alphaf_2,'String'));
Alpham = str2double(get(handles.Input_Alpham,'String'));
Vf = str2double(get(handles.Input_Vf,'String'));
HT = str2double(get(handles.Input_Hadjust,'String'));
% Mechanics of Composite Materials with Matlab, George Z. Voyiadjis and Peter I. Kattan
E1 = Vf*Ef_1+Em*(1-Vf);
nu_12 = Vf*nu_f_12+nu_m*(1-Vf);
```

```
Alpha1 = (Alphaf_1*Ef_1*Vf+Alpham*Em*(1-Vf))/(Ef_1*Vf+Em*(1-Vf));
Alpha2 = (Alphaf_2-Em*nu_f_12*(Alpham-Alphaf_1)*(1-Vf)/E1)*Vf+(Alpham+Ef_1*nu_m*(Alpham-
Alphaf_1)*Vf/E1)*(1-Vf);
% select the E2 calculating type from Halpin&Tsai and equal stress
kf = Ef_1*Ef_2/(2*Ef_1*(1-nu_f_12*Ef_2/Ef_1-nu_f_23)+Ef_2*(1-2*nu_f_12));
%kf = Ef_2/3/(1-nu_f_23-nu_f_12*Ef_2/Ef_1);
%kf = Ef_1/3/(1-2*nu_f_12);
%kf = Ef_2/(1-nu_f_23-Ef_2*nu_f_12^2/Ef_1)/2;
km = Em/3/(1-2*nu_m);
etaK = (kf/km-1)/(kf/km+HT);
switch get(handles.E2_type,'Value')
   case 1
      etaE = (Ef_2/Em-1)/(Ef_2/Em+HT);
      E2 = Em*(1+HT*etaE*Vf)/(1-etaE*Vf);
      etaG = (Gf_12/Gm-1)/(Gf_12/Gm+HT);
      G12 = Gm*(1+HT*etaG*Vf)/(1-etaG*Vf);
            K = km*(1+HT*etaK*Vf)/(1-etaK*Vf);
   case 2
      E2 = 1/(Vf/Ef_2+(1-Vf)/Em);
      G12 = 1/(Vf/Gf_12+(1-Vf)/Gm);
      K = 1/(Vf/kf+(1-Vf)/km);
end
% calculate poisson ratio and shear modulus of 23 direction
% An Introduction to Composite Materials, D. Hull and T.W. Clyne

%K = 1/(Vf/kf+(1-Vf)/km);
nu_21 = nu_12*E2/E1;
nu_23 = 1-nu_21-E2/2/K+E2*(1-2*nu_12)/2/E1;
%nu_23 = 1-E2/K/2-2*nu_12*nu_21;
%nu_23 = 1-nu_21-E2/3/K;
%nu_23 = 1-nu_12*Em/Ef_2-E2*((3*Vf*(1-2*nu_f_12))/Ef_2+(3*(1-Vf)*(1-2*nu_m))/Em)/3;
G23 = E2/2/(1+nu_23);
% Output composite properties in table
Matrix_output = [E1 E2 G12 G23 nu_12 nu_23 Alpha1 Alpha2];
set(handles.Output_ply_table,'data',Matrix_output);
set(handles.Input_E1,'string',E1);
set(handles.Input_E2,'string',E2);
set(handles.Input_G12,'string',G12);
set(handles.Input_nu_12,'string',nu_12);
guidata(hObject, handles);

function Input_E1_Callback(hObject, eventdata, handles)
function Input_E1_CreateFcn(hObject, eventdata, handles)
if ispc && isequal(get(hObject,'BackgroundColor'), get(0,'defaultUicontrolBackgroundColor'))
   set(hObject,'BackgroundColor','white');
end

function Input_E2_Callback(hObject, eventdata, handles)
function Input_E2_CreateFcn(hObject, eventdata, handles)
if ispc && isequal(get(hObject,'BackgroundColor'), get(0,'defaultUicontrolBackgroundColor'))
   set(hObject,'BackgroundColor','white');
end

function Input_nu_12_Callback(hObject, eventdata, handles)
function Input_nu_12_CreateFcn(hObject, eventdata, handles)
if ispc && isequal(get(hObject,'BackgroundColor'), get(0,'defaultUicontrolBackgroundColor'))
   set(hObject,'BackgroundColor','white');
```

```
end

function Input_G12_Callback(hObject, eventdata, handles)
function Input_G12_CreateFcn(hObject, eventdata, handles)
if ispc && isequal(get(hObject,'BackgroundColor'), get(0,'defaultUicontrolBackgroundColor'))
    set(hObject,'BackgroundColor','white');
end

function Input_Theta_Callback(hObject, eventdata, handles)
function Input_Theta_CreateFcn(hObject, eventdata, handles)
if ispc && isequal(get(hObject,'BackgroundColor'), get(0,'defaultUicontrolBackgroundColor'))
    set(hObject,'BackgroundColor','white');
end

function PlyEx_Callback(hObject, eventdata, handles)
function PlyGxy_Callback(hObject, eventdata, handles)

function Plynu_xy_Callback(hObject, eventdata, handles)
function Plyeta_xyx_Callback(hObject, eventdata, handles)

function Input_ply_thickness_Callback(hObject, eventdata, handles)
function Input_ply_thickness_CreateFcn(hObject, eventdata, handles)
if ispc && isequal(get(hObject,'BackgroundColor'), get(0,'defaultUicontrolBackgroundColor'))
    set(hObject,'BackgroundColor','white');
end

function Input_ply_orientation_Callback(hObject, eventdata, handles)
function Input_ply_orientation_CreateFcn(hObject, eventdata, handles)
if ispc && isequal(get(hObject,'BackgroundColor'), get(0,'defaultUicontrolBackgroundColor'))
    set(hObject,'BackgroundColor','white');
end

function Symmetric_type_Callback(hObject, eventdata, handles)

function Symmetric_type_CreateFcn(hObject, eventdata, handles)

if ispc && isequal(get(hObject,'BackgroundColor'), get(0,'defaultUicontrolBackgroundColor'))
    set(hObject,'BackgroundColor','white');
end

function Calculate_laminar_Callback(hObject, eventdata, handles)
% define ply data source
E1 = str2double(get(handles.Input_E1,'String'));
E2 = str2double(get(handles.Input_E2,'String'));
G12 = str2double(get(handles.Input_G12,'String'));
nu_12 = str2double(get(handles.Input_nu_12,'String'));
X = str2double(get(handles.Input_X,'String'));
X1 = str2double(get(handles.Input_X1,'String'));
Y = str2double(get(handles.Input_Y,'String'));
Y1 = str2double(get(handles.Input_Y1,'String'));
S = str2double(get(handles.Input_S,'String'));
Fxybar = str2double(get(handles.Input_Fxybar,'String'));
% Choose the data source from predefined, Jose Daniel Diniz Melo
switch get(handles.Database,'Value')
    case 2
        %IM7/977
```

```
        E1=191;E2=9.94;G12=7.79;nu_12=0.35;
X=3.25;X1=1.60;Y=0.062;Y1=0.098;S=0.075;
set(handles.Input_E1,'string',E1);set(handles.Input_E2,'string',E2);
set(handles.Input_G12,'string',G12);set(handles.Input_nu_12,'string',nu_12);
set(handles.Input_X,'string',X);set(handles.Input_X1,'string',X1);
set(handles.Input_Y,'string',Y);set(handles.Input_Y1,'string',Y1);
set(handles.Input_S,'string',S);
    case 3
        %T800/Cytec
        E1=162.00;E2=9.00;nu_12=0.40;G12=5;
        X=3.768;X1=1.656;Y=0.056;Y1=0.150;S=0.098;
        set(handles.Input_E1,'string',E1);set(handles.Input_E2,'string',E2);
set(handles.Input_G12,'string',G12);set(handles.Input_nu_12,'string',nu_12);
set(handles.Input_X,'string',X);set(handles.Input_X1,'string',X1);
set(handles.Input_Y,'string',Y);set(handles.Input_Y1,'string',Y1);
set(handles.Input_S,'string',S);
    case 4
        %T700 C-Ply 55
        E1=121;E2=8;nu_12=0.3;G12=4.7;
        X=2.53;X1=1.7;Y=0.066;Y1=0.22;S=0.093;
        set(handles.Input_E1,'string',E1);set(handles.Input_E2,'string',E2);
set(handles.Input_G12,'string',G12);set(handles.Input_nu_12,'string',nu_12);
set(handles.Input_X,'string',X);set(handles.Input_X1,'string',X1);
set(handles.Input_Y,'string',Y);set(handles.Input_Y1,'string',Y1);
set(handles.Input_S,'string',S);
    case 5
        %T700 C-Ply 64
        E1=140.8;E2=9.3;nu_12=0.3;G12=5.8;
X=2.944;X1=1.983;Y=0.066;Y1=0.220;S=0.093;
set(handles.Input_E1,'string',E1);set(handles.Input_E2,'string',E2);
set(handles.Input_G12,'string',G12);set(handles.Input_nu_12,'string',nu_12);
set(handles.Input_X,'string',X);set(handles.Input_X1,'string',X1);
set(handles.Input_Y,'string',Y);set(handles.Input_Y1,'string',Y1);
set(handles.Input_S,'string',S);
    case 6
        %AS4/3501
        E1=138;E2=8.96;nu_12=0.3;G12=7.1;
X=1.447;X1=1.447;Y=0.052;Y1=0.206;S=0.093;
set(handles.Input_E1,'string',E1);set(handles.Input_E2,'string',E2);
set(handles.Input_G12,'string',G12);set(handles.Input_nu_12,'string',nu_12);
set(handles.Input_X,'string',X);set(handles.Input_X1,'string',X1);
set(handles.Input_Y,'string',Y);set(handles.Input_Y1,'string',Y1);
set(handles.Input_S,'string',S);
    case 7
        %IM6/epoxy
        E1=203;E2=11.2;nu_12=0.32;G12=8.4;
X=3.500;X1=1.540;Y=0.056;Y1=0.150;S=0.098;
set(handles.Input_E1,'string',E1);set(handles.Input_E2,'string',E2);
set(handles.Input_G12,'string',G12);set(handles.Input_nu_12,'string',nu_12);
set(handles.Input_X,'string',X);set(handles.Input_X1,'string',X1);
set(handles.Input_Y,'string',Y);set(handles.Input_Y1,'string',Y1);
set(handles.Input_S,'string',S);
    case 8
        %AS4/PEEK
        E1=134;E2=8.9;nu_12=0.28;G12=5.1;
X=2.130;X1=1.100;Y=0.080;Y1=0.200;S=0.160;
set(handles.Input_E1,'string',E1);set(handles.Input_E2,'string',E2);
set(handles.Input_G12,'string',G12);set(handles.Input_nu_12,'string',nu_12);
```

```
set(handles.Input_X,'string',X);set(handles.Input_X1,'string',X1);
set(handles.Input_Y,'string',Y);set(handles.Input_Y1,'string',Y1);
set(handles.Input_S,'string',S);
   case 9
      %Kevlar/epoxy
      E1=76;E2=5.5;nu_12=0.34;G12=2.3;
X=1.400;X1=0.235;Y=0.012;Y1=0.053;S=0.034;
set(handles.Input_E1,'string',E1);set(handles.Input_E2,'string',E2);
set(handles.Input_G12,'string',G12);set(handles.Input_nu_12,'string',nu_12);
set(handles.Input_X,'string',X);set(handles.Input_X1,'string',X1);
set(handles.Input_Y,'string',Y);set(handles.Input_Y1,'string',Y1);
set(handles.Input_S,'string',S);
   case 10
      %IM7/8552
      E1=171;E2=9.08;nu_12=0.32;G12=5.29;
X=2.326;X1=1.200;Y=0.062;Y1=0.200;S=0.0815;
set(handles.Input_E1,'string',E1);set(handles.Input_E2,'string',E2);
set(handles.Input_G12,'string',G12);set(handles.Input_nu_12,'string',nu_12);
set(handles.Input_X,'string',X);set(handles.Input_X1,'string',X1);
set(handles.Input_Y,'string',Y);set(handles.Input_Y1,'string',Y1);
set(handles.Input_S,'string',S);
   case 11
      %IM7/MTM45
E1=175;E2=8.2;nu_12=0.33;G12=5.5;
X=2.500;X1=1.700;Y=0.069;Y1=0.169;S=0.043;
set(handles.Input_E1,'string',E1);set(handles.Input_E2,'string',E2);
set(handles.Input_G12,'string',G12);set(handles.Input_nu_12,'string',nu_12);
set(handles.Input_X,'string',X);set(handles.Input_X1,'string',X1);
set(handles.Input_Y,'string',Y);set(handles.Input_Y1,'string',Y1);
set(handles.Input_S,'string',S);
end
% Get ply orientation, thickness data and count the ply numbers input
Ply_angle = str2num(get(handles.Input_ply_orientation,'String'));
Ply_thickness = str2num(get(handles.Input_ply_thickness,'String'));
numcount = numel(Ply_thickness);
vector_length = numel(Ply_angle)-numcount;
if vector_length ~= 0;
errordlg('The length of orientation and thickness vector not consistent','Input Error');
return
end
% get the real matrix of ply angle and ply thickness
Ply_angle2 = zeros(1,numcount-1);
Ply_angle3 = zeros(1,numcount);
Ply_thickness2 = zeros(1,numcount-1);
Ply_thickness3 = zeros(1,numcount);
switch get(handles.Symmetric_type,'Value')
   case 1
      rPly_angle = Ply_angle;
      rPly_thickness = Ply_thickness;
      rnumcount = numcount;
   case 2
      for j = 1:numcount-1
         Ply_thickness2(j) = Ply_thickness(numcount-j);
         Ply_angle2(j) = Ply_angle(numcount-j);
      end
      rnumcount = numcount*2-1;
      rPly_thickness = [Ply_thickness Ply_thickness2];
      rPly_angle = [Ply_angle Ply_angle2];
```

```
    case 3
        for k = 1:numcount;
            Ply_thickness3(k) = Ply_thickness(numcount+1-k);
            Ply_angle3(k) = Ply_angle(numcount+1-k);
        end
        rnumcount = numcount*2;
        rPly_thickness = [Ply_thickness Ply_thickness3];
        rPly_angle = [Ply_angle Ply_angle3];
end
set(handles.Output_total_thickness,'String',sum(rPly_thickness));
% define the complaince matrix
%S11 = 1/E1;
%S12 = -nu_12/E1;
%S22 = 1/E2;
%S66 = 1/G12;
%S = [S11 S12 0;S12 S22 0;0 0 S66];
nu_21=nu_12*E2/E1;
tnu=1-nu_12*nu_21;
Q11=E1/tnu;
Q22=E2/tnu;
Q12=nu_21*E1/tnu;
Q66=G12;
Q=[Q11 Q12 0;
    Q12 Q22 0;
    0 0 Q66];
% Formulas and equations for the classical laminate theory, Vincent Calard
A = zeros(3,3);
B = zeros(3,3);
D = zeros(3,3);
h=zeros(1,rnumcount+1);
for j=1:rnumcount+1;
    if j==1
        h(j)=-sum(rPly_thickness)/2;
    else
        h(j)=h(j-1)+rPly_thickness(j-1);
    end
end
for i = 1:rnumcount
    c = cos(rPly_angle(i)*pi/180);
    s = sin(rPly_angle(i)*pi/180);
    T = [c^2 s^2 2*c*s;
        s^2 c^2 -2*c*s;
        -c*s c*s c^2-s^2];
    T1 = [c^2 s^2 c*s;
        s^2 c^2  -c*s;
        -2*c*s 2*c*s c^2-s^2];
%    Sbar = T1*S*T;
%    Cbar = inv(Sbar);
Qbar=T\Q*T1;
%Qbar(:,3)=Qbar(:,3)/2;
%Q(3,3)=Q(3,3)/2;
    for m = 1:3
        for n = 1:3
            A(m,n) = A(m,n)+Qbar(m,n)*(h(i+1)-h(i));
            B(m,n) = B(m,n)+Qbar(m,n)*((h(i+1))^2-(h(i))^2)/2;
            D(m,n) = D(m,n)+Qbar(m,n)*(h((i+1))^3-(h(i))^3)/3;
        end
    end
```

```
end
%lCbar = lCbar/sum(rPly_thickness);
ABBD = [A B;B D];
abbd=inv(ABBD);
a=abbd(1:3,1:3);
%Matrix_stiffness_complaince_laminar = [lSbar lCbar];
set(handles.Stiffness_Complaince_laminar_table,'data',ABBD);
% get the elastic matrix and other parameters for output table
Ex = 1/a(1,1)/sum(rPly_thickness);
Ey = 1/a(2,2)/sum(rPly_thickness);
Gxy = 1/a(3,3)/sum(rPly_thickness);
nu_xy = -a(1,2)/a(1,1);
nu_yx = -a(1,2)/a(2,2);
eta_xyx = a(1,3)/a(1,1);
eta_xyy = a(2,3)/a(2,2);
Matrix_elastic_laminar = [Ex Ey Gxy nu_xy nu_yx eta_xyx eta_xyy]';
set(handles.Laminar_table,'data',Matrix_elastic_laminar);
% Evaluate the trace
% For the trace calculation, the [Q1] uses tensional notation, multiple 2
% Q1=Q';
Q1=[Q11 Q12 0;
   Q12 Q22 0;
   0 0 2*Q66];
% Handle with Table 1----------
Tr=trace(Q1);
Qbarxx=Q11/Tr;
Qbar11=Qbar(1,1)/Tr;
Qbaryy=Q22/Tr;
Qbarxy=Q12/Tr;
Qbarss=Q66/Tr;
%assignin('base','Tr',Tr);
%assignin('base','Qbarxx',Qbarxx);
%assignin('base','Qbar11',Qbar11);
%assignin('base','Qbaryy',Qbaryy);
%assignin('base','Qbarxy',Qbarxy);
%assignin('base','Qbarss',Qbarss);
switch get(handles.Tick_Tr,'Value')
   case 1
Table1=[Qbarxx Qbaryy Qbarxy Qbarss Qbar11 Tr];
figure('Position',[100 100 550 100]);
uitable('Units','normalized','Position',...
          [0 0 1 1], 'Data', Table1,'ColumnName',{'Qbarxx','Qbaryy','Qbarxy','Qbarss','Qbar11','Tr'});
end
% Handle with Table 2----------
ca=a';
cA=A';
Table2_1=(2*ca(1,2)+ca(3,3))/ca(2,2);
Table2_2=ca(1,1)/ca(2,2);
Table2_3=2*(cA(1,2)+2*cA(3,3))/cA(1,1);
Table2_4=cA(2,2)/cA(1,1);
%assignin('base','Table2_1',Table2_1);
%assignin('base','Table2_2',Table2_2);
%assignin('base','Table2_3',Table2_3);
%assignin('base','Table2_4',Table2_4);
switch get(handles.Tick_Table2,'Value')
   case 1
Table2=[Table2_1 Table2_2 Table2_3 Table2_4 Tr];
figure('Position',[100 100 550 100]);
```

```
uitable('Units','normalized','Position',[0 0 1 1],...
'Data', Table2,'ColumnName',{'Table2_1','Table2_2','Table2_3','Table2_4','Tr'});
end
% Handle with Table 3----------
Table3_k=sqrt(Ex/Ey);
Table3_n=sqrt(2*(Ex/Ey-nu_xy)+Ex/Gxy);
Table3_1=Table3_n+1;
Table3_2=(Table3_n-1)/Table3_k;
Table3_3=(Table3_n+1+Table3_k)*Table3_n;
Table3_4=Table3_n+2*Table3_k;
Table3_5=(Table3_n+1)*Table3_k-nu_xy;
%assignin('base','Table3_1',Table3_1);
%assignin('base','Table3_2',Table3_2);
%assignin('base','Table3_3',Table3_3);
%assignin('base','Table3_4',Table3_4);
%assignin('base','Table3_5',Table3_5);
switch get(handles.Tick_nk,'Value')
   case 1
Table3=[Table3_1 Table3_2 Table3_3 Table3_4 Table3_5];
figure('Position',[100 100 550 100]);
uitable('Units','normalized','Position',[0 0 1 1],...
'Data', Table3,'ColumnName',{'n+1','(n-1)/k','(1+k+n)n','2k+n','k(1+n)-nu'});
end
% Handle with Figure 3----------
Fxx=1/X/X1;Fx=1/X-1/X1;Fyy=1/Y/Y1;Fy=1/Y-1/Y1;Fss=1/S^2;Fxy=Fxybar*sqrt(Fxx*Fyy);
gx=Fx*Q11+Fy*Q12;gy=Fy*Q22+Fx*Q12;
gxy=Fxx*Q11*Q12+Fyy*Q22*Q12+Fxy*(Q11*Q22+Q12^2);
gxx=Fxx*Q11^2+Fyy*Q12^2+2*Fxy*Q12*Q11;
gyy=Fxx*Q12^2+Fyy*Q22^2+2*Fxy*Q12*Q22;
gss=Fss*Q66^2;
Tug=[3/8 3/8 1/4 1/2 0 0;
   1/2 -1/2 0 0 0 0;
   1/8 1/8 -1/4 -1/2 0 0;
   1/8 1/8 3/4 -1/2 0 0;
   1/8 1/8 -1/4 1/2 0 0;
   0 0 0 0 0.5 0.5;
   0 0 0 0 0.5 -0.5];
u17=Tug*[gxx;gyy;gxy;gss;gx;gy];
Tgu=[u17(1) u17(2) u17(3) 0 0 0 0 0;
   u17(1) -u17(2) u17(3) 0 0 0 0 0;
   u17(4) 0 -u17(3) 0 0 0 0 0;
   u17(5) 0 -u17(3) 0 0 0 0 0;
   0 0 0 u17(2)/2 u17(3) 0 0 0;
   0 0 0 u17(2)/2 -u17(3) 0 0 0;
   0 0 0 0 0 u17(6) u17(7) 0;
   0 0 0 0 0 u17(6) -u17(7) 0;
   0 0 0 0 0 0 0 u17(7)];
%plot envelop
switch get(handles.Tick_Env,'Value')
   case 1
figure;
for theta=0:15:90
g19=Tgu*[1;cos(2*theta*pi/180);cos(4*theta*pi/180);sin(2*theta*pi/180);sin(4*theta*pi/180);1;cos(2*th
eta*pi/180);sin(2*theta*pi/180)];
g11=g19(1);g22=g19(2);g12=g19(3);g1=g19(7);g2=g19(8);
syms x y;ezplot(g11*x^2+g22*y^2+2*g12*x*y+g1*x+g2*y-1,[-0.035 0.035 -0.035 0.035]);
hold on;axis auto;
xlabel('\epsilon_1');ylabel('\epsilon_2');%grid on;
```

```
title('Strain envelops');
end
end
%plot omni strain
switch get(handles.Tick_Omni,'Value')
   case 1
   figure;
for i=0:1:72
for theta=0:1:72
g19=Tgu*[1;cos(2*5*theta*pi/180);cos(4*5*theta*pi/180);sin(2*5*theta*pi/180);sin(4*5*theta*pi/180);
1;cos(2*5*theta*pi/180);sin(2*5*theta*pi/180)];
g11=g19(1);g22=g19(2);g12=g19(3);g1=g19(7);g2=g19(8);
a=g11*cos(i*5*pi/180).^2+2*g12*cos(i*5*pi/180).*sin(i*5*pi/180)+g22*sin(i*5*pi/180).^2;
b=g1*cos(i*5*pi/180)+g2*sin(i*5*pi/180);
R(theta+1)=-b./a/2+sqrt((b./a/2).^2+1./a);
end
R_omni(i+1)=min(R);
end
%assignin('base','R',R);
%assignin('base','R_omni',R_omni);
i=0:1:72;
alp=5*i*pi/180;
polar(alp,R_omni,'-r');
hold on;
polar(alp,R_omni*1.5,'-b');
hold on;
R_min=min(R_omni);
ang=0:0.01:2*pi;
xp=R_min*cos(ang);
yp=R_min*sin(ang);
plot(xp,yp,'--m','LineWidth',2);
hold on;
title('Omni strain');
end
%plot omni strain
%figure;syms x y;
%ezplot(Fxx*x^2+Fyy*y^2+Fx*x+Fy*y+Fxy*x*y-1, [-2.5 5 -0.15 0.1]);
%title('Stress space');
%f=figure;
%uitable(f, 'Data', u17,...
%          'ColumnName',{'u17'});
%       f=figure;
%uitable(f, 'Data', g19,...
%          'ColumnName',{'g19'});
% Handle with Figure 3----------
guidata(hObject, handles);

function Output_total_thickness_Callback(hObject, eventdata, handles)
function Output_total_thickness_CreateFcn(hObject, eventdata, handles)
if ispc && isequal(get(hObject,'BackgroundColor'), get(0,'defaultUicontrolBackgroundColor'))
   set(hObject,'BackgroundColor','white');
end

function Plot_laminar_Callback(hObject, eventdata, handles)
% define ply data source
E1 = str2double(get(handles.Input_E1,'String'));
E2 = str2double(get(handles.Input_E2,'String'));
```

```
G12 = str2double(get(handles.Input_G12,'String'));
nu_12 = str2double(get(handles.Input_nu_12,'String'));
% Get ply orientation, thickness data and count the ply numbers inputed
Ply_angle = str2num(get(handles.Input_ply_orientation,'String'));
Ply_thickness = str2num(get(handles.Input_ply_thickness,'String'));
numcount = numel(Ply_thickness);
vector_length = numel(Ply_angle)-numcount;
if vector_length ~= 0;
errordlg('The length of orientation and thickness vector not consistent','Input Error');
return
end
% get the real arrays of ply angle and ply thickness
Ply_angle2 = zeros(1,numcount-1);
Ply_angle3 = zeros(1,numcount);
Ply_thickness2 = zeros(1,numcount-1);
Ply_thickness3 = zeros(1,numcount);
switch get(handles.Symmetric_type,'Value')
   case 1
      rPly_angle = Ply_angle;
      rPly_thickness = Ply_thickness;
      rnumcount = numcount;
   case 2
      for j = 1:numcount-1
         Ply_thickness2(j) = Ply_thickness(numcount-j);
         Ply_angle2(j) = Ply_angle(numcount-j);
      end
      rnumcount = numcount*2-1;
      rPly_thickness = [Ply_thickness Ply_thickness2];
      rPly_angle = [Ply_angle Ply_angle2];
   case 3
      for k = 1:numcount;
         Ply_thickness3(k) = Ply_thickness(numcount+1-k);
         Ply_angle3(k) = Ply_angle(numcount+1-k);
      end
      rnumcount = numcount*2;
      rPly_thickness = [Ply_thickness Ply_thickness3];
      rPly_angle = [Ply_angle Ply_angle3];
end
nu_21=nu_12*E2/E1;
tnu=1-nu_12*nu_21;
Q11=E1/tnu;
Q22=E2/tnu;
Q12=nu_21*E1/tnu;
Q66=G12;
Q=[Q11 Q12 0;
   Q12 Q22 0;
   0 0 Q66];
% Formulas and equations for the classical laminate theory, Vincent Calard

h=zeros(1,rnumcount+1);
for j=1:rnumcount+1;
   if j==1
      h(j)=-sum(rPly_thickness)/2;
   else
      h(j)=h(j-1)+rPly_thickness(j-1);
   end
end
```

```
theta = 1:90;

for L = 1:length(theta)
   A = zeros(3,3);
B = zeros(3,3);
D = zeros(3,3);
for i = 1:rnumcount
   c = cos((theta(L)+rPly_angle(i))*pi/180);
   s = sin((theta(L)+rPly_angle(i))*pi/180);
   T = [c^2 s^2 2*c*s;
      s^2 c^2 -2*c*s;
      -c*s c*s c^2-s^2];
   T1 = [c^2 s^2 c*s;
      s^2 c^2  -c*s;
      -2*c*s 2*c*s c^2-s^2];
Qbar=T\Q*T1;
   for m = 1:3
      for n = 1:3
         A(m,n) = A(m,n)+Qbar(m,n)*(h(i+1)-h(i));
         B(m,n) = B(m,n)+Qbar(m,n)*((h(i+1))^2-(h(i))^2)/2;
         D(m,n) = D(m,n)+Qbar(m,n)*(h((i+1))^3-(h(i))^3)/3;
      end
   end
end
ABBD = [A B;B D];
abbd=inv(ABBD);
a=abbd(1:3,1:3);
Ex(L) = 1/a(1,1)/sum(rPly_thickness);
Ey(L) = 1/a(2,2)/sum(rPly_thickness);
Gxy(L) = 1/a(3,3)/sum(rPly_thickness);
nu_xy(L) = -a(1,2)/a(1,1);
eta_xyx(L) = a(1,3)/a(1,1);
end
% Plot the title
rPly_angle = num2str(rPly_angle);
rPly_thickness = num2str(rPly_thickness);
G{1} = '\theta: ';
G{2} = rPly_angle;
G{3} = 't: ';
G{4} = rPly_thickness;
angle_thickness = [G{ISO899-2:2003,  #140}];
% select plot items
switch get(handles.Laminar_Ex,'Value')+get(handles.Laminar_Gxy,'Value')
   case 1
      figure;
      if get(handles.Laminar_Ex,'Value')
         plot(theta,Ex,'b-o','linewidth',2); hold on;
         legend('Ex'); hold on;
         xlabel('Angle in degree(\theta)');
         ylabel('Modulus(GPa)');
         title(angle_thickness);
      else
         plot(theta,Gxy,'m-*','linewidth',2); hold on;
         legend('Gxy'); hold on;
         xlabel('Angle in degree(\theta)');
         ylabel('Modulus(GPa)');
```

```
            title(angle_thickness);
        end
    case 2
        figure;
        plot(theta,Ex,'b-o',theta,Gxy,'m-*','linewidth',2); hold on;
        legend('Ex','Gxy'); hold on;
        xlabel('Angle in degree(\theta)');
        ylabel('Modulus(GPa)');
        title(angle_thickness);
end

switch get(handles.Laminar_nu_xy,'Value')+get(handles.Laminar_eta_xyx,'Value')
    case 1
        figure;
        if get(handles.Laminar_nu_xy,'Value')
            plot(theta,nu_xy,'g-o'); hold on;
            legend('\nu_x_y'); hold on;
            xlabel('Angle in degree(\theta)');
            ylabel('Poisson ratio(\nu_x_y) & interaction ratio(\eta_X_y_x)');
            title(angle_thickness);
        else
            plot(theta,eta_xyx,'r-*','linewidth',2); hold on;
            legend('\eta_x_y_x'); hold on;
            xlabel('Angle in degree(\theta)');
            ylabel('Poisson ratio(\nu_x_y) & interaction ratio(\eta_X_y_x)');
            title(angle_thickness);
        end
    case 2
        figure;
        plot(theta,nu_xy,'g-o',theta,eta_xyx,'r-*'); hold on;
        legend('\nu_x_y','\eta_x_y_x'); hold on;
        xlabel('Angle in degree(\theta)');
        ylabel('Poisson ratio(\nu_x_y) & interaction ratio(\eta_X_y_x)');
        title(angle_thickness);
end

function Laminar_Ex_Callback(hObject, eventdata, handles)

function Laminar_Gxy_Callback(hObject, eventdata, handles)

function Laminar_nu_xy_Callback(hObject, eventdata, handles)

function Laminar_eta_xyx_Callback(hObject, eventdata, handles)

function Volumn_Callback(hObject, eventdata, handles)
function Volumn_CreateFcn(hObject, eventdata, handles)
if ispc && isequal(get(hObject,'BackgroundColor'), get(0,'defaultUicontrolBackgroundColor'))
    set(hObject,'BackgroundColor','white');
end

% --- Executes on button press in Plot_Vf.
function Plot_Vf_Callback(hObject, eventdata, handles)
% Get input data
Ef_1 = str2double(get(handles.Input_Ef_1,'String'));
Ef_2 = str2double(get(handles.Input_Ef_2,'String'));
Em = str2double(get(handles.Input_Em,'String'));
```

```
Gf_12 = str2double(get(handles.Input_Gf_12,'String'));
%Gf_23 = str2double(get(handles.Input_Gf_23,'String'));
Gm = str2double(get(handles.Input_Gm,'String'));
nu_f_12 = str2double(get(handles.Input_nu_f_12,'String'));
nu_f_23 = str2double(get(handles.Input_nu_f_23,'String'));
nu_m = str2double(get(handles.Input_nu_m,'String'));
Alphaf_1 = str2double(get(handles.Input_Alphaf_1,'String'));
Alphaf_2 = str2double(get(handles.Input_Alphaf_2,'String'));
Alpham = str2double(get(handles.Input_Alpham,'String'));
HT = str2double(get(handles.Input_Hadjust,'String'));
Vf = 0:0.01:1;
% calculate E1,nu_12,Alpha
pE1 = Ef_1*Vf+Em*(1-Vf);
pnu_12 = nu_f_12*Vf+nu_m*(1-Vf);
pAlpha1 = (Alphaf_1*Ef_1*Vf+Alpham*Em*(1-Vf))./(Ef_1*Vf+Em*(1-Vf));
pAlpha2 = Alphaf_2*Vf+Alpham*(1-Vf);
% Halpin & Tsai E2,G12
etaE = (Ef_2/Em-1)/(Ef_2/Em+HT);
etaG = (Gf_12/Gm-1)/(Gf_12/Gm+HT);
phE2 = Em*(1+HT*etaE*Vf)./(1-etaE*Vf);
phG12 = Gm*(1+HT*etaG*Vf)./(1-etaG*Vf);
% Equal stress E2,G12
peE2 = 1./(Vf/Ef_2+(1-Vf)/Em);
peG12 = 1./(Vf/Gf_12+(1-Vf)/Gm);
% Calculate nu_23,G23
kf = Ef_1*Ef_2/(2*Ef_1*(1-nu_f_12*Ef_2/Ef_1-nu_f_23)+Ef_2*(1-2*nu_f_12));
%kf = Ef_2/3/(1-nu_f_23-nu_f_12*Ef_2/Ef_1);
%kf = Ef_2/(1-nu_f_23-Ef_2*nu_f_12^2/Ef_1)/2;
km = Em/3/(1-2*nu_m);
etaK = (kf/km-1)/(kf/km+HT);
K = km.*(1+HT*etaK*Vf)./(1-etaK*Vf);
Ke = 1./(Vf/kf+(1-Vf)/km);
%K = 1./(Vf/kf+(1-Vf)/km);
phnu_21 = pnu_12.*phE2./pE1;
%phnu_23 = 1-phnu_21-phE2/3./K;
phnu_23 = 1-phnu_21-phE2/2./K+phE2.*(1-2*pnu_12)/2./pE1;
%phnu_23 = 1-phE2./K/2-2*pnu_12.^2.*phE2./pE1;
penu_21 = pnu_12.*peE2./pE1;
%penu_23 = 1-peE2./Ke/2-2*pnu_12.^2.*peE2./pE1;
penu_23 = 1-penu_21-peE2/2./Ke+peE2.*(1-2*pnu_12)/2./pE1;
%penu_23 = 1-penu_21-peE2/3./K;
%phnu_23 = 1-pnu_12*Em/Ef_2-phE2.*((3*Vf*(1-2*nu_f_12))/Ef_2+(3*(1-Vf)*(1-2*nu_m))/Em)/3;
phG23 = phE2./2./(1+phnu_23);
%penu_23 = 1-pnu_12*Em/Ef_2-peE2.*((3*Vf*(1-2*nu_f_12))/Ef_2+(3*(1-Vf)*(1-2*nu_m))/Em)/3;
peG23 = peE2./2./(1+penu_23);

switch get(handles.Volumn,'Value');
   case 1
      figure;
      plot(Vf,pE1,'r-*',Vf,phE2,'g-o',Vf,peE2,'b-+','LineWidth',2);hold on;
      legend('E1','E2 in Halpin&Tsai','E2 in Equal stress'); hold on;
      xlabel('Volume fraction');
      ylabel('Modulus(GPa)');
    case 2
      figure;
      plot(Vf,phG12,'r-*',Vf,peG12,'r-o',Vf,phG23,'g-*',Vf,peG23,'g-o');
```

```
        legend('G12 in Halpin&Tsai','G12 in Equal stress','G23 in Halpin&Tsai','G23 in Equal stress'); hold
on;
        xlabel('Volume fraction');
        ylabel('Modulus(GPa)');
    case 3
        figure;
        plot(Vf,pnu_12,'r-*',Vf,phnu_21,'b-+',Vf,penu_21,'b-o',Vf,phnu_23,'c-+',Vf,penu_23,'c-o');
        legend('\nu_1_2','\nu_2_1 in Halpin&Tsai','\nu_2_1 in Equal stress','\nu_2_3 in
Halpin&Tsai','\nu_2_3 in Equal stress'); hold on;
        xlabel('Volume fraction');
        ylabel('Poisson ratio(\nu)');
    case 4
        figure;
        plot(Vf,pAlpha1,'r-o',Vf,pAlpha2,'b-*');
        legend('\alpha_1','\alpha_2'); hold on;
        xlabel('Volume fraction');
        ylabel('Thermal coefficient of expansion(\alpha /K)');
    case 5
        figure;
        plot(Vf,K,'r-o',Vf,Ke,'b-*');
        legend('K in Halpin & Tsai','K in Equal stress'); hold on;
        xlabel('Volume fraction');
        ylabel('Bulk modulus (GPa))');
end

function Input_Hadjust_Callback(hObject, eventdata, handles)
function Input_Hadjust_CreateFcn(hObject, eventdata, handles)
if ispc && isequal(get(hObject,'BackgroundColor'), get(0,'defaultUicontrolBackgroundColor'))
    set(hObject,'BackgroundColor','white');
end

% --- Executes on button press in Tick_Tr.
function Tick_Tr_Callback(hObject, eventdata, handles)

% --- Executes on button press in Tick_Table2.
function Tick_Table2_Callback(hObject, eventdata, handles)

% --- Executes on button press in Tick_nk.
function Tick_nk_Callback(hObject, eventdata, handles)

function Input_X_Callback(hObject, eventdata, handles)

% --- Executes during object creation, after setting all properties.
function Input_X_CreateFcn(hObject, eventdata, handles)
if ispc && isequal(get(hObject,'BackgroundColor'), get(0,'defaultUicontrolBackgroundColor'))
    set(hObject,'BackgroundColor','white');
end

function Input_X1_Callback(hObject, eventdata, handles)

% --- Executes during object creation, after setting all properties.
function Input_X1_CreateFcn(hObject, eventdata, handles)
if ispc && isequal(get(hObject,'BackgroundColor'), get(0,'defaultUicontrolBackgroundColor'))
    set(hObject,'BackgroundColor','white');
end
```

```
function Input_Y_Callback(hObject, eventdata, handles)

% --- Executes during object creation, after setting all properties.
function Input_Y_CreateFcn(hObject, eventdata, handles)
if ispc && isequal(get(hObject,'BackgroundColor'), get(0,'defaultUicontrolBackgroundColor'))
    set(hObject,'BackgroundColor','white');
end

function Input_Y1_Callback(hObject, eventdata, handles)

% --- Executes during object creation, after setting all properties.
function Input_Y1_CreateFcn(hObject, eventdata, handles)
if ispc && isequal(get(hObject,'BackgroundColor'), get(0,'defaultUicontrolBackgroundColor'))
    set(hObject,'BackgroundColor','white');
end

function Input_S_Callback(hObject, eventdata, handles)

% --- Executes during object creation, after setting all properties.
function Input_S_CreateFcn(hObject, eventdata, handles)
if ispc && isequal(get(hObject,'BackgroundColor'), get(0,'defaultUicontrolBackgroundColor'))
    set(hObject,'BackgroundColor','white');
end

function Input_Fxybar_Callback(hObject, eventdata, handles)

% --- Executes during object creation, after setting all properties.
function Input_Fxybar_CreateFcn(hObject, eventdata, handles)
if ispc && isequal(get(hObject,'BackgroundColor'), get(0,'defaultUicontrolBackgroundColor'))
    set(hObject,'BackgroundColor','white');
end

% --- Executes on selection change in Database.
function Database_Callback(hObject, eventdata, handles)

% --- Executes during object creation, after setting all properties.
function Database_CreateFcn(hObject, eventdata, handles)
if ispc && isequal(get(hObject,'BackgroundColor'), get(0,'defaultUicontrolBackgroundColor'))
    set(hObject,'BackgroundColor','white');
end

% --- Executes on button press in Tick_Env.
function Tick_Env_Callback(hObject, eventdata, handles)

% --- Executes on button press in Tick_Omni.
function Tick_Omni_Callback(hObject, eventdata, handles)
```

APPENDIX C: MATLAB CODE FOR 3-POINT BENDING

This software was developed to process the experimental data of laminated composites subjected to 3-point bending. Figure C1 shows the GUI of this tool.

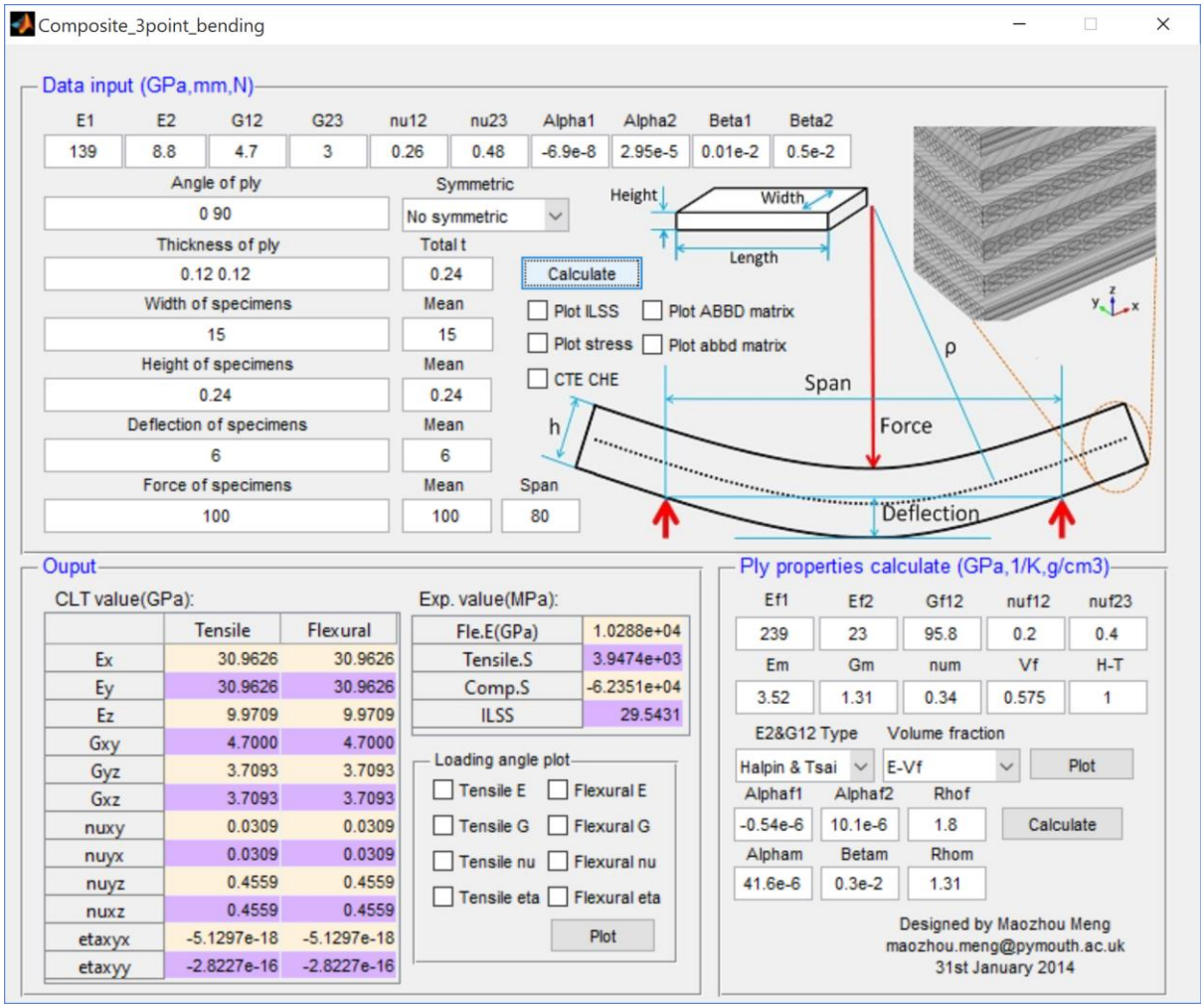

Figure C1. The GUI of 3-point bending calculator

```
function varargout = Composite_3point_bending(varargin)
% Designed by Maozhou Meng in Plymouth University, 31st January 2014
% Begin initialization code - DO NOT EDIT
gui_Singleton = 1;
gui_State = struct('gui_Name',       mfilename, ...
                   'gui_Singleton',  gui_Singleton, ...
                   'gui_OpeningFcn', @Composite_3point_bending_OpeningFcn, ...
                   'gui_OutputFcn',  @Composite_3point_bending_OutputFcn, ...
                   'gui_LayoutFcn',  [] , ...
                   'gui_Callback',   []);
if nargin && ischar(varargin{1})
    gui_State.gui_Callback = str2func(varargin{1});
```

```
end

if nargout
   [varargout{1:nargout}] = gui_mainfcn(gui_State, varargin{ISO899-2:2003,  #140});
else
   gui_mainfcn(gui_State, varargin{ISO899-2:2003,  #140});
end
% End initialization code - DO NOT EDIT

% --- Executes just before Composite_3point_bending is made visible.
function Composite_3point_bending_OpeningFcn(hObject, eventdata, handles, varargin)
handles.output = hObject;

% Update handles structure
guidata(hObject, handles);
axes(handles.diagram);
imshow('m_diagram.jpg');

% --- Outputs from this function are returned to the command line.
function varargout = Composite_3point_bending_OutputFcn(hObject, eventdata, handles)
varargout{1} = handles.output;

function InE1_Callback(hObject, eventdata, handles)

% --- Executes during object creation, after setting all properties.
function InE1_CreateFcn(hObject, eventdata, handles)
if ispc && isequal(get(hObject,'BackgroundColor'), get(0,'defaultUicontrolBackgroundColor'))
   set(hObject,'BackgroundColor','white');
end

function InE2_Callback(hObject, eventdata, handles)

% --- Executes during object creation, after setting all properties.
function InE2_CreateFcn(hObject, eventdata, handles)
if ispc && isequal(get(hObject,'BackgroundColor'), get(0,'defaultUicontrolBackgroundColor'))
   set(hObject,'BackgroundColor','white');
end

function InG12_Callback(hObject, eventdata, handles)
% --- Executes during object creation, after setting all properties.
function InG12_CreateFcn(hObject, eventdata, handles)
if ispc && isequal(get(hObject,'BackgroundColor'), get(0,'defaultUicontrolBackgroundColor'))
   set(hObject,'BackgroundColor','white');
end

function InG23_Callback(hObject, eventdata, handles)
% --- Executes during object creation, after setting all properties.
function InG23_CreateFcn(hObject, eventdata, handles)
%       See ISPC and COMPUTER.
if ispc && isequal(get(hObject,'BackgroundColor'), get(0,'defaultUicontrolBackgroundColor'))
   set(hObject,'BackgroundColor','white');
end

function Innu12_Callback(hObject, eventdata, handles)
```

```
% --- Executes during object creation, after setting all properties.
function Innu12_CreateFcn(hObject, eventdata, handles)
if ispc && isequal(get(hObject,'BackgroundColor'), get(0,'defaultUicontrolBackgroundColor'))
    set(hObject,'BackgroundColor','white');
end

function Innu23_Callback(hObject, eventdata, handles)
% --- Executes during object creation, after setting all properties.
function Innu23_CreateFcn(hObject, eventdata, handles)
if ispc && isequal(get(hObject,'BackgroundColor'), get(0,'defaultUicontrolBackgroundColor'))
    set(hObject,'BackgroundColor','white');
end

function InL_Callback(hObject, eventdata, handles)
% --- Executes during object creation, after setting all properties.
function InL_CreateFcn(hObject, eventdata, handles)
if ispc && isequal(get(hObject,'BackgroundColor'), get(0,'defaultUicontrolBackgroundColor'))
    set(hObject,'BackgroundColor','white');
end

function Ina_Callback(hObject, eventdata, handles)
% --- Executes during object creation, after setting all properties.
function Ina_CreateFcn(hObject, eventdata, handles)
if ispc && isequal(get(hObject,'BackgroundColor'), get(0,'defaultUicontrolBackgroundColor'))
    set(hObject,'BackgroundColor','white');
end

% --- Executes on selection change in Symmetric.
function Symmetric_Callback(hObject, eventdata, handles)
% --- Executes during object creation, after setting all properties.
function Symmetric_CreateFcn(hObject, eventdata, handles)
if ispc && isequal(get(hObject,'BackgroundColor'), get(0,'defaultUicontrolBackgroundColor'))
    set(hObject,'BackgroundColor','white');
end

function Inh_Callback(hObject, eventdata, handles)
% --- Executes during object creation, after setting all properties.
function Inh_CreateFcn(hObject, eventdata, handles)
if ispc && isequal(get(hObject,'BackgroundColor'), get(0,'defaultUicontrolBackgroundColor'))
    set(hObject,'BackgroundColor','white');
end

function Tt_Callback(hObject, eventdata, handles)
% --- Executes during object creation, after setting all properties.
function Tt_CreateFcn(hObject, eventdata, handles)
if ispc && isequal(get(hObject,'BackgroundColor'), get(0,'defaultUicontrolBackgroundColor'))
    set(hObject,'BackgroundColor','white');
end

% --- Executes on button press in Cal.
function Cal_Callback(hObject, eventdata, handles)
% Get input data
E1 = 1e9*str2double(get(handles.InE1,'String'));
E2 = 1e9*str2double(get(handles.InE2,'String'));
G12 = 1e9*str2double(get(handles.InG12,'String'));
G23 = 1e9*str2double(get(handles.InG23,'String'));
```

```
nu12 = str2double(get(handles.Innu12,'String'));
nu23 = str2double(get(handles.Innu23,'String'));
InL = 1e-3*str2double(get(handles.InL,'String'));
Ina = str2num(get(handles.Ina,'String'));
Int = 1e-3*str2num(get(handles.Int,'String'));
Inw = 1e-3*str2num(get(handles.Inw,'String'));
Inh = 1e-3*str2num(get(handles.Inh,'String'));
Ind = 1e-3*str2num(get(handles.Ind,'String'));
Inf = str2num(get(handles.Inf,'String'));
Alpha1 = str2double(get(handles.InAlpha1,'String'));
Alpha2 = str2double(get(handles.InAlpha2,'String'));
Beta1 = str2double(get(handles.InBeta1,'String'));
Beta2 = str2double(get(handles.InBeta2,'String'));
numcount = numel(Int);
vector_length = numel(Ina)-numcount;
if vector_length ~= 0;
errordlg('The length of orientation and thickness vector not consistent','Input Error');
return
end
% get the real matrix of ply angle and ply thickness
Ina2 = zeros(1,numcount-1);
Int2 = zeros(1,numcount-1);
Ina3 = zeros(1,numcount);
Int3 = zeros(1,numcount);
switch get(handles.Symmetric,'Value')
   case 1
      rIna = Ina;
      rInt = Int;
      rnumcount = numcount;
   case 2
      for j = 1:numcount-1
         Int2(j) = Int(numcount-j);
         Ina2(j) = Ina(numcount-j);
      end
      rnumcount = numcount*2-1;
      rInt = [Int Int2];
      rIna = [Ina Ina2];
   case 3
      for k = 1:numcount;
         Int3(k) = Int(numcount+1-k);
         Ina3(k) = Ina(numcount+1-k);
      end
      rnumcount = numcount*2;
      rInt = [Int Int3];
      rIna = [Ina Ina3];
end
set(handles.Tt,'String',1e3*sum(rInt));
% define the complaince matrix
S11 = 1/E1;
S12 = -nu12/E1;
S22 = 1/E2;
S23 = -nu23/E2;
S44 = 1/G23;
S66 = 1/G12;
S = [S11 S12 S12 0 0 0;
   S12 S22 S23 0 0 0;
   S12 S23 S22 0 0 0;
   0 0 0 S44 0 0;
```

```
   0 0 0 0 S66 0;
   0 0 0 0 0 S66];
%define the CTE and CHE vector
A123=[Alpha1;Alpha2;Alpha2;0;0;0];
B123=[Beta1;Beta2;Beta2;0;0;0];
% calculate the stiffness matrix of laminate
h=zeros(1,rnumcount+1);
for j=1:rnumcount+1;
   if j==1
      h(j)=-sum(rInt)/2;
   else
      h(j)=h(j-1)+rInt(j-1);
   end
end
A = zeros(6,6);
B = zeros(6,6);
D = zeros(6,6);
Sbar11=zeros(1,rnumcount);
Cbar11=zeros(1,rnumcount);
Cbar12=zeros(1,rnumcount);
Cbar26=zeros(1,rnumcount);
Cbar16=zeros(1,rnumcount);
Cbar66=zeros(1,rnumcount);
Ek=zeros(1,rnumcount);
Nt=zeros(6,1);
Nc=zeros(6,1);
for i = 1:rnumcount
   c = cos((rIna(i))*pi/180);
   s = sin((rIna(i))*pi/180);
T = [c^2 s^2 0 0 0 2*c*s;
   s^2 c^2 0 0 0 -2*c*s;
   0 0 1 0 0 0;
   0 0 0 c s 0;
   0 0 0 -s c 0;
   -c*s c*s 0 0 0 c^2-s^2];
T1 = [c^2 s^2 0 0 0 c*s;
   s^2 c^2 0 0 0 -c*s;
   0 0 1 0 0 0;
   0 0 0 c s 0;
   0 0 0 -s c 0;
   -2*c*s 2*c*s 0 0 0 c^2-s^2];
Sbar = T1\S*T;
Cbar=inv(Sbar);
Axyzk=T1*A123;
Bxyzk=T1*B123;
Sbar11(i)=Sbar(1,1);
Ek(i)=1/Sbar11(i);
Cbar11(i)=Cbar(1,1);
Cbar12(i)=Cbar(1,2);
Cbar16(i)=Cbar(1,6);
Cbar26(i)=Cbar(2,6);
Cbar66(i)=Cbar(6,6);
   for m = 1:6
      for n = 1:6
         A(m,n) = A(m,n)+Cbar(m,n)*(h(i+1)-h(i));
         B(m,n) = B(m,n)+Cbar(m,n)*((h(i+1))^2-(h(i))^2)/2;
         D(m,n) = D(m,n)+Cbar(m,n)*(h((i+1))^3-(h(i))^3)/3;
      end
```

```
    end
    for k=1:6
        Nt(k)=Nt(k)+Cbar(k,:)*Axyzk*rInt(i);
        Nc(k)=Nc(k)+Cbar(k,:)*Bxyzk*rInt(i);
    end
end
ABBD = [A B;B D];abbd=inv(ABBD);
a=abbd(1:6,1:6);b=abbd(1:6,7:12);d=abbd(7:12,7:12);
Axyz=a*Nt;
Bxyz=a*Nc;
a11=a(1,1);a12=a(1,2);a13=a(1,3);a16=a(1,6);
a22=a(2,2);a23=a(2,3);a26=a(2,6);a44=a(4,4);a55=a(5,5);a66=a(6,6);
b11=b(1,1);b12=b(1,2);b16=b(1,6);
d11=d(1,1);d12=d(1,2);d16=d(1,6);
tEx=1/(a11*sum(rInt));tEy=1/a22/sum(rInt);tEz=1/a(3,3)/sum(rInt);
tGxy=1/a66/sum(rInt);tGyz=1/a44/sum(rInt);tGxz=1/a55/sum(rInt);
tnuxy = -a12/a11;tnuyx = -a12/a22;
tnuyz = -a23/a22;tnuxz = -a13/a11;
tetaxyx = a16/a11;tetaxyy = a26/a22;
fEx=12/d(1,1)/sum(rInt)^3;fEy=12/d(2,2)/sum(rInt)^3;fEz=12/d(3,3)/sum(rInt)^3;
fGxy=12/d(6,6)/sum(rInt)^3;fGyz=12/d(4,4)/sum(rInt)^3;fGxz=12/d(5,5)/sum(rInt)^3;
fnuxy = -d(1,2)/d(1,1);fnuyx = -d(1,2)/d(2,2);
fnuyz = -d(3,2)/d(2,2);fnuxz = -d(3,1)/d(1,1);
fetaxyx = d(1,6)/d(1,1);fetaxyy = d(2,6)/d(2,2);
Tensile = [tEx/1e9 tEy/1e9 tEz/1e9 tGxy/1e9 tGyz/1e9 tGxz/1e9 tnuxy tnuyx tnuyz tnuxz tetaxyx
tetaxyy]';
Flexural = [fEx/1e9 fEy/1e9 fEz/1e9 fGxy/1e9 fGyz/1e9 fGxz/1e9 fnuxy fnuyx fnuyz fnuxz fetaxyx
fetaxyy]';
set(handles.Laminate_table,'data',[Tensile Flexural]);
%plot ABBD-abbd matrix
    switch get(handles.ABBD1_plot,'Value')
    case 1
        figure('Position',[100 100 950 240]);
uitable('Units','normalized','Position',...
            [0 0 1 1], 'Data', ABBD);
    end
    switch get(handles.abbd2_plot,'Value')
    case 1
        figure('Position',[100 100 950 240]);
uitable('Units','normalized','Position',...
            [0 0 1 1], 'Data', abbd);
    end
%plot CTE and CHE
    switch get(handles.CTECHE,'Value')
    case 1
        figure('Position',[200 200 400 200]);
uitable('Units','normalized','Position',...
            [0 0 1 1], 'Data', [Axyz,Bxyz],...
            'ColumnName',{'CTE','CHE'},...
            'RowName',{'x','y','z','yz','xz','xy'});
    end
% process experimental data
mw=mean(Inw);mh=mean(Inh);md=mean(Ind);mf=mean(Inf);
set(handles.mw,'string',mw*1e3);
set(handles.mh,'string',mh*1e3);
set(handles.md,'string',md*1e3);
set(handles.mf,'string',mf);
%evaluate flexural modulus
```

```
Ef=InL^3*mf/(md*4*mw*mh^3);
%evaluate tensile and compression stress
   switch get(handles.stress_plot,'Value')
   case 1
      figure;
   end
     t_stress=zeros(1,rnumcount);
     c_stress=zeros(1,rnumcount);
for k=1:rnumcount
     z=h(k):0.1*(h(k+1)-h(k)):h(k+1);
     stress=Ek(k)*z*mf*InL*d11/4/mw;
     t_stress(k)=max(stress);
     c_stress(k)=min(stress);
   switch get(handles.stress_plot,'Value')
   case 1
     plot(stress/1e6,z*1e3);hold on;
      xlabel('Stress(MPa)');
      ylabel('z(mm)');
      title('Normal stress-Through thickness');
      grid on;
   end
end
max_t_stress=max(t_stress);
max_c_stress=min(c_stress);
%t_stress=E_t*mh*mf*InL*d11/8/mw;
%c_stress=E_c*mh*mf*InL*d11/8/mw;
%evaluate interlaminar shear stress
Qx=mf/2/mw;
maxILSSk=zeros(1,rnumcount);
for k=1:rnumcount
     z=h(k):0.1*(h(k+1)-h(k)):h(k+1);
   if k==1
   ILSS_xz=-((Cbar11(k)*b11+Cbar12(k)*b12+Cbar16(k)*b16)*(z-h(k))+...
      0.5*(Cbar11(k)*d11+Cbar12(k)*d12+Cbar16(k)*d16)*(z.^2-h(k)^2))*Qx;
      ILSS_yz=-((Cbar16(k)*b11+Cbar26(k)*b12+Cbar66(k)*b16)*(z-h(k))+...
      0.5*(Cbar16(k)*d11+Cbar26(k)*d12+Cbar66(k)*d16)*(z.^2-h(k)^2))*Qx;
   ILSS_local=ILSS_xz*cos((rIna(k))*pi/180)+ILSS_yz*sin((rIna(k))*pi/180);
   switch get(handles.ILSS_plot,'Value')
   case 1
      figure;
      plot(ILSS_xz/1e6,z*1e3,'b-',ILSS_local/1e6,z*1e3,'ro');hold on;
      xlabel('Interlaminar shear stress(MPa)');
      ylabel('z(mm)');
      legend('Globle ILSS','Local ILSS');
      title('ILSS-Through thickness');
   end
         maxILSSk(k)=max(ILSS_xz);
   else
block_xz=0;
block_yz=0;
         for j=1:(k-1)
            block_xz=block_xz-((Cbar11(j)*b11+Cbar12(j)*b12+Cbar16(j)*b16)*((h(j+1)-h(j)))+...
         0.5*(Cbar11(j)*d11+Cbar12(j)*d12+Cbar16(j)*d16)*((h(j+1)^2-h(j)^2)))*Qx;
       block_yz=block_yz-((Cbar16(j)*b11+Cbar26(j)*b12+Cbar66(j)*b16)*((h(j+1)-h(j)))+...
         0.5*(Cbar16(j)*d11+Cbar26(j)*d12+Cbar66(j)*d16)*((h(j+1)^2-h(j)^2)))*Qx;
         end
         ILSS_xz=block_xz-((Cbar11(k)*b11+Cbar12(k)*b12+Cbar16(k)*b16)*(z-h(k))+...
         0.5*(Cbar11(k)*d11+Cbar12(k)*d12+Cbar16(k)*d16)*(z.^2-h(k)^2))*Qx;
```

```
            ILSS_yz=block_yz-((Cbar16(k)*b11+Cbar26(k)*b12+Cbar66(k)*b16)*(z-h(k))+...
        0.5*(Cbar16(k)*d11+Cbar26(k)*d12+Cbar66(k)*d16)*(z.^2-h(k)^2))*Qx;
     ILSS_local=ILSS_xz*cos((rIna(k))*pi/180)+ILSS_yz*sin((rIna(k))*pi/180);
   switch get(handles.ILSS_plot,'Value')
   case 1
      plot(ILSS_xz/1e6,z*1e3,'b-',ILSS_local/1e6,z*1e3,'ro');hold on;
   end
        maxILSSk(k)=max(ILSS_xz);
   end
end

     maxILSS=max(maxILSSk);
     set(handles.Exp_table,'data',[Ef/1e9;max_t_stress/1e6;max_c_stress/1e6;maxILSS/1e6]);
guidata(hObject, handles);


function Inw_Callback(hObject, eventdata, handles)

% --- Executes during object creation, after setting all properties.
function Inw_CreateFcn(hObject, eventdata, handles)
if ispc && isequal(get(hObject,'BackgroundColor'), get(0,'defaultUicontrolBackgroundColor'))
   set(hObject,'BackgroundColor','white');
end

function mw_Callback(hObject, eventdata, handles)
% --- Executes during object creation, after setting all properties.
function mw_CreateFcn(hObject, eventdata, handles)
if ispc && isequal(get(hObject,'BackgroundColor'), get(0,'defaultUicontrolBackgroundColor'))
   set(hObject,'BackgroundColor','white');
end

function Int_Callback(hObject, eventdata, handles)
% --- Executes during object creation, after setting all properties.
function Int_CreateFcn(hObject, eventdata, handles)
if ispc && isequal(get(hObject,'BackgroundColor'), get(0,'defaultUicontrolBackgroundColor'))
   set(hObject,'BackgroundColor','white');
end

function mh_Callback(hObject, eventdata, handles)
% --- Executes during object creation, after setting all properties.
function mh_CreateFcn(hObject, eventdata, handles)
if ispc && isequal(get(hObject,'BackgroundColor'), get(0,'defaultUicontrolBackgroundColor'))
   set(hObject,'BackgroundColor','white');
end

function Ind_Callback(hObject, eventdata, handles)
% --- Executes during object creation, after setting all properties.
function Ind_CreateFcn(hObject, eventdata, handles)
if ispc && isequal(get(hObject,'BackgroundColor'), get(0,'defaultUicontrolBackgroundColor'))
   set(hObject,'BackgroundColor','white');
end
function md_Callback(hObject, eventdata, handles)
% --- Executes during object creation, after setting all properties.
function md_CreateFcn(hObject, eventdata, handles)
if ispc && isequal(get(hObject,'BackgroundColor'), get(0,'defaultUicontrolBackgroundColor'))
   set(hObject,'BackgroundColor','white');
```

```
end

function Inf_Callback(hObject, eventdata, handles)
% --- Executes during object creation, after setting all properties.
function Inf_CreateFcn(hObject, eventdata, handles)
if ispc && isequal(get(hObject,'BackgroundColor'), get(0,'defaultUicontrolBackgroundColor'))
    set(hObject,'BackgroundColor','white');
end

function mf_Callback(hObject, eventdata, handles)
% --- Executes during object creation, after setting all properties.
function mf_CreateFcn(hObject, eventdata, handles)
if ispc && isequal(get(hObject,'BackgroundColor'), get(0,'defaultUicontrolBackgroundColor'))
    set(hObject,'BackgroundColor','white');
end

% --- Executes on button press in tE.
function tE_Callback(hObject, eventdata, handles)
% --- Executes on button press in tG.
function tG_Callback(hObject, eventdata, handles)
% --- Executes on button press in tnu.
function tnu_Callback(hObject, eventdata, handles)
% --- Executes on button press in teta.
function teta_Callback(hObject, eventdata, handles)
% --- Executes on button press in fE.
function fE_Callback(hObject, eventdata, handles)
% --- Executes on button press in fG.
function fG_Callback(hObject, eventdata, handles)
% --- Executes on button press in fnu.
function fnu_Callback(hObject, eventdata, handles)
% --- Executes on button press in feta.
function feta_Callback(hObject, eventdata, handles)
function InEf1_Callback(hObject, eventdata, handles)
% --- Executes during object creation, after setting all properties.
function InEf1_CreateFcn(hObject, eventdata, handles)
if ispc && isequal(get(hObject,'BackgroundColor'), get(0,'defaultUicontrolBackgroundColor'))
    set(hObject,'BackgroundColor','white');
end

function InEf2_Callback(hObject, eventdata, handles)
% --- Executes during object creation, after setting all properties.
function InEf2_CreateFcn(hObject, eventdata, handles)
if ispc && isequal(get(hObject,'BackgroundColor'), get(0,'defaultUicontrolBackgroundColor'))
    set(hObject,'BackgroundColor','white');
end

function InGf12_Callback(hObject, eventdata, handles)
% --- Executes during object creation, after setting all properties.
function InGf12_CreateFcn(hObject, eventdata, handles)
if ispc && isequal(get(hObject,'BackgroundColor'), get(0,'defaultUicontrolBackgroundColor'))
    set(hObject,'BackgroundColor','white');
end

function Innuf12_Callback(hObject, eventdata, handles)
% --- Executes during object creation, after setting all properties.
function Innuf12_CreateFcn(hObject, eventdata, handles)
```

```
if ispc && isequal(get(hObject,'BackgroundColor'), get(0,'defaultUicontrolBackgroundColor'))
    set(hObject,'BackgroundColor','white');
end

function Innuf23_Callback(hObject, eventdata, handles)
% --- Executes during object creation, after setting all properties.
function Innuf23_CreateFcn(hObject, eventdata, handles)
if ispc && isequal(get(hObject,'BackgroundColor'), get(0,'defaultUicontrolBackgroundColor'))
    set(hObject,'BackgroundColor','white');
end

% --- Executes on button press in Cal_ply.
function Cal_ply_Callback(hObject, eventdata, handles)
% Get In data
Ef1 = str2double(get(handles.InEf1,'String'));
Ef2 = str2double(get(handles.InEf2,'String'));
Em = str2double(get(handles.InEm,'String'));
Gf12 = str2double(get(handles.InGf12,'String'));
Gm = str2double(get(handles.InGm,'String'));
nuf12 = str2double(get(handles.Innuf12,'String'));
nuf23 = str2double(get(handles.Innuf23,'String'));
num = str2double(get(handles.Innum,'String'));
Vf = str2double(get(handles.InVf,'String'));
HT = str2double(get(handles.InHT,'String'));
Alphaf1 = str2double(get(handles.InAlphaf1,'String'));
Alphaf2 = str2double(get(handles.InAlphaf2,'String'));
Alpham = str2double(get(handles.InAlpham,'String'));
Rhof = str2double(get(handles.InRhof,'String'));
Rhom = str2double(get(handles.InRhom,'String'));
Betam = str2double(get(handles.InBetam,'String'));
% Evaluate
E1 = Vf*Ef1+Em*(1-Vf);
nu12 = Vf*nuf12+num*(1-Vf);
kf = Ef1*Ef2/(2*Ef1*(1-nuf12*Ef2/Ef1-nuf23)+Ef2*(1-2*nuf12));
km = Em/3/(1-2*num);
switch get(handles.E2type,'Value')
    case 1
        etaE = (Ef2/Em-1)/(Ef2/Em+HT);
        E2 = Em*(1+HT*etaE*Vf)/(1-etaE*Vf);
        etaG = (Gf12/Gm-1)/(Gf12/Gm+HT);
        G12 = Gm*(1+HT*etaG*Vf)/(1-etaG*Vf);
        etaK = (kf/km-1)/(kf/km+HT);
        K = km*(1+HT*etaK*Vf)/(1-etaK*Vf);
    case 2
        E2 = 1/(Vf/Ef2+(1-Vf)/Em);
        G12 = 1/(Vf/Gf12+(1-Vf)/Gm);
        K = 1/(Vf/kf+(1-Vf)/km);
end
nu21 = nu12*E2/E1;
nu23 = 1-nu21-E2/2/K+E2*(1-2*nu12)/2/E1;
G23 = E2/2/(1+nu23);
Alpha1 = (Alphaf1*Ef1*Vf+Alpham*Em*(1-Vf))/(Ef1*Vf+Em*(1-Vf));
Alpha2 = (Alphaf2-Em*nuf12*(Alpham-Alphaf1)*(1-Vf)/E1)*Vf+(Alpham+Ef1*num*(Alpham-
Alphaf1)*Vf/E1)*(1-Vf);
Rhoc=Rhof*Vf+Rhom*(1-Vf);
Beta1=Em*Rhoc*Betam/(E1*Rhom);
Beta2=(1+num)*Rhoc*Betam/Rhom-Beta1*nu12;
```

```
set(handles.InE1,'string',E1);
set(handles.InE2,'string',E2);
set(handles.InG12,'string',G12);
set(handles.InG23,'string',G23);
set(handles.Innu12,'string',nu12);
set(handles.Innu23,'string',nu23);
set(handles.InAlpha1,'string',Alpha1);
set(handles.InAlpha2,'string',Alpha2);
set(handles.InBeta1,'string',Beta1);
set(handles.InBeta2,'string',Beta2);
guidata(hObject, handles);

function InEm_Callback(hObject, eventdata, handles)
% --- Executes during object creation, after setting all properties.
function InEm_CreateFcn(hObject, eventdata, handles)
if ispc && isequal(get(hObject,'BackgroundColor'), get(0,'defaultUicontrolBackgroundColor'))
    set(hObject,'BackgroundColor','white');
end

function InGm_Callback(hObject, eventdata, handles)
% --- Executes during object creation, after setting all properties.
function InGm_CreateFcn(hObject, eventdata, handles)
if ispc && isequal(get(hObject,'BackgroundColor'), get(0,'defaultUicontrolBackgroundColor'))
    set(hObject,'BackgroundColor','white');
end

function Innum_Callback(hObject, eventdata, handles)
% --- Executes during object creation, after setting all properties.
function Innum_CreateFcn(hObject, eventdata, handles)
if ispc && isequal(get(hObject,'BackgroundColor'), get(0,'defaultUicontrolBackgroundColor'))
    set(hObject,'BackgroundColor','white');
end

function InVf_Callback(hObject, eventdata, handles)
% --- Executes during object creation, after setting all properties.
function InVf_CreateFcn(hObject, eventdata, handles)
if ispc && isequal(get(hObject,'BackgroundColor'), get(0,'defaultUicontrolBackgroundColor'))
    set(hObject,'BackgroundColor','white');
end

function InHT_Callback(hObject, eventdata, handles)
% --- Executes during object creation, after setting all properties.
function InHT_CreateFcn(hObject, eventdata, handles)
if ispc && isequal(get(hObject,'BackgroundColor'), get(0,'defaultUicontrolBackgroundColor'))
    set(hObject,'BackgroundColor','white');
end
% --- Executes on selection change in E2type.
function E2type_Callback(hObject, eventdata, handles)
% --- Executes during object creation, after setting all properties.
function E2type_CreateFcn(hObject, eventdata, handles)
if ispc && isequal(get(hObject,'BackgroundColor'), get(0,'defaultUicontrolBackgroundColor'))
    set(hObject,'BackgroundColor','white');
end
% --- Executes on button press in Plot_tf.
function Plot_tf_Callback(hObject, eventdata, handles)
% Get input data
E1 = 1e9*str2double(get(handles.InE1,'String'));
```

```
E2 = 1e9*str2double(get(handles.InE2,'String'));
G12 = 1e9*str2double(get(handles.InG12,'String'));
G23 = 1e9*str2double(get(handles.InG23,'String'));
nu12 = str2double(get(handles.Innu12,'String'));
nu23 = str2double(get(handles.Innu23,'String'));
Ina = str2num(get(handles.Ina,'String'));
Int = 1e-3*str2num(get(handles.Int,'String'));
numcount = numel(Int);
vector_length = numel(Ina)-numcount;
if vector_length ~= 0;
errordlg('The length of orientation and thickness vector not consistent','Input Error');
return
end
% get the real matrix of ply angle and ply thickness
Ina2 = zeros(1,numcount-1);
Int2 = zeros(1,numcount-1);
Ina3 = zeros(1,numcount);
Int3 = zeros(1,numcount);
switch get(handles.Symmetric,'Value')
   case 1
      rIna = Ina;
      rInt = Int;
      rnumcount = numcount;
   case 2
      for j = 1:numcount-1
         Int2(j) = Int(numcount-j);
         Ina2(j) = Ina(numcount-j);
      end
      rnumcount = numcount*2-1;
      rInt = [Int Int2];
      rIna = [Ina Ina2];
   case 3
      for k = 1:numcount;
         Int3(k) = Int(numcount+1-k);
         Ina3(k) = Ina(numcount+1-k);
      end
      rnumcount = numcount*2;
      rInt = [Int Int3];
      rIna = [Ina Ina3];
end
% define the complaince matrix
S11 = 1/E1;
S12 = -nu12/E1;
S22 = 1/E2;
S23 = -nu23/E2;
S44 = 1/G23;
S66 = 1/G12;
S = [S11 S12 S12 0 0 0;
   S12 S22 S23 0 0 0;
   S12 S23 S22 0 0 0;
   0 0 0 S44 0 0;
   0 0 0 0 S66 0;
   0 0 0 0 0 S66];
% calculate ABBD matrix of laminate
h=zeros(1,rnumcount+1);
for j=1:rnumcount+1;
   if j==1
      h(j)=-sum(rInt)/2;
```

```
    else
        h(j)=h(j-1)+rInt(j-1);
    end
end
theta=0:1:90;
L=length(theta);
tEx=zeros(1,L);tEy=zeros(1,L);
tGxy=zeros(1,L);tGyz=zeros(1,L);tGxz=zeros(1,L);
tnuxy=zeros(1,L);tnuyx=zeros(1,L);
tnuyz=zeros(1,L);tnuxz=zeros(1,L);
tetaxyx=zeros(1,L);tetaxyy=zeros(1,L);
fEx=zeros(1,L);fEy=zeros(1,L);
fGxy=zeros(1,L);fGyz=zeros(1,L);fGxz=zeros(1,L);
fnuxy=zeros(1,L);fnuyx=zeros(1,L);
fnuyz=zeros(1,L);fnuxz=zeros(1,L);
fetaxyx=zeros(1,L);fetaxyy=zeros(1,L);
for j=1:L
A = zeros(6,6);
B = zeros(6,6);
D = zeros(6,6);
    for i = 1:rnumcount
    c = cos((theta(j)+rIna(i))*pi/180);
    s = sin((theta(j)+rIna(i))*pi/180);
T = [c^2 s^2 0 0 0 2*c*s;
    s^2 c^2 0 0 0 -2*c*s;
    0 0 1 0 0 0;
    0 0 0 c s 0;
    0 0 0 -s c 0;
    -c*s c*s 0 0 0 c^2-s^2];
T1 = [c^2 s^2 0 0 0 c*s;
    s^2 c^2 0 0 0 -c*s;
    0 0 1 0 0 0;
    0 0 0 c s 0;
    0 0 0 -s c 0;
    -2*c*s 2*c*s 0 0 0 c^2-s^2];
Sbar = T1\S*T;
Cbar=inv(Sbar);
        for m = 1:6
            for n = 1:6
                A(m,n) = A(m,n)+Cbar(m,n)*(h(i+1)-h(i));
                B(m,n) = B(m,n)+Cbar(m,n)*((h(i+1))^2-(h(i))^2)/2;
                D(m,n) = D(m,n)+Cbar(m,n)*(h((i+1))^3-(h(i))^3)/3;
            end
        end
    end
ABBD = [A B;B D];abbd=inv(ABBD);
a=abbd(1:6,1:6);d=abbd(7:12,7:12);
a11=a(1,1);a12=a(1,2);a13=a(1,3);a16=a(1,6);
a22=a(2,2);a23=a(2,3);a26=a(2,6);
a44=a(4,4);a55=a(5,5);a66=a(6,6);
tEx(j)=1/(a11*sum(rInt));tEy(j)=1/a22/sum(rInt);tEz(j)=1/a(3,3)/sum(rInt);
tGxy(j)=1/a66/sum(rInt);tGyz(j)=1/a44/sum(rInt);tGxz(j)=1/a55/sum(rInt);
tnuxy(j) = -a12/a11;tnuyx(j) = -a12/a22;
tnuyz(j) = -a23/a22;tnuxz(j) = -a13/a11;
tetaxyx(j) = a16/a11;tetaxyy(j) = a26/a22;
fEx(j)=12/d(1,1)/sum(rInt)^3;fEy(j)=12/d(2,2)/sum(rInt)^3;fEz(j)=12/d(3,3)/sum(rInt)^3;
fGxy(j)=12/d(6,6)/sum(rInt)^3;fGyz(j)=12/d(4,4)/sum(rInt)^3;fGxz(j)=12/d(5,5)/sum(rInt)^3;
fnuxy(j) = -d(1,2)/d(1,1);fnuyx(j) = -d(1,2)/d(2,2);
```

```
fnuyz(j) = -d(3,2)/d(2,2);fnuxz(j) = -d(3,1)/d(1,1);
fetaxyx(j) = d(1,6)/d(1,1);fetaxyy(j) = d(2,6)/d(2,2);
end
% Plot tensile and flexural elastic properties
switch get(handles.tE,'Value')+get(handles.fE,'Value')
   case 1
      figure;
      if get(handles.tE,'Value')
         plot(theta,tEx/1e9,'b-o',theta,tEy/1e9,'b-*',theta,tEz/1e9,'b-+'); hold on;
         legend('Tensile Ex','Tensile Ey','Tensile Ez'); hold on;
         xlabel('Angle in degree(\theta)');
         ylabel('Modulus(GPa)');
      else
         plot(theta,fEx/1e9,'m-o',theta,fEy/1e9,'m-*',theta,fEz/1e9,'m-+'); hold on;
         legend('Flexural Ex','Flexural Ey','Flexural Ez'); hold on;
         xlabel('Angle in degree(\theta)');
         ylabel('Modulus(GPa)');
      end
   case 2
      figure;
      plot(theta,tEx/1e9,'b-o',theta,tEy/1e9,'b-*',theta,tEz/1e9,'b-',...
         theta,fEx/1e9,'mo',theta,fEy/1e9,'m*',theta,fEz/1e9,'m+'); hold on;
      legend('Tensile Ex','Tensile Ey','Tensile Ez','Flexural Ex','Flexural Ey','Flexural Ez'); hold on;
      xlabel('Angle in degree(\theta)');
      ylabel('Modulus(GPa)');
end
switch get(handles.tG,'Value')+get(handles.fG,'Value')
   case 1
      figure;
      if get(handles.tG,'Value')
         plot(theta,tGxy/1e9,'b-o',theta,tGyz/1e9,'b-*',theta,tGxz/1e9,'b-+'); hold on;
         legend('Tensile Gxy','Tensile Gyz','Tensile Gxz'); hold on;
         xlabel('Angle in degree(\theta)');
         ylabel('Modulus(GPa)');
      else
         plot(theta,fGxy/1e9,'m-o',theta,fGyz/1e9,'m-*',theta,fGxz/1e9,'m-+'); hold on;
         legend('Flexural Gxy','Flexural Gyz','Flexural Gxz'); hold on;
         xlabel('Angle in degree(\theta)');
         ylabel('Modulus(GPa)');
      end
   case 2
      figure;
      plot(theta,tGxy/1e9,'b-o',theta,tGyz/1e9,'b-*',theta,tGxz/1e9,'b-+',...
         theta,fGxy/1e9,'m-o',theta,fGyz/1e9,'m-*',theta,fGxz/1e9,'m-+'); hold on;
      legend('Tensile Gxy','Tensile Gyz','Tensile Gxz',...
         'Flexural Gxy','Flexural Gyz','Flexural Gxz'); hold on;
      xlabel('Angle in degree(\theta)');
      ylabel('Modulus(GPa)');
end
switch get(handles.tnu,'Value')+get(handles.fnu,'Value')
   case 1
      figure;
      if get(handles.tnu,'Value')
         plot(theta,tnuxy,'b-o',theta,tnuyz,'b-*',theta,tnuxz,'b-+'); hold on;
         legend('Tensile tnuxy','Tensile tnuyz','Tensile tnuxz'); hold on;
         xlabel('Angle in degree(\theta)');
         ylabel('Poisson ratio');
      else
```

```
            plot(theta,fnuxy,'m-o',theta,fnuyz,'m-*',theta,fnuxz,'m-+'); hold on;
            legend('Flexural fnuxy','Flexural fnuyz','Flexural fnuxz'); hold on;
            xlabel('Angle in degree(\theta)');
            ylabel('Poisson ratio')
        end
    case 2
        figure;
        plot(theta,tnuxy,'b-o',theta,tnuyz,'b-*',theta,tnuxz,'b-+',...
            theta,fnuxy,'m-o',theta,fnuyz,'m-*',theta,fnuxz,'m-+'); hold on;
        legend('Tensile tnuxy','Tensile tnuyz','Tensile tnuxz',...
            'Flexural fnuxy','Flexural fnuyz','Flexural fnuxz'); hold on;
        xlabel('Angle in degree(\theta)');
        ylabel('Poisson ratio')
end
switch get(handles.teta,'Value')+get(handles.feta,'Value')
    case 1
        figure;
        if get(handles.teta,'Value')
            plot(theta,tetaxyx,'b-o',theta,tetaxyy,'b-*'); hold on;
            legend('Tensile tetaxyx','Tensile tetaxyy'); hold on;
            xlabel('Angle in degree(\theta)');
            ylabel('Interaction ratio');
        else
            plot(theta,fetaxyx,'m-o',theta,fetaxyx,'m-*'); hold on;
            legend('Flexural fetaxyx','Flexural fetaxyy'); hold on;
            xlabel('Angle in degree(\theta)');
            ylabel('Poisson ratio')
        end
    case 2
        figure;
        plot(theta,tetaxyx,'b-o',theta,tetaxyy,'b-*',theta,fetaxyx,'m-o',theta,fetaxyx,'m-*'); hold on;
        legend('Tensile tetaxyx','Tensile tetaxyy','Flexural fetaxyx','Flexural fetaxyy'); hold on;
        xlabel('Angle in degree(\theta)');
        ylabel('Poisson ratio')
end
guidata(hObject, handles);


% --- Executes on selection change in elastic_Vf.
function elastic_Vf_Callback(hObject, eventdata, handles)
% --- Executes during object creation, after setting all properties.
function elastic_Vf_CreateFcn(hObject, eventdata, handles)
if ispc && isequal(get(hObject,'BackgroundColor'), get(0,'defaultUicontrolBackgroundColor'))
    set(hObject,'BackgroundColor','white');
end

% --- Executes on button press in Plot_Vf.
function Plot_Vf_Callback(hObject, eventdata, handles)
Ef1 = str2double(get(handles.InEf1,'String'));
Ef2 = str2double(get(handles.InEf2,'String'));
Gf12 = str2double(get(handles.InGf12,'String'));
nuf12 = str2double(get(handles.Innuf12,'String'));
nuf23 = str2double(get(handles.Innuf23,'String'));
Em = str2double(get(handles.InEm,'String'));
Gm = str2double(get(handles.InGm,'String'));
num = str2double(get(handles.Innum,'String'));
HT = str2double(get(handles.InHT,'String'));
```

```
Vf = 0:0.01:1;
% calculate E1,nu12
pE1 = Ef1*Vf+Em*(1-Vf);
pnu12 = nuf12*Vf+num*(1-Vf);
% Halpin & Tsai E2,G12
etaE = (Ef2/Em-1)/(Ef2/Em+HT);
etaG = (Gf12/Gm-1)/(Gf12/Gm+HT);
phE2 = Em*(1+HT*etaE*Vf)./(1-etaE*Vf);
phG12 = Gm*(1+HT*etaG*Vf)./(1-etaG*Vf);
% Equal stress E2,G12
peE2 = 1./(Vf/Ef2+(1-Vf)/Em);
peG12 = 1./(Vf/Gf12+(1-Vf)/Gm);
% Calculate nu23,G23
kf = Ef1*Ef2/(2*Ef1*(1-nuf12*Ef2/Ef1-nuf23)+Ef2*(1-2*nuf12));
km = Em/3/(1-2*num);
etaK = (kf/km-1)/(kf/km+HT);
K = km.*(1+HT*etaK*Vf)./(1-etaK*Vf);
Ke = 1./(Vf/kf+(1-Vf)/km);
phnu21 = pnu12.*phE2./pE1;
phnu23 = 1-phnu21-phE2/2./K+phE2.*(1-2*pnu12)/2./pE1;
penu21 = pnu12.*peE2./pE1;
penu23 = 1-penu21-peE2/2./Ke+peE2.*(1-2*pnu12)/2./pE1;
phG23 = phE2./2./(1+phnu23);
peG23 = peE2./2./(1+penu23);
switch get(handles.elastic_Vf,'Value');
   case 1
      figure;
      plot(Vf,pE1,'r-*',Vf,phE2,'g-o',Vf,peE2,'b-+','LineWidth',2);hold on;
      legend('E1','E2 in Halpin&Tsai','E2 in Equal stress'); hold on;
      xlabel('Volume fraction');
      ylabel('Modulus(GPa)');
%        axis([0,1,0,50]);
   case 2
      figure;
      plot(Vf,phG12,'r-*',Vf,peG12,'r-o',Vf,phG23,'g-*',Vf,peG23,'g-o');
      legend('G12 in Halpin&Tsai','G12 in Equal stress','G23 in Halpin&Tsai','G23 in Equal stress'); hold
on;
      xlabel('Volume fraction');
      ylabel('Modulus(GPa)');
   case 3
      figure;
      plot(Vf,pnu12,'r-*',Vf,phnu21,'b-+',Vf,penu21,'b-o',Vf,phnu23,'c-+',Vf,penu23,'c-o');
      legend('\nu12','\nu21 in Halpin&Tsai','\nu21 in Equal stress','\nu23 in Halpin&Tsai','\nu23 in Equal
stress'); hold on;
      xlabel('Volume fraction');
      ylabel('Poisson ratio(\nu)');
   case 4
      figure;
      plot(Vf,K,'r-o',Vf,Ke,'b-*');
      legend('K in Halpin & Tsai','K in Equal stress'); hold on;
      xlabel('Volume fraction');
      ylabel('Bulk modulus(GPa)');
end


% --- Executes on button press in ILSS_plot.
function ILSS_plot_Callback(hObject, eventdata, handles)
```

```
% --- Executes on button press in stress_plot.
function stress_plot_Callback(hObject, eventdata, handles)
% --- Executes on button press in ABBD1_plot.
function ABBD1_plot_Callback(hObject, eventdata, handles)
% --- Executes on button press in abbd2_plot.
function abbd2_plot_Callback(hObject, eventdata, handles)
function InAlphaf1_Callback(hObject, eventdata, handles)
% --- Executes during object creation, after setting all properties.
function InAlphaf1_CreateFcn(hObject, eventdata, handles)
if ispc && isequal(get(hObject,'BackgroundColor'), get(0,'defaultUicontrolBackgroundColor'))
    set(hObject,'BackgroundColor','white');
end

function InAlphaf2_Callback(hObject, eventdata, handles)
% --- Executes during object creation, after setting all properties.
function InAlphaf2_CreateFcn(hObject, eventdata, handles)
if ispc && isequal(get(hObject,'BackgroundColor'), get(0,'defaultUicontrolBackgroundColor'))
    set(hObject,'BackgroundColor','white');
end

function InRhof_Callback(hObject, eventdata, handles)
% --- Executes during object creation, after setting all properties.
function InRhof_CreateFcn(hObject, eventdata, handles)
if ispc && isequal(get(hObject,'BackgroundColor'), get(0,'defaultUicontrolBackgroundColor'))
    set(hObject,'BackgroundColor','white');
end

function InAlpham_Callback(hObject, eventdata, handles)
% --- Executes during object creation, after setting all properties.
function InAlpham_CreateFcn(hObject, eventdata, handles)
if ispc && isequal(get(hObject,'BackgroundColor'), get(0,'defaultUicontrolBackgroundColor'))
    set(hObject,'BackgroundColor','white');
end

function InBetam_Callback(hObject, eventdata, handles)
% --- Executes during object creation, after setting all properties.
function InBetam_CreateFcn(hObject, eventdata, handles)
if ispc && isequal(get(hObject,'BackgroundColor'), get(0,'defaultUicontrolBackgroundColor'))
    set(hObject,'BackgroundColor','white');
end

function InRhom_Callback(hObject, eventdata, handles)

% --- Executes during object creation, after setting all properties.
function InRhom_CreateFcn(hObject, eventdata, handles)
if ispc && isequal(get(hObject,'BackgroundColor'), get(0,'defaultUicontrolBackgroundColor'))
    set(hObject,'BackgroundColor','white');
end

function InAlpha1_Callback(hObject, eventdata, handles)
% --- Executes during object creation, after setting all properties.
function InAlpha1_CreateFcn(hObject, eventdata, handles)
if ispc && isequal(get(hObject,'BackgroundColor'), get(0,'defaultUicontrolBackgroundColor'))
    set(hObject,'BackgroundColor','white');
end
```

```
function InAlpha2_Callback(hObject, eventdata, handles)
% --- Executes during object creation, after setting all properties.
function InAlpha2_CreateFcn(hObject, eventdata, handles)
if ispc && isequal(get(hObject,'BackgroundColor'), get(0,'defaultUicontrolBackgroundColor'))
    set(hObject,'BackgroundColor','white');
end

function InBeta1_Callback(hObject, eventdata, handles)
% --- Executes during object creation, after setting all properties.
function InBeta1_CreateFcn(hObject, eventdata, handles)
if ispc && isequal(get(hObject,'BackgroundColor'), get(0,'defaultUicontrolBackgroundColor'))
    set(hObject,'BackgroundColor','white');
end

function InBeta2_Callback(hObject, eventdata, handles)
% --- Executes during object creation, after setting all properties.
function InBeta2_CreateFcn(hObject, eventdata, handles)
if ispc && isequal(get(hObject,'BackgroundColor'), get(0,'defaultUicontrolBackgroundColor'))
    set(hObject,'BackgroundColor','white');
end
% --- Executes on button press in CTECHE.
function CTECHE_Callback(hObject, eventdata, handles)
```

APPENDIX D: MATLAB CODE FOR 4-POING BENDING

This software was developed to process the experimental data of laminated composites subjected to 4-point bending. Figure D1 shows the GUI of this tool. Normally, the machine records the deflection at load-point in 4-point bending test, however the equations to calculate the flexural properties provided by ISO standard are based on the deflection at mid-point. User can choose the deflection at both mid-point and load-point.

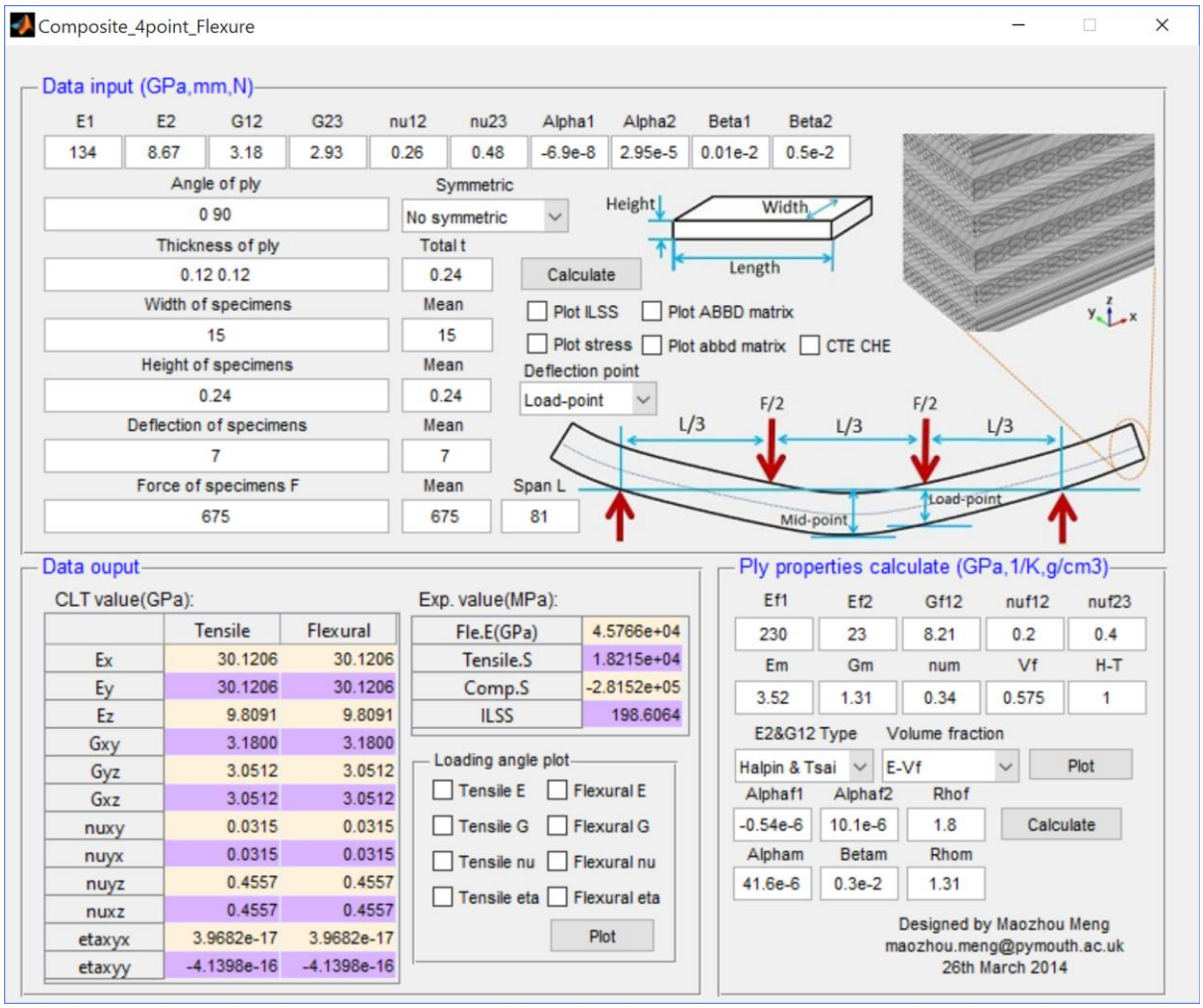

Figure D1. The GUI of 4-point bending calculator

```
function varargout = Composite_4point_Flexure(varargin)
% Designed by Maozhou Meng in Plymouth University, 31st January 2014
% Begin initialization code - DO NOT EDIT
gui_Singleton = 1;
gui_State = struct('gui_Name',       mfilename, ...
```

```
                'gui_Singleton',  gui_Singleton, ...
                'gui_OpeningFcn', @Composite_4point_Flexure_OpeningFcn, ...
                'gui_OutputFcn',  @Composite_4point_Flexure_OutputFcn, ...
                'gui_LayoutFcn',  [] , ...
                'gui_Callback',   []);
if nargin && ischar(varargin{1})
   gui_State.gui_Callback = str2func(varargin{1});
end

if nargout
   [varargout{1:nargout}] = gui_mainfcn(gui_State, varargin{ISO899-2:2003,  #140});
else
   gui_mainfcn(gui_State, varargin{ISO899-2:2003,  #140});
end
% End initialization code - DO NOT EDIT

% --- Executes just before Composite_4point_Flexure is made visible.
function Composite_4point_Flexure_OpeningFcn(hObject, eventdata, handles, varargin)

% Choose default command line output for Composite_4point_Flexure
handles.output = hObject;

% Update handles structure
guidata(hObject, handles);
axes(handles.diagram);
imshow('m_diagram.jpg');
% --- Outputs from this function are returned to the command line.
function varargout = Composite_4point_Flexure_OutputFcn(hObject, eventdata, handles)
% Get default command line output from handles structure
varargout{1} = handles.output;

function InE1_Callback(hObject, eventdata, handles)

% --- Executes during object creation, after setting all properties.
function InE1_CreateFcn(hObject, eventdata, handles)
%       See ISPC and COMPUTER.
if ispc && isequal(get(hObject,'BackgroundColor'), get(0,'defaultUicontrolBackgroundColor'))
   set(hObject,'BackgroundColor','white');
end

function InE2_Callback(hObject, eventdata, handles)
% hObject    handle to InE2 (see GCBO)
% --- Executes during object creation, after setting all properties.
function InE2_CreateFcn(hObject, eventdata, handles)
if ispc && isequal(get(hObject,'BackgroundColor'), get(0,'defaultUicontrolBackgroundColor'))
   set(hObject,'BackgroundColor','white');
end

function InG12_Callback(hObject, eventdata, handles)
% --- Executes during object creation, after setting all properties.
function InG12_CreateFcn(hObject, eventdata, handles)
if ispc && isequal(get(hObject,'BackgroundColor'), get(0,'defaultUicontrolBackgroundColor'))
   set(hObject,'BackgroundColor','white');
end

function InG23_Callback(hObject, eventdata, handles)
```

```
% hObject    handle to InG23 (see GCBO)
% --- Executes during object creation, after setting all properties.
function InG23_CreateFcn(hObject, eventdata, handles)
if ispc && isequal(get(hObject,'BackgroundColor'), get(0,'defaultUicontrolBackgroundColor'))
    set(hObject,'BackgroundColor','white');
end

function Innu12_Callback(hObject, eventdata, handles)
function Innu12_CreateFcn(hObject, eventdata, handles)
if ispc && isequal(get(hObject,'BackgroundColor'), get(0,'defaultUicontrolBackgroundColor'))
    set(hObject,'BackgroundColor','white');
end

function Innu23_Callback(hObject, eventdata, handles)
function Innu23_CreateFcn(hObject, eventdata, handles)
if ispc && isequal(get(hObject,'BackgroundColor'), get(0,'defaultUicontrolBackgroundColor'))
    set(hObject,'BackgroundColor','white');
end
function InL_Callback(hObject, eventdata, handles)
% --- Executes during object creation, after setting all properties.
function InL_CreateFcn(hObject, eventdata, handles)
if ispc && isequal(get(hObject,'BackgroundColor'), get(0,'defaultUicontrolBackgroundColor'))
    set(hObject,'BackgroundColor','white');
end

function Ina_Callback(hObject, eventdata, handles)
% --- Executes during object creation, after setting all properties.
function Ina_CreateFcn(hObject, eventdata, handles)
if ispc && isequal(get(hObject,'BackgroundColor'), get(0,'defaultUicontrolBackgroundColor'))
    set(hObject,'BackgroundColor','white');
end
% --- Executes on selection change in Symmetric.
function Symmetric_Callback(hObject, eventdata, handles)
% --- Executes during object creation, after setting all properties.
function Symmetric_CreateFcn(hObject, eventdata, handles)
if ispc && isequal(get(hObject,'BackgroundColor'), get(0,'defaultUicontrolBackgroundColor'))
    set(hObject,'BackgroundColor','white');
end
function Inh_Callback(hObject, eventdata, handles)
% --- Executes during object creation, after setting all properties.
function Inh_CreateFcn(hObject, eventdata, handles)
if ispc && isequal(get(hObject,'BackgroundColor'), get(0,'defaultUicontrolBackgroundColor'))
    set(hObject,'BackgroundColor','white');
end
function Tt_Callback(hObject, eventdata, handles)
% --- Executes during object creation, after setting all properties.
function Tt_CreateFcn(hObject, eventdata, handles)
if ispc && isequal(get(hObject,'BackgroundColor'), get(0,'defaultUicontrolBackgroundColor'))
    set(hObject,'BackgroundColor','white');
end
% --- Executes on button press in Cal.
function Cal_Callback(hObject, eventdata, handles)
% Get input data
E1 = 1e9*str2double(get(handles.InE1,'String'));
E2 = 1e9*str2double(get(handles.InE2,'String'));
G12 = 1e9*str2double(get(handles.InG12,'String'));
G23 = 1e9*str2double(get(handles.InG23,'String'));
```

```
nu12 = str2double(get(handles.Innu12,'String'));
nu23 = str2double(get(handles.Innu23,'String'));
InL = 1e-3*str2double(get(handles.InL,'String'));
Ina = str2num(get(handles.Ina,'String'));
Int = 1e-3*str2num(get(handles.Int,'String'));
Inw = 1e-3*str2num(get(handles.Inw,'String'));
Inh = 1e-3*str2num(get(handles.Inh,'String'));
Ind = 1e-3*str2num(get(handles.Ind,'String'));
Inf = str2num(get(handles.Inf,'String'));
Alpha1 = str2double(get(handles.InAlpha1,'String'));
Alpha2 = str2double(get(handles.InAlpha2,'String'));
Beta1 = str2double(get(handles.InBeta1,'String'));
Beta2 = str2double(get(handles.InBeta2,'String'));
numcount = numel(Int);
vector_length = numel(Ina)-numcount;
if vector_length ~= 0;
errordlg('The length of orientation and thickness vector not consistent','Input Error');
return
end
% get the real matrix of ply angle and ply thickness
Ina2 = zeros(1,numcount-1);
Int2 = zeros(1,numcount-1);
Ina3 = zeros(1,numcount);
Int3 = zeros(1,numcount);
switch get(handles.Symmetric,'Value')
   case 1
      rIna = Ina;
      rInt = Int;
      rnumcount = numcount;
   case 2
      for j = 1:numcount-1
         Int2(j) = Int(numcount-j);
         Ina2(j) = Ina(numcount-j);
      end
      rnumcount = numcount*2-1;
      rInt = [Int Int2];
      rIna = [Ina Ina2];
   case 3
      for k = 1:numcount;
         Int3(k) = Int(numcount+1-k);
         Ina3(k) = Ina(numcount+1-k);
      end
      rnumcount = numcount*2;
      rInt = [Int Int3];
      rIna = [Ina Ina3];
end
set(handles.Tt,'String',1e3*sum(rInt));
% define the complaince matrix
S11 = 1/E1;
S12 = -nu12/E1;
S22 = 1/E2;
S23 = -nu23/E2;
S44 = 1/G23;
S66 = 1/G12;
S = [S11 S12 S12 0 0 0;
   S12 S22 S23 0 0 0;
   S12 S23 S22 0 0 0;
   0 0 0 S44 0 0;
```

```
   0 0 0 0 S66 0;
   0 0 0 0 0 S66];
%define the CTE and CHE vector
A123=[Alpha1;Alpha2;Alpha2;0;0;0];
B123=[Beta1;Beta2;Beta2;0;0;0];
% calculate the stiffness matrix of laminate
h=zeros(1,rnumcount+1);
for j=1:rnumcount+1;
   if j==1
      h(j)=-sum(rInt)/2;
   else
      h(j)=h(j-1)+rInt(j-1);
   end
end
A = zeros(6,6);
B = zeros(6,6);
D = zeros(6,6);
Sbar11=zeros(1,rnumcount);
Cbar11=zeros(1,rnumcount);
Cbar12=zeros(1,rnumcount);
Cbar26=zeros(1,rnumcount);
Cbar16=zeros(1,rnumcount);
Cbar66=zeros(1,rnumcount);
Ek=zeros(1,rnumcount);
Nt=zeros(6,1);
Nc=zeros(6,1);
for i = 1:rnumcount
   c = cos((rIna(i))*pi/180);
   s = sin((rIna(i))*pi/180);
T = [c^2 s^2 0 0 0 2*c*s;
   s^2 c^2 0 0 0 -2*c*s;
   0 0 1 0 0 0;
   0 0 0 c s 0;
   0 0 0 -s c 0;
   -c*s c*s 0 0 0 c^2-s^2];
T1 = [c^2 s^2 0 0 0 c*s;
   s^2 c^2 0 0 0 -c*s;
   0 0 1 0 0 0;
   0 0 0 c s 0;
   0 0 0 -s c 0;
   -2*c*s 2*c*s 0 0 0 c^2-s^2];
Sbar = T1\S*T;
Cbar=inv(Sbar);
Axyzk=T1*A123;
Bxyzk=T1*B123;
Sbar11(i)=Sbar(1,1);
Ek(i)=1/Sbar11(i);
Cbar11(i)=Cbar(1,1);
Cbar12(i)=Cbar(1,2);
Cbar16(i)=Cbar(1,6);
Cbar26(i)=Cbar(2,6);
Cbar66(i)=Cbar(6,6);
   for m = 1:6
      for n = 1:6
         A(m,n) = A(m,n)+Cbar(m,n)*(h(i+1)-h(i));
         B(m,n) = B(m,n)+Cbar(m,n)*((h(i+1))^2-(h(i))^2)/2;
         D(m,n) = D(m,n)+Cbar(m,n)*(h((i+1))^3-(h(i))^3)/3;
      end
```

```
    end
    for k=1:6
        Nt(k)=Nt(k)+Cbar(k,:)*Axyzk*rInt(i);
        Nc(k)=Nc(k)+Cbar(k,:)*Bxyzk*rInt(i);
    end
end
ABBD = [A B;B D];abbd=inv(ABBD);
a=abbd(1:6,1:6);b=abbd(1:6,7:12);d=abbd(7:12,7:12);
Axyz=a*Nt;
Bxyz=a*Nc;
a11=a(1,1);a12=a(1,2);a13=a(1,3);a16=a(1,6);
a22=a(2,2);a23=a(2,3);a26=a(2,6);a44=a(4,4);a55=a(5,5);a66=a(6,6);
b11=b(1,1);b12=b(1,2);b16=b(1,6);
d11=d(1,1);d12=d(1,2);d16=d(1,6);
tEx=1/(a11*sum(rInt));tEy=1/a22/sum(rInt);tEz=1/a(3,3)/sum(rInt);
tGxy=1/a66/sum(rInt);tGyz=1/a44/sum(rInt);tGxz=1/a55/sum(rInt);
tnuxy = -a12/a11;tnuyx = -a12/a22;
tnuyz = -a23/a22;tnuxz = -a13/a11;
tetaxyx = a16/a11;tetaxyy = a26/a22;
fEx=12/d(1,1)/sum(rInt)^3;fEy=12/d(2,2)/sum(rInt)^3;fEz=12/d(3,3)/sum(rInt)^3;
fGxy=12/d(6,6)/sum(rInt)^3;fGyz=12/d(4,4)/sum(rInt)^3;fGxz=12/d(5,5)/sum(rInt)^3;
fnuxy = -d(1,2)/d(1,1);fnuyx = -d(1,2)/d(2,2);
fnuyz = -d(3,2)/d(2,2);fnuxz = -d(3,1)/d(1,1);
fetaxyx = d(1,6)/d(1,1);fetaxyy = d(2,6)/d(2,2);
Tensile = [tEx/1e9 tEy/1e9 tEz/1e9 tGxy/1e9 tGyz/1e9 tGxz/1e9 tnuxy tnuyx tnuyz tnuxz tetaxyx
tetaxyy]';
Flexural = [fEx/1e9 fEy/1e9 fEz/1e9 fGxy/1e9 fGyz/1e9 fGxz/1e9 fnuxy fnuyx fnuyz fnuxz fetaxyx
fetaxyy]';
set(handles.Laminate_table,'data',[Tensile Flexural]);
%plot ABBD-abbd matrix
    switch get(handles.ABBD1_plot,'Value')
    case 1
        figure('Position',[100 100 950 240]);
uitable('Units','normalized','Position',...
            [0 0 1 1], 'Data', ABBD);
    end
    switch get(handles.abbd2_plot,'Value')
    case 1
        figure('Position',[100 100 950 240]);
uitable('Units','normalized','Position',...
            [0 0 1 1], 'Data', abbd);
    end
%plot CTE and CHE
    switch get(handles.CTECHE,'Value')
    case 1
        figure('Position',[200 200 400 200]);
uitable('Units','normalized','Position',...
            [0 0 1 1], 'Data', [Axyz,Bxyz],...
            'ColumnName',{'CTE','CHE'},...
            'RowName',{'x','y','z','yz','xz','xy'});
    end
% process experimental data
mw=mean(Inw);mh=mean(Inh);md=mean(Ind);mf=mean(Inf);
set(handles.mw,'string',mw*1e3);
set(handles.mh,'string',mh*1e3);
set(handles.md,'string',md*1e3);
set(handles.mf,'string',mf);
%evaluate flexural modulus
```

```
    switch get(handles.point,'Value')
    case 1
        Ef=5*InL^3*mf/(md*27*mw*mh^3);
    case 2
        Ef=23*InL^3*mf/(md*104*mw*mh^3);
    end
%evaluate tensile and compression stress
    switch get(handles.stress_plot,'Value')
    case 1
        figure;
    end
       t_stress=zeros(1,rnumcount);
       c_stress=zeros(1,rnumcount);
for k=1:rnumcount
       z=h(k):0.1*(h(k+1)-h(k)):h(k+1);
       stress=Ek(k)*z*mf*InL*d11/6/mw;
       t_stress(k)=max(stress);
       c_stress(k)=min(stress);
    switch get(handles.stress_plot,'Value')
    case 1
       plot(stress/1e6,z*1e3);hold on;
        xlabel('Stress(MPa)');
        ylabel('z(mm)');
        title('Normal stress-Through thickness');
        grid on;
    end
end
max_t_stress=max(t_stress);
max_c_stress=min(c_stress);
%evaluate interlaminar shear stress
Qx=mf/2/mw;
maxILSSk=zeros(1,rnumcount);
for k=1:rnumcount
       z=h(k):0.1*(h(k+1)-h(k)):h(k+1);
    if k==1
    ILSS_xz=-((Cbar11(k)*b11+Cbar12(k)*b12+Cbar16(k)*b16)*(z-h(k))+...
        0.5*(Cbar11(k)*d11+Cbar12(k)*d12+Cbar16(k)*d16)*(z.^2-h(k)^2))*Qx;
        ILSS_yz=-((Cbar16(k)*b11+Cbar26(k)*b12+Cbar66(k)*b16)*(z-h(k))+...
        0.5*(Cbar16(k)*d11+Cbar26(k)*d12+Cbar66(k)*d16)*(z.^2-h(k)^2))*Qx;
    ILSS_local=ILSS_xz*cos((rIna(k))*pi/180)+ILSS_yz*sin((rIna(k))*pi/180);
    switch get(handles.ILSS_plot,'Value')
    case 1
        figure;
        plot(ILSS_xz/1e6,z*1e3,'b-',ILSS_local/1e6,z*1e3,'ro');hold on;
        xlabel('Interlaminar shear stress(MPa)');
        ylabel('z(mm)');
        legend('Globle ILSS','Local ILSS');
        title('ILSS-Through thickness');
    end
            maxILSSk(k)=max(ILSS_xz);
    else
block_xz=0;
block_yz=0;
            for j=1:(k-1)
                block_xz=block_xz-((Cbar11(j)*b11+Cbar12(j)*b12+Cbar16(j)*b16)*((h(j+1)-h(j)))+...
            0.5*(Cbar11(j)*d11+Cbar12(j)*d12+Cbar16(j)*d16)*((h(j+1)^2-h(j)^2)))*Qx;
          block_yz=block_yz-((Cbar16(j)*b11+Cbar26(j)*b12+Cbar66(j)*b16)*((h(j+1)-h(j)))+...
            0.5*(Cbar16(j)*d11+Cbar26(j)*d12+Cbar66(j)*d16)*((h(j+1)^2-h(j)^2)))*Qx;
```

```
        end
        ILSS_xz=block_xz-((Cbar11(k)*b11+Cbar12(k)*b12+Cbar16(k)*b16)*(z-h(k))+...
        0.5*(Cbar11(k)*d11+Cbar12(k)*d12+Cbar16(k)*d16)*(z.^2-h(k)^2))*Qx;
            ILSS_yz=block_yz-((Cbar16(k)*b11+Cbar26(k)*b12+Cbar66(k)*b16)*(z-h(k))+...
        0.5*(Cbar16(k)*d11+Cbar26(k)*d12+Cbar66(k)*d16)*(z.^2-h(k)^2))*Qx;
      ILSS_local=ILSS_xz*cos((rIna(k))*pi/180)+ILSS_yz*sin((rIna(k))*pi/180);
   switch get(handles.ILSS_plot,'Value')
   case 1
      plot(ILSS_xz/1e6,z*1e3,'b-',ILSS_local/1e6,z*1e3,'ro');hold on;
   end
        maxILSSk(k)=max(ILSS_xz);
   end
end

      maxILSS=max(maxILSSk);
      set(handles.Exp_table,'data',[Ef/1e9;max_t_stress/1e6;max_c_stress/1e6;maxILSS/1e6]);
guidata(hObject, handles);

function Inw_Callback(hObject, eventdata, handles)
% --- Executes during object creation, after setting all properties.
function Inw_CreateFcn(hObject, eventdata, handles)
if ispc && isequal(get(hObject,'BackgroundColor'), get(0,'defaultUicontrolBackgroundColor'))
   set(hObject,'BackgroundColor','white');
end

function mw_Callback(hObject, eventdata, handles)
% --- Executes during object creation, after setting all properties.
function mw_CreateFcn(hObject, eventdata, handles)
if ispc && isequal(get(hObject,'BackgroundColor'), get(0,'defaultUicontrolBackgroundColor'))
   set(hObject,'BackgroundColor','white');
end

function Int_Callback(hObject, eventdata, handles)
% --- Executes during object creation, after setting all properties.
function Int_CreateFcn(hObject, eventdata, handles)
if ispc && isequal(get(hObject,'BackgroundColor'), get(0,'defaultUicontrolBackgroundColor'))
   set(hObject,'BackgroundColor','white');
end
function mh_Callback(hObject, eventdata, handles)
% --- Executes during object creation, after setting all properties.
function mh_CreateFcn(hObject, eventdata, handles)
if ispc && isequal(get(hObject,'BackgroundColor'), get(0,'defaultUicontrolBackgroundColor'))
   set(hObject,'BackgroundColor','white');
end

function Ind_Callback(hObject, eventdata, handles)
% --- Executes during object creation, after setting all properties.
function Ind_CreateFcn(hObject, eventdata, handles)
if ispc && isequal(get(hObject,'BackgroundColor'), get(0,'defaultUicontrolBackgroundColor'))
   set(hObject,'BackgroundColor','white');
end

function md_Callback(hObject, eventdata, handles)
% --- Executes during object creation, after setting all properties.
function md_CreateFcn(hObject, eventdata, handles)
if ispc && isequal(get(hObject,'BackgroundColor'), get(0,'defaultUicontrolBackgroundColor'))
```

```
    set(hObject,'BackgroundColor','white');
end

function Inf_Callback(hObject, eventdata, handles)
% --- Executes during object creation, after setting all properties.
function Inf_CreateFcn(hObject, eventdata, handles)
if ispc && isequal(get(hObject,'BackgroundColor'), get(0,'defaultUicontrolBackgroundColor'))
    set(hObject,'BackgroundColor','white');
end

function mf_Callback(hObject, eventdata, handles)
% --- Executes during object creation, after setting all properties.
function mf_CreateFcn(hObject, eventdata, handles)
if ispc && isequal(get(hObject,'BackgroundColor'), get(0,'defaultUicontrolBackgroundColor'))
    set(hObject,'BackgroundColor','white');
end

% --- Executes on button press in tE.
function tE_Callback(hObject, eventdata, handles)
% --- Executes on button press in tG.
function tG_Callback(hObject, eventdata, handles)
% --- Executes on button press in tnu.
function tnu_Callback(hObject, eventdata, handles)
% --- Executes on button press in teta.
function teta_Callback(hObject, eventdata, handles)
function fE_Callback(hObject, eventdata, handles)
% --- Executes on button press in fG.
function fG_Callback(hObject, eventdata, handles)
% --- Executes on button press in fnu.
function fnu_Callback(hObject, eventdata, handles)
% --- Executes on button press in feta.
function feta_Callback(hObject, eventdata, handles)
function InEf1_Callback(hObject, eventdata, handles)

% --- Executes during object creation, after setting all properties.
function InEf1_CreateFcn(hObject, eventdata, handles)
if ispc && isequal(get(hObject,'BackgroundColor'), get(0,'defaultUicontrolBackgroundColor'))
    set(hObject,'BackgroundColor','white');
end

function InEf2_Callback(hObject, eventdata, handles)
% --- Executes during object creation, after setting all properties.
function InEf2_CreateFcn(hObject, eventdata, handles)
if ispc && isequal(get(hObject,'BackgroundColor'), get(0,'defaultUicontrolBackgroundColor'))
    set(hObject,'BackgroundColor','white');
end

function InGf12_Callback(hObject, eventdata, handles)
% --- Executes during object creation, after setting all properties.
function InGf12_CreateFcn(hObject, eventdata, handles)
if ispc && isequal(get(hObject,'BackgroundColor'), get(0,'defaultUicontrolBackgroundColor'))
    set(hObject,'BackgroundColor','white');
end

function Innuf12_Callback(hObject, eventdata, handles)
% --- Executes during object creation, after setting all properties.
```

```
function Innuf12_CreateFcn(hObject, eventdata, handles)
if ispc && isequal(get(hObject,'BackgroundColor'), get(0,'defaultUicontrolBackgroundColor'))
    set(hObject,'BackgroundColor','white');
end

function Innuf23_Callback(hObject, eventdata, handles)

% --- Executes during object creation, after setting all properties.
function Innuf23_CreateFcn(hObject, eventdata, handles)
if ispc && isequal(get(hObject,'BackgroundColor'), get(0,'defaultUicontrolBackgroundColor'))
    set(hObject,'BackgroundColor','white');
end


% --- Executes on button press in Cal_ply.
function Cal_ply_Callback(hObject, eventdata, handles)
% Get In data
Ef1 = str2double(get(handles.InEf1,'String'));
Ef2 = str2double(get(handles.InEf2,'String'));
Em = str2double(get(handles.InEm,'String'));
Gf12 = str2double(get(handles.InGf12,'String'));
Gm = str2double(get(handles.InGm,'String'));
nuf12 = str2double(get(handles.Innuf12,'String'));
nuf23 = str2double(get(handles.Innuf23,'String'));
num = str2double(get(handles.Innum,'String'));
Vf = str2double(get(handles.InVf,'String'));
HT = str2double(get(handles.InHT,'String'));
Alphaf1 = str2double(get(handles.InAlphaf1,'String'));
Alphaf2 = str2double(get(handles.InAlphaf2,'String'));
Alpham = str2double(get(handles.InAlpham,'String'));
Rhof = str2double(get(handles.InRhof,'String'));
Rhom = str2double(get(handles.InRhom,'String'));
Betam = str2double(get(handles.InBetam,'String'));
% Evaluate
E1 = Vf*Ef1+Em*(1-Vf);
nu12 = Vf*nuf12+num*(1-Vf);
kf = Ef1*Ef2/(2*Ef1*(1-nuf12*Ef2/Ef1-nuf23)+Ef2*(1-2*nuf12));
km = Em/3/(1-2*num);
switch get(handles.E2type,'Value')
    case 1
        etaE = (Ef2/Em-1)/(Ef2/Em+HT);
        E2 = Em*(1+HT*etaE*Vf)/(1-etaE*Vf);
        etaG = (Gf12/Gm-1)/(Gf12/Gm+HT);
        G12 = Gm*(1+HT*etaG*Vf)/(1-etaG*Vf);
        etaK = (kf/km-1)/(kf/km+HT);
        K = km*(1+HT*etaK*Vf)/(1-etaK*Vf);
    case 2
        E2 = 1/(Vf/Ef2+(1-Vf)/Em);
        G12 = 1/(Vf/Gf12+(1-Vf)/Gm);
        K = 1/(Vf/kf+(1-Vf)/km);
end
nu21 = nu12*E2/E1;
nu23 = 1-nu21-E2/2/K+E2*(1-2*nu12)/2/E1;
G23 = E2/2/(1+nu23);
Alpha1 = (Alphaf1*Ef1*Vf+Alpham*Em*(1-Vf))/(Ef1*Vf+Em*(1-Vf));
Alpha2 = (Alphaf2-Em*nuf12*(Alpham-Alphaf1)*(1-Vf)/E1)*Vf+(Alpham+Ef1*num*(Alpham-
Alphaf1)*Vf/E1)*(1-Vf);
```

```
Rhoc=Rhof*Vf+Rhom*(1-Vf);
Beta1=Em*Rhoc*Betam/(E1*Rhom);
Beta2=(1+num)*Rhoc*Betam/Rhom-Beta1*nu12;
set(handles.InE1,'string',E1);
set(handles.InE2,'string',E2);
set(handles.InG12,'string',G12);
set(handles.InG23,'string',G23);
set(handles.Innu12,'string',nu12);
set(handles.Innu23,'string',nu23);
set(handles.InAlpha1,'string',Alpha1);
set(handles.InAlpha2,'string',Alpha2);
set(handles.InBeta1,'string',Beta1);
set(handles.InBeta2,'string',Beta2);
guidata(hObject, handles);

function InEm_Callback(hObject, eventdata, handles)
% --- Executes during object creation, after setting all properties.
function InEm_CreateFcn(hObject, eventdata, handles)
if ispc && isequal(get(hObject,'BackgroundColor'), get(0,'defaultUicontrolBackgroundColor'))
    set(hObject,'BackgroundColor','white');
end

function InGm_Callback(hObject, eventdata, handles)
function InGm_CreateFcn(hObject, eventdata, handles)
if ispc && isequal(get(hObject,'BackgroundColor'), get(0,'defaultUicontrolBackgroundColor'))
    set(hObject,'BackgroundColor','white');
end

function Innum_Callback(hObject, eventdata, handles)
% --- Executes during object creation, after setting all properties.
function Innum_CreateFcn(hObject, eventdata, handles)
if ispc && isequal(get(hObject,'BackgroundColor'), get(0,'defaultUicontrolBackgroundColor'))
    set(hObject,'BackgroundColor','white');
end

function InVf_Callback(hObject, eventdata, handles)
% --- Executes during object creation, after setting all properties.
function InVf_CreateFcn(hObject, eventdata, handles)
if ispc && isequal(get(hObject,'BackgroundColor'), get(0,'defaultUicontrolBackgroundColor'))
    set(hObject,'BackgroundColor','white');
end

function InHT_Callback(hObject, eventdata, handles)
% --- Executes during object creation, after setting all properties.
function InHT_CreateFcn(hObject, eventdata, handles)
if ispc && isequal(get(hObject,'BackgroundColor'), get(0,'defaultUicontrolBackgroundColor'))
    set(hObject,'BackgroundColor','white');
end

% --- Executes on selection change in E2type.
function E2type_Callback(hObject, eventdata, handles)
% --- Executes during object creation, after setting all properties.
function E2type_CreateFcn(hObject, eventdata, handles)
if ispc && isequal(get(hObject,'BackgroundColor'), get(0,'defaultUicontrolBackgroundColor'))
    set(hObject,'BackgroundColor','white');
end
```

```
% --- Executes on button press in Plot_tf.
function Plot_tf_Callback(hObject, eventdata, handles)
% Get input data
E1 = 1e9*str2double(get(handles.InE1,'String'));
E2 = 1e9*str2double(get(handles.InE2,'String'));
G12 = 1e9*str2double(get(handles.InG12,'String'));
G23 = 1e9*str2double(get(handles.InG23,'String'));
nu12 = str2double(get(handles.Innu12,'String'));
nu23 = str2double(get(handles.Innu23,'String'));
Ina = str2num(get(handles.Ina,'String'));
Int = 1e-3*str2num(get(handles.Int,'String'));
numcount = numel(Int);
vector_length = numel(Ina)-numcount;
if vector_length ~= 0;
errordlg('The length of orientation and thickness vector not consistent','Input Error');
return
end
% get the real matrix of ply angle and ply thickness
Ina2 = zeros(1,numcount-1);
Int2 = zeros(1,numcount-1);
Ina3 = zeros(1,numcount);
Int3 = zeros(1,numcount);
switch get(handles.Symmetric,'Value')
   case 1
      rIna = Ina;
      rInt = Int;
      rnumcount = numcount;
   case 2
      for j = 1:numcount-1
         Int2(j) = Int(numcount-j);
         Ina2(j) = Ina(numcount-j);
      end
      rnumcount = numcount*2-1;
      rInt = [Int Int2];
      rIna = [Ina Ina2];
   case 3
      for k = 1:numcount;
         Int3(k) = Int(numcount+1-k);
         Ina3(k) = Ina(numcount+1-k);
      end
      rnumcount = numcount*2;
      rInt = [Int Int3];
      rIna = [Ina Ina3];
end
% define the complaince matrix
S11 = 1/E1;
S12 = -nu12/E1;
S22 = 1/E2;
S23 = -nu23/E2;
S44 = 1/G23;
S66 = 1/G12;
S = [S11 S12 S12 0 0 0;
   S12 S22 S23 0 0 0;
   S12 S23 S22 0 0 0;
   0 0 0 S44 0 0;
   0 0 0 0 S66 0;
```

```
   0 0 0 0 0 S66];
% calculate ABBD matrix of laminate
h=zeros(1,rnumcount+1);
for j=1:rnumcount+1;
   if j==1
      h(j)=-sum(rInt)/2;
   else
      h(j)=h(j-1)+rInt(j-1);
   end
end
theta=0:1:90;
L=length(theta);
tEx=zeros(1,L);tEy=zeros(1,L);
tGxy=zeros(1,L);tGyz=zeros(1,L);tGxz=zeros(1,L);
tnuxy=zeros(1,L);tnuyx=zeros(1,L);
tnuyz=zeros(1,L);tnuxz=zeros(1,L);
tetaxyx=zeros(1,L);tetaxyy=zeros(1,L);
fEx=zeros(1,L);fEy=zeros(1,L);
fGxy=zeros(1,L);fGyz=zeros(1,L);fGxz=zeros(1,L);
fnuxy=zeros(1,L);fnuyx=zeros(1,L);
fnuyz=zeros(1,L);fnuxz=zeros(1,L);
fetaxyx=zeros(1,L);fetaxyy=zeros(1,L);
for j=1:L
A = zeros(6,6);
B = zeros(6,6);
D = zeros(6,6);
   for i = 1:rnumcount
   c = cos((theta(j)+rIna(i))*pi/180);
   s = sin((theta(j)+rIna(i))*pi/180);
T = [c^2 s^2 0 0 0 2*c*s;
   s^2 c^2 0 0 0 -2*c*s;
   0 0 1 0 0 0;
   0 0 0 c s 0;
   0 0 0 -s c 0;
   -c*s c*s 0 0 0 c^2-s^2];
T1 = [c^2 s^2 0 0 0 c*s;
   s^2 c^2 0 0 0 -c*s;
   0 0 1 0 0 0;
   0 0 0 c s 0;
   0 0 0 -s c 0;
   -2*c*s 2*c*s 0 0 0 c^2-s^2];
Sbar = T1\S*T;
Cbar=inv(Sbar);
      for m = 1:6
         for n = 1:6
            A(m,n) = A(m,n)+Cbar(m,n)*(h(i+1)-h(i));
            B(m,n) = B(m,n)+Cbar(m,n)*((h(i+1))^2-(h(i))^2)/2;
            D(m,n) = D(m,n)+Cbar(m,n)*(h((i+1))^3-(h(i))^3)/3;
         end
      end
   end
ABBD = [A B;B D];abbd=inv(ABBD);
a=abbd(1:6,1:6);d=abbd(7:12,7:12);
a11=a(1,1);a12=a(1,2);a13=a(1,3);a16=a(1,6);
a22=a(2,2);a23=a(2,3);a26=a(2,6);
a44=a(4,4);a55=a(5,5);a66=a(6,6);
tEx(j)=1/(a11*sum(rInt));tEy(j)=1/a22/sum(rInt);tEz(j)=1/a(3,3)/sum(rInt);
tGxy(j)=1/a66/sum(rInt);tGyz(j)=1/a44/sum(rInt);tGxz(j)=1/a55/sum(rInt);
```

```
tnuxy(j) = -a12/a11;tnuyx(j) = -a12/a22;
tnuyz(j) = -a23/a22;tnuxz(j) = -a13/a11;
tetaxyx(j) = a16/a11;tetaxyy(j) = a26/a22;
fEx(j)=12/d(1,1)/sum(rInt)^3;fEy(j)=12/d(2,2)/sum(rInt)^3;fEz(j)=12/d(3,3)/sum(rInt)^3;
fGxy(j)=12/d(6,6)/sum(rInt)^3;fGyz(j)=12/d(4,4)/sum(rInt)^3;fGxz(j)=12/d(5,5)/sum(rInt)^3;
fnuxy(j) = -d(1,2)/d(1,1);fnuyx(j) = -d(1,2)/d(2,2);
fnuyz(j) = -d(3,2)/d(2,2);fnuxz(j) = -d(3,1)/d(1,1);
fetaxyx(j) = d(1,6)/d(1,1);fetaxyy(j) = d(2,6)/d(2,2);
end
% Plot tensile and flexural elastic properties
switch get(handles.tE,'Value')+get(handles.fE,'Value')
   case 1
      figure;
      if get(handles.tE,'Value')
         plot(theta,tEx/1e9,'b-o',theta,tEy/1e9,'b-*',theta,tEz/1e9,'b-+'); hold on;
         legend('Tensile Ex','Tensile Ey','Tensile Ez'); hold on;
         xlabel('Angle in degree(\theta)');
         ylabel('Modulus(GPa)');
      else
         plot(theta,fEx/1e9,'m-o',theta,fEy/1e9,'m-*',theta,fEz/1e9,'m-+'); hold on;
         legend('Flexural Ex','Flexural Ey','Flexural Ez'); hold on;
         xlabel('Angle in degree(\theta)');
         ylabel('Modulus(GPa)');
      end
   case 2
      figure;
      plot(theta,tEx/1e9,'b-o',theta,tEy/1e9,'b-*',theta,tEz/1e9,'b-',...
         theta,fEx/1e9,'mo',theta,fEy/1e9,'m*',theta,fEz/1e9,'m+'); hold on;
      legend('Tensile Ex','Tensile Ey','Tensile Ez','Flexural Ex','Flexural Ey','Flexural Ez'); hold on;
      xlabel('Angle in degree(\theta)');
      ylabel('Modulus(GPa)');
end
switch get(handles.tG,'Value')+get(handles.fG,'Value')
   case 1
      figure;
      if get(handles.tG,'Value')
         plot(theta,tGxy/1e9,'b-o',theta,tGyz/1e9,'b-*',theta,tGxz/1e9,'b-+'); hold on;
         legend('Tensile Gxy','Tensile Gyz','Tensile Gxz'); hold on;
         xlabel('Angle in degree(\theta)');
         ylabel('Modulus(GPa)');
      else
         plot(theta,fGxy/1e9,'m-o',theta,fGyz/1e9,'m-*',theta,fGxz/1e9,'m-+'); hold on;
         legend('Flexural Gxy','Flexural Gyz','Flexural Gxz'); hold on;
         xlabel('Angle in degree(\theta)');
         ylabel('Modulus(GPa)');
      end
   case 2
      figure;
      plot(theta,tGxy/1e9,'b-o',theta,tGyz/1e9,'b-*',theta,tGxz/1e9,'b-+',...
         theta,fGxy/1e9,'m-o',theta,fGyz/1e9,'m-*',theta,fGxz/1e9,'m-+'); hold on;
      legend('Tensile Gxy','Tensile Gyz','Tensile Gxz',...
         'Flexural Gxy','Flexural Gyz','Flexural Gxz'); hold on;
      xlabel('Angle in degree(\theta)');
      ylabel('Modulus(GPa)');
end
switch get(handles.tnu,'Value')+get(handles.fnu,'Value')
   case 1
      figure;
```

```
        if get(handles.tnu,'Value')
            plot(theta,tnuxy,'b-o',theta,tnuyz,'b-*',theta,tnuxz,'b-+'); hold on;
            legend('Tensile tnuxy','Tensile tnuyz','Tensile tnuxz'); hold on;
            xlabel('Angle in degree(\theta)');
            ylabel('Poisson ratio');
        else
            plot(theta,fnuxy,'m-o',theta,fnuyz,'m-*',theta,fnuxz,'m-+'); hold on;
            legend('Flexural fnuxy','Flexural fnuyz','Flexural fnuxz'); hold on;
            xlabel('Angle in degree(\theta)');
            ylabel('Poisson ratio')
        end
    case 2
        figure;
        plot(theta,tnuxy,'b-o',theta,tnuyz,'b-*',theta,tnuxz,'b-+',...
            theta,fnuxy,'m-o',theta,fnuyz,'m-*',theta,fnuxz,'m-+'); hold on;
        legend('Tensile tnuxy','Tensile tnuyz','Tensile tnuxz',...
            'Flexural fnuxy','Flexural fnuyz','Flexural fnuxz'); hold on;
        xlabel('Angle in degree(\theta)');
        ylabel('Poisson ratio')
end
switch get(handles.teta,'Value')+get(handles.feta,'Value')
    case 1
        figure;
        if get(handles.teta,'Value')
            plot(theta,tetaxyx,'b-o',theta,tetaxyy,'b-*'); hold on;
            legend('Tensile tetaxyx','Tensile tetaxyy'); hold on;
            xlabel('Angle in degree(\theta)');
            ylabel('Interaction ratio');
        else
            plot(theta,fetaxyx,'m-o',theta,fetaxyx,'m-*'); hold on;
            legend('Flexural fetaxyx','Flexural fetaxyy'); hold on;
            xlabel('Angle in degree(\theta)');
            ylabel('Poisson ratio')
        end
    case 2
        figure;
        plot(theta,tetaxyx,'b-o',theta,tetaxyy,'b-*',theta,fetaxyx,'m-o',theta,fetaxyx,'m-*'); hold on;
        legend('Tensile tetaxyx','Tensile tetaxyy','Flexural fetaxyx','Flexural fetaxyy'); hold on;
        xlabel('Angle in degree(\theta)');
        ylabel('Poisson ratio')
end
guidata(hObject, handles);


% --- Executes on selection change in elastic_Vf.
function elastic_Vf_Callback(hObject, eventdata, handles)
% --- Executes during object creation, after setting all properties.
function elastic_Vf_CreateFcn(hObject, eventdata, handles)
if ispc && isequal(get(hObject,'BackgroundColor'), get(0,'defaultUicontrolBackgroundColor'))
    set(hObject,'BackgroundColor','white');
end

% --- Executes on button press in Plot_Vf.
function Plot_Vf_Callback(hObject, eventdata, handles)
Ef1 = str2double(get(handles.InEf1,'String'));
Ef2 = str2double(get(handles.InEf2,'String'));
Gf12 = str2double(get(handles.InGf12,'String'));
```

```
nuf12 = str2double(get(handles.Innuf12,'String'));
nuf23 = str2double(get(handles.Innuf23,'String'));
Em = str2double(get(handles.InEm,'String'));
Gm = str2double(get(handles.InGm,'String'));
num = str2double(get(handles.Innum,'String'));
HT = str2double(get(handles.InHT,'String'));
Vf = 0:0.01:1;
% calculate E1,nu12
pE1 = Ef1*Vf+Em*(1-Vf);
pnu12 = nuf12*Vf+num*(1-Vf);
% Halpin & Tsai E2,G12
etaE = (Ef2/Em-1)/(Ef2/Em+HT);
etaG = (Gf12/Gm-1)/(Gf12/Gm+HT);
phE2 = Em*(1+HT*etaE*Vf)./(1-etaE*Vf);
phG12 = Gm*(1+HT*etaG*Vf)./(1-etaG*Vf);
% Equal stress E2,G12
peE2 = 1./(Vf/Ef2+(1-Vf)/Em);
peG12 = 1./(Vf/Gf12+(1-Vf)/Gm);
% Calculate nu23,G23
kf = Ef1*Ef2/(2*Ef1*(1-nuf12*Ef2/Ef1-nuf23)+Ef2*(1-2*nuf12));
km = Em/3/(1-2*num);
etaK = (kf/km-1)/(kf/km+HT);
K = km.*(1+HT*etaK*Vf)./(1-etaK*Vf);
Ke = 1./(Vf/kf+(1-Vf)/km);
phnu21 = pnu12.*phE2./pE1;
phnu23 = 1-phnu21-phE2/2./K+phE2.*(1-2*pnu12)/2./pE1;
penu21 = pnu12.*peE2./pE1;
penu23 = 1-penu21-peE2/2./Ke+peE2.*(1-2*pnu12)/2./pE1;
phG23 = phE2./2./(1+phnu23);
peG23 = peE2./2./(1+penu23);
switch get(handles.elastic_Vf,'Value');
   case 1
      figure;
      plot(Vf,pE1,'r-*',Vf,phE2,'g-o',Vf,peE2,'b-+','LineWidth',2);hold on;
      legend('E1','E2 in Halpin&Tsai','E2 in Equal stress'); hold on;
      xlabel('Volume fraction');
      ylabel('Modulus(GPa)');
%        axis([0,1,0,50]);
   case 2
      figure;
      plot(Vf,phG12,'r-*',Vf,peG12,'r-o',Vf,phG23,'g-*',Vf,peG23,'g-o');
      legend('G12 in Halpin&Tsai','G12 in Equal stress','G23 in Halpin&Tsai','G23 in Equal stress'); hold
on;
      xlabel('Volume fraction');
      ylabel('Modulus(GPa)');
   case 3
      figure;
      plot(Vf,pnu12,'r-*',Vf,phnu21,'b-+',Vf,penu21,'b-o',Vf,phnu23,'c-+',Vf,penu23,'c-o');
      legend('\nu12','\nu21 in Halpin&Tsai','\nu21 in Equal stress','\nu23 in Halpin&Tsai','\nu23 in Equal
stress'); hold on;
      xlabel('Volume fraction');
      ylabel('Poisson ratio(\nu)');
   case 4
      figure;
      plot(Vf,K,'r-o',Vf,Ke,'b-*');
      legend('K in Halpin & Tsai','K in Equal stress'); hold on;
      xlabel('Volume fraction');
      ylabel('Bulk modulus(GPa)');
```

```
end

% --- Executes on button press in ILSS_plot.
function ILSS_plot_Callback(hObject, eventdata, handles)
function stress_plot_Callback(hObject, eventdata, handles)

% --- Executes on button press in ABBD1_plot.
function ABBD1_plot_Callback(hObject, eventdata, handles)
% --- Executes on button press in abbd2_plot.
function abbd2_plot_Callback(hObject, eventdata, handles)
function InAlphaf1_Callback(hObject, eventdata, handles)
% --- Executes during object creation, after setting all properties.
function InAlphaf1_CreateFcn(hObject, eventdata, handles)
if ispc && isequal(get(hObject,'BackgroundColor'), get(0,'defaultUicontrolBackgroundColor'))
    set(hObject,'BackgroundColor','white');
end
function InAlphaf2_Callback(hObject, eventdata, handles)
% --- Executes during object creation, after setting all properties.
function InAlphaf2_CreateFcn(hObject, eventdata, handles)
if ispc && isequal(get(hObject,'BackgroundColor'), get(0,'defaultUicontrolBackgroundColor'))
    set(hObject,'BackgroundColor','white');
end
function InRhof_Callback(hObject, eventdata, handles)
% --- Executes during object creation, after setting all properties.
function InRhof_CreateFcn(hObject, eventdata, handles)
if ispc && isequal(get(hObject,'BackgroundColor'), get(0,'defaultUicontrolBackgroundColor'))
    set(hObject,'BackgroundColor','white');
end
function InAlpham_Callback(hObject, eventdata, handles)
% --- Executes during object creation, after setting all properties.
function InAlpham_CreateFcn(hObject, eventdata, handles)
if ispc && isequal(get(hObject,'BackgroundColor'), get(0,'defaultUicontrolBackgroundColor'))
    set(hObject,'BackgroundColor','white');
end

function InBetam_Callback(hObject, eventdata, handles)
% --- Executes during object creation, after setting all properties.
function InBetam_CreateFcn(hObject, eventdata, handles)
if ispc && isequal(get(hObject,'BackgroundColor'), get(0,'defaultUicontrolBackgroundColor'))
    set(hObject,'BackgroundColor','white');
end
function InRhom_Callback(hObject, eventdata, handles)
% --- Executes during object creation, after setting all properties.
function InRhom_CreateFcn(hObject, eventdata, handles)
if ispc && isequal(get(hObject,'BackgroundColor'), get(0,'defaultUicontrolBackgroundColor'))
    set(hObject,'BackgroundColor','white');
end
function InAlpha1_Callback(hObject, eventdata, handles)
% --- Executes during object creation, after setting all properties.
function InAlpha1_CreateFcn(hObject, eventdata, handles)
if ispc && isequal(get(hObject,'BackgroundColor'), get(0,'defaultUicontrolBackgroundColor'))
    set(hObject,'BackgroundColor','white');
end
function InAlpha2_Callback(hObject, eventdata, handles)
% --- Executes during object creation, after setting all properties.
function InAlpha2_CreateFcn(hObject, eventdata, handles)
if ispc && isequal(get(hObject,'BackgroundColor'), get(0,'defaultUicontrolBackgroundColor'))
```

```
    set(hObject,'BackgroundColor','white');
end

function InBeta1_Callback(hObject, eventdata, handles)

% --- Executes during object creation, after setting all properties.
function InBeta1_CreateFcn(hObject, eventdata, handles)
if ispc && isequal(get(hObject,'BackgroundColor'), get(0,'defaultUicontrolBackgroundColor'))
    set(hObject,'BackgroundColor','white');
end

function InBeta2_Callback(hObject, eventdata, handles)
% --- Executes during object creation, after setting all properties.
function InBeta2_CreateFcn(hObject, eventdata, handles)
if ispc && isequal(get(hObject,'BackgroundColor'), get(0,'defaultUicontrolBackgroundColor'))
    set(hObject,'BackgroundColor','white');
end

% --- Executes on button press in CTECHE.
function CTECHE_Callback(hObject, eventdata, handles)

% --- Executes on selection change in point.
function point_Callback(hObject, eventdata, handles)

% --- Executes during object creation, after setting all properties.
function point_CreateFcn(hObject, eventdata, handles)
if ispc && isequal(get(hObject,'BackgroundColor'), get(0,'defaultUicontrolBackgroundColor'))
    set(hObject,'BackgroundColor','white');
end
```